INTERFEROMETRIC TECHNIQUES FOR MEASURING FLOW VELOCITY FIELDS

Pilar Arroyo, Paz Alvarez, Nieves Andrés and Manuel Quintanilla
Dpto. Física Aplicada, Universidad de Zaragoza, Pedro Cerbuna 12, 50009 - Zaragoza, Spain

Summary Holographic interferometry and digital speckle pattern interferometry as techniques for measuring out-of-plane velocity fields are presented. The feasibility of introducing phase shifting techniques in order to improve the accuracy of holographic interferometry is investigated. The techniques are demonstrated in a Rayleigh-Bénard convective flow.

INTRODUCTION

Interferometry includes a range of optical techniques for measuring phase differences between two waves. If the two waves come from the same object but separated in time by an interval ΔT, the phase differences $\Delta\phi$ will be related with the local displacements, **d**, occurred to the object in that time interval. It can be shown that

$$\Delta\phi = \mathbf{K}\cdot\mathbf{d} \tag{1}$$

where $\mathbf{K} = (2\pi/\lambda)\,[\mathbf{u}_o - \mathbf{u}_i]$ is the sensitivity vector, being $\mathbf{u}_o$ and $\mathbf{u}_i$ unity vectors in the observation and illumination directions respectively. Thus, by measuring $\Delta\phi$ the projection of **d** along the direction of **K** can be inferred.

Holographic interferometry (HI) and digital speckle pattern interferometry (DSPI) are two whole-field interferometric techniques,[1] that mainly differ in the way the phase differences are detected. In HI, the two object waves are holographically recorded. A reconstruction of the hologram, using a pointwise beam, produces an interference pattern over the object real image, i.e. an *interferogram*, where the brightest fringes correspond to phase differences such that

$$\Delta\phi = 2\,n\,\pi, \quad n = 0, \pm 1, \pm 2, \ldots \tag{2}$$

with the integer n being known as the fringe order.

In DSPI, also known as TV-holography, the holographic plate is replaced by a video camera as the recording medium. In this case, the camera records the interference between an speckled object wave and a reference wave (*specklegram*), whose relative angle is kept as small as possible due to the low spatial resolution of the CCD sensors. Two specklegrams, corresponding to the two object waves, are recorded separately in different camera frames. The absolute intensity difference between them produces a *speckle interferogram*, i.e. a speckled image, whose mean intensity depends sinusoidally on $\Delta\phi$. Now, the brightest fringes correspond to phase differences such that

$$\Delta\phi = (2\,n + 1)\,\pi\,, \quad n = 0, \pm 1, \pm 2, \ldots \tag{3}$$

The most straightforward techniques for automatically measuring the phase $\Delta\phi$ from an interferogram[2] are based on the detection of the image intensity with reported accuracies of the order of 0.2 π. However, in complicated interferograms, reliable fringe numbering may be impossible. Alternatively, the phase can be directly measured by using phase shifting techniques. In this case, a known phase change is superimposed to the deformation phase between the two object waves. A different interferogram will be obtained for each phase change. The deformation phase is now obtained at each CCD pixel by a simple equation involving the intensity pixel in several interferograms. The main advantage of these phase shifting techniques are that the processing is very simple and the precision is about an order of magnitude better than that of the intensity based techniques. Besides, fringe numbering is not a problem even with complicated interferograms. The main drawback is that it is not always feasible to introduce the phase shifting devices.

HI and DSPI are very widely used in solid mechanics for the measurement of deformations and displacements. Here, we present the investigation carried out in order to extend such techniques to the measurement of flow velocity fields. In HI and DSPI as flow velocimetry techniques, the object waves consists on the light scattered by the tracers in a fluid plane that is formed by illumination with a sheet like laser beam. This means that the illumination direction $\mathbf{u}_i$ is determined by the fluid plane and so, the sensitivity vector **K** is always an out-of-plane vector. Thus, HI and DSPI as velocimetry techniques are more sensitive to out-of-plane velocity components than to in-plane components. Different velocity components can be measured by changing $\mathbf{u}_o$. However, since the flows are usually unsteady, the interferograms for each different $\mathbf{u}_o$ have to be recorded simultaneously. In HI, the three components can be obtained from the same hologram by changing the location of the reconstruction beam. In DSPI only one component can be obtained with one camera. Although a system with three cameras may be designed, it looks more convenient to combine PIV (particle image velocimetry) and DSPI, which will require only two cameras.

PHASE SHIFTING HOLOGRAPHIC INTERFEROMETRY

HI as a velocimetry technique has already been demonstrated[3-4] but using intensity based methods for the interferogram analysis. Here, we present the investigation carried out in order to introduce phase shifting techniques. Figure 1 shows the experimental setup used in our experiments. As compared with previous setups[3], the main difference is the use of different reference beams to record each of the two object waves. The phase shifts are introduced in the reconstruction process by changing the relative phase between the two reconstruction beams. Two very small angle wedges (~ 6 arcmin) are placed in one reconstruction beam. The phase shift is introduced by displacing one wedge while not moving the other. About 2π / mm is the rate of shift introduced by this system.

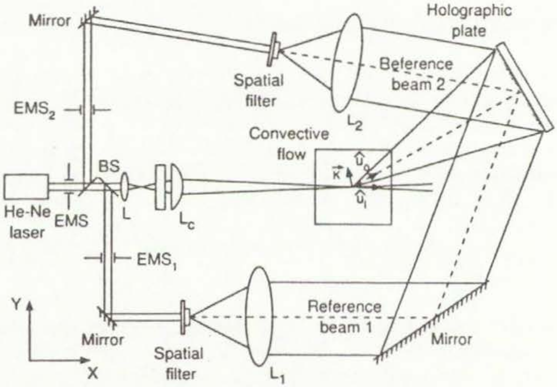

Figure 1. Experimental PSHI setup (top view).

PSHI has been setup in a Rayleigh-Bénard convective flow. The convective cell consists of a 20 mm thick plexiglass frame placed between two 10 mm thick cooper plates. The cell, whose inside dimensions are 25 x 25 x 12.5 mm, is filled with an aqueous glycerol solution. The fluid is seeded with 5 μm diameter latex particles. Flow velocities have been selected in the range of a few μm/sec, to match our recording capabilities.

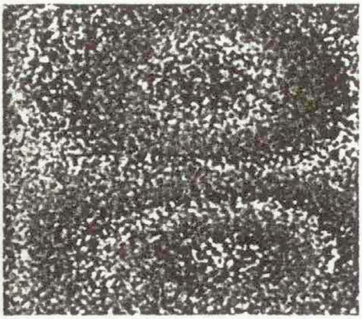
Figure 2. PSHI wrapped phase map

A 17 mW He-Ne laser has been used for illumination. Three appropriately synchronized electromechanical shutters have been used to produce two 5 ms exposures at a time interval of 41.5 ms. The holographic plate has been placed at 20° from the illumination direction, which makes the setup mainly sensitive to the V_y field.

Figure 2 shows the wrapped modulo 2π phase map, visualized as gray levels with a gray of 255 corresponding to a phase of 2π. It has been obtained from a plane at 6 mm from the wall. Although some improvement is still needed, the image is much better than any of the interferograms used to retrieve the phase. The maximum displacement is about 2 μm, which corresponds to a velocity of 43 μm/s.

DIGITAL SPECKLE PATTERN INTERFEROMETRY

DSPI has never before been used as a velocimetry technique. Figure 3 shows the experimental setup used in our experiments. It corresponds to the case where both the object and the reference beams are speckle fields. The speckled reference beam is produced by the light passing through a ground glass plate. Both reference and object beams have been combined by means of a beamsplitter placed in front of the CCD camera lens. As seen in figure 3, the sensitivity vector is at 45° with the illumination direction.

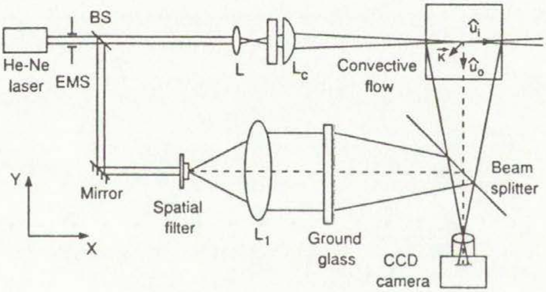

Figure 3. Experimental DSPI setup (top view).

Series of 15 specklegrams have been recorded with a digital camera at a frequency of 15 frames per second. Exposure time for each frame was 8 ms. Figure 4 shows the speckle interferograms obtained from two succesive specklegrams ($\Delta T = 66.66$ ms) or from two alternate specklegrams ($\Delta T = 132.32$ ms) corresponding to the same series. It can be seen that the number of fringes doubles as the ΔT doubles. Figure 4 also clearly shows where the zero velocity component occurs: it corresponds to the dark fringe that is common to both interferograms. These speckle interferograms have been obtained from the same $y = 6$ mm plane used in the PSHI experiments. However, the flow was setup at lower velocities because the modulus of the sensitivity vector is bigger in the DSPI configuration due to its different direction. The maximum 45° displacement is about 0.75 μm in figure 4a and 1.25 μm in figure 4b. The corresponding maximum 45° velocity component is about 10 μm/sec.

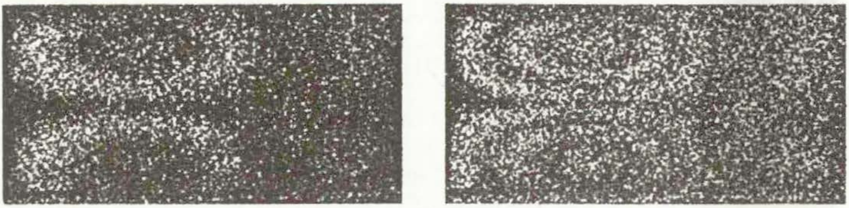

a) b)

Figure 4: DSPI speckle interferograms for: a) $\Delta T = 66.66$ ms; b) $\Delta T = 132.32$ms.

CONCLUSION

Phase shifting holographic interferometry and digital speckle pattern interferometry as techniques for measuring out-of-plane velocity fields have been described. It has been shown that both techniques are based on the same principles, mainly differing in the recording medium. Thus, DSPI can be viewed as the digital version of HI. In the future, we plan to introduce phase shifting techniques in DSPI.

ACKNOWLEDGMENTS

This research was partially supported by the University of Zaragoza under the Research Support Programme and by DGES under grant PB96-039-C03-02.

REFERENCES

1. Jones R., Wykes C.: Holographic and speckle interferometry. Cambridge University Press, Cambridge, 1989.
2. Robinson D. W., Reid G. T. eds.: Interferogram analysis: digital fringe pattern measurement techniques. Institute of Physics Publishing, Bristol 1993.
3. Andrés N., Arroyo M. P., Quintanilla M.: Velocity measurements in a convective flow by holographic interferometry. *Appl. Opt.* **36**, pp 6997 - 7007, 1997.
4. Andrés N., Arroyo M. P., Quintanilla M., Hinrichs H., Hinsch K.: Holographic interferometry as a velocimetry technique in gaseous flows. *IMechE.* **C541**, pp 3 - 9, 1998.

LIMITS OF DIVISION NON-METALLIC ENGAGING - METALLIC MOULD IN THE COMPOSITION MATERIAL OF THE GRANULE B_4C - (TI-NI-MO)

Belousov V.Y., Dubrovskaya G.N., Olekseenko N.V.
Cherkassy Institute of Engineering and Technology, 460 Shevchenko BLVD,
Cherkassy 257006, Ukraine

Abstract. Nonmetallic inclusion-metallic matrix interface structure in refractory compound-based composite materials seriously affects such events as plastic strain and rupture. Boron carbide (Ti-Ni-Mo) binder granule material structure was studied by X-ray phase and microspectrum analysis. Study of phase makeup of B_4C-metallic binder transition zone revealed existence of two-phase zone consisting of bond and carbon phases.

Plastic strain and rupture of refractory compound-based composite materials used in manufacture of drilling tools for oil and gas industry significantly depend upon nonmetallic binder-metallic matrix interface structure. Strong phase interface-binder is one of the important factors for production of superstrong materials [1].

This project analysed composite material based on boron carbide granules (~150-300 μm) with Ti-Ni-Mo binder and shows its possible applications in drilling tools for oil and gas industry [2]. X-ray structure and microscopic methods of analysis were used for this project. X-ray phase analysis was conducted on D5000 diffractometer in CuK_α radiation, and X-ray microscopic analysis was conducted on Stereoscan 200 electron microscope. Measurements of microhardness were taken to evaluate mechanical properties of alloy. Testing was done by means of indentor depression on Micromet (Buehler-Met AG, Switzerland) with automatic load. Lap surface impressions were made with Vickers pyramid at 50 H load.

Fig. 1 shows composition bond structure with well-defined transition zone growth of carbide granule-metallic binder 12 μm in width. Pulished reports indicate that a transition zone for boron carbide-metal system has a phase composition of both boron carbide and metal [3]. Analysis of phase composition of B_4C- (Ti-Ni-Mo) metallic binder interface was done by means of comparing results of X-ray microspectral (fig.2) and phase analyses (fig.3). X-ray phase analysis did not reveal any boride phases in the material, which indicates no boron diffusion from B_4C. The transition zone registered presence of three elements - Ti, Mo, and C. Testing results lead to the conclusion that B_4C- (Ti-Ni-Mo) metallic binder granule transition zone develops titanium carbide and solid solutions of molybdenum in titanium carbide, with titanium carbide located closer to B_4C carbide granules and present in far smaller quantities that (Ti,Mo)C.

Presence of solid solution of molybdenum in titanium carbide leads to higher overall strength of material as well as improvement of such properties as bending strength and thermodynamic stability, which indicates a stronger interface chemical bond and guarantees lower possibility of material rupture along carbide granule-metallic binder interfaces.

Fig. 4. shows results of microdurometric tests of B_4C-metallic binder (Ti-Ni-Mo) granule transition zone. At was found that microhardness of transition zone 7-12 μm wide gradually decreases from $45\text{x}10^3$ MPa to $20\text{x}10^3$ MPa with moving away from carbide granule, which is explained by a higher quantity of molybdenum in (TiMo)C solid solution.

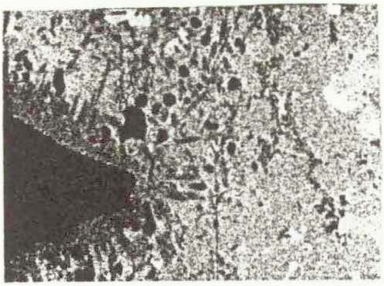

Fig 1. Carbide-metallic binder interface structure for B_4C- (Ti-Ni-Mo), magn. 450.

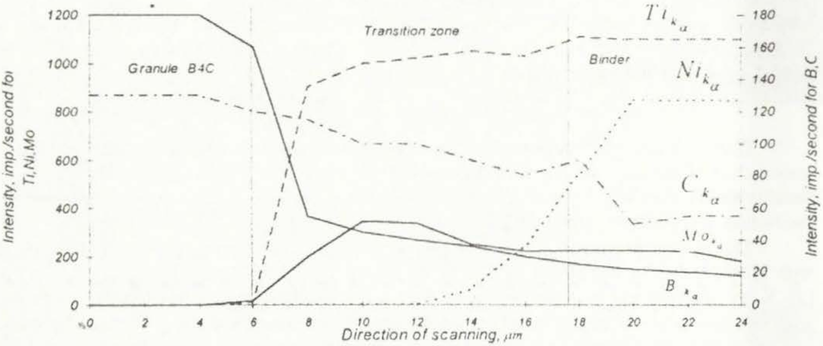

Fig 2. Concentration distribution of elements in characteristic X-ray radiation.

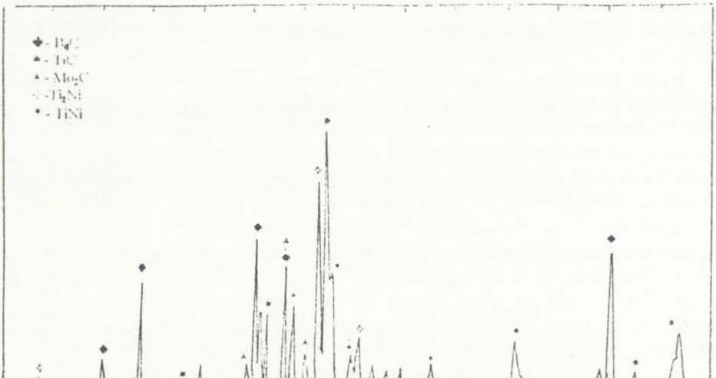

Fig. 3 . Diffractogram of phase composition of B_4C- (Ti-Ni-Mo) composite

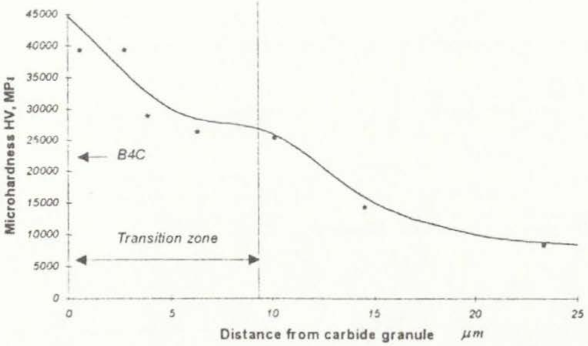

Fig.4. Change of microhardness on the surface of composition in B_4C granule - (Ti-Ni-Mo) binder contact zone

References:

1.Belousov V.J. Long-lived detail of machines with the composite material. 1984, Lviv university, 180p

2.Luzak L.D. Dissertation :05.02.04/ Ivano-Frankovsk, institute from oil and gas, 1988, -170 p.

3. Kislij P.S., Kusenkova M.A., Bondaruc N.I., Grabchuk B.I. Carbide boron. - Kiev: Naukova dumka, 1988.-216p.

4. Dubrovskaja G.N., Belousov V.J., Oleksijenko N.V. Structureformed in the alloys on the basis of carbide boron - (Ti-Ni-Mo) binder, which receive . Collection Nation. Academia Ukraine " Materials on the basis of carbide", Kiev,1995. p.66.

SHAPE DEFORMATION ANALYZIS OF RAIL CAR BRAKES WITH USING IMAGE PROCESSING TECHNIQUES

Piotr Boguś[*], Stanisław Bocian[**]

[*]Medical Academy of Gdańsk, Department of Physics and Biophysics, Dębinki 1, 80-211 Gdańsk, Poland

[**]Research-Development Rail Vehicles Center, Warszawska 181, 61-055 Poznań, Poland

Summary The paper presents the current state of the researches on modern rail car brakes diagnosing and supervising. Our considerations concern the estimation of the brake friction parts wear by measuring friction elements thickness using image processing techniques.

INTRODUCTION

The application of the pattern recognition and image processing to a technical equipment diagnosing became very popular last time. New techniques from this field allow to use a camera collaborating with a computer vision system instead of a human being. The main task in such an approach is a diagnosing basing on part shapes deformations.

In the literature one can find many methods and approaches to similar problmes[1-5] among others some based on neural networks[6], among others the methods taken from robot vision systems where the main task is similar and focuses on parts recognition of parts in the robot visual field[7-8].

PROBLEM DESCRIPTION

The state of the car brakes is shown by the wear of mechanical friction parts and can be determined by estimating the thickness of break friction elements. The general diagrammatic bottom view of break disk with friction lining is presented on Figure 1.

The main task of the diagnostic image system is to measure the friction lining thickness (denote as d on Figure 1) and the external side of break disk thickness (denote as c on Figure 1). Figure 1 presents also characteristic fragments of the image using to scaling the image dimensions. There are elements which fix brake blocks (fixed distance a) and control lines which limit internal, minimal for safe work, thickness of a break disk (fixed distance b). Distances a and b are used to scale in two perpendicular dimensions.

On a typical car running set axis there are two disks and a co-operating with each of them pair of friction elements – brake blocks. In a high-speed running sets there are three disks with six blocks. Hence it needs to use corresponding four or six cameras.

In general, a schema of the visual system will consist of CCD cameras, stroboscopic tubes, a/d converters, signal processors and computer PC with image analysing and data base systems. The measurement will be performed during a rail car moving with the maximum velocity of 5 km/h. An example image obtained by using a CCD camera is presented on Figure 2.

APPROACHES TO THE PROBLEM

We consider the following approaches to the above presented problem:

1. A manual estimation of thickness bases on the image presented to the user on the computer monitor. This is the simplest solution assumed at the initial stage of a system developing.

2. An approach which takes into consideration some properties characteristic for the given problem. Sometimes such solutions appear simple and fast but they are limited to the given unique case. For a

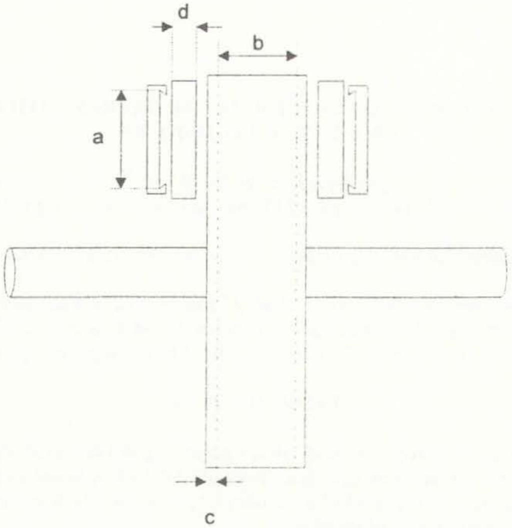

Figure 1. The general diagrammatic bottom view of rail car brakes

situation when the objects of interest on the image have enough stable positions we consider methods based on one dimension edge detection.

3. An approach which bases on simply image processing methods like segmentation (by edge detection techniques) and next a simply analysis to find the position of the relevant object and it dimensions. They very often are limited only to the unique given specific case. In this approach very promising seems methods of detecting elements with a prior known shapes[8] and so called, model based recognition[7], where the input images and their objects are matching with a set of predefined models.

4. An approach which uses full pattern recognition techniques. Here one must prepare the full image analysis using one of three main methods:

- Global feature method which considers features base on the properties like brightness, colour, texture etc. This methods are very popular in some applications (e.g. for medical images) but in the described above problem they do not seem to be very useful (especially because of their complexity and long calculation time).
- Structural feature method which considers features base on geometrical properties like edges, angles, lines, arcs, holes, borders etc. These methods seem the most interesting in presented here problem.
- Relational dependencies method which considers relations between objects often describe by graphs. This approach usually needs some extra knowledge about the given image. This knowledge can significantly improve the image analysis. The main problem here is the choice of the right method of knowledge representation (e.g. graphs, frames etc.).

After feature analysis basing on a training set one should perform learning to prepare image segmentation and classification or automatic clustering in feature space to obtain image segmentation and next recognition of parts and finding their characteristics.

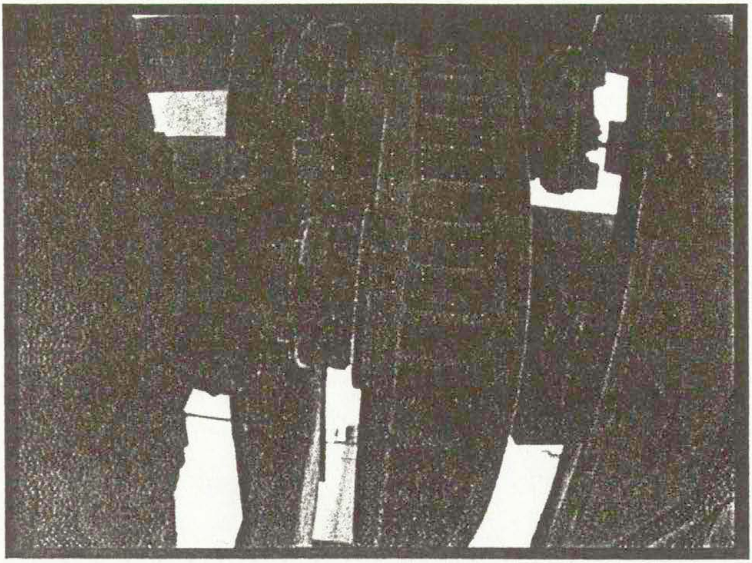

Figure 2 An example image of the rail car brakes.

CONCLUSION

On the current state of research we have not been built a full image acquisition system yet hence most of our consideration are preliminary. We were testing only exemplary images taken by a single camera without a full vision system.

REFERENCES

1. Castleman K. R.: Digital Images Processing. Prentice Hall, New Jersey 1996.
2. Gose E., Johnsonbaugh R., Jost S.: Pattern Recognition and Image Analysis. Prentice Hall, New Jersey1996.
3. Pavlidis T.: Grafika i przetwarzanie obrazów. WNT, Warszawa 1987.
4. Prasad L., Iyener S. S.: Wavelet Analysis with Applications to Image Processing. CRC Press, New York 1997.
5. Woźnicki J.: Podstawowe techniki przetwarzania obrazu. WKŁ, Warszawa 1996.
6. Bishop C. M.: Neural Networks for Pattern Recognition. Clarendon Press, Oxford 1995.
7. Chin R. T., Dyer C. R.: Model-Based Recognition in Robot Vision. *ACM Computing Surveys* **18**, pp. 67-108, 1986.
8. Tadeusiewicz R.: Systemy wizyjne robotów przemysłowych. WNT, Warszawa 1992.

Simultaneous DPIV measurements of two-phase particle-liquid flow

J. Bolinder[1], Wu Zhi Lei and L. Fuchs
Lund Institute of Technology
Division of Fluid Mechanics
Box 118, 221 00 Lund, Sweden

Introduction

Modeling solid particle transport in a liquid turbulent flow is a difficult subject due to the equal importance of most of the terms in the particle equation of motion. Experimental methods, such as particle image velocimetry (PIV), may provide information in complex flow situations that currently may not be obtained by numerical simulations.

The principle of PIV is to illuminate the flow field of interest by a plane light sheet from a pulsed laser, usually a frequency doubled Nd:YAG laser. The flow is seeded with small tracer particles, which scatter the laser light. The illuminated flow plane is imaged on to a photographic film, or a CCD chip, in which case one talks about digital PIV (DPIV). The tracer particles appear as light spots in the flow image. By illuminating the flow field twice, with a known time separation, one may determine the velocity field in the flow plane from the distance traveled by the tracer particles during the two light pulses. This is usually done by cross-correlating small interrogation areas in the images. Since one in PIV actually measures the velocity of the tracer particles, the method is well suited for measuring the dispersed phase of a two-phase flow, where the dispersed phase may be either solid particles, bubbles or dropplets.

There are a few previous simultaneous PIV or PTV (particle tracking) measurements of two phases reported in the literature. Hassan et al. (1992) used particle tracking velocimetry to measure the velocity of both phases of a liquid-bubble flow. McCluskey et al. (1993) used PIV to measure both phases of an air-particle jet. Sakakibara et al. (1996) also measured in an air-particle jet by DPIV, and provided results on the particle-fluid velocity correlation and the extra dissipation due to the particle motion relative the fluid. Common for all these studies is that the bubbles or particles are much bigger than the tracer particles used to measure the continuous phase, so that in the flow images the two kinds of particles are easy to distinguish by their different image size and intensity. Then some kind of threshold technique is used to separate the two phases in the images.

The goal of the present project is to measure by DPIV simultaneously the instantaneous velocity field of both phases of a particle-liquid flow. Then we may obtain a two-dimensional picture of the instantaneous velocity-slip field of the two phases, and we may also calculate the spatial correlation of the two velocity fields. The basic idea is to use two cameras to take simultaneous images of the same flow region. By using fluorescing particles for either the particle phase or the tracer particles, and a filter in front of one camera to filter out the Mie-scattered laser light, only the fluorescing particles will appear in one image. In the other image, both particles will appear. By using the information of the location of the fluorescing particles in the first image, the corresponding particles may be removed in the second image. The pleasant thing about this technique compared to the previously reported, is that the two kinds of particles may be of the same size.

---

[1] Corresponding author

Flow facility and Measurement system

For testing purposes we have measured the flow created by a magnetic stirrer in a small rectangular plexiglass box. The flow is highly turbulent, and the mean flow shows some large-scale vortex structures. The continuous phase is water. The tracer particles (Expancel) are spherical with a diameter of 10-20 μm, and a density very close to that of water. The dispersed phase consists of fluorescing particles of about 75 μm, which are slightly heavier than water. The fluorescing particles are doped with Rhodamine B, and may be excited by the green 532 nm light of an Nd:YAG laser. The fluorescence is in orange, with a max around 590 nm.

The DPIV system consists of a frequency-doubled Nd:YAG laser with two oscillators of 25 mJ each, with a common beam outlet, and two cross-correlation CCD-cameras with a resolution of 1280x1024 pixels. Since the light source is common for both cameras, they will capture the flow at exactly the same time. The cameras are made to look at the same flow region by means of a beam-splitter and mirror system, see Fig. 1.

Image processing algorithm

The first step is to correlate simultaneously taken images from the two cameras to get the displacement field of the images. This is necessary, since with the present camera set-up it is not possible to get perfectly overlapping images. A typical misalignment of a few pixels is obtained (one pixel corresponds to about 50 μm in the flow plane). This displacement field is then used to identify matching pairs of fluorescing particles in the two images.

The position of the particle peaks in the filtered image is determined to sub-pixel accuracy by fitting a two-dimensional Gaussian function to the pixel intensities about each peak. Then the local image displacement is added to find the most likely position of the corresponding particle in the unfiltered image. If no peak is detected at the expected position, the eight closest pixels are checked to see if any of them is a peak. For typically 50-90 % of the cases a peak is detected at the first expected position, and the number of complete misses is in the range of 1-10 %. For a successful matching it is also required that the peak intensities are of the same order of magnitude, as defined by a factor of allowed deviation. Generally speaking, the algorithm works best for strong peaks, with a degrading behavior for weak peaks, which may be explained by an increasing sensitivity to background noise for weaker peaks.

Once a matching peak is detected in the unfiltered image, it is removed by a locally adapting scheme to be able to remove as much as possible of the peak, while at the same time leaving neighbor peaks untouched. A search is performed from the peak center and outwards, and as long as the pixel intensities are decreasing they are replaced by a locally determined background value. An example of a small part of the unfiltered image field before and after images of the fluorescing particles are removed is shown in Fig. 2.

To get out the velocity field of the two phases, a "standard" cross-correlation PIV technique is then applied to the filtered image and the image processed unfiltered image.

Sample results

In Fig. 3a is shown an example of the instantaneous velocity field of the fluorescing particles, obtained by a direct PIV analysis of the high-pass filtered image. The magnetic stirring bar is located just outside the right side of the picture, which shows the velocity field in a cross-plane through the plexiglass box. The water surface is at the top of the picture, the left and lower sides are walls, and the right side cuts through the water slightly to the left of the box center. The slip velocity field, i.e. the velocity difference between the fluorescing and the tracer particles, is shown for the same instant in Fig. 3b. Local spots of high velocity slip may be identified, with a magnitude frequently larger than one pixel, which is significantly higher than the expected measurement accuracy of about 0.1 pixel.

The present results show the capabilities of the developed methods. The next step will be to do measurements in a well-defined flow configuration, with a more uniform size distribution of fluorescing particles.

References

Hassan, Y. A., Blanchat, T. K., Seeley Jr, C. H., and Canaan, R. E., 1992, "Simultaneous velocity measurements of both components of a two-phase flow using particle image velocimetry", *Int. J. Multiphase Flow* **18**:3, 371-395.

McCluskey, D. R., Elgaard, C., Easson, W. J., and Greated, C. A., 1993, "The application of PIV to turbulent two-phase flows", *Flow Visualization and Image Analysis*, F.T.M. Nieuwstadt (ed.), Kluwer Academic Publishers, 207-226.

Sakakibara, J., Wicker, R. B., and Eaton, J. K., 1996, "Measurements of the particle-fluid velocity correlation and the extra dissipation in a round jet", *Int. J. Multiphase Flow* **22**:5, 863-881.

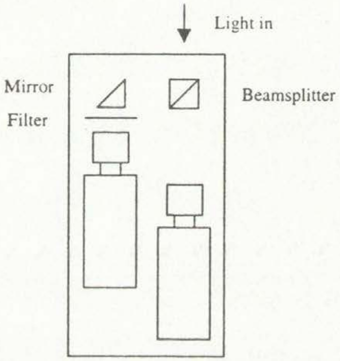

Fig. 1 Camera set-up

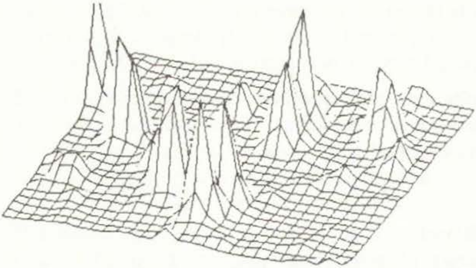

Fig. 2a Detail of unfiltered image showing images of both fluorescing and tracer particles

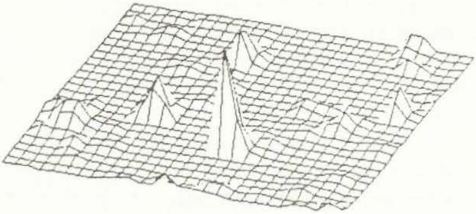

Fig. 2b Same detail as in Fig. 2a after removal of images of fluorescing particles

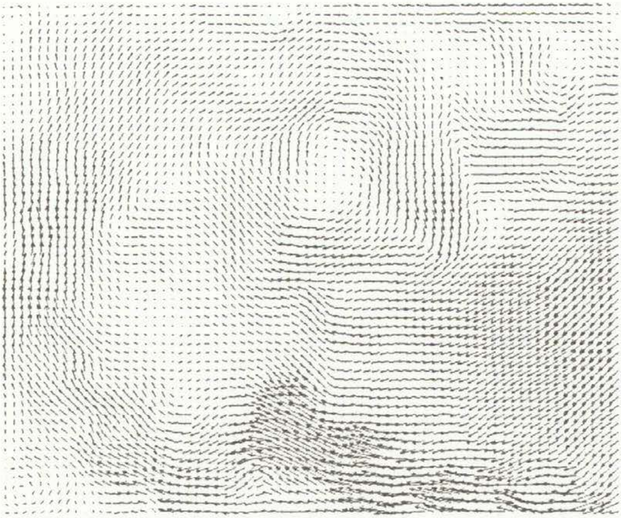

Fig. 3a Instantaneous velocity field of fluorescing particles

Fig. 3b Instantaneous slip velocity field, i.e. velocity field of fluorescing particles less the velocity field of tracer particles. The vector scale in Fig. 3b is twice that in Fig. 3a.

VIDEOGRAMMETRIC SYSTEM FOR MEASUREMENTS OF MOVEMENT AND DEFORMATION OF REAL-SCALED HELICOPTER ROTOR BLADES

S.Bosnyakov, V.Koulesh, A.Morozov, N.Tarasov, S.Fonov

Central Aero-Hydrodynamic institute, Zhukovsky, 140160, Russia

Summary. Helicopter's blade during its rotation accomplishes a complex spatial movement and deformation. This Blade Deformation Measuring System (BDMS) was developed to measure parameters of the real-scaled blade movement and its bending-twisting deformation. This system operates under videogrammetry principles. The basic principles of registration of video-images and processing of results of measurements are stated. Brief description of the system design is given. This system was tested during experimental investigations of blade deformations of the real upper rotor of Kamov-26 helicopter with radius 6.5 m on the VP-5 rotor test facility in TsAGI's T-101 wind tunnel. The tests have shown opportunity of twist deformation measurements of the blade with a root-mean-square error lower 3-6 angular minutes and bend deformations measurements with an error of 0.3-0.6 mm. The technique of calibration of Blade Deformation Measurement System and appropriate software had been developed and tested.

Introduction

At the end of 70's - beginning of 80's in Central Aero-Hydrodynamic Institute (TsAGI) a lot of attention was paid to development and using in experimental researches of optical systems for non-contact measurements of a trajectory of the movement and deformations of models and full-scale blades. The first type system was based on a laser differential interferometric method [1]. It was used in TsAGI's T-105 wind tunnel and provided researches of blades of small-scaled rotor models with a diameter up to 3m.

At the end of 80's for investigation of blades of full-scale rotors on a hover ring and in TsAGI's T-101 wind tunnel the laser scanning system was developed and entered in practice of tests. Operation of this system was based on determination of time intervals between pulses of light reflected by retro-reflectors located in pairs on the blade during it was scanning by laser light sheet. The main restrictions in operation of this system have appeared insufficient stability of the optic-mechanical scanner and instability of He/Ne laser in conditions of high vibrations on a rotor test device.

Recently a number of videogrammetric methods were developed in the TsAGI for measurement of geometrical parameters of the form, movement and deformation of the elements of an aircraft design [2-3]. These videogrammetric methods are based on using the videocameras with CCD-array, modern computer facilities and methods of numerical images processing. In this paper the basic principles, design feature and the results of application of videogrammetric system for investigation of the full-scale blade of a carrying helicopter rotor are presented.

BDMS brief description

The basic diagram of the measurement system is shown in Fig.1. The upper surface of the blade under test is painted in black color. A set of the light-reflective markers is located on this surface in given sections along radius in pairs near to leading and trailing edges. The diameter of reflective elements increases from 5 mm on near section up to 10 mm on the end of the blade.

The measurement head installs on the rotor hub top flange and is turned by an optical axis of the videocamera along the blade with markers with angle about minus 6 degrees from above to a plane of rotation of the blades. In the measurement head the videocamera and flash (stroboscopic) light source with the power supply are placed.

The described videogrammetric Blade Deformation Measurement System (BDMS) was developed on the basis of two synchronized analog CCD-cameras. The measurement head has an adjustable platform on which the videocameras and flash-lamp arrangement are installed. The adjustable platform provides to change the angle of the videocameras optical inclination axis in a range from 0 up to 10 degrees. Inside the case of the measurement head the electronic blocks of system are placed too. The optical and electronic blocks are closed by a cowling-cover (Fig.2).

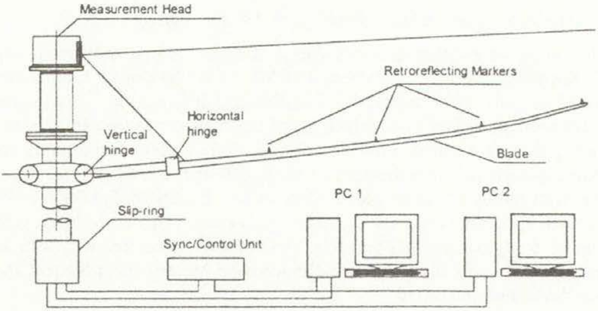

Fig.1. Block diagram of videogrammetric system

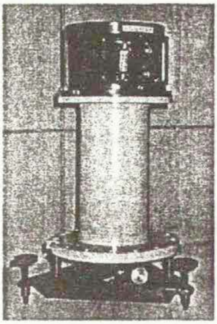

Fig.2. Measurement head

The system of the acquisition and processing of the images has two personal "Pentium" computers. The pulsing lamp was synchronized with two CCD-cameras. Synchronization of two analog CCD-cameras with shift of phases at 0.25 of period at division of even and odd fields provides frequency of measurements equal 100 Hz. In analog cameras the electronic shutters are available application of which allows to increase contrast of the markers images and stability of system operation at presence of extraneous light exposure of the blade. The measurement system provides continuous registration of the images consequence during 2…10 seconds.

The system works as follows. At determined azimuths of the blade during it rotation the flash lamp illuminates the blade. The videocamera registers the image on which the markers are seen by the brightest points on dark background. By determining of two-dimensional coordinates of these images of markers it is possible to calculate the spatial coordinates of each marker of the blade.

Calibration of measuring system

The calibration is more impotent procedure of measurements by videogrammetric technique [4]. This procedure should establish the mathematical relations between 3D coordinates of mark points in object coordinate system connected with the helicopter rotor under test and measured coordinates on their video-image.

The developed in this work calibration facility contains two basic units: an adjustable platform for installation of the measuring head and reference lattice with a set of markers. The general scheme of calibration setup is shown in Fig.3. The adjustable platform contains the laser pointer, which creates the base z-axis of the object coordinate system. Horizontal position of the measurement head base plane is checked by the inclinometer placed on upper surface of the lower flange of the support column. Accuracy of the level or inclinometer must be better then 30 angular seconds.

The reference lattice includes the set of markers with diameter 10 and 5 mm. These markers are located in the chess order. An interval on a vertical (along an y-axis) between six rods is equal

160 mm. On each rod 10 markers with a step of 90 mm on a horizontal (along an x-axis) are located. The normal error (standard deviation) arrangement of centers of markers in units of a rectangular grid does not exceed 0.2 mm. The reference lattice contains the laser target located on a plate in the middle between fourth and fifth rods. The laser target in pair of laser pointer provides the precision alignment of the reference lattice relatively measurement head.

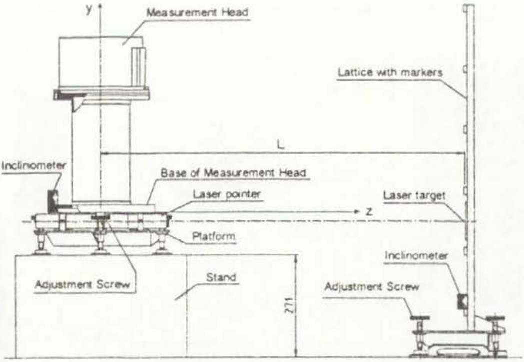

Fig.3. Scheme of calibration facility

The calibration of videogrammetric system is usually made in laboratory conditions then measurement head is established on the flange of a helicopter rotor hub without additional tuning. At calibration of the measurement head with analog CCD-cameras the measure lattice was placed at two position on distances 2286 and 4761 mm from the measuring head. The value of root-mean-square deviations for the analog camera was equal 0.756 mm on an x-axis and 0.372 mm on an y-axis.

Experimental setup and measurement results

The general exterior (photo) and block-diagram (draw) of experimental facilities in the T-101 wind tunnel are presented in Fig.4. The glass-fiber-plastic blades of the upper rotor system of Kamov-26 helicopter were used during these tests. Diameter of this rotor equals 13 m. One blade carries four pairs of the retroreflectors placed in sections on relative radius $r = 0.4, 0.6, 0.8, 0.98$. The speed of the acquisition of the information was 100 Hz, and the duration of sample was equaled about 2 seconds that corresponded about to 8 revolutions of a carrying rotor.

The examples of the measurements results of the rotor blade flap (a) and angle (b) distributions vs azimuth on flight regimes with thrust $T = 0$ and 1000 kg with different helicopter device attack angle α are shown in Fig.5. The distributions of bending-twisting deformation on a) hover regime ($V = 0$; $T = 800$ kg; N=256 rpm and b) on flight regime ($V = 35$ m/sec; $\alpha = -3$ degrees; $T = 1000$ kg; $N = 256$ rpm) are presented in Fig.6.

The estimations showed the root-mean-square error of measurement of coordinates of markers does not exceed 0.3…0.7 mm on radius of 5 m. The error of measurement of twist deformation depends on distance between markers and makes size about 3…7 angular minutes.

References

1. D.D.Gribanov, V.P.Kulesh, A.K.Martynov, A.A.Orlov, S.D.Fonov, "Laser-optical method for investigation of movement trajectory and bending-twist deformations of blades of carrying rotor models", *Science transactions of TsAGI*, v.XI, No. 6, pp.88-95, 1980.

2. V.P.Kulesh, S.D.Fonov, "Measurement of movement and deformation parameters of plane model in wind tunnel by videogrammetric method", - *Science transactions of TsAGI*, v.XXIX, No.1-2, pp.165-176, 1998.

3. V.P.Kulesh, S.D.Fonov, V.A.Yakovlev, "Application of optical and interference methods in experimental aerodynamics", *AGARD-CP-601*, pp.(17-1)-(17-12), 1998.

4. W.L.Snow, B.A.Childers, M.R.Shortis, "The calibration of video cameras for quantitative measurements", *EISA, paper #93-078*, 1993.

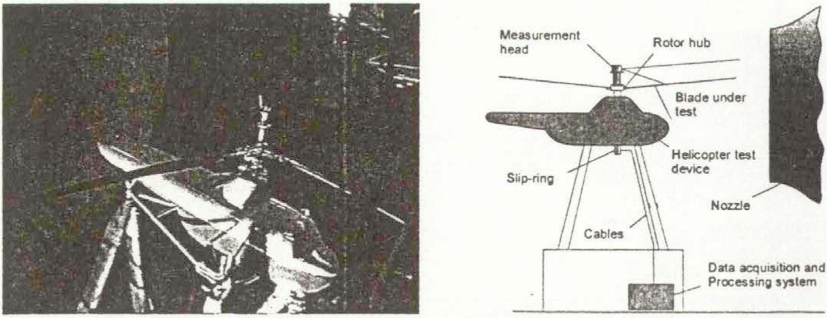

Fig.4. Photo and scheme of experimental facilities in T-101 wind tunnel

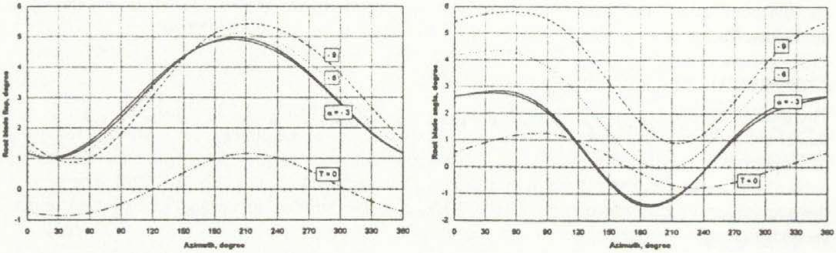

(a) (b)

Fig.5. Flap and angle of the blade movement

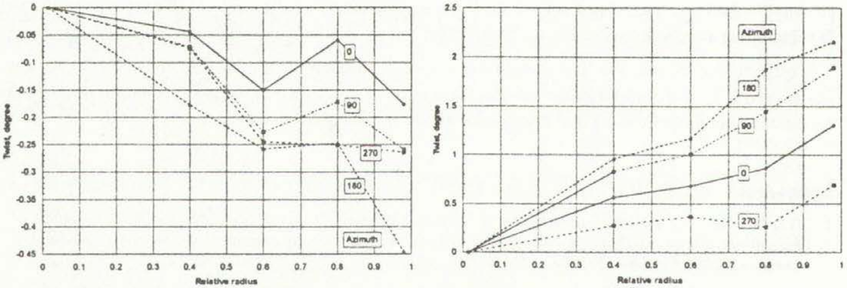

(a) (b)

Fig.6. Bending and twisting deformation of the blade

ENHANCEMENT OF THERMOGRAPHIC IMAGES QUALITY USING PYROSIGNAL DIGITAL FRAME-BY-FRAME PROCESSING

Ihor Bozhenko, Zenon Hrytskiv and Piotr Kondratov

State University "Lvivska Polytechnika" , S. Bandery 12, 290646 Lviv, Ukraine

Summary Thermovision cameras, based on pyrovidicon, are widely used in thermal phenomena investigation including applied mechanics. It is known that pyrovidicon target has an effect of piezoelectricity. As a result, special interference aggravate the quality of thermographic images. Besides external sources, some influence may be generated by thermovision camera units that ensure action of obturator. The last is the integral part of pyrovidicon camera. Peculiarities of mentioned influence and details of its sources are discussed Special processor for this influence decrease is proposed. Image quality enhancement is based on pyrosignal processing by the processor. The nature of influence is discussed and results of signal processing are illustrated.

INTRODUCTION

Thermovision cameras, based on pyrovidicon, are widely used in thermal phenomena investigation including applied mechanics. As an example, the investigation of thermal images of metallic samples under a mechanical loading may be adduced. Unfortunately, numerous of interference prevent to reach optimal parameters concerning thermal sensitivity, thermal resolution, high quality image receipt in general.

It especially concerns to thermovision cameras with obturator that permits to receive static thermal image of stationary object by motionless camera. In comparison with cameras, based on panoramic or orbital motion, in such cameras the amplitude of useful signal decreases. Correspondingly, the influence of the interference of different nature increases. This problem partly is elucidate in[1].

Usually, the influence of the interference, stipulated by technological peculiarities and shortcomings of pyrovidicon target and obturator manufacturing, on the quality of the images is considered. Negative influence of pyrosignal noise components, generated by target and video amplifier input circuits, is also known.

At the same time, in known scientific sources, a problem of negative influence of mechanical interference is not considered. However, this interference, because of piezosensitivity of target, may noticeably aggravate the infrared thermography of objects.

SOURCES OF MECHANICAL INFLUENCE

The obturator and units that ensure rotation are the main sources of mechanical influence or vibration. Typical synchro drive consists of motor, rotation moment transfer unit, opto-electronics synchronization system, obturator mount units. In spite of aspiration to decrease the influence of vibration by corresponding design and elements of springing use, this influence is noticeable on the thermal image. Obturator rotation has to be synchronize with frame scanning frequency. As a result, horizontal black-and-white strips appear on the monitor screen. Number of strips depends on the peculiarities of vibration.

An analysis of the obturation system elements permitted to concretize the next possible sources of vibration:
- motor (usually direct current electromotor), the bearings and collector, first of all;
- errors in the unit of rotation moment transmission manufacture: axes uncoincidence, inexactitude of the main bearing making;
- defects of making and poor balancing of obturator.

IMAGES QUALITY ENHANCEMENT

The main way to thermographic images quality enhancement consists in use pyrosignal digital frame-by-frame processing [2]. The processing foresees an analog signal conversion to its digital version with necessary accuracy (usually 8 bits). Obturation of thermal radiation creates pyrosignal U_{ps} that consists of base pedestal signal U_p and useful signal U_u. The last is positive if obturator is open, and negative if obturator is closed.

On the next step an algorithm of frame-by-frame subtraction is realized. As a result, we receive the signal

$$U_r = (U_p + U_u) - (U_p - U_u) = 2U_u .$$

This kind of processing permits to decrease the level of noise including "mechanical" interference, components of which have the same polarity in two adjacent frames: these components selfcompensate in resultant signal.

The second algorithm - frame-by-frame accumulation - consists in n-divisible repetition of previous algorithm with summing up and middle value determination of resultant signals U_{ri}. The output signal

$$U_o = (1/n) \sum_{i=1}^{n} U_{ri} = (1/n) \sum_{i=1}^{n} 2U_{ui} \cong 2U_u .$$

At the same time the noise component of pyrosignal will be mitigated as more as larger value n because of its asynchronous character.

It is more difficult to foresee the action of frame-by-frame accumulation algorithm on pyrosignal with mechanical interference. In spite of synchronous "mechanism" of their formation, their action is accompanied by many factors that destroy synchronism and intensively influence on momentary value of vibrations amplitude which reach the target. There are time and temperature changes in the elements of drive and in elements of electromotor springing. The appearance of asynchronism permits to use successfully the procedure of frame-by-frame accumulation in the aim of mechanical influence visibility decrease.

PROCESSOR STRUCTURE

The processor that was designed and used in experiment, consists of the next units:- analog-to-digital conversion unit;- frame memory unit;- arithmetic and logic unit;- accumulation memory unit;- display memory unit;- display unit;- interface unit.
The last one ensures the communication with personal computer.

Peculiarity of pyrosignal processing consists in the pedestal component existence in input signal. As it was mentioned above, this component is not useful. As the result, useful component of pyrosignal are processed in analog-to-digital converter unit by only several bits. It is evident that the quality of thermographic images may be enhanced by all (8) bits use for processing.

To solve this problem we have suggested additional unit to processor structure - analog subtraction unit at the input of processor. In accordance with this proposal the procedure of two adjacent frames subtraction is realized in the unit. The signal, that is subjected to analog-to-digital conversion, consists on useful part only and may be quantized by all bit scale.

A model of 1-inch pyrovidicon camera was used in experiments. The useful component to mechanical interference component ratio was estimated as 1/0.04. The interference became invisible if the number of accumulated frames were more than 64.

CONCLUSION

The interference, stipulated by mechanical influence of obturator on pyrovidicon target, is able to create a visible noise on the thermovision system monitor screen. In the case of still images the noise may be mitigated by pyrosignal frame-by-frame processing with two main procedures: Frame-by-frame subtraction and frame-by-frame accumulation. There is the reason to perform procedure of subtraction with analog signal on the input of processor.

REFERENCES

1. Gaussorguos G.: La Thermographie Infrarouge. Technique et Documentation. Lavoisier, Paris 1994.
2. Kolobrodov V., Rybalka V.: Pyroelectric Camera Modulation Transfer Function. *Optical Engineering* Vol. 34 No. 4, pp 1044-1048, 1995.

THE QUATERNIONIC FOURIER TRANSFORM AND ITS APPLICATIONS IN TEXTURE SEGMENTATION

Thomas Buelow
Christian-Albrechts-Universitaet zu Kiel
Institut fuer Informatik und Praktische Mathematik, Kognitive Systeme,
Preusserstr. 1-9, 24105 Kiel, Germany
tbl@informatik.uni-kiel.de, http://www.informatik.uni-kiel.de/~tbl/

ABSTRACT

The quaternionic Fourier transform (QFT) is introduced as a modification of the 2D complex Fourier transform. We analyze the symmetry properties of the QFT and find that according to these properties the 2D Hartley transform,the complex Fourier transform and the QFT can be regarded as three levels of a hierarchy of 2D harmonic transforms. Based on the QFT a new definition of the analytic signal in 2D is proposed.

Quaternionic Gabor filters are introduced and shown to provide an approximation to the 2D quaternionic analytic signal. The local phase of a real 2D signal is defined as the angular phase of its quaternionic Gabor filter response. We show that there is a close relation between the local intrinsically 2D structure of a signal and its local phase as defined above. Applications to the image processing task of texture segmentation are presented.

CONDITIONAL PIV ANALYSIS OF A JET IN A CROSS FLOW

R. Camussi*, A. Stella**, T. Kowalewski***, G. Guj*, F. Stella**
*D.I.M.I., Univ. Roma Tre, Via della Vasca Navale 79, I-00146 Roma, Italy
**Dip. Ing. Mecc. e Aer., Univ. di Roma «La Sapienza», Via Eudossiana 18, I-00184 Roma, Italy
***Polish Academy of Sciences, IPPT PAN, Swietokrzyska 21, PL 00-049, Warszawa, Poland.

Summary: A conditional PIV acquisition technique and averaging procedure is developed to study coherent structures forming in the interaction between a jet and a cross stream. The experiment is conducted in a water tunnel and the jet is forced by a mechanical device. Sequences of images are acquired synchronized to the external forcing and with a fixed phase. Instantaneous and averaged velocity and vorticity 2D fields are obtained for several flow conditions.

INTRODUCTION

The study of jets exhausting in cross-flows is an important aspect for many physical problems and applications in engineering and environmental aspects. The importance of the subject have stimulated several experimental studies in air and water facilities[1]. For the case of water experiments, most of the studies have been conducted by flow visualizations which, even if often of fundamental importance for preliminary understanding of the physical behaviors, lead to qualitative results. For more quantitative analyses in water experiments, the use of PIV seems to be straightforward. Indeed, the PIV technique provides a good connection between the clear features observed by visualizations[2], and the need of a quantification of the velocity or vorticity magnitudes. From a physical viewpoint, one of the basic aspects which needs clarifications by more quantitative analyses, is the influence of the principal non-dimensional parameters (namely the jet-to-cross stream velocity ratio $R=U_j/U_?$ and the typical Reynolds number $Re_j= U_? D_j/\nu$, where U_j and $U_›$ represent respectively the jet and cross-stream velocity and D_j the jet diameter) on the vorticity dynamics mechanisms and coherent structures evolution. In particular the basic flow structures we consider are the pair of counter rotating vortices which forms inside the jet flow when it bends under the effect of the cross stream[3], and the ring-like structures which instead are formed on the upper shear layer of the jet as an effect of a destabilization mechanism of Kelvin-Helmholtz type[4]. A new technique for phase averaging and conditional PIV acquisitions has been developed and applied to a test case in a water tunnel at low Re_j. Present technique is based on the idea that the mechanism of destabilization and formation of the coherent structures which mostly influence the fluid dynamics, may be induced by a mechanical forcing of the issuing jet which is also synchronized with the PIV acquisitions to permit the analysis of the mean fields by ensemble averages.

EXPERIMENTAL FACILITY, PIV SYSTEM AND CONDITIONAL TECHNIQUE

Experiments were carried out in a water tunnel available at the Aerodynamics laboratory of the Department of Mechanics and Aeronautics, of the University "La Sapienza" of Rome. The tunnel has a converging nozzle with a contraction ratio of 10. The test chamber of *0.5 m* of length has square section of $0.1x0.1\ m^2$. Perpendicular to one side is flush mounted a nozzle with circular section of *5 mm* diameter. Also within the jet, the working fluid is water. The velocity of the free stream fluid was fixed to *0.02 m/s* and the corresponding value of Re_j was around 100. The velocity ratio R considered ranges from about 2 up to 4.5. A 2 Watt, continuous, laser is used to produce a light sheet illuminating a plane within the flow. The sheet, obtained by a laser ray crossing a cylindrical lens, has been positioned in the plane containing the jet axis, to measure the *longitudinal* velocity field. A second measurement campaign to measure the *transverse* velocity field has been performed producing an illuminating plane perpendicular to the jet axis. Tracer particles of lycopodium are added both to the jet and the cross stream. Particles mean diameter is 30 m and the density is 0.31 times water density. A CCD monochrome camera (optical sensitive pixels arranged in a frame of 756 horizontal lines and 581 vertical columns.) and a frame grabber board attached to the PC are utilized to capture and acquire images of the illuminated particles in the observation area. The frame is divided into two fields, one containing the odd numbered lines and one the even ones. The shutter time has been varied depending on R, and fixed at 15 ms for R=2, 12 ms for R=3 and 9 ms for R=4 and 4.5. The images captured by the CCD camera are acquired on-line by the 8-bit A/D converter of a VFG-100 image processing board. For the purposes of conditional PIV acquisition, a sequence of 4 images is stored in a buffer using an initial resolution of 6 bits then extended to 8 bits throughout zero-padding. According to classical Digital PIV (DPIV) approach[5,6], velocity is measured applying a cross-correlation technique between pairs of successive images separated by a known time delay t. In the implemented DPIV *technique*[7], pairs of images to be correlated are earned by a single CCD frame extracting the two fields corresponding to odds and even lines and with a time delay t=20 ms. The effective image size is therefore reduced to 744 x 252 pixels. t=20 ms is the minimum time interval between correlated images, but it can be increased considering pairs of fields extracted from different frames of a sequence. Interrogation windows of 48 x 24 pixels, 50 % overlapped, have been correlated to evaluate particles displacement. The matrix of in-plane velocity vectors, whose point of application is the center of an IW, is composed of 31 rows in the horizontal direction and 21 columns in the vertical one. The scale factor is 1:0.098 for the longitudinal velocity fields and 1:0.107 for the transverse ones, i.e. 1 mm in the physical space corresponds respectively to 0.098 mm and 0.107 mm on the sensor of the CCD camera. The velocity spatial resolution in the physical space is 2.4 mm for the longitudinal fields and almost 2.6 mm for the transverse ones. Particles displacement is determined with a resolution extended to ½ pixel throughout interpolation, corresponding to about 0.05 mm. In order to improve the accuracy of this calculation, images are processed in advance via software to enhance signal to noise ratio. Images enhancement consists in producing a binary image basing on a threshold level: pixels with intensities larger than or equal to the threshold are preserved, while the rest is set to zero, so that the final image contains only black or white pixels. The dynamic range $DR=V_{Pmax}/V_{pmin}$ of the available PIV system in the adopted experimental conditions is thus 45:1 for the vertical velocity and 22.5:1 for the horizontal one. The conditional acquisition procedure has been implemented in order to collect images of particles in the illuminated plane phase-locked with coherent structures position and convection. This has required to apply jet forcing to produce a controllable and periodic flow during its destabilization. Forcing is accomplished introducing a velocity perturbation in jet upstream flow at the frequency f_D of the preferred mode of destabilization, experimentally determined. Synchronization between jet external forcing and image capturing is managed via software. The procedure consists in acquiring the external synchronization signal provided by the CCD video camera module, basing on which a trigger condition is supplied to a signal generator through its external triggering port. The trigger signal start the generation of a square waves train (TTL 50% duty cycle) with the appropriate f_D ensuring phase-locking with image acquisition timing. Perturbation of jet upstream velocity is accomplished by means of a mechanical device, locally squeezing jet flexible pipe and driven by the amplified TTL signal. The time interval t_{PT} from the beginning of jet excitation signal to the first image acquisition (*pre-trigger time*) as well as the delay t_{IMG} among the four images of a sequence, determine phase-delay between acquired images and coherent structures position. The first parameter has not been changed during present measurement campaign and set equal to 10s. The time shift t_{IMG} has been maintained equal to 200 ms in all tested cross-flow conditions, with the exception of case R=3 for which further acquisitions with t_{IMG}=100 ms and t_{IMG}=300 ms have been carried out to assess the related phase variation. The statistical analysis is based on about 50 realizations per image (for each flow condition 200 images have been acquired). Each image has been processed to achieve the instantaneous velocity and vorticity field and, for each flow condition, the ensamble averages have been performed over the fields corresponding to the same phase delay.

SOME RESULTS

In Fig.1, an example of the ensemble average obtained with the forcing, is reported. The figure corresponds to a velocity ratio *R=3* and a time delay between images of 300 ms. It is evident that the vorticity contours at known phase delay permit the analysis of the evolution of the coherent structures. More specifically, being the images obtained by the light sheet positioned perpendicular to the wall, the presence and evolution of the ring-like structures forming in the shear layer may be observed. The difference between the vorticity contour at different delay is a signature of the unsteadiness of the phenomenon especially for relatively large distances from the jet exhaust. Indeed, it is clearly observed the formation of a strong ring vortex at the exit of the jet having the same vorticity as the wall boundary layer at the upper side and the opposite on the lower side. This appears as a steady structure which is always observed at any flow condition. After few diameters from the jet, the destabilization of the upper shear layer is clearly observed with the formation of annular structures whose signature is given by couples of positive or jet-like (counter-clockwise on the upper side) and negative or wake-like (clockwise on the lower side) vorticity. Taking into account that the positive and negative values of the vorticity amplitude are reported with the same resolution, it seems evident that the vorticity associated to the upper shear layer is stronger (for R=3) than what is observed in the lower one. This is a typical behavior observed for R>2. Even if with different magnitude, it seems that there is always a coupling between upper (with positive vorticity) and lower (with negative vorticity) structures: the shear layer instability on the upper side, leads to the formation of a strong vortex with positive vorticity which detaches from the steady structures at the jet exit. As soon as it is formed, a

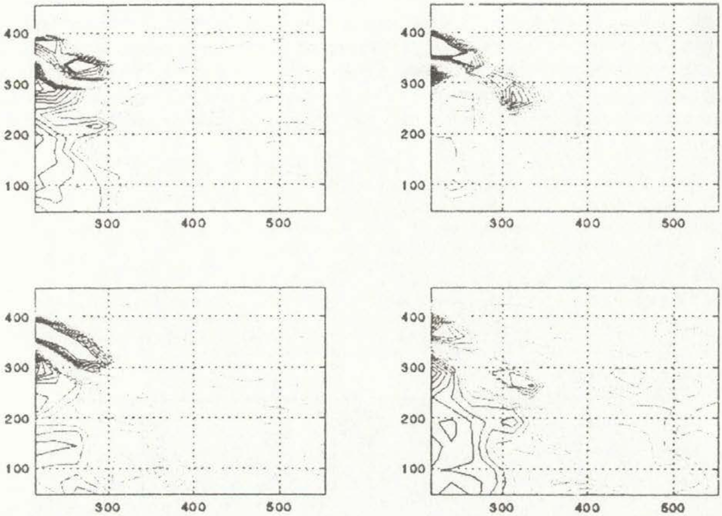

Figure 1. Contour plots of the averaged longitudinal vorticity . The evolution of a ring vortex is evidenced by the rectangular windows

secondary vortex with weaker vorticity of opposite sign is also formed and it moves coupled to the first one. This appears as the signature of a ring vortex. Taking into account the magnitude of the mean velocity of the cross stream and the time delay between the images, the use of the conditional averages allows us to follow the evolution of a ring during a total time interval of 900ms. This is shown by the enhanced regions of the figure. It is also observed that when the vortex is sufficiently far from the jet, the positive vorticity of the upper side decreases faster that the negative one on the lower side. Analogous results are obtained in the other cases at R>3 (not reported here for brevity). It has been also observed that significant differences are instead documented with respect to the observations at R=2. In particular the main transitional behavior seems to be the passage from a steady state to an unsteady nature of the ring-like structures of the shear layer. The analysis of the averaged vorticity contour corresponding to the transverse light sheet, substantially indicates the steady nature of the counter rotating vortices. As an example in Fig. 2 we report the averaged vorticity for a fixed position and time delay and for increasing R. It is shown that an increase in the velocity ratio leads to a faster formation of the vortex pair which, anyway, are formed even for lower R. The conditional analysis in this case is less useful than for the longitudinal cases, confirming previous results obtained by flow visualizations[1].

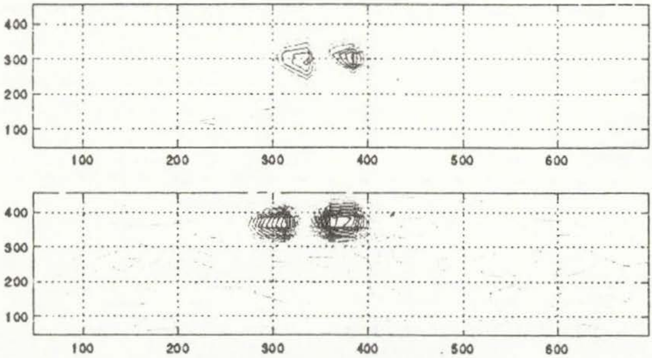

Figure 2. Contour plots of the averaged vorticity. Each plot corresponds to a phase of 1200m/s from the start of the perturbation and to the position of the light sheet parallel to the wall. The two images correspond to R=3 and R=4 (from up to below).

REFERENCES

1. Kelso, R.M., Lim, T.T. and Perry, A.E., An experimental study of round jets in cross flows. *J. Fluid Mech.*, **306**, pp. 111-144, 1996.
2. Adrian R.J., Particle imaging techniques for experimental fluid mechanics, *Ann. Rev. Fluid Mech.*, **23**, pp.261-304, 1991.
3. Broadwell J.E. and Breidenthal R.E., Structure and mixing of a transverse jet in incompressible flow, *J. Fluid Mech.*, **148**, pp. 405-412, 1984.
4. Andreopulos J., On the structures of jets in cross-flows. *J. Fluid Mech.*, Vol. **157**, pp. 163-197, 1985.
5. Willert, CE; Gharib M Digital particle image velocimetry. *Exp. in fluids*, **10**, pp. 181-193, 1991.
6. Westerweel J. Digital particle image velocimetry – Theory and Application. Delft: Delft University Press, 1993.
7. Hiller W., Koch S., Kowalewski T.A., Stella F, Onset of natural convection in a cube, *J. Heat and mass transfer*, **16**, pp.3251-3263, 1993.
8. Quenot G.M., Pakleza J., Kowalewski T.A. Particle image velocimetry with optical flow, *Exp. in Fluids* **25**, pp. 177-189, 1998.

PRINCIPAL COMPONENTS ANALYSIS FOR PIV APPLICATIONS

A. Cenedese, A. Pocecco*, G. Querzoli***
**DITS - Università di Roma "La Sapienza"*
***Dip. Ingegneria del Territorio, Università di Cagliari*

Introduction

During last decade the experimental flow investigation based on image analysis (PIV and PTV) received a big development due to the improvement of hardware support and acquisition systems (digital cameras and image acquisition cards). PIV technique is based on the detection of the displacement of seeding particles which can represent, for their characteristics, the flow [1]. In PIV the displacement is calculated by analysing images acquired at known times, the images are subdivided in sub-domains and the mean particles displacement is calculated by means of auto or cross-correlation. By using cross-correlation it is possible to increase the dynamical range of measurement but it requires the acquisition of two distinct images. Several techniques were suggested in order to obtain two single-exposed images:

- Cross-correlation cameras, which can acquire two digital images, commonly with 1000x1000 pixels.
- Digital cameras equipped with narrow-band optical filters and using lasers emitting at different wavelength [2].
- A photo camera, with a laser system emitting two different colour laser beam, acquires a multiexposed colour image. A successive separation into two images utilising the colour information is required in order to apply cross-correlation technique.

The present work proposes a method, based on the detection of the principal components of the image, to obtain two single-exposed images from a colour digital PIV image.

Experimental set-up

Figure 1 shows a PIV image, taken from the EUROPIV database of CIRA (Italian Centre for Aerospace Research), representing a free jet in air. The seeding used was olive oil droplets of 1 μm diameter. In this experiment was utilised a system composed of a Nd-Yag laser emitting laser pulses at 532 nm and a dye laser which provides laser pulses at 635 nm, with a frequency equal to 12.5 Hz. The delay between pulses was adjustable between 50 ns and 10 ms. The two laser beams were made into sheets by cylindrical lenses and superimposed in the test section. The image was acquired, using a photo camera, on a film whose spatial resolution is 90 lines/mm. The colour negative was subsequently digitised by means of a scanner at 2700 dpi.

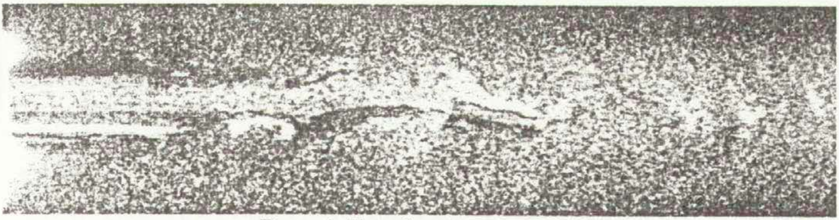

Figure 1. The colour image acquired

Colour separation by principal components analysis

A pixel of a digital image can be represented by its three component RGB, so the easiest way to obtain two single-exposed PIV images from a colour multiexposed image is represented by the separation of the original image into three images representing its Red, Green and Blue components (figure 2). Generally the colours of particles image do not correspond to RGB bands, so the particles image acquired with the green laser are partially present in the red and blue channels, the same happens with the red laser. This results in strong correlation peaks located in the origin of the cross-correlation function.

A method to overcome this problem is based on the determination of the image principal components [3]. As each pixel can be represented in the RGB domain with its co-ordinates, by detecting the principal directions of the correlation tensor of the pixels distribution, it is possible to obtain a different frame of reference with an orthogonal basis in which colour bands are independent. Let K=M×N be the image dimension (in pixels) and F a K×3 matrix whose columns are obtained by ordering, for each band, the intensity of pixels A_i (i=1, 2, 3) after having subtracted the respective mean values:

$$A_i = \begin{bmatrix} a_{11} & a_{21} & . & a_{1N} \\ . & . & . & . \\ . & . & . & . \\ a_{M1} & a_{M2} & . & a_{MN} \end{bmatrix} \qquad F_i^T = \begin{bmatrix} a_{11} & \dots & a_{M1} & a_{21} & \dots & a_{M2} & \dots & a_{1N} & \dots & a_{MN} \end{bmatrix}$$

The correlation tensor of the pixels distribution is given by:

$$[\Sigma] = \frac{1}{M \times N}[F]^T[F]$$

Due to the symmetry of matrix Σ its eigenvector matrix Φ is real. The relation between RGB space and the new components is:

$$[F_p] = [F][\Phi]$$

The three new bands, which represent the principal components of the image, are then normalised in a 0-255 levels scale.

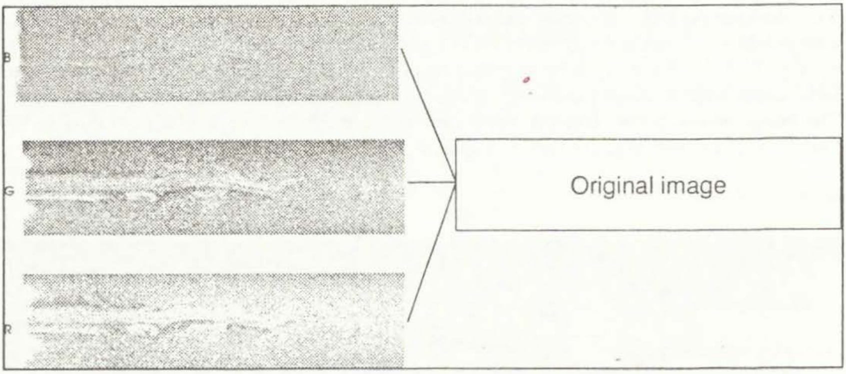

Figure 2. The three RGB components of the image

Results of PIV analysis

Figure 3 shows the velocity vector field obtained from the analysis, conducted using cross-correlation technique, of the two images which represent the R and G components of the image of figure 1. It is clear how the interference amongst the colour bands does not allow the reconstruction of the flow field.

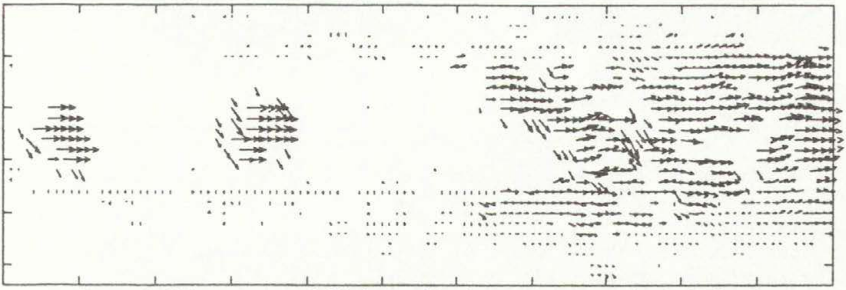

Figure 3. Velocity vector field obtained by the image separated in RGB bands

In order to improve the results, the procedure described above was applied to the colour image. Two images obtained from the principal components analysis were utilised to evaluate the velocity vector field. The results, illustrated in figure 4, indicates that in most cases the errors due to autocorrelation peaks have been eliminated.

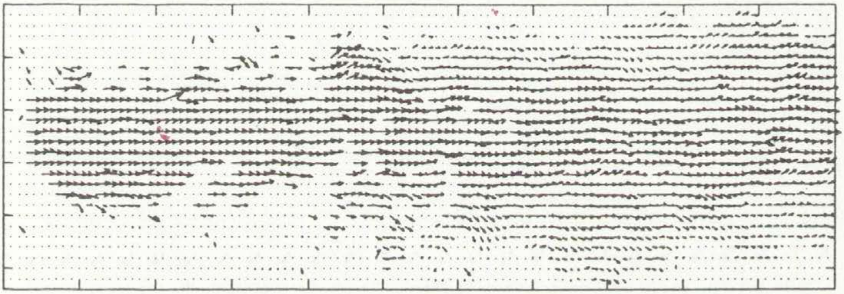

Figure 4. Velocity vector field obtained by the image separated in Principal Components

Figure 5a illustrates the cross-correlation function calculated on sub-domains extracted from two images separated in RGB bands, it is clear how in this case the correlation peak located in the origin of coordinates dominates. The cross-correlation function, calculated on the same sub-domains extracted from images separated in principal components (figure 5b), presents only the valid correlation peak. Thus allowing the exact detection of the particles diplacement.

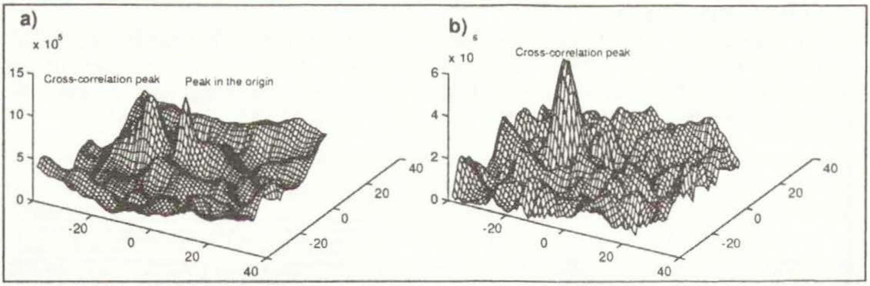

Figure 5. Comparison between the cross-correlation function calculated on images separated in: a) RGB bands, b) Principal components.

References

1. Adrian R. J., Keane R. D., 1992, *"Theory of cross-correlation analysis of PIV images"*, Applied Scientific Research, vol. 49, pp. 191-215.
2. Cenedese A., Panicali F., Pocecco A., Romano G.P., 1997, *"L'analisi di immagine per lo studio dell'ingresso di un treno in galleria"*, 14th Congresso Nazionale AIDAA.
3. Melli, 1991, *"L'elaborazione digitale delle immagini"*, F. Angeli ed.

ADVANCED EVALUATION METHODS IN PARTICLE IMAGE VELOCIMETRY

T.P. Dewhirst, J. Kompenhans, M. Raffel, O. Ronneberger
Institute of Fluid Mechanics, Bunsenstraße 10, Göttingen, D-37073

Summary

A number of algorithmic evaluation methods have recently been gaining attention which offer the possibility of higher accuracy or more robust flow velocity field measurements by means of PIV measurements. An overview of some of these methods will be presented along with the approach being taken by DLR Göttingen. The suitability of these methods for application to other measurement fields is also considered

Introduction

Particle Image Velocimetry (PIV) has gained increased acceptance and interest over the last ten years, mainly due to the availability of high resolution, high quality CCD cameras and the exponential increase in cheap computing power, memory and storage. These factors together have allowed PIV to be transformed from using wet-film for image acquisition with its associated data bottlenecks to being a completely digital process. A wide range of PIV systems are available commercially which can allow the capture of high spatial resolution velocity maps at a reasonable temporal resolution.

While the hardware involved in PIV has been developing almost constantly over the years, the basic principles of PIV evaluation have not altered much since the first double exposure film recordings were analysed by the application of Young's fringes analysis methods [1]. Today, most PIV analysis routines are based upon simple two dimensional Fourier transforms, which, when coupled with the Wiener-Khintchine theorem yields the correlation plane of the region under investigation. There are however a number of well documented limitations to this method, namely:

- Only limited spatial gradients in the flow can be accomidated
- A lack of proper normalisation of the correlation results in an intolerence of rapidly varying image backgrounds
- Limited choice of interrogation areas due to the 2^N limitations of Fast Fourier Transform (FFT) routines

Several approaches have been suggested to overcome some of these limitations. To overcome the first limitation a number of solutions have been proposed which can be split into roughly two groups, one using recursion to gain a higher spatial resolution [2, 6, 9, 4] and the second using either a non-linear image warping or a technique refered to as "optical flow" [11, 8, 5]. Work currently being carried out in our laboratory aims to tackle the second and third shortcomings, namely the proper normalisation of the correlation function to allow for non-uniform backgrounds and also the possibility of having irregularly shaped interrogation areas. These

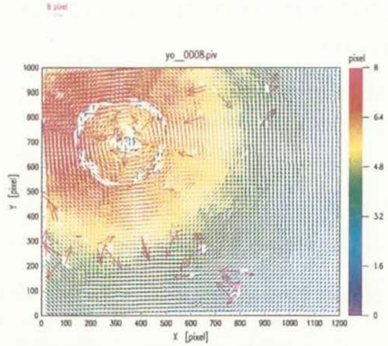

Figure 1: Regular FFT based correlation analysis of vortex with irregular seeding

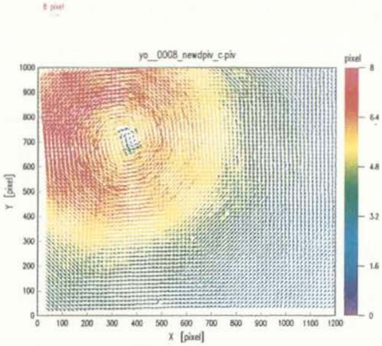

Figure 2: Improved FFT based correlation analysis of vortex with irregular seeding

features can be of great use in analysing flows of interest which are close to solid boundaries in the flow [10].

Advanced Correlation Algorithms

As previously stated, a properly normalised correlation is considered essential to the correct analysis of PIV images [3], however until now this was only possible if a direct correlation was carried out. This is a time consuming and lengthy process, requiring N^4 operations for an NxN pixel image. It has been shown that in fact this correlation can be carried out with FFT's, considerably reducing the time required for an analysis [10]. A good example of the effect this improved correlation can have on the analysis of a typical PIV image can be seen in figures 1 and 2. The location of a ring of outliers in figure 1 corresponds to a ring of inhomogenous seeding caused by the fluid dynamical behaviour of the particles and the flow field (figure 3). When using the properly normalised correlation it can be seen that this dropout does not occur (figure 2).

Peak Fitting

Another possible area of improvement in PIV analysis is in using a more sophisticated peak fitting algorithm. Until now the most popular method for finding the sub-pixel displacement of the correlation was to use a three point Gaussian fit [12, 9]. However, this makes the assumption that the correlation peak is a Gaussian in shape. The approach taken by the DLR is that if the shape of the correlation peak can be found then a Gaussian can be fit to the data using the Levenberg-Marqardt method [7]. This can be shown to be useful in reducing the effects of peak locking [13] which can occur when the particle image diameters are reduced to around one pixel in diameter. As an example of this routine, the PIV image which produced the velocity maps in figures 1 and 2 were formed into a two dimensional histogram of velocities. It can be seen quite readily that the velocities gained when using the normal three point Gaussian fit tend to cluster around integer pixel values more than when the more sophisticated peak fitting routine is used (see figure 4).

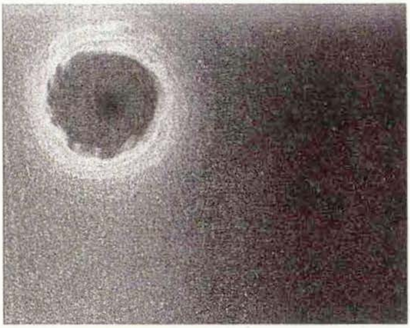

Figure 3: PIV image showing inhomogeneous seeding

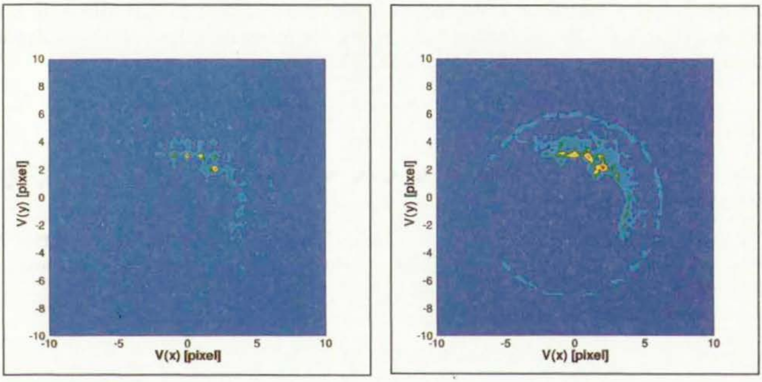

Figure 4: Histogram of displacement distribution of evaluations in figures 1 and 2 - (left) Regular 3-point Gaussian fit and (right) Gaussian fit by Levenberg-Marqardt method

References

[1] R.J. Adrian. Particle Imaging Techniques for Experimental Fluid Dynamics *Ann. Rev. Fluid Mechanics*, 1991, pp261-304, Vol 23

[2] E.A. Cowan & S. G. Monismith. A hybrid digital particle tracking velocimetry technique *Experiments in Fluids*, 1997, pp199-211, Vol 22

[3] A.M. Fincham & G.R. Spedding. Low cost, high resolution DPIV for measurement of turbulent fluid flow *Experiments in Fluids*, 1997, pp449-462, Vol 23

[4] D.P. Hart. Super-Resolution PIV by Recursive Local-Correlation *Proceedings of VSJ-SPIE98*, 1998

[5] H.T. Huang, H.E. Fiedler & J.J. Wang. Limitation and Improvement of PIV, Part II: Particle image distortion, a novel technique *Experiments in Fluids*, 1993, pp263-273, Vol 15

[6] R.D. Keane, R.J. Adrian & Y. Zhang. Super-resolution particle image velocimetry *Measurement Science and Technology*, 1995, pp1202-1215, Vol 2

[7] W.H. Press *et. al.*. Numerical Recipies in C: the art of scientific computing - 2nd ed. *Cambridge University Press*, 1992

[8] G.M. Quénot, J. Pakleza & T.A. Kowalewski. *8th International Symposium on Flow Visualisation*, 1998 Sorrento

[9] M. Raffel, C. Willert & J. Kompenhans. Particle Image Velocimetry: A Practical Guide *Springer-Verlag*, 1998

[10] O. Ronneberger, M. Raffel & J. Kompenhans. Advanced Evaluation Algorithms for Standard and Dual Plane Particle Image Velocimetry *9th Internation Symposium on Applications of Laser Techniques to Fluid Mechanics*, 1998

[11] P.T. Tokumaru & P.E. Dimotakis. Image correlation velocimetry *Experiments in Fluids*, 1995 pp1-15, Vol 19

[12] J. Westerweel. Digital Particle Image Velocimetry. Theory and Application. *PhD Thesis*, 1993, Delft University Press, Delft.

[13] J. Westerweel. Effect of Sensor Geometry on the Performance of PIV Interrogation *9th Internation Symposium on Applications of Laser Techniques to Fluid Mechanics*, 1998

STRAIN SOLITARY WAVE EVOLUTION IN FINITE NONLINEARLY ELASTIC SOLID RODS

G. V. Dreiden, A. V. Porubov, A. M. Samsonov, I. V. Semenova

A.F.Ioffe Physical Technical Institute,
26, Polytekhnicheskaya, St.Petersburg, 194021, Russia

Summary. Results are presented from theory and experiments carried out to excite and observe a localized nonlinear longitudinal strain wave (soliton) in nonlinearly elastic solid rods. It is shown that such a wave conserves its amplitude and shape during its propagation in a waveguide. The process of soliton reflection from both the free and bounded tips of the rod is studied.

INTRODUCTION

Solitons in fluids were observed and generated many times. It was the most surprising fact, however, that despite of almost similar description of stresses in fluids and solids, longitudinal strain solitons have not been observed in nonlinearly elastic waveguides. The envelope solitary waves governed by the nonlinear Schroedinger equation were widely considered; another famous soliton in a solid, being modelled as a ball chain, has been found by Frenkel and Kontorova in 1938 and became useful for crystalline lattice models. However, there must be a soliton in solids in the form of a nonlinear long quasistationary localized strain wave, propagating either along an interface or inside a waveguide (a density soliton). This latter soliton must propagate without change of shape in a uniform rod while its shape will vary in presence of inhomogeneities. In the last case the amplification or focusing may occur, in other words, the soliton amplitude will increase, while its width will decrease simultaneously. The process of soliton formation is as follows. When a powerful strain wave propagates in a nonlinearly elastic solid, the curvating of a wave front can increase rapidly right up to the irreversible deformations appearance. This phenomenon can be balanced with a wave dispersion inside a waveguide, having small, finite but not an infinitesimal cross section size, that is in close correspondence with an appropriate balance in a shallow water wave theory.

SOLITON OBSERVATION

Numerical simulation of various initial pulses generation and propagation subjected to the Double Dispersion Equation model [1] (i.e., of a non-stationary problem) have shown the dependence of both mass and a tail type behind a solitary wave upon the mass (duration) of initial pulse. It was found that a sharp pulse provides a solitary wave with a decaying oscillating tail behind, while a massive one leads to the solitary wave train followed by the oscillating wave trains, having an almost sinusoidal envelope wave.

In order to avoid any plastic flow of a specimen and to keep the *elastic* type of deformations the parameters of an initial pulse should satisfy the following condition for the finite strain tensor component (C_{xx}): $|\sqrt{1+2C_{xx}} - 1| < Y_0$, where Y_0 is the yield point of a material. The amplitude of an initial pulse should be given in order to balance nonlinear and dispersive features of a waveguide.

The parameters of tentative initial pulse (pressure at the shock front and the pulse duration) and the corresponding solitary wave in a rod were summarized in [2]. Following the analytical results obtained we have chosen the transparent polystyrene SD-3 with $\nu = 0.35$; $\beta = -6\,10^{10}$ N/m^2; $c_0 = 1.8\,10^3$ m/s as an appropriate material to manufacture a solid nonlinearly elastic waveguide.

Solitons in a transparent solid rod were formed in our experiments from an initial shock wave, which was initiated in a liquid, surrounding the waveguide, by means of the laser explosive evaporation of a metal, covering a foil target surface, that was placed in water nearby the input edge of the waveguide. The pulse duration was equal to 20 nanosec. The power density of laser radiation acting on the target was measured by the energy control unit and was kept constant and equal to $2.3\,10^8$ W/cm^2 during the experiment. In [3] we presented the study of a weak shock in a water, generated by laser evaporation of a metallic foil. It was shown that this wave consists of a very narrow compression zone (0.1μm) followed by a long (1 mm) tension area. The parameters of this wave are quite similar to those which are necessary for strain soliton generation. So far as the values of acoustical wave resistance of both water and polysterene are quite close, that allows to input a wave in a specimen without considerable losses of power on the interface.

The apparatus used for generation and observation of strain solitons consisted of a channel to produce the strain wave in a solid from a weak shock wave in water cell, a synchronizer, a holographic interferometer and a control unit for measuring the laser pulse energy. Observations were made in the direction perpendicular to that of wave propagation by means of the second pulsed laser used for holographic interferometry. The two parallel cut-offs were made along the rod in order to make transparent its central part. First exposure of the hologram was made in an absense of a shock wave in a specimen, that allowed to produce a hologram of unperturbed waveguide, the second one was synchronized with the prescribed stage of elastic wave propagation. Carrying fringes on interferograms occured due to the rotation of an optical wedge between exposures. Therefore the wave pattern was visualised due to the carrier fringe shift ΔK, which amplitude was used for direct calculations.

SOLITON EVOLUTION IN FINITE RODS

The typical interferogram of the solitary wave in the rod of constant cross section is shown in Fig. 1, where the direction of a wave motion is shown by an arrow. The left and right edges of the frame are located, respectively, at 75 mm and 125 mm from the input edge of the rod. Sharp kink on the right side of the photograph corresponds to a weak shock wave (A), that has produced the strain soliton. The fringe shift, representing a soliton, was extracted and plotted separately below the observation area image for convenience only. The longitudinal strain soliton is, in fact, the density wave, but not at all the lateral surface elevation wave (as it could be on a water surface). The secondary shock wave is imprinted in the middle of soliton. This shock was produced due to reflections of the initial shock from a tip of the rod and from target's foil consequently. The fringes in surrounding water remain undisturbed, that confirms the fact that the wave under study propagates in the rod.

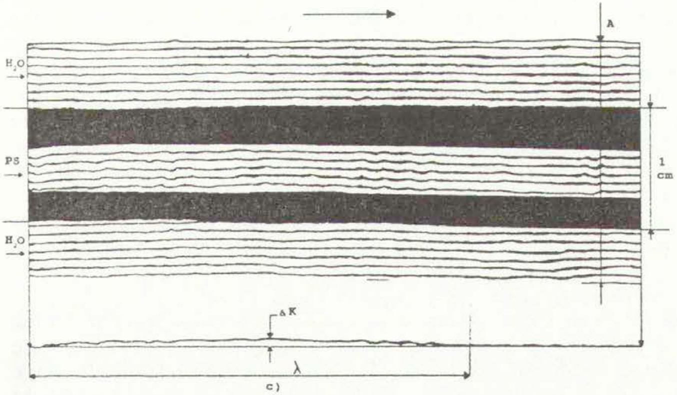

Figure 1. Wave pattern in the polysterene rod and in surroinding water, showing the strain soliton (c). The behaviour of a single fringe is depicted under the interferogram.

To check that the excited strain wave possesses indeed the soliton feature to conserve its shape, it is necessary to follow in observations its propagation along an extended elastic waveguide. However, the more absorbing is a waveguide material for linear elastic waves, the much shorter distance is to be sufficient to detect the constant shape wave propagation. Interferograms recorded at different areas of the waveguide allow to detect the evolution of the wave pattern in the rod and to visualize the process of soliton formation and its succeeding propagation along the waveguide. We observed that shock waves (which are residuals of the initial shock wave used for soliton generation) decay quickly, moving along the rod, however, their velocities remain higher than both the sound velocity in polystyrene and the soliton velocity (from one frame to another the soliton lags behind them). The soliton exhibits a rather extended trough-shaped longitudinal wave, which is not followed by any tensile wave. Moving along the rod, the soliton does not undergo any noticeable change of its shape and amplitude; confirming by that the well known major property of any nonlinear solitary wave, which is detected now in a nonlinear elastic wave propagation. The lack of attenuation is the second distinctive soliton feature in comparison with any linear pulse, that is expected to disappear in the polysterene at the 10 radii distance from the input due to wave dispersion and dissipation losses; even a shock wave attenuates dramatically moving along the polysterene rod.

The following quantitative estimations of the soliton parameters were reached. The soliton length λ was measured directly from the interferogram, and the soliton amplitude A was calculated from the carrier fringe shift ΔK obtained by reconstruction of doubly exposed holograms and shown on interferogram. The value of A was found by means of the following formula:

$$A = -\lambda_0 \Delta K / \{2h[(n_1 - 1)(1 - 2\nu) + \nu(n_1 - n_0)]\} \qquad (1)$$

where n_0 and n_1 are transparency indices of water and deformed material respectively, λ_0 is the light wavelength. $2h < R_0$ is rod's thickness along the detecting laser light direction. We obtained the following parameters for a typical recorded soliton: $A = 2.82 \cdot 10^{-4}$; $\lambda = 32.5$ mm >> $R_0 = 5$ mm, that are in a good agreement with our theoretical estimations.

The following arguments may confirm the observation of the strain solitary wave in our experiments. Firstly, there is no tensile area behind the observed long compressive wave, that is a typical feature of the localized nonlinear waves. Tensile areas, if any, can be easily detected using the same apparatus: the fringes would be shifted in an opposite direction. However, nothing was observed behind the soliton except straight fringes, i.e., the rod was free of strain after the soliton propagation. Secondly, even at the distances, exceeding dozens of rod's radii, both the shape and the wave parameters remain permanent and do not exhibit any essential distortions in the uniform rod, that is, the nonlinear strain wave possesses one of the most distinctive feature of a soliton. The distance chosen for our observations seems to be sufficiently large, because polystyrene is well known to be an effective absorber of acoustic and shock waves. The last was confirmed by considerable decay of the remainder of the initial shock wave, which moved ahead of the soliton, as it is shown in Fig. 1.

The next set of experiments has been devoted to the process of soliton reflection from both the free and bounded tips of the rod. As it follows from theory and numerical simulations when reflecting from the free tip soliton has to change its "polarity" and become the wave of rarefaction. However, wave of such type can not propagate in a polysterene rod. Thus, it has to disappear quickly after the soliton reflection. In experiments we have proved this conclusion. On the contrary, while reflecting from the bounded tip the soliton has to conserve its parameters and pass back with the same shape and amplitude as the one incident to the tip. The only difference is some phase shift occuring as a result of reflection. The experimentally recorded patterns of soliton reflection show the considerable rise of wave amplitude near the tip at the moment of reflection, and the reflected soliton propagating back and having the same shape and amplitude. The phase shift is difficult to record using our apparatus.

CONCLUSIONS

Thus, using the laser generator of weak shock waves and the holographic interferometry setup, we have successfully generated, detected and recorded the strain solitary wave (the soliton) inside the nonlinearly elastic solid rod. Soliton detection may allow to introduce a new one-pulse technology in nondestructive testing, to determine intrinsic physical properties of nonlinearly elastic materials and the waveguide parameters, e.g., the 3d order elastic moduli, which values are not reliably measured for many structural materials up to now. They can be of use for study of inhomogeneities and cavities, in particular, when the ultrasonic technique cannot be applied. However, the main and general result of the study seems to be the proof of energy transfer for quite a long distance in elastic solids made of materials, which are not sufficiently transparent for linear strain waves and ultrasonic waves due to dispersive and dissipative features.

REFERENCES

1. Samsonov A.M., Nonlinear strain waves in elastic waveguides. In: "Nonlinear waves in solids", A.Jeffrey, J.Engelbrecht eds., Springer. Wien-New York. 349-382, 1994.
2. Samsonov A.M., Sokurinskaya E.V., *Sov.Phys.Techn.Phys.*, **33**, 8, 989-991, 1988.
3. M.A.Harith, A.Salvetti, D.P.Singh, V.Palleschi, M.Vaselli, G.V.Dreiden, Yu.I.Ostrovsky, I.V.Semenova. *Journ.Appl.Phys.* **66**, 11, 5194-5197, 1989.

OPTICAL FLOW TECHNIQUE USED TO CHARACTERISE THE FLOW INSIDE DIFFERENT CAVITIES INTERACTING WITH A BOUNDARY LAYER

Afif Elcafsi, Alecsandra Rambert and Pierre Gougat
LIMSI-CNRS, B.P. 133 91403 Orsay FRANCE

Abstract An Optical Flow technique based on the use of Dynamic Programming has been applied to Particle Image Velocimetry yielding a significant increase in the accuracy and spatial resolution of the velocity field. We applied this technique to characterize the interaction between a laminar boundary layer and cavities of different shape factor.

The experimental characterisation of the interaction between a boundary layer and a cavity was developed in order to valid a three dimensional computation code based on the L.E.S. method (Large Eddies Simulation). The main application of this work is the study of the pollutant transport and dispersion in a street canyon.

INTODUCTION

The optical flow method (Quenot[1]) offers a new approach for analyzing flow images. It largely improves spatial accuracy and minimises the number of spurious vectors. Application of this method may help in quantitative analyses of several challenging problems of fluid mechanics, as well as in full plane validation of their numerical counterparts. This technique has been tested for calibrated synthetic sequences of images (Quénot et al.[2]). It was observed that the accuracy remains better than 0.5 pixels/frame.

We have used this technique in order to characterize flow velocity field inside cavities interacting with a boundary layer, configuration which is similar to a canyon street. Much attention has been directed to the study of the various canyon flow regimes (DePaul and Sheih[3]) since air flow is responsible for the transport of properties such as pollutants, heat and moisture. Canyon geometry is an important determinant of characteristic airflow observed within urban canyons. The transition between flows is determined by canyon geometry

EXPERIMENTAL DEVICE

The experimental configuration is presented in Figure 1. The cavities we tested have different length ratio (h_2/L: 0.5; 1; 2).

At the entry of the cavity, the boundary layer is laminar and it is matching with a Blasius profile (U_∞ is equal to 1.27 m/s). The boundary layer velocity profile was measured using a hot wire. The velocity field inside the cavity was measured using an Argon laser and a Pulnix digital camera (768×484 pixels). *Lycopodium* particles and smoke were used as seeding. The image processing was made by PIV using the optical flow technique. Measurements were made for the both planes (XY) and (YZ).

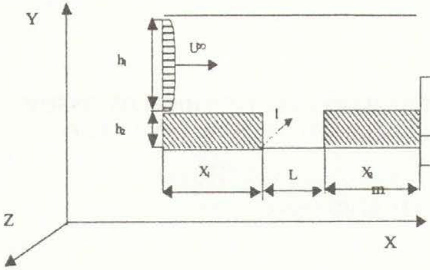

h_1 (m)	h_2 (m)	l (m)	L (m)	X1 (m)	X2 (m)	h_2/L
0.075	0.05;0.1;0.2	0.08	0.1	0.2	0.3	0.5;1;2

Figure 1 Geometrical configuration

OPTICAL FLOW COMPUTATION

Optical flow computation consists in extracting a dense velocity field from an image sequence assuming that the intensity is conserved during the displacement. Several techniques have been developed for the computation of optical flow. The technique that was chosen for DPIV application was introduced by Quénot[1] as Orthogonal Dynamic Programming (ODP) algorithm for optical flow detection from a pair of images. It has been extended to be able to operate on longer sequences of images and to search for subpixel displacement. Compared with other optical flow approaches or to the classical correlation based DPIV, the optical flow has the following advantages: (i) it can be applied simultaneously to sequences of more than two images; (ii) it performs a global image match by enforcing continuity and regularity constrains on the flow field. This helps in ambiguous or low particle density regions; (iii) It provides dense velocity fields (neither holes nor border offsets); (iiii) local correlation is iteratively searched for in regions whose shape is modified by the flow, instead of being searched by fixed windows. This greatly improves the accuracy in regions with strong velocity gradients.

EXPERIMENTAL RESULTS

Velocity fields obtained inside the different cavities are presented in Figures 2, Figure 3 and Figure 4.

For the cavity of ($h_2/L=0.5$) shape factor, two counter rotating vortex are observed with eddies of smaller dimensions turning around them (Figure 2a and 2b). A numerical result was obtained by L.E.S. (Large Eddies Simulation) for the same geometrical configuration and in the same flow conditions (Figure 2c).

For the cavity of ($h_2/L=1$) shape factor, only one vortex was observed (Figure 3b). The cavity of ($h_2/L=2$) shape factor is characterised by a more complex structure (Figure 4b): one greater vortex and other smaller size vortex of opposite sing. For the three cavities a velocity field measurement made in the YZ plane show that the flow can't be considered only bidimensionnal (Figures 2b, 3b and 4b).

Measurements made after the cavities showed that the boundary layer was no longer laminar. A spectral frequency analysis of the hot wire signals was realised which showed that the frequencies were in the low frequency domain (<200 Hz). This perturbation of the boundary layer was due to the exit of the vortex structures from the cavity. The flow visualisation (Figure 5a) confirms the perturbation of the laminar boundary layer. The velocity field obtained in theses conditions show the translation movement of the vortex in this region (Figure 5b).

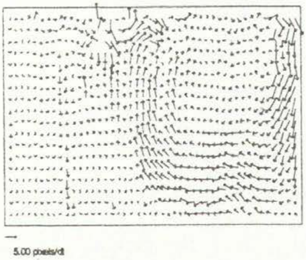

Figure 2a

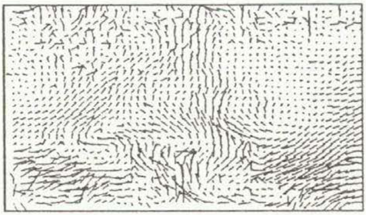

Figure 2b

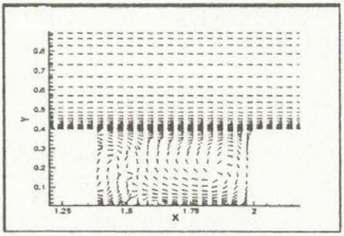

Figure 2c

Figure 2 Flow velocity fields obtained inside the cavity ($h_2/L=0.5$)
2a. (XY plane) 2b. (YZ plane) 2c. (XY plane: numerical results)

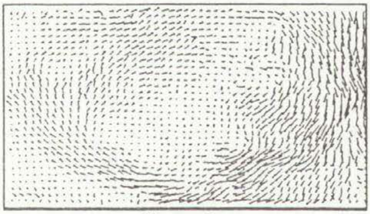

Figure 3a

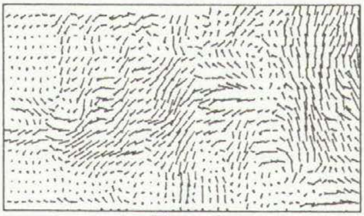

Figure 3b

Figure 3 Flow velocity fields inside the cavity ($h_2/L=1$) (3a. (XY plane);3b. (YZ plane))

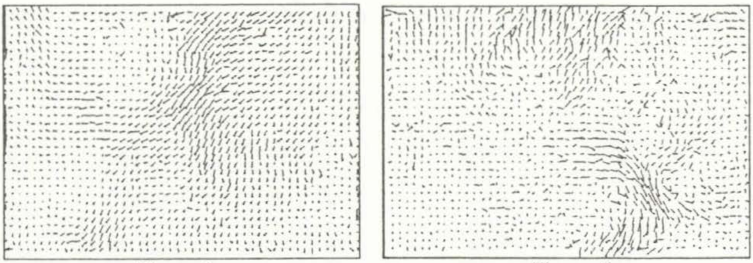

Figure 4a Figure 4b

Figure 4 Velocity field inside the cavity ($h_2/L=2$ (4a. (XY plane), 4b. (YZ plane))

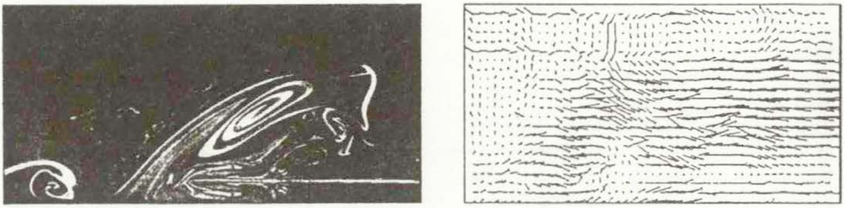

Figure 5a Figure 5b

Figure 5 Smoke visualisation of vortex release from the cavity ($h_2/L=1$) (5a) and the corresponding velocity field (5b)

CONCLUSION

An Optical Flow technique based on the use of Dynamic Programming has been successfully applied to Digital Particle Image Velocimetry yielding a significant increase in the accuracy and spatial resolution. Results have been presented for an interaction between a boundary layer and a cavity modelling the flow in a canyon street. Using this algorithm, a dense velocity vector field for every pixel of the image could be obtained.

Preliminary experimental investigations show that optical flow method can be successfully applied to extract velocity fields on smoke seeding image sequences on which classical cross-correlation DPIV fails.

An important future development of the optical flow technique is its extension to three-dimensional velocity fields computation for which Dynamic Programming search is very well suited.

REFERENCES

1. Quénot, G.M. 1992, The Orthogonal Algorithm for Optical Flow detection using Dynamical Programming, Proc. IEE ICASSP, San Francisco, vol. 3, pp. 249-252.

2. Quénot, G.M., Pakleza, J. and Kowalewski, T. 1998, Particle Image Velocimetry with Optical Flow, Experimental in Fluids vol. 25, 177-189, 1998.

3. DePaul F. T. and Sheih C.M. 1986, Measurements of wind velocity in a street canyon, Atmospheric Environment vol. 20, pp. 455-459.

Comparative study of correlation-based PIV evaluation methods

R. Fei, L. Gui, W. Merzkirch
Lehrstuhl für Strömungslehre
Universität Essen, D-45117 Essen, Germany

Many evaluation methods applied to planar PIV data sets are based on correlation schemes. Optical correlation resulting in visible patterns of Young's interference fringes has been abandoned in favour of digital image processing methods. The correlation algorithms reported by Cenedese and Paglialunga (1990), Adrian (1991), Willert and Gharib (1991) can be accelerated by the FFT. Another means of acceleration is the „error correlation" (Hart 1996). The correlation function also serves for evaluating the planar data field if the velocimetry is performed by particle tracking (Huang et al. 1993; Kemmerich and Rath 1994; Okamoto et al. 1995). The evaluation methods reported by Gui and Merzkirch (1996,1997) for tracking ensembles of particle images („minimum quadratic difference" (MQD), „minimum absolute difference" (MAD) method) also incorporate the correlation function. The following algorithms that are described in the given references are investigated regarding their performance when certain parameters of the data sets and the evaluation procedure are varied (see table):

Algorithm	Evaluation function
Correlation A	$\Phi(m,n)=\sum_{i=0}^{M-1}\sum_{j=0}^{N-1} g_1(i,j)\,.\,g_2(i+m,j+n)$
Correlation B	$\Phi(m,n)=\frac{1}{(M-m)\cdot(N-n)}\sum_{i=0}^{M-m-1}\sum_{j=0}^{N-n-1}\left[g_1(i,j)-\overline{g_1}\right]\cdot\left[g_2(i+m,j+n)-\overline{g_2}\right]$ $\textit{für} \quad m\geq 0,\ n\geq 0$
Correlation C	$\Phi(m,n)=\sum_{i=0}^{M-m-1}\sum_{j=0}^{N-n-1}\left[g_1(i,j)-\overline{g_1}\right]\cdot\left[g_2(i+m,j+n)-\overline{g_2}\right]$
Error Correlation	$\Phi(m,n)=1-\frac{1}{(M-m)(N-n)}\sum_{i=0}^{M-m-1}\sum_{j=0}^{N-n-1}\left\vert g_1(i,j)-g_2(i+m,j+n)\right\vert$ $\textit{für}: m\geq 0, \quad n\geq 0$
Correlation-Tracking	$\Phi(m,n)=\sum_{i=0}^{M-1}\sum_{j=0}^{N-1}\left[g_1(i,j)-\overline{g_1}\right].\left[g_2(i+m,j+n)-\overline{g_2}\right]$
MQD-Tracking	$D(m,n)=\sum_{i=0}^{M-1}\sum_{j=0}^{N-1}\left[g_1(i,j)-g_2(i+m,j+n)\right]^2$

MAD-Tracking	$D(m,n)=\sum_{i=0}^{M-1}\sum_{j=0}^{N-1}\lvert g_1(i,j)-g_2(i+m,j+n)\rvert$

The algorithms are compared by applying them to the evaluation of simulated (artificial) PIV recordings, in which the particle images are distributed stochastically and have a Gaussian grey value distribution. (Willert and Gharib 1991; Westerweel et al. 1997). The influence of three different parameters on the evaluation accuracy is studied.:

1. Particle displacement

60 simulated pairs of PIV recordings of size 768x512 pixels and particle displacements ranging from 0,05 to 5 pixels are generated. The RMS values of the evaluation errors, with reference to the known true displacement, are shown in Fig. 1 for the different algorithms used. The errors determined for the tracking algorithms are periodical functions with the periodicity of 1 pixel. The MQD method here produces the smallest error. The pattern shown for the correlation algorithms A,B,C can be improved by applying the window off-set technique (Westerweel et al. 1997) so that the displacement to be measured is reduced to values below 1 pixel.

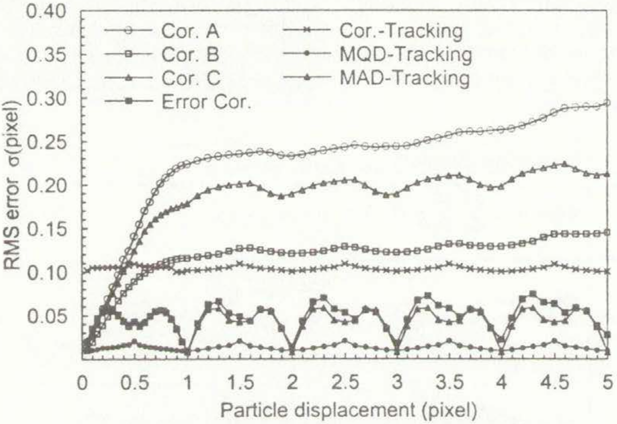

Fig. 1 Evaluation accuracy as function of particle displacement

2. Interrogation window size

15 window sizes ranging from 16x16 to 128x128 pixels are used for the evaluation. The resulting RMS errors are shown in Fig. 2. The tendency is similar for all algorithms tested. The influence of the window size is prominent for small windows. Low RMS error values for small window sizes are mandatory for resolving small scale flow structures.

3. Non-uniform velocity fields

While the previous examples correspond to a constant velocity flow we use here the simulation of a PIV recording taken in a flow with strong non-uniformities (vortical flow). The influence of the interrogation window size on the evaluation accuracy is tested; the RMS error shown in Fig. 3 is the average error for the whole field evaluated. Each algorithm has a critical value for which the RMS error is minimal. The increase of the RMS error for increasing window sizes beyond the minimum must be explained with the increasing non-uniformity of the particle image displacements included in the windows of larger size.

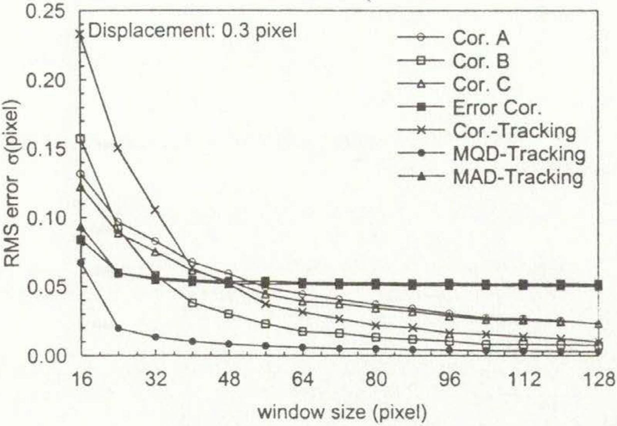

Fig. 2 Evaluation accuracy as function of interrogation window size in uniform flow

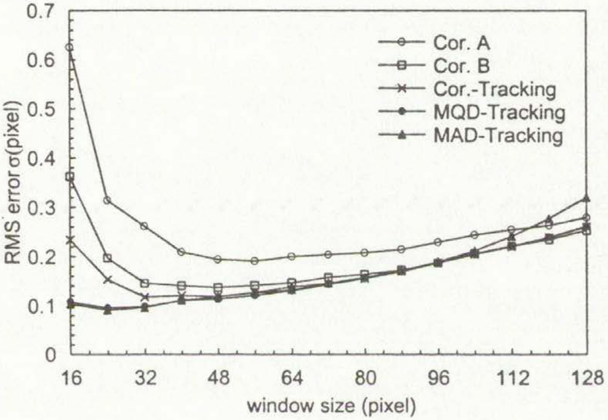

Fig. 3 Evaluation accuracy as function of interrogation window size in non-uniform flow

These parametric studies allow to select the appropriate evaluation algorithm if a specific accuracy is desired or needed. Additional parameters that are also investigated and of practical interest are the influence of particle image size and evaluation speed.

Acknowledgement
This research is supported by Deutscher Akademischer Austauschdienst (DAAD) with a grant for R. Fei.

References

Adrian, R.J. 1991: Particle-imaging techniques for experimental fluid mechanics. Annu.Rev.Fluid Mech. 23, 261-304.

Cenedese, A.; Paglialunga, A. 1990: Digital direct analysis for a multiexposed photograph in PIV. Exp. Fluids 8, 273-280.

Gui, L.; Merzkirch, W. 1996: A method of tracking ensembles of particle images. Exp. Fluids 21, 465-468.

Gui, L.; Merzkirch, W. 1997: A fast mask technique for the phase-separated evaluation of two phase PIV recordings. 7th International Conference on „Laser Anemometry Advances and Applications", September 8-11, Karlsruhe.

Hart, D.P. 1996: Sparse array image correlation. 8th Int. Sym. on Applications of Laser Techniques to Fluid Mechanics, July 8-11, Lisbon, Portugal.

Huang, H.T.; Fiedler, H.E.; Wang, J.J. 1993: Limitation and improvement of PIV. Part I: Limitation of conventional techniques due to deformation of particle image patterns. Exp. Fluids 15, 168-174.

Kemmerich, T., Rath, H.J. 1994: Multi-level convolution filtering technique for digital laser-speckle-velocimetry. Exp. Fluids 17, 315-322.

Okamoto, K.; Hassan, Y.A.; Schmidl, W.D. 1995: New tracking algorithm for particle image velocimetry. Exp. Fluids 19, 342-347.

Westerweel, J.; Dabiri, D.; Gharib, M. 1997: The effect of a discrete window offset on the accuracy of cross-correlation analysis of digital PIV recordings. Exp. Fluids 23, 20-28.

Willert, C.E.; Gharib, M. 1991: Digital particle image velocimetry. Exp. Fluids 10, 181-193.

INDUSTRY CONTROL OF GEOMETRICAL PARAMETERS OF RAILWAY WHEELS BY VIDEOGRAMMETRIC METHOD

S. D. Fonov, V. P. Koulesh, V. D. Vermel, V. F. Zabolujev

Central Aero-Hydrodynamic Institute, Zhukovsky, 140160, Russia

Summary. The videogrammetric system was developed and applied to industrial control of the geometrical parameters of railway wheels. The measuring system uses three videogrammetric channels. Two of them apply the laser light sheet scheme. These channels have a measurement range of 500×500 mm. The measurement errors of each of the two coordinates do not exceed 0.15 mm. The third channel is constructed under a shadowgraphic scheme on base of a light beam of radial rays and provides the measurements of the wheel rolling surface geometry. This channel has a measurement range of 120×180 mm and measurement tolerance of 0.05 mm. The measurement system has been placed in operation on the industrial conveyor at Vyksunsky steel works. It operates in real time with the conveyor.

Introduction

Traditionally different optical methods are extensively applied at the Central Aero-Hydrodynamic Institute (TsAGI) for non-contact measurements in aerodynamic experiments [1,2]. In the last years a number of the optical systems was developed in the TsAGI for measurement of geometrical parameters. These systems are based on the videogrammetric method and intended for three typical applications:

- measurement of movement and deformation of the aircraft models in wind tunnel [3];
- measurement of movement and deformation of blades of full-scaled helicopter rotors [4];
- measurement of geometrical parameters of the different complex shape objects.

This paper presents one practical case of the third application. The videogrammetric system in this case uses video cameras with CCD-array, modern computer facilities and methods of numerical images processing. This system is intended for industrial control of geometrical parameters of the railway wheels at Vyksunsky steel works.

Measuring system brief description

The measuring system for industrial control is built-in on an existing factory conveyor line and structurally includes two basic subsystems:

1. Optico-mechanical stand located on the conveyor and including, first, a electrical & hydraulic system of transportation of the wheel to a measurements zone and its rotation with technological control facilities and, second, a videogrammetric system, located on a rigid metal skeleton. The whole stand is cover by light-proof box (Fig.1).
2. Central digital-control system built on the base of the "Pentium" personal computer. This system is installed at a special control room.

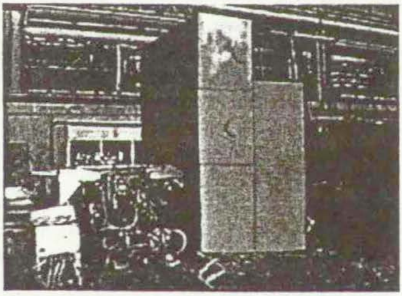

Fig. 1. The exteriors of the optico-mechanical stand

The videogrammetric system consists of the following main principal partitions:

- an optical system;
- a digital system of the acquisition and processing of the image information and control system operating in rate of the conveyor;

- an original technique and means of calibration;
- software package.

The structural scheme of the video-optical system is presented on Fig. 2. The system contains three video-optical channels - A, B and C [5].

The A and B channel is intended to measure geometrical parameters of a relief of inside and outside surface of the wheel (top and bottom in a position of the control). These channels are based on the same principle of a cutting light sheet [6]. Each of the A and B channels contains two functional units mounted on a general rigid frame: a laser projector and analogue CCD camera. The laser projector creates a light sheet falling in radial section on a surface of the wheel. It contains a continuously operated He/Ne laser with power of radiation about 1 mW with wavelength of 0.6328 microns and optical lens system including spherical and cylindrical lenses. The optical axes of both laser projectors are located vertically at a distance about 300 mm from the wheel axis and are directed towards each other. The light sheets are passed through the wheel axis. In front of objective of each video camera a red optical filter is installed, which lets the laser radiation pass and cuts radiation of a blue-green spectrum range. The optical axes of CCD-cameras are directed under an angle about 45 degrees to a light sheet.

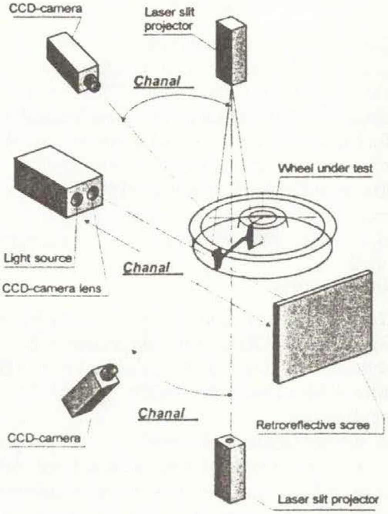

Fig. 2. The structural scheme of the video-optical system

The C channel is intended to measure parameters of rolling surface profile of the wheel felloe. This channel is built under the shadowgraphic scheme with radial beams. The C channel contains the source of a radial light beam and analog CCD camera both mounted at one side of the wheel, and retroreflective screen installed at the other side of it. The optical axis of video camera of the channel C is oriented horizontally, perpendicular to the light sheet and is positioned at a distance of the wheel radius (about 485 mm) from the axis of rotation. The C channel camera is supplied with a blue-green optical filter, which prevents the He/Ne laser radiation from passing into the camera. The light source contains a condenser lens and blue-green optical filter.

The digital image acquisition and processing system is implemented on base of a «Pentium» personal computer equipped with additional specialized boards connected to it's information bus. These boards are: a standard videomultiplexer "Data Translation CPX-7", a standard board of a digitization of the video-images "Data Translation QCAP-55", and a non-standard board of the parallel input/output interface.

Calibration technique

Accuracy of measurement of geometrical parameters depends on accuracy of determination and stability of all parameters of the functionally complex operating characteristic of each of the three channels. The calibration is performed with the help of a special developed calibration facility, which can provide:

- initial and periodic adjustment of measuring system;
- calibration of system with obtaining of the operating characteristic parameters and estimation of measurement tolerance;
- metrological certification and verifications of measuring system.

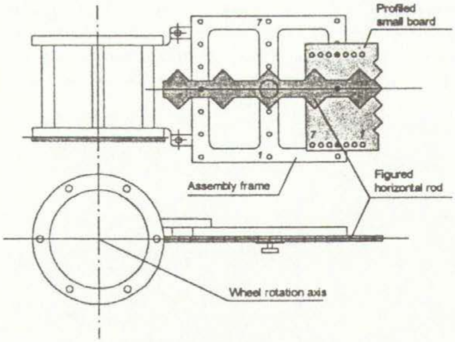

Fig. 3. Calibration facility

The structure of the calibration facility is shown on Fig. 3. The calibration facility has an assembly frame, figured horizontal rod and profiled small board installed sequentially on an assembly frame. This facility provides establishment of 35 marker node points (7 positions of the rod in the vertical direction by 5 marker node points in the horizontal direction) for each of three A, B and C channels. The measurement area in two axes (the view fields) for A, B and C channels is graphically represented in Fig. 4. This area is correlated with the CCD-array frame projection. The circles indicate the reference points that are established during calibration.

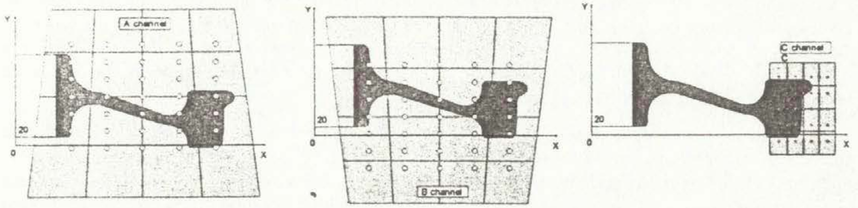

Fig. 4. View areas and reference point for calibration

The results of numerous calibrations showed that measurement tolerance (root-mean-square value) for channels A and B does not exceed 0.1mm and for channel C – 0.05mm.

Sequence of measurements

The measurement process, which is fairly complex, can be outlined as follows. When a wheel comes to the measuring stand, the system locks the conveyor to prevent next wheel's arrival. The wheel is lifted to measurement position with the help of hydraulic mechanism. At the same time the wheel is driven into rotation with a period of 20 seconds.

As the wheel is being turned, a required number of its radial sections are examined by getting images from the 3 channels. While the wheel is turning between two subsequent examined sections preliminary processing of the images is carried out: the coordinates of points of three channels are combined into whole contour of radial section (Fig.5) and the results are stored.

Usually one wheel revolution is enough to get images of the required number of sections. However, if it is necessary to investigate a wheel in greater number of radial sections, it can be done during several revolutions of the wheel. When the measurements are over, the wheel is lowered to the conveyor. Then the conveyor is be unlocked and the measurement stand is ready to receive the next wheel.

While the wheel is being lowered, the system makes final processing of the measurement data. The measured separate radial sections are bound together and compared with the wheel mathematical model and the generalized geometrical parameters of the wheel are determined.

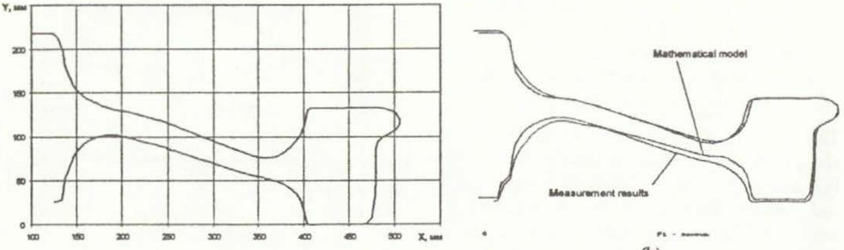

(a)

(b)

Fig. 5. Graphic presentation of measurement results and their comparing with mathematical model

By the moment, when the stand is ready to accept the next wheel, the results of measurement of the previous wheel are ready. The whole cycle of the measurement of one wheel takes 43 seconds. The generalized geometrical parameters are stored in a database in tabular format text files. The most important parameters selected by administrator are displayed on the screen of the conveyor inspector. The contours of sections of the wheel are represented in the graphic form on the screen of the monitor. An example of the monitor screen output is shown on Fig. 5(b). In this picture a contour given by mathematical model is also shown. The system supports the animated representation of this graphic information.

This measuring system provides measurements of 6…12 radial sections per wheel revolution and has productivity of about 80 wheels per hour. It is necessary to note that the duration of graphic representation of results or animation can not be performed during 43 seconds period, therefore this feature cannot be enabled in the automatic check mode. It will be necessary either temporary to stop the conveyor or to miss to check some of the wheels. To enable the features of graphic results representation and animation in automatic mode will require connection of an additional personal computer.

References

1. V. P. Kulesh, S. D. Fonov, V. A. Yakovlev, "Application of optical and interference methods in experimental aerodynamics", *AGARD-CP-601*, pp.(17-1)-(17-12), 1998.
2. D. D. Gribanov, V. P. Kulesh, A. K. Martynov, A. A. Orlov, S. D. Fonov, "Laser-optical method for investigation of movement trajectory and bending-twist deformations of blades of carrying rotor models", *Science transactions of TsAGI*, v.XI, No. 6, pp.88-95, 1980.
3. V. P. Kulesh, S. D. Fonov, "Plane models both movement and deformation parameters measurement in wind tunnel using the videogrammetric method", - *Science transactions of TsAGI*, v.XXIX, No.1-2, pp.165-176, 1998.
4. S. Bosnyakov, V. Kulesh, A. Morozov, S. Fonov, "Videogrammetric system for study of movement and deformation of real-scale helicopter rotor blades", ICHSPP'98, p.38.
5. V. Vermel, V. Koulesh, S. Fonov, et al, "Method for determination of detail geometrical parameters and device for carrying same into effect", *Russian Patent No. RU 2105265 C1, In.Cl. 6 G01B11/24*, Bull. No.5, 1998
6. K. K. Hitati, "Device for detail shape determination", – *Japan Claim No. 61-53643, In.Cl. G01B11/24*, 1986.

VISUALIZATION OF HEAT TRANSFER ENHANCEMENT REGIONS MODIFIED BY THE INTERACTION OF INCLINED IMPINGING JETS INTO CROSSFLOW

Elzbieta Fornalik*, Yu Yamamoto**, Wei Chen**,
Kazuyoshi Nakabe** and Kenjiro Suzuki**

*University of Mining and Metallurgy AGH, Al. Mickiewicza 30, 30–059 Krakow, Poland
**Department of Mechanical Engineering, Kyoto University, Kyoto 606-8501, Japan

Summary Visualization of heat transfer enhancement regions was made for a pair of jets obliquely discharged into a crossflow. The present study was provided to examine the interaction between the two oblique jets and also to compare two cases of vertical and oblique jets. The temperatures of the heat transfer target surface were visualized with thermochromic liquid crystal sheets. The colors of the liquid crystal images taken by a CCD camera were transformed accurately and effectively into the temperatures by means of the neural network technique to obtain Nusselt number distributions on the target surface. Fluorescent dyes were added to the jet fluid to visualize also the cross-sectional flow patterns with the light sheet of a laser. The most important parameter used in the present study was the velocity ratio VR of the jet to the crossflow besides Reynolds number. It was observed that the behaviors of large-scale longitudinal vortices generated by the oblique jets were affected by the mutual interaction between the two jets. The locations of the longitudinal vortices were found to correspond well to the Nusselt number contours, the ridgelines of which, in particular, were situated almost parallel to the axes of the longitudinal vortex. The two ridgetops or peaks were observed in the Nusselt number contours. In the case of the oblique jets, the upstream peak was higher than the downstream one in higher VR ratio, while in the case of vertical jet the downstream peak was always higher than the upstream one.

ABSTRACT

As an effective method to enhance heat and mass transfer, impinging jets have been used in many industrial applications; the drying process of papers and films, the tempering process of glass, the annealing process of steel, the cooling process of gas turbine system and electronic components, etc. Numerous analytical and experimental studies have been made to investigate the basic heat transfer characteristics of jet impingement; Gardon and Akfirat[1-2], Sparrow and Lovell[3], Pamadi and Belov[4], Goldstein et al.[5], Goldstein and Franchett[6], Chang and Mills[7], Lytle and Webb[8], Lee et al.[9], San, J.Y. et al.[10], etc. They have examined the effects of Reynolds number, nozzle-to-plate distance, nozzle configurations, jet temperature, and jet orientation upon the heat transfer performance of the jet impingement under the conditions of air impinging jet onto a flat surface without crossflow. Effects of crossflow on jet impingement heat transfer also have been examined by Metzger and Korstad[11], Sparrow et al.[12], Bouchez and Goldstein[13], Goldstein and Behbahani[14], Al-Sanea[15], etc.

The authors previously focused on the jet orientation under crossflow conditions to intentionally generate large-scale steady vortices and enhance local heat transfer coefficients, and carried out the flow visualizations and heat transfer experiments for an obliquely discharged jet into crossflow[16-17]. A single jet was installed on the duct wall opposite to the heat transfer target wall so as to impinge obliquely on the target wall. The jet orientation was defined with two angles; one is a pitch angle measured up from the nozzle-installed wall and the other a skew angle measured relatively to the crossflow direction. The visualization results demonstrated that a pair of counter-rotating longitudinal vortices generated by the oblique jet elongate heat transfer enhancement regions spanwisely and streamwisely.

In the present study, the attention was paid to the effects of flow and thermal interactions between two oblique jets on jet impingement heat transfer. Visualizations were made for flow and heat transfer fields modified by the interaction between the two jets obliquely discharged into crossflow. Then, the heat transfer characteristics were compared between vertical and oblique jet cases.

Figure 1 shows a schematic illustration of the flow configuration together with the present experimental set-up. The two oblique jets were situated in in-line arrangement with a streamwise distance of 10 nozzle-diameters. The skew angels measured relatively to the crossflow direction were set to be +90 degrees for the upstream-side jet, Jet 1, and -90 degrees for the downstream-side one, Jet 2, while the pitch angle measured up from the nozzle-installed wall was fixed at 45 degrees for both jets. The pitch angles of both jets were changed to be 90 degrees for the vertical impingement case.

Cross-sectional jet flow fields were, first, visualized with the addition of fluorescent dyes or tracer particles illuminated by a planar Nd:YAG pulse laser light. The cross-sectional images of flow pattern were taken with a CCD camera set up downstream. The velocity vectors were calculated by using the scattering images of the particles and the PIV (particle image velocimetry) system. Thermochromic liquid crystal was used to estimate the surface temperatures of heat transfer target plate[18]. Another CCD camera was set up above the top plate, that is the target plate, of the test section to monitor the liquid crystal colors through the plate. The hierarchy neural network method proposed by Kimura[19] was applied to transform the color images into temperature distributions and then into the Nusselt number distributions.

Figure 3 shows a typical snapshot image of the cross-sectional flow patterns at x/d = 20 downstream of the two oblique jets. d and x, respectively, denote the diameter of the jet nozzle and the streamwise distance from the center of the upstream nozzle. The Reynolds number based on the hydraulic diameter of rectangular test section was equal to be 5,000. The cross-sectional flow visualization clearly reveals that three major large-scale longitudinal vortices, V1, V3 and V4, not the two pairs of the counter-rotating vortices inferred from the above-mentioned single jet case, are generated in the downstream of the two jets, together with one more obscure small-scale vortex, V2. V3 and V4 denotes a pair of longitudinal vortices generated by the downstream-side jet, Jet 2, while V1 and V2 a pair of the vortices by the upstream-side jet, Jet 1. Although it is difficult to find the image of V2 vortex in Fig. 3, the rotating motion of the V2 vortex was observed on the monitoring screen of video cassette-tape recorder. The vortex, V3, dominantly affects the behavior of the V2 vortex, although the V2 vortex should be relatively intense similar to V3 according to Refs. 16 and 17. It is, therefore, found that the interaction between the two in-line oblique jets has significant influence on the formation of longitudinal vortex.

The heat transfer enhancement regions were observed corresponding to the locations of the above-mentioned longitudinal vortices generated by the two oblique jets. And, also flow patterns and heat transfer distributions were compared between the oblique and vertical cases of the two jets. Figure 2 shows the contours of Nusselt number distributions on the target plate in the cases of (a) VR = 3 and (b) VR = 5 under the same Reynolds number, Re = 5,000. It is clearly seen in this figure that the Nusselt number distributions depend on the velocity ratio, VR, and two peaks appear in both Nusselt number contours. The upstream peak to which Jet 1 mainly contributed was higher than the downstream one in larger VR cases, and vice versa in smaller VR cases. In the case of the vertical impinging jet, on the other hand, the downstream peak is always higher than the upstream one. Close observation reveals that the ridgelines of the Nusselt number contours, that is, the lines connecting the maximum positions in the spanwise Nusselt number distribution at every streamwise location were situated almost parallel to the axes of the vortex centers. The valley between the ridgelines corresponds to a relatively lower Nusselt number region in the middle of the V2 and V3 vortices. These two vortices may obstruct the crossflow especially in the vicinity of the target surface, identified with the vortex visualized in the previous study[16]. More details about relations between vertically and obliquely discharged jets will be given in the presentation of the Colloquium.

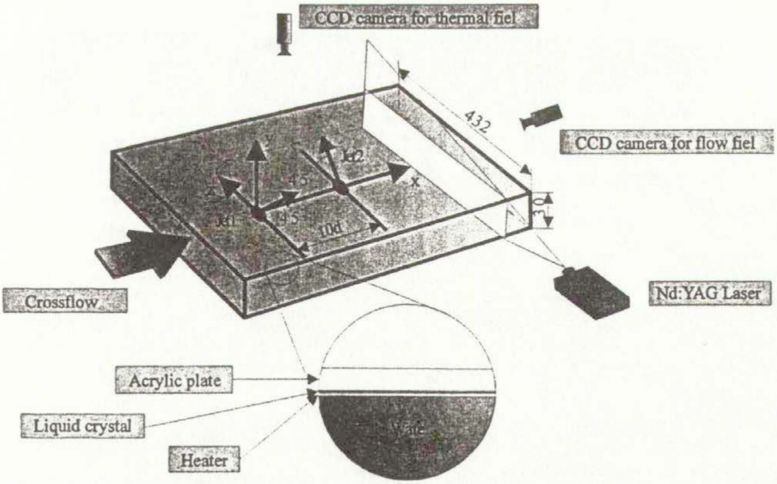

Fig. 1. Flow configuration.

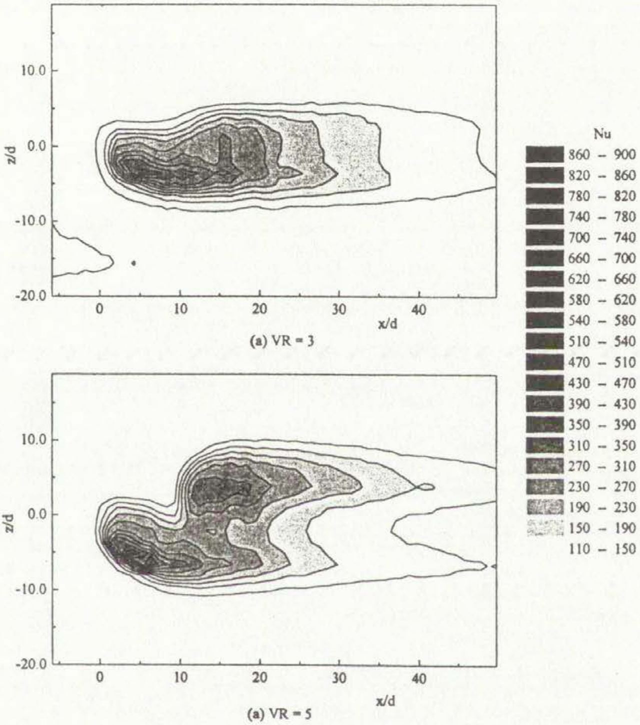

(a) VR = 3

(a) VR = 5

Fig. 2. Distributions of Nusselt number (2 inclined jets and Re = 3000).

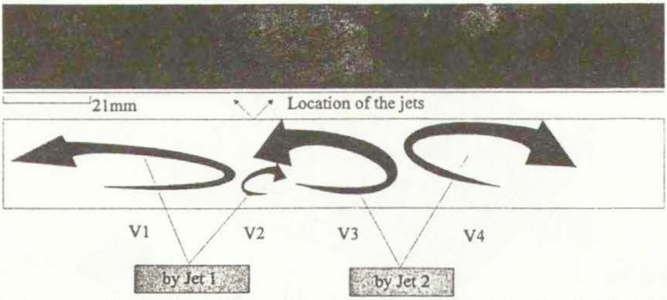

Fig. 3. Flow visualization of two oblique jets (Re = 3000, VR = 5 and x/d = 20).

REFERENCES

1 Gardon, R. and Akfirat, J.C.: The Role of Turbulence in Determining the Heat-Transfer Characteristics of Impinging Jets. *Int. J. Heat Mass Transfer* **8**, pp.1261-1272, 1965.

2 Gardon, R. and Akfirat, J.C.: Heat Transfer Characteristics of Impinging Two-Dimensional Air Jets. *Trans. ASME: J. Heat Transfer* **88**, pp.101-108, 1966.

3 Sparrow, E.M. and Lovell, B.J.: Heat Transfer Characteristics of an Obliquely Impinging Circular Jet. *Trans. ASME: J. Heat Transfer* **102**, pp.202-209, 1980.

4 Pamadi, B. N. and Belov I. A.: A Note on the Heat Transfer Characteristics of Circular Impinging Jet. *Int. J. Heat Mass Transfer* **23**, pp.783-787, 1980.

5 Goldstein R.J., Behbahani, A.I. and Heppelmann, K.K.: Streamwise Distribution of the Recovery Factor and the Local Heat Transfer Coefficient to an Impinging Circular Air Jet. *Int. J. Heat Mass Transfer* **29-8**, pp.1227-1235, 1986.

6 Goldstein, R.J. and Franchett, M.E.: Heat Transfer from a Flat Surface to an Oblique Impinging Jet. *Trans. ASME: J. Heat Transfer* **110**, pp.84-90, 1988.

7 Chang, B.H. and Mills, A.F.: Computation of Heat Transfer from Impinging Turbulent Jets. *Proc. 6th Int. Symp. on Transport Phenomena in Thermal Engineering*, 1993.

8 Lytle, D. and Webb, B.W.: Air Jet Impingement Heat Transfer at Low Nozzle-Plate Spacings. *Int. J. Heat Mass Transfer* **37-12**, pp.1687-1697, 1994.

9 Lee, S.J., Lee, J.H. and Lee, D.H.: Local Heat Transfer Measurements from an Elliptic jet impinging on a Flat Plate using Liquid Crystal. *Int. J. Heat Mass Transfer* **37-6**, pp.967-976, 1994.

10 San, J.Y., Huang, C.H. and Shu, M.H.: Impingement Cooling of a Confined Circular Air Jet. *Int. J. Heat Mass Transfer* **40-6**, pp.1355-1364, 1997.

11 Metzger, D.E. and Korstad, R.J.: Effects of Crossflow on Impingement Heat Transfer. *Trans. ASME: J. Eng. Power* **94**, pp.35-42, 1972.

12 Sparrow, E.M., Goldstein, R.J. and Rouf, M.A.: Effect of Nozzle-Surface Separation Distance on Impingement Heat Transfer for a Jet in a Crossflow. *Trans. ASME: J. Heat Transfer* **97**, pp.528-533, 1975.

13 Bouchez, J.P. and Goldstein, R.J.: Impingement Cooling from a Circular Jet in a Cross Flow. *Int. J. Heat Mass Transfer* **18**, pp.719-730, 1975.

14 Goldstein, R.J. and Behbahani, A.I.: Impingement of a Circular Jet with and without Cross Flow. *Int. J. Heat Mass Transfer* **25**, pp.1377-1382, 1982.

15 Al-Sanea, S.: A Numerical Study of the Flow and Heat-Transfer Characteristics of an Impinging Laminar Slot-Jet Including Crossflow Effects. *Int. J. Heat Mass Transfer* **35**, pp.2501-2513, 1992.

16 Nakabe, K., Suzuki K., Inaoka K., Higashio A., Acton J. S. and Chen W.: Generation of Longitudinal Vortices in Internal Flows with an Inclined Impinging Jet and Enhancement of Target Plate Heat Transfer. *Int. J. Heat and Fluid Flow* **19**, pp.573-581, 1998.

17 Nakabe, K., Yamamoto Y., Fornalik E., Chen W. and Suzuki K.: Visualizations of Obliquely Discharged Jet Flows and Their Heat Transfer Enhancement Regions. *CD-Rom Proc. 8th Int'l. Symp. on Flow Visual.*, ISBN 09533991 0 9, Sorrento 1998.

18 Nakabe, K., Higashio, A., Chen, W., Suzuki, K. and Kim, J.H.: An Experimental Study on the Flow and Heat Transfer Characteristics of Longitudinal Vortices Induced by an Inclined Impinging Jet into a Crossflow (Measurements of Heat Transfer Coefficients Using Thermochromic Liquid Crystal). *Proc. 11th Int. Heat Transfer Conf.* **5**, pp.439-444, 1998.

19 Kimura I., Kuroe Y. and Ozawa M.: Application of Neural Networks to Quantitative Flow Visualization. *J. Flow Visualization and Image Processing* **1**, pp.261-269, 1993.

QUANTITATIVE ANALYSIS OF MELTING BY IMAGE PROCESSING TECHNIQUE

Józef Gościk
Bialystok University of Technology, Wiejska 45C, PL 15-351 Bialystok, Poland

Summary Image processing is applied to investigate melting of a subcooled paraffin. In general, the experimental method proposed is to make analysis of the visual information automatically by means of digital processing. The technique was applied: to visualise steady state melt contours strongly influenced by natural convection, to obtain quantitative data such as area of regions occupied by either phase, to detect shape and location of the solid-liquid interface, and finally to obtain volume of the material melted.

INTRODUCTION

Melting / solidification attracts still attention because of wide application to industrial purposes and frequent occurrence in nature. More recently, strong efforts have been made to understand better and to develop the best mathematical models and numerical algorithms suitable for prediction strongly conjugated solid-liquid phase change processes when occur with assistance of natural convection. One, among many others interesting aspects of the investigations, is a complex behaviour of the solid-liquid interface and consequently melt contours. Two approaches can be distinguished in experimental methods applied for this subject. First one, invasive, which is based on a posterior deduction and estimation of the front location from measured temperatures fields. Second, non-invasive, are the optical methods. Present knowledge of the author says that such approach is mostly performed in traditional way what means that visual information is recorded by a conventional camera. The aim of the work is to propose an idea of how analysis of the aspects mentioned could be make automatically by use a technique successively applied in the image processing/machine vision.

EXPERIMENTAL APPARATUS

When solid-liquid phase change process occurs in a chamber specially prepared for the visualisation, some backlight discloses the solid state matter as the black region and the liquid is transparent (white). The feature is ideal for automatic detection of individual groups of pixels, which characterise the same intensities in individual phases, and consequently for digital processing capabilities[1]. To carry out the idea into practice, an experimental set up was completed. It consists of a test unit where the phase change process studied takes place, illuminating accessories and complete system for image acquiring and processing.

Heat Transfer Apparatus

The experimental study of the melting process is performed in a specially designed test unit. The unit has a form a cube which two metallic vertical walls are thermally active. In details, one of the vertical sidewall is maintained at uniform temperature which is lower than θ^* (θ^* being the phase change temperature) and the opposite one at the temperature which is greater than θ^*. All the remaining walls were made of plexiglas. The proposed configuration allows obtaining visual observation and record melting evolution. The more detailed description of the unit can be found elsewhere[2]. N-octadecan (99%) was chosen as a test material. This substance has the liquid phase transparent and solid core that block the light passing through.

Illumination

The essential effect that creates shadows was attained by background illumination. In the experiment it was a diffuse white light source (200W) located at the backside of the test unit. This arrangement provided possibilities for the camera to acquire images as shadowed two regions, very distinct, with respect to light intensity. Because of transparency of the liquid phase the configuration gives only information on total quantity of the melt. To make the experiment fully automatic it is necessary to separate region of interest (ROI) which physically corresponds to the entire region filled by the phase change material. To do this lighting system was completed by front light 45° (two halogen lamps 200W) illuminating on front of the test unit. The ROI was prepared by painting borders of the plexiglas plate with matt red paint.

Video equipment and image processing system

The system for analysis of visual information consists of two essential parts: equipment operating on analog video signals and digital part for sampling signals. Video equipment consists of Sony DXC-950P 3CCD colour video camera with VCL-714BXEA zoom lens attached to, Sony camera adapter CMA-D2, Sony remote control unit RM-C950 and Sony trinitron colour video monitor PVM-14M4E. Thus, collected video equipment allows to very comfortable location on the object by adjusting iris, focusing and zooming manually as well as automatically. CCD camera, for image acquisition and processing is connected to the computer (Pentium 200MMX, Windows NT) where Matrox Meteor frame grabber resides, specially designed for acquisition RGB video format signals. Image processing operations were performed on 740x542 pixel size images using specialised software Matrox Inspector[3] (Ver. 2.1). The program provides also camera interfacing and access to grab features of digitizer.

IMAGE PROCESSING

At the stage of research project the main interest was concentrated on analysis of the final, steady state regime when melting process is terminated because of the subcooling. The time scale of an experimental run ranges from 8 to 12 hours depending on parameters of the experiment. Thus, the images were grabbed manually and saved on the disc. The image processing was performed in three main steps. Step 1 *calibration* of the image for which script code was prepared that detects edges and corners of ROI (all the operations at the step were performed on the original signal - the CCD camera works with video signal mode 24bit, 3-band RGB). Step 2 *phase change front determination* that means a detection of contour which correspond solid-liquid interface (first of all the RGB signal was analysed for rejection artificial effect of the uneven back lighting, next image gradient determination, gradient histogram equalisation and finally abstraction previously locked image were performed). Step 3 *area measurement* of the region occupied by liquid phase taking the solid core as a background black regions (the step was performed in a sequence of following operation: format acquired image converted from RGB (all band) to the 8 bit unsigned format, next binarized, segmented and finally proceed by blob analysis procedure).

CONCLUSIONS

The technique has been applied to a number of experimental runs, from which the results obtained were also worked out traditionally by making photographs and the planimeter. As expected, the comparison showed that image processing methodology is more accurate, flexible and much more fast. The conclusion seems to be very important because the hardware requirements in general are considerably less demanding than that used in the experiments reported (B/W camera provided that ROI is specially prepared and unique marked, low cost typical frame grabber).

REFERENCES

1. Russ, John C.: The Image Processing Handbook. 2nd ed., CRC Press, Inc., Boca Raton, Florida 1995.
2. Gościk,J., Kołodziejczyk,W. An experimental investigation of melting of the subcooled pure nonmetallic material (in preparation).
3. Matrox Inspector Ver. 2.1 User Guide. Matrox Electronic Systems Ltd., Canada, Quebec 1997.

Pedagogical Applications of Photoelastodynamics for Solid Mechanics and Dynamics of Structures

Yves GOURINAT, Agus Sigit PRAMONO
École Nationale Supérieure d'Ingénieurs de Constructions Aéronautiques
1, Place Émile Blouin 31056 TOULOUSE FRANCE

ABSTRACT

This paper presents developments realized on photoelastodynamic bench of ENSICA's Department of Mechanical Engineering. Classical wave, vibrating, shock and rotating parts theories, were compared with color pictures of isochromic lines obtained with rapid camera and urethane resin specimens. For non-linear shock and large deflection, explicit code LS-DYNA has been used. Then, the facility has been used to analyse dynamic work of gears for power transmission, in comparison with numerical computations performed at ENSICA. In addition, this development has lead to a demonstration which is now included in engineering first year general courseware, about stress analysis. It is now planned to visualize vibrating membrane waves eigenshapes in isotropic and orthotropic membrane.

I INTRODUCTION AND PRESENTATION OF BENCH

Photoelasticity is often used to visualize structural strains in resin specimens of at surface of real parts. This process, based on birefringency of transparent materials, related with stresses, allows a global view of informations concerning plane stress field : direction and relative values of principal stresses by isoclinic and isochromic patterns (ref.[1]).

With classical photoelastic materials, strains induced by volumic loads are generally not sufficient for convenient visualization ; this limitation obliges in fact to simulate those loads by contact applied forces, which makes the model more approximative. Membrane compression and shear waves could be observed with high speed cameras and low module resins (ref.[2]). The main problem is due to high speed of wave propagation in resins, combined with the necessity to have a significant photoelastic constant of material. The plane stress membrane compression and shear wave propagation speeds are respectively :

$$c_L = c\sqrt{\frac{1-\nu}{(1+\nu)(1-2\nu)}} \quad \text{and} \quad c_T = \sqrt{\frac{G}{\rho}} = c\sqrt{\frac{1}{2(1+\nu)}}$$

where : $c = \sqrt{\frac{E}{\rho}}$: basic bar tension-compression propagation speed

E, ν, G, ρ : Young's and shear moduli, Poisson's ratio and specific mass of elastic material

$c_P = c\sqrt{\frac{1}{1-\nu^2}}$: classical plane strain wave propagation speed.

With classical resins, c range is 1800 m/s, which leads to ultra-rapid mechanical phenomena, practically impossible to observe, the total time of propagation of mechanical perturbation across standard test part (200mm) being approximately 100 μs.

Urethane resins present interesting mechanical characteristics for this purpose : $E = 7$ MPa, $\nu = 0.46$, $\rho = 1100$ kg/m^3, which lead to $c = 80$ m/s. Using this type of material, we have developped at ENSICA a pedagogical bench for visualization of dynamic plane phenomena, based on a classical photoelastic test-bench (fig.1), basically for pedagogical demonstrations for elastodynamic and structural dynamics coursewares, and also for developments of gear and local dynamic investigations.

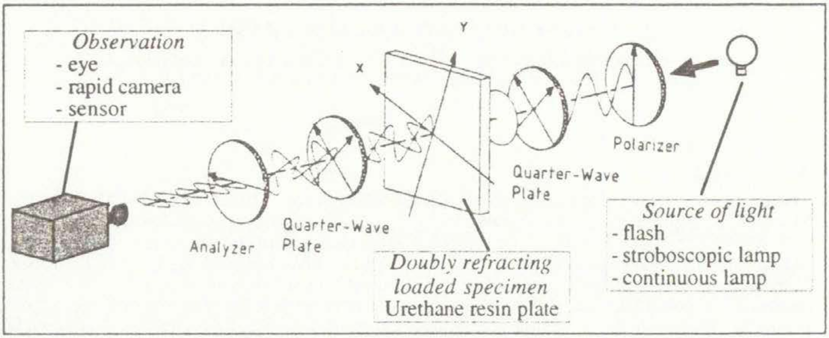

Figure 1 : Photoelastodynamic Bench.

We have focused on visualization of isochromic patterns, which can be defined as lines where the difference of principal plane stresses is constant ; thus, isochromic fringes are level-curves of in-plane shear stress.

On isochromic fringe number n : $\sigma_B - \sigma_A = 2\tau_P = n\,\sigma_i$

where : σ_A, σ_B, τ_P : in-plane principal and shear stresses in loaded specimen
σ_i : isochromic fringe unitary stress value.

This value is obtained by simple tensile test of material : $\sigma_i = \dfrac{\lambda_i}{k_p t}$

where : λ_i : wavelength of observed isochromic fringe
k_P : photoelastic constant of specimen material
t : thickness of specimen.

Isoclinic patterns being eliminated by two quarter wave plates, isochromic remaining "maps" were observed by different ways : stroboscopic lamp with classical observation or continuous lamp with high speed photo (color) or video (monochromatic) camera.

II APPLICATION TO SIMPLE ELASTODYNAMIC CASES

The bench was used to test the capability to demonstrate effects of centrifuge volumic forces on rotating parts. The simple two blades system, consisting in rotating beam has been tested first (fig.2). Other rotating shapes were also considered (fig.3).

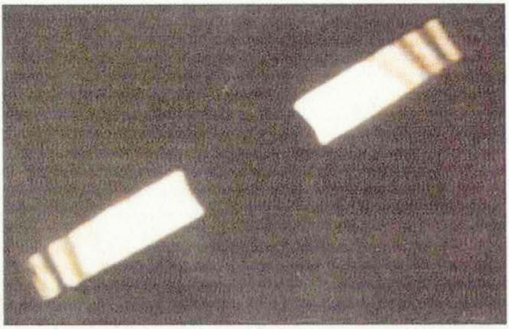

Fig.2 : Rotating beam vizualized with rapid camera (2500 images/sec).

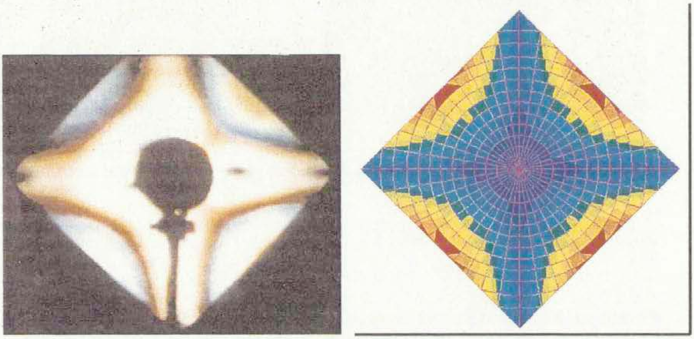

Fig.3 : Stroboscobic visualization and numerical Samcef implicit model of square rotating plate.

Shock loads were then approached, in a first step on classical rectagular plates (fig.4), and after on clamped beam (fig.5), with filmed observation of free vibrations after shock, in accordance with beam eigenshapes.

Fig.4 : Photographic visualization of isochroms at shock contact on rectangular plate.

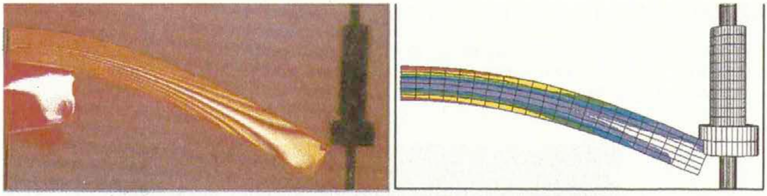

Fig.5 : Photoelastodynamic image and LS-DYNA explicit model of shocked bending beam.

III APPLICATION TO GEAR POWER TRANSMISSION DYNAMIC APPROACH

The bench is now used to investigate dynamic stress distribution in working gears, with 20/23 teeth transmission. Considering previous experiences, the stress value precision for comparison with analytical and numerical models, can be considered as reliable with 15% margin. This allows qualitative and quantitative qualifications for different theoretical approaches.

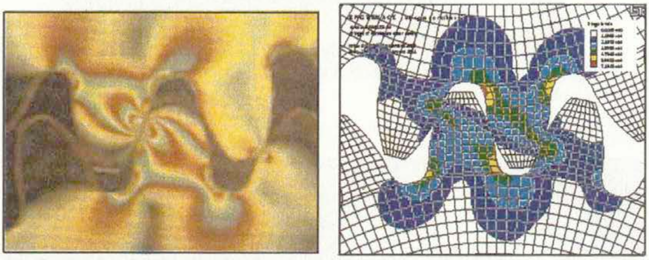

Fig.6 : Photoelastodynamic image and LS-DYNA explicit model of gear teeth transmission.

IV CONCLUSION

The photoelastodynamic approach is now included in basic engineering training of ENSICA, as complement and practical activity related with solid media and dynamics of structures coursewares. This method allows various simple and pedagogical demonstrations, but also qualitative and quantitave complementary datas for elastic mechanisms models.

Developments now in progress consider permanent vibrating eigenshapes systems in isotropic and orthotropic membranes. The interest of orthotropic materials consists in applications to composites, with dynamic global behavior, and also local approach of resin/fiber interfaces.

REFERENCES :

[1] Durelli A.J., Rilley W.F. Introduction to Photomechanics. Prentice-Hall, 1965.

[2] Dally J.W. An introduction to Dynamic Photoelasticity. Experimental Mechanics, 1980.

[3] Hallquist J.O., Stillman D.W., Lin T.L. LS-Dyna Reference Book. Livermore Software Technology Corporation, 1994.

[4] Meyer M.A. Dynamic Behavior of Materials. John Wiley & Sons, 1994.

[5] Gourinat Y. Pramono A.S. Stress Propagation in Infinite Plate and Stress Distribution on Spur Gears Transmission by Dynamic Photoelasticity. European Conference, Spacecraft Structures, Materials and Mechanical Testing (ESA,CNES,DLR,DGLR) SM98-101, Braunschweig, 1998.

MEASUREMENTS OF TEMPERATURE OF DROPS WHEN IN FLIGHT

F. Hervy (1,2) and F. Feuillebois (1)
(1) PMMH, ESPCI, 10 rue Vauquelin, 75005 Paris, France
(2) CEPr, Saclay, 91895 Orsay Cedex, France

Simulation tests of aircraft icing have been usually performed with clouds of supercooled water drops whose median volume diameter was about 20 μm. For these sizes, drops were assumed to be at the static temperature of the flow. There is a recent interest in simulating freezing drizzle (diameters up to 500 μm) and it is necessary to measure drop temperatures before impaction on obstacles because the cooling time increases with drops size and may become larger than the transport duration of drops.

There exist some techniques which can be used for droplet temperature measurement, like rainbow angle measurement, dual burst technique or extended phase doppler anemometer [1]. These techniques are applicable only if the refractive index variation of the liquid varies significantly with temperature. However, this is not the case for water from the supercooled state (around -40 °C) up to 50 °C. So, we choose another method based on Laser Induced Fluorescence (LIF) of a dilute organic dye.

Guilbault [2] has pointed out that fluorescent molecules like rhodamine B are very sensitive to a temperature variation (temperature quenching), and Nakajima et *al.* [3] have used this organic dye to measure the temperature of a liquid flow by Planar LIF (PLIF). We show here that LIF could be employed for temperature measurement of a liquid phase dispersed in a gas. A theoretical analysis using quantum mechanics, geometrical optics and generalized Lorenz-Mie Theory (GLMT) yields, for low rhodamine B concentration C and a drop diameter D smaller than the beam diameter w_0, the following expression for the intensity of fluorescence emitted by a drop crossing a laser beam at a distance y from the axis :

$$I_f = K_{opt} K_{spect} I_0 C D^3 e^{\frac{\beta}{T}} e^{-\left(\frac{\sqrt{2}y}{w_0}\right)^2}, \qquad (1)$$

where I_0 is the incident intensity on the beam axis, T is the volume average drop temperature (in K), K_{opt} and K_{spect} are constants depending on the optical setup and characteristics of fluorescent molecules, respectively. The constant β has to be determined by calibration. A validation of equation (1) was performed with a simple experimental setup. A monodisperse injector, filled with a water solution containing 10^{-4} mol.l^{-1} of rhodamine B, was placed vertically and produced periodically droplets with a nominal diameter of 92 μm. The initial temperature of droplets was known and adjustable. Tests on polydisperse sprays were done using the injector in some peculiar modes. Falling drops were illuminated by a 60 mW Ar-ion laser (with $\lambda = 514.5$ nm) and fluorescent red light was collected on a photomultiplier after passing through a pass band filter centered at 600 nm (maximum peak of rhodamine B fluorescence). Signals were then analyzed on an oscilloscope.

The results confirmed that the equation (1) is correct for temperature above 293 K. Although accuracy is limited here to 0.5 K due to thermal probe uncertainty, the measured value of coefficient β indicated that the accuracy on temperature measurement could reach 0.1 K.

References

[1] Riethmuller M. L. Développements récents dans les techniques de granulométrie-laser. In *4^e Congrès Francophone de Vélocimétrie Laser*, Poitiers-Futuroscope, 1994. Paper 1.1.

[2] Guilbault G. G. *Practical Fluorescence: Theory, Methods and Techniques.* Dekker, 1973.

[3] Nakajima T. Utsunomiya M. Ikeda Y. and Matsumoto R. Simultaneous measurements of velocity and temperature of water using ldv and fluorescence technique. In *5th Int. Symp. on Appl. of LASER Tech. to Fluid Mech.*, Lisbon, 1991. Paper 12.1.

A THREE-DIMENSIONAL POINT LOCALIZATION TECHNIQUE

D. Ircha[1] , T.A. Kowalewski[2], A. Cybulski[2], R. Krajewski[3]
[1]Laboratory of Medical Physics, Warsaw University, Hoza 69, PL 00-681 Warszawa
[2]Polish Academy of Sciences, IPPT PAN, Swietokrzyska 21, PL 00-049 Warszawa
[3]Medical University of Warsaw & Czerniakowski Hospital, Stepinska 19, PL 00-739 Warszawa

Summary Three-dimensional localisation of an arbitrary tool or the particles in flow in 3D scene is developed. It combines three arbitrarily localized cameras and system of calibration points. Least square data fitting is used to solve set of algebraic equations obtained for points localized at three planes of the cameras. At the present stage an accuracy below 1 mm is obtained for a typical 0.2 m^3 3-D scene. Quasi real-time (10 fps) data evaluation can be achieved using 32-bit frame grabber (AM-STD) and 450 MHz Pentium II processor. The primary application of the system is live tracking of a surgical tool within an operative field and displaying tool's position on a set of diagnostic tomographic images.

INTRODUCTION

An accurate description of observed phenomena plays a significant role in the experimental mechanics. It is obvious that real world is three-dimensional in space. However, for a long time the complexity of three-dimensional systems forced us to rely on theoretical models and data acquisition tools, which used two-dimensional description of the real world. Such approach, even if sometimes successful, needs real i.e. three-dimensional experiment to be verified. With this objective in view several three-dimensional recording systems have been developed in the last decade. In fluid mechanics stereoscope viewing systems has been adapted to follow particle tracks [1] or to acquire three-dimensional velocity vector field (3-D PIV) [2,3]. Three-dimensional visualization of the complex flow or mechanical structures became possible with the development of holographic tools. But probably most revolutionary progress is observed in medicine [4], where the tomographic reconstruction of three-dimensional images became standard nowadays. In the following we would like to describe our efforts to construct three-dimensional tracking system based on the directional observation system. It is extended version of a natural stereoscopic viewing set. Our primary aim is to provide real time 3-D navigation system for surgery, but system can be applied as well for particle tracking in fluid mechanics or machine vision control in robotics.

DATA ACQUISITION APPARATUS AND PROCEDURE

The acquisition system consists of three synchronised CCD cameras, arbitrary located in 3D space. Two identical monochrome CCIR cameras (Sony XC77CE) and one RGB colour camera (Sony XC003) are used. Presently, the colour information is used only to enrich human observation of the viewing area. Data acquisition system is based on a single 32bit PCI frame grabber AM-STD (Imaging Technology Inc.) equipped with a dual RGB input port. Two monochrome cameras and the red channel of the RGB camera are connected to the three separate inputs of the board, i.e. the red, green and blue channels. In such a way simultaneous acquisition of three video channels into computer memory is made possible. Each video channel has 8-bit, 768x548 pixels resolution. Images from the cameras are continuously displayed on three video monitors to help in adjusting the cameras. They can be displayed on SVGA screen through the frame grabber too.

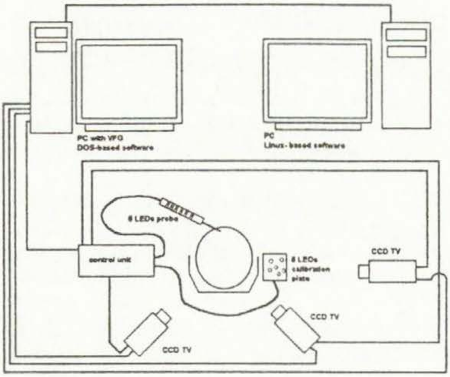

Figure 1. Schematic of the acquisition system: DOS based acquisition computer with three cameras; active markers (LEDs) are used in the tracked tool and the calibrator. The second PC running Linux is used to display the actual tool position within pre-loaded set of the tomographic images.

Our target is a model of surgical tool, 15cm long plexiglas rod moving freely in about $0.3m^3$ observation volume. One of the problems appearing in building tracking procedure is searching and identification of the object of interest to calculate its position in the video frame. There are several algorithms to localise a known pattern, but most of them are too slow to be use in real time systems. Our system is based on active markers, easy for identification and localisation light emitting diodes implemented in the rod. Their location in the rod is known, hence using only two markers it is sufficient to calculate geometry of the rod axis. In real situation however, some diodes can be hidden or outside viewing area, situation unacceptable in medical applications. Hence, six LEDs are used, each of them separately triggered by the acquisition software. Seven images are taken for each evaluation step, one for each LED switched on and the reference image with all markers switched off. The differential images give easy to localize spot of one switched diode only. Using information from all three cameras their position in the space is calculated. The triggering of the LEDs, image acquisition, pre-processing of images and localization of the LED centroids are performed synchronously for all three cameras. These operations and the three-dimensional reconstruction of the rod axis are performed running especially designed code written under DOS extender (Watcom). We choose this *archaic* operating system, as it is one of the last easy to program real time systems available nowadays. The PCI based system allows us to perform calculations during acquisition and memory transfer times, hence the whole process is accomplished within time of seven frames (280ms) taken at each tracking step.

THREE-DIMENSIONAL RECONSTRUCTION

Three-dimensional reconstruction of the tool position is based on the analysis of two-dimensional images taken by the cameras. Two different viewing points are sufficient to reconstruct 3-D world coordinates of the point. For an arbitrary three-dimensional body the problem can be solved approximately only, even for large number of viewing points. Here, we are looking for the position of the tool axis, a two-dimensional object defined by two points in

3D space. For inconvenient alignments of the axis the use of only two viewing cameras may generate large evaluation errors. Hence, our tracking system is based on the three cameras, allowing to solve the system of underlying equations for an arbitrary position of the markers.

The three-dimensional stereoscopic reconstruction is based on solving a system of algebraic equations representing transformation of 3-D world coordinates of a point to the 2-D image coordinates in plane of the viewing camera. For an arbitrary position of the camera the transformation matrix between the coordinate systems of the object and the camera is defined by three Euler angles (φ,ψ,θ), three components of the translation vector (T_x,T_y,T_z), and the projection scales (S_x,S_y). Neglecting optical deformations, two coefficients, for the horizontal and vertical scale of the camera sensor, are sufficient to describe the projection. Hence, eight coefficients are sufficient to describe transformation of unknown vector $\mathbf{V}_{[x,y,z]}$ in world coordinates to its image $\mathbf{v}_{[x',y']}$ at the camera plane. Each camera looks at the same point $\mathbf{V}_{[x,y,z]}$ generating different image $\mathbf{v}$. Two cameras are sufficient to get four equations for three unknowns. The eight transformation coefficients must be found by the calibration procedure. Mathematically the two camera (stereo) reconstruction is represented by simple to solve, overestimated system of algebraic equations. However, a physical image taken by the camera is in fact rather far from its analytical counterpart. Due to the optical deformations, finite resolution of the camera and inaccuracy of the calibration procedure, by solving the set of equations directly in the best case large errors are obtained, and in the worst - there is no solution at all. To overcome this difficulty a least-square minimisation problem is solved. For three cameras we obtain system of six equations for the three unknowns. Additional correction of the accuracy is achieved by fitting calculated points along straight line describing the rod axis.

The main part of the 3-D reconstruction is calibration of the camera system. The set of eight unknown transformation coefficients must be found for each camera with high accuracy, otherwise the errors of inverse transformation are unacceptable. Theoretically images of four points should be sufficient to solve the problem. But non-linearity of the camera model, the noise errors and discrete character of the information given by the camera do not allow to compute the parameters directly. Therefore least-square minimisation method (Levenberg-Marquardt-Algorithm) is used. The function to minimise is

$$L(\varphi,\psi,\theta,T_x,T_y,T_z,S_x,S_y) = \sum_i \|\mathbf{v}_i - \Omega(\varphi,\psi,\theta,T_x,T_y,T_z,S_x,S_y;\mathbf{V}_i)\|$$

To avoid the algorithm from getting caught in a local minimum, a choice of proper initial values is critical. The physically justified constrains on the result are used to reverse the search path in case of dead-locks.

Each camera is calibrated for a fixed position using a 10x10cm matrix of triggered LEDs. Using our automated search algorithm the calibration procedure needs only the world coordinates of the diodes as the input. The accuracy of the calculated transformation is tested performing inverse operation, the calibration matrix is moved and its new position calculated and compared with the known displacement. Experimenting with different configurations and number of points used we found that minimum five points are necessary to converge the algorithm. Perhaps optimal from the practical point of view is set of 10-12 points. Increasing number of points to about 200 points gives only slight improvement. Above these number of points round-errors of the algorithm often deteriorate the result. The typical accuracy obtained is 0.3mm for about 250mm viewing area. It is close to the theoretical limit determined by the camera resolution. Figure 2 displays example of the information shown on the computer screen during calibration-testing procedure.

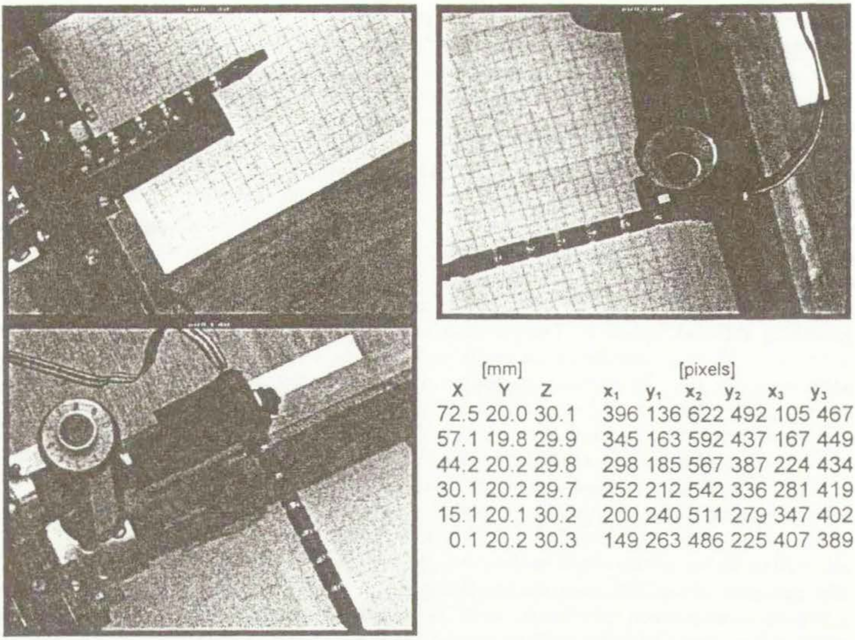

[mm]			[pixels]					
X	Y	Z	x_1	y_1	x_2	y_2	x_3	y_3
72.5	20.0	30.1	396	136	622	492	105	467
57.1	19.8	29.9	345	163	592	437	167	449
44.2	20.2	29.8	298	185	567	387	224	434
30.1	20.2	29.7	252	212	542	336	281	419
15.1	20.1	30.2	200	240	511	279	347	402
0.1	20.2	30.3	149	263	486	225	407	389

Figure 2. Testing the tracking system. Images of the rod with five triggered LEDs seen by the three cameras. The coordinates are simultaneously updated in the forth window. The LEDs are identified by the program and their world position calculated. The inverse transformation is used to calculate their position in the camera plane and to set markers on the real time images. The coordinates found are simultaneously updated in the forth window: first three columns the world coordinates, next columns - the pixel positions within each image.

Having position of the tool in the world coordinates the second set of transformations has to be performed, to visualize the tool position within medical images. For this purpose each set of the tool coordinates, updated periodically by the acquisition computer, is transmitted by serial port to the visualization computer. The stack of images from the magnetic resonance (usually 50-60 equidistant slices) are used to generate volumetric data of the object. The specially designed software allows to display instantaneously three cross-sections of the volume and the reconstructed surface image. The delivered coordinates of the tool are used to calculated position of its tip in the select set of the slices and to show its position within volumetric cut of the surface image.

LITERATURE

1.Hearing F., Leue C., Wierzimok D., Jähne B. Particle tracking velocimetry, *Exp. Fluids* **24**, 10-16, 1996

2.Arroyo M.P., Greated C.A. Stereoscopic particle image velocimetry, *Meas. Sci. Tech.* **2**, 1181-1186, 1991

3.Prasad A.K., Adrian R.J. Stereoscopic particle image velocimetry applied to fluid flows, *Exp. Fluids*, **15**, 49-60, 1993.

4.Apuzzo M.L.J., New dimensions of neurosurgery in the realm of high technology: possibilities, practicalities, realities, *Neurosurgery* **38**, 625-637, 1996.

APPLICATION OF ULTRASONIC COMPUTER TOMOGRAPHY IN SOLID MECHANICS.

Volodymyr V. Koshovy
Karpenko Physico-Mechanical Institute of National Academy of Sciences of Ukraine,
5, Naukova Street, Lviv, 2900601, Ukraine·

Summary. Theoretical and applied problems of development and use of ultrasonic computer tomographic methods and systems for non-destructive evaluation (NDE) of the material state in the product are considered in the report. Results concern following questions: USCT in problems of NDE of the material defective state and USCT in problems of NDE of the material predefective state Accordingly, new USCT technologies for analysis of internal defective structure of highly inhomogeneous materials, for material structure analysis, for analysis of inhomogeneous stress-deformed state (SDS) of material have been presented.

Methodology of the investigations

Image processing methods, including methods of the acoustic (ultrasonic) image restoration, are very actual in solid mechanics because they allow to increase effectivity of technical diagnostics (TD)[1]. From standpoint of aims of TD it is necessary to select two probable states of the product material. The first state, when a defect in the material already has been formed, may be characterized as defective material state (DMS). And the second state, the predefective material state (PDMS), when a defect is not yet formed, but exist so changes in the spatial (volume) distribution (SD) of the physico-mechanical features (PMF) of the material, including parameters of stress-deformed state (SDS), which under certain conditions might initiate defect origination.

Methods of the acoustic image restoration (RAI) are the most respective for evalution different material states in solid mechanics. Among these methods ultrasonic computerized tomography (USCT) are the most perspective. Article is dedicated to research and creation of new ultrasonic and information technologies based on the principles of USCT. Obtained results are relevant to the following problems: application USCT for the evaluation of DMS; application USCT for the evaluation of PDMS.

In the first estimation of DSM, one should take into account the following facts: a defect is an accidental and low-probable phenomena; the most part of solid does not have defects; the presence of a defect is characterized by the acoustic parameters jump on its borders.

Describing PDSM, one should pay attention to the absence of jump-like changes of acoustic parameters and to the presence of anomalous areas with small (weak contrast) PMF changes, which are being described by fluent functions of spatial coordinates. These facts should be taken into account for developing of USCT technologies and systems.

Value of control information, determining mechanic properties of solid, are being consisted not in the information about whole internal structure of solid (or product), but only in the information about its difference from «undefective» standard. The control system based on RAI methods should provide high sensibility and effectiveness. To satisfy these requirements, we propose the methodology of control of wide class of solid objects, form of which allows to represent their volume as a set of uniform elements (sections). This methodology consist of the following steps:

- relative division of investigated area of solid object into typical or equal zones of attention, and collecting of data in these zones in consecutive or parallel ways;
- formation of the «statistical standard» of «nondefectiveness» of the zone of attention;
- detection with high effectiveness and reliability of «defective» zones of attention:
- restoration of the acoustic images of defective zones only, in order to get the characteristics of defects, sufficient for diagnostics.

Defective state of material.

This methodology of application of RAI methods in solid mechanics is implemented in developing of USCT system for defectoscopy of wide class of solid objects, that can be presented as a set of uniform elements[2]. In this method, one restores only tomographic image of the differences of «defective» section from some «nondefective» standard. The solid object may be relatively divided into a set of 2D sections, and the method of coaxial projections may be used for RAI.

In report main principles of the developed method of adaptive projection formation (APF) have been stated[3]. One is built into US tomograph (UST) for NDT of toroid with multy-layer strand adhesive structure from carbon-carbon composite material. The UST detects on working frequency 150 kHz cracks (at least 10mm), differences in density (at least 10%), porosity (at least 5 mm) with random defects orientation. The object is conventionally divided on 128 zones of attention in the form of radial sections. 64-channev piezoelectric transducer covers the perimeter of each section, sounds each sections in 512 directions and measures the amplitude of US signal in shadow made for each direction. The US waves cover uniformingly the surface of the section.

Each measurement is a ray integral (projection). The method of APF uses an operation of developing of new projection data formed by introducing adaptive threshold for each measuring direction, a formation of sum image of restoring function of defectivity, an inverse projection of sum image and following filtration. After a final inverse projection result image describes the spatial distribution of defect in an object. Fig.1 shows the examples of defective sections, i.e. Fig.2,a shows the image of a difference in material density, Fig.2,b - a cluster of small porosity. These defects can not be detected by the traditional shadow method.

The predefective state of material.

The process of origin of defects in solid are connected to the formation of inhomogeneous spatial distribution (SD) of PMF. Existing defects cause inhomogeneous SD of PMF of different nature, and the development of inhomogeneous SD of PMF initiate the formation and further development of defects. That is why we need to identify the SD of PMF in order to evaluate the solid areas in which the defects may arise. In the PDMS the spatial changes of acoustic characteristics from the average or initial value constitute a few or even fractions of a percent. Therefore, the changes of US parameters (velocities of US waves) are small, and there is need for high-precision instrumentation for measurements of time intervals (ray projections) and methods that allow to measure time with relative deviation not larger than ~ 10^{-4}%.

In report USCT methods and systems, that is developed to evaluate SD of PMC in solid material and SD of internal stress of the plate objects, surface of which may be analyzed only from one side, have been described. The time of propagation of the wave along the ray projections is an informational characteristic of US signals for restoration SD of PMF. These projection are measured using the mirror-shadow method. USCT allows to detect SD of elastic properties of material (modulus of elasticity, shear modulus, etc.) by the SD of velocities of longitudinal and transverse US waves, using the known relationships of strength and technological characteristics of material (modulus of rupture, hardness, etc.) based on the specified experimentally the correlated relation with the velocities of propagation of US waves.

In the process of developing of RAI algorithms the specialties of SD of reconstructed characteristics - spatial low frequency and small contrast - were taken into account. We also took into account a need in providing the high productiveness of control. The developed algorithm requires less time for RAI than the method, that uses 2D Fourier transform and convolution, and may be used to reconstruct 3D spatial distributions. Two steps in the algorithm (the first step - sum image, the second one - reconstructed image of PMF SD) provide higher productiveness of control.

Using the created USCT system, some number of experimental acoustic images of SD of PMF in the solid object has been obtained. The data were collected from the surface of steel plate (thickness is equal 26 mm), in which the central part of the control area is heated by a high-frequency current. For diagnostics of thin objects the information about SD of PMF in the whole object is required. Fig.2 represents the experimental result of reconstruction of SD of relative changes in elastic modulus δE% in vertical plane perpendicular to surface of plate. The restored acoustic image shows that the heating in the central area causes changes in mechanical properties of material, and allows to evaluate SD of inhomogeneities and their approximate geometric shape relatively easy.

Conclusion.

The developed physical methods, information technologies and technical devices, that are based on the principles of ultrasonic computerized tomography, open new possibilities for research of defective and predefective states of solid materials and diagnostics of objects comparing to destructive, computer and traditional methods of acoustic defectoscopy and structuremetry. The further development of these methods will allow to increase significantly the reliability and the sensibility of material investigations by nondesructive ultrasonic methods.

REFERENCES

1. Koshovy V.: Methods of restoring of the acoustical images and their applications to Non-Destructive Testing in Civil Engineering. *Proceedings of International Symposium NDT-CE'95*, Berlin, September 1995,pp 1153-1156, DGZFP, Berlin 1995.
2. Koshovy V.V., Kryvin Ye.V., and Romanyshyn I.M.: Ultrasonic computing tomograghy in nondestrutive testing and technical diagnostics. *Physico-chemical mechanics of materials*, vol.33, N5, pp. 31-41, 1997.
3. Koshovy V.V., Kryvin Ye.V.,Kuriy V.P.: Restoration of the acoustic images at ultrasonic testing of products. *Technical Diagnostics and NDT*, vol.6, pp. 11-18, 1988 (in Russian).

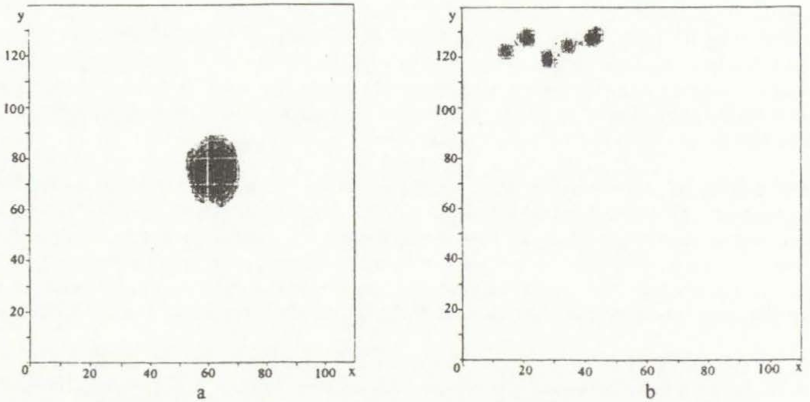

Fig.1. Experimental restored tomographic acoustic images of defects in product sections (a-different density $\delta\rho \approx 10\%$, b- porosity; x,y- in mm).

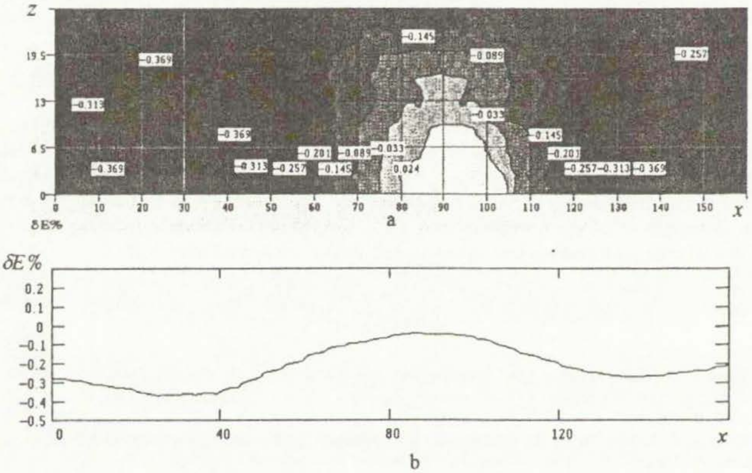

Fig.2. Tomographic (a) and graphic (b, for depth 13 mm) images of relative change of Young's modulus $\delta E\%$ (average on volume $E_0=218{,}3\cdot10^9$Pa) of material in section perpendicular to surface of thick-sheet sample (thickness 26 mm).

IMAGE PROCESSING IN QUANTITATIVE EVALUATION OF TWO-PHASE FLOW PROBLEMS

Tomasz A. Kowalewski

Polish Academy of Sciences, IPPT PAN, Swietokrzyska 21
PL 00-049 Warszawa, Poland. E-mail: tkowale@ippt.gov.pl

Summary: Examples of the image processing methods applied to the several *classical* problems of two phase flow are given. Images of oscillating droplets are used to obtain quantitative data about material properties, image analysis of growing vapour bubble allows to evaluate the evaporation rate and local interface velocity. Simultaneous measurements of temperature and velocity fields using liquid crystal tracers are exemplified for a solidification problem.

During the last decade solid state CCD camera and frame grabber replaced the classical photographic methods in many areas of experimental fluid mechanics. There are several reasons for this development. Partly it is due to the inherent characteristics of the CCD camera itself, like the linear response of the output signal to the amount of the collected light and well defined, mechanically stable geometry of the images. Nearly immediate access to the information stored and the on-line evaluation of the digital images is another important feature, allowing fast control and adjustment of the experimental conditions. These benefits, together with incredible development of the personal computers market allow to built relatively easily powerful acquisition systems, used not only for observation and registration of the flow, but to perform quantitative flow measurements. Comparing with *classical* measuring techniques used in fluid mechanics, the acquisition and evaluation of images has very important advantage: the quantitative information are gained for a full two or three dimensional flow field at a time. This is specifically important for two-phase flow. Two-phase flow was always difficult to treat both experimentally and theoretically. A large number of parameters describing the flow can be defined, depending on the complexity of the problem. The quantitative experimental data, essential for verification of the models used, are not easy to obtain. Local velocity, temperature and concentration fluctuations, interface motion or deformation are difficult to describe using point measurements only. Therefore, 2-D or 3-D full flow field acquisition methods became the only alternative, especially for analysing transient flow phenomena. With this objective in view new experimental techniques based on application of image processing techniques were developed by the author and his co-workers to analyse selected problems. In this paper a few examples of our visualisation and evaluation methods based on digital imaging techniques will be presented.

The first application of image processing methods concerns analysis of small liquid jets and droplets, also under evaporation conditions. Basic parameters of the evaporation process, the evaporation rate and the surface temperature can be studied by analysis of oscillating and simultaneously evaporating droplets [1-2]. In our experimental set-up the droplets were typically 0.1-0.3mm in diameter and moving at a few metres per second. They were illuminated with short LED pulses. The images were captured and recorded under a microscope by a CCD camera and then recorded with the help of an imaging board. One of the visualisation method used is based on the principle of multi-exposure of a transient object on a single video frame. Due to the high dynamic response and the linearity of a CCD sensor, multi-exposed images can be evaluated by using specially developed software (Fig. 1).

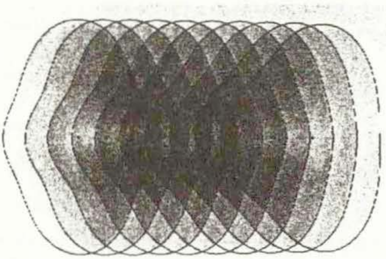

Fig. 1. Image and evaluated contour (solid line) of a multiexposed oscillating ethanol droplet of 0.21mm mean size; time interval 7.8μs, illumination time 200ns.

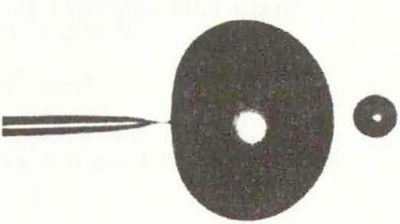

Fig. 2. Break-up of an ethanol jet; separation of the droplet and creation of the small satellite. The droplet mean size 0.1mm, illumination time 200ns.

This allows determination of the droplet diameter (or volume) as well as its oscillating frequency. From these parameters the droplet evaporation rate as well as the dynamic surface tension - proportional to the surface temperature - could be determined [3-4].

Break-up of the liquid jet is another example were novel imaging techniques, based on CCD video camera and image processing, improved the experimental ability to record the relatively fast phenomena appearing in the small conical region of the jet tip when a droplet separates (Fig. 2) [5]. Important details about geometry and dynamics of the separation process were gained making use of special feature of the CCD, i.e. the frame transfer. A modified standard CCD sensor allowed us to obtain a full-frame shift of sensor charges within an adjustable period of 160us to 20ms. Due to the movement of sensor charges, observed effectively as a movement of the sensor plane, short sequences of images can be registered (like in a classical streak camera). This was directly processed via a frame grabber. The facility used here allowed the division of the sensor field into a sequence of separate images, with its vertical format and framing period inversely proportional to the total number of images recorded. The triggering ability of the system (within 1us) allowed its use for studying hardly reproducible events, for example boiling and burst of evaporating liquid jets, separation of the droplet and propagation of shock waves in gases or a metal rod [6,7].

Similar experimental set-up was applied to analyse shape and velocity of growing single vapour bubble (Fig.3) [8]. The typical bubble diameter of 0.1-0.3mm and its relatively fast growth rate enforced application of high speed illumination and acquisition techniques. The new tracer-less PIV evaluation scheme [9] applied to images allowed us to obtain local velocity of the interface (Fig. 4). Details of the shape development of the bubble and velocity of the interface were studied using especially developed image processing scheme. The edge detection procedure allowed us to resolve location of the contour within 2-3μm resolution. The bubble contour interpolated using Bézier polynomials was used to evaluate the local curvature and both, the tangential and the normal components of the interface velocity, data very important for evaporation models.

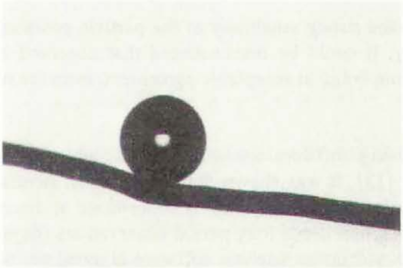

Fig. 3. Vapour bubble of methyl alcohol growing at the wire. Bubble diameter 200µm.

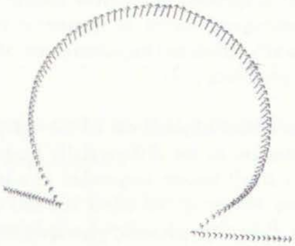

Fig. 4. Velocity vectors of the bubble interface evaluated using PIV method.

Our full field measurement of the primary flow parameters, i.e. velocity and temperature fields, is based on a computational analysis of the colour and displacement of liquid crystals used as tracers [10]. The method described combines Digital Particle Image Thermometry (DPIT) and Digital Particle Image Velocimetry (DPIV). Full 2-D temperature and velocity fields are determined from a pair of colour images taken for the selected cross-section of the flow. Furthermore, a 3-D flow structure can be reconstructed from a few sequential measurements, if the flow relaxation time is sufficiently long. Application of the DPIT&V method for the solidification problem (freezing of water) is shown in Fig. 5 [11]. The formation of ice has been studied for natural convection developed in a small cavity with cooled lid. Freezing of water from the top wall to some extend resembles a directional crystal growth in a Bridgman furnace. Flow visualization and image analysis performed allowed us to find complex flow structures developed in the cavity. The temperature and velocity fields together with the interface geometry can be directly compared with their numerical counterparts, allowing detailed verification of computational models used.

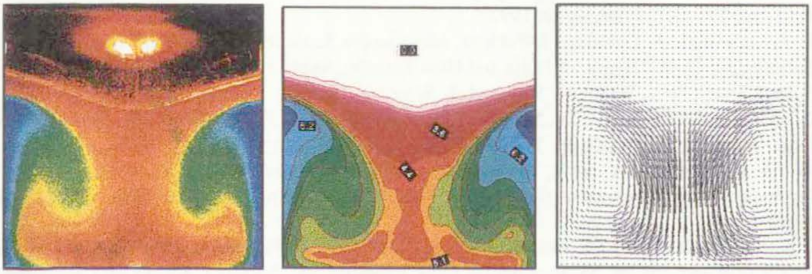

(a) (b) (c)

Fig. 5. Freezing of water from the top in the lid cooled plexiglas cavity. Recorded colour image of liquid crystal tracers (a), evaluated temperature (b) and velocity (c) fields. Time step - 3600s after cooling starts; The top wall temperature T_c=-10°C, external temperature T_{ext}= 20°C,

In some cases measurement of the velocity field is not sufficiently detailed to understand complexity of the flow pattern. The residual changes of the flow boundary may result in evidently different flow patterns. Detection of these differences in not an easy task. For this particles suspended in the flow medium. Due to the strong sensitivity of the particle position to small additional forces or numerical inaccuracy, it could be demonstrated that observed and numerically simulated trajectories are often far from being in acceptable agreement, even for well known problems [12].

Another direct application of the image processing software appeared by analysis of tracers concentration in the differentially heated cavity [13]. It was shown that even almost neutrally buoyant small tracers suspended in a laminar recirculating flow tend to concentrate at discrete locations. However, the effect is small and its detection needs long period observations (days or weeks). Especially developed acquisition system and image analysis software allowed periodic sampling of the tracers position and automatic reconstruction of their three-dimensional distribution in the cavity.

Literature

1. Hiller, T.A. Kowalewski, *Surface tension measurements by the oscillating droplet method*, Physico-Chem. Hydrodynam. **11**, pp. 103-112, 1989.
2. E. Becker, W.J. Hiller, T.A. Kowalewski, *Experimental and theoretical investigations of large amplitude oscillations of liquid droplets*, J. Fluid Mech. **231**, pp. 189-210, 1991
3. B. Stuckrad, W.J. Hiller, T.A. Kowalewski, *Measurement of dynamic surface tension by the oscillating droplet method*, Exp. in Fluids, **15**, pp. 332-340, 1993.
4. T.A. Kowalewski, D. Bruhn, *Nonlinear Oscillations of Viscous Droplets*, Proc. of Jap.-Centr. Europ. Workshop on Adv. Comp. in Eng., Pultusk 1994, pp.63-68, IPPT PAN, W-wa 1994.
5. T.A. Kowalewski, *On the separation of droplets from a liquid jet*, Fluid Dynamics Research, **17**, pp. 121-145, 1996.
6. T.A. Kowalewski, W.J. Hiller, M. Behnia, *An experimental study of evaporating small diameter jets*, Physics of Fluids A **5**, pp. 1883-1890, 1993.
7. W.J. Hiller, T.A. Kowalewski, Th. Tatarczyk, *High speed frame transfer CCD*, in: Proc. 20th Int. Congr. of High Speed Photography and Photonics, 1992 Victoria, Canada, SPIE Vol. 1801, pp. 595-601, Washington 1993.
8. T. Kowalewski, A. Cybulski, J. Pakleza, *Microscopic Scale Investigation of Vapor Bubble in Boiling Liquid.* 10th Symp. of Mass and Heat Transfer, Sept., 14 - 18, 1998, Swieradow Zdroj, Poland, Prace Polit. Wroclaw. 53/9, vol. 1, Wroclaw 1998.
9. G. Quénote, J. Pakleza, T.A. Kowalewski, *Particle Image Velocimetry with Optical Flow*, Experiments in Fluids **25**, pp. 177-189, 1998.
10. W. Hiller, T.A. Kowalewski, *Simultaneous measurement of the temperature and velocity fields in thermal convective flows, Flow Visualization IV*, pp. 617-622, Hemisphere, Paris 1987.
11. T.A. Kowalewski, A. Cybulski, M. Rebow, *Particle Image Velocimetry and Thermometry in Freezing Water* 8th Int. Symposium on Flow Visualization, Sorrento, eds. G.M. Carlomagno and I. Grant, CD ROM Proceedings ISBN 0953399109 , pp. 24.1-24.8, Edinburgh, 1998.
12. P.M. Mitgau, W.J. Hiller, T.A. Kowalewski, *Verfolgung von Teilchen in einer dreidimensionalen Strömung*, ZAMM **74**(5), pp. T394--396, 1994.
13. A. Yarin, T.A. Kowalewski, W. Hiller, St. Koch, *Distribution of particles suspended in 3D laminar convection flow*, , Physics of Fluids, **8**, pp. 1130-1140, 1996.

Examples of colour images and some references can be found at the Web page: http://www.ippt.gov.pl/~tkowale/

DEFORMATIONS CONTROL AND MEASUREMENT WITH THE HELP OF SPECKLES

V.I.Lachno, A.A.Prijemko, I.A.Eksperiandova

Kharkov Aviation Institute, str.Chkalova,17, Kharkov, Ukraine

The perfection of mechanical experimental techniques and devices is based on the opportunities of the optical-physical measurements [1]. The more promising is the idea of using the speckles, obtained as a result of interaction between the laser radiation and the surface of the object. The proposed report presents the results of the solutions of a number of theoretical and applied problems on speckle-measurements of deformations. The analysis of the mechanical deformation is submitted as a problem on the configuration measurement of the deformed surface in definite intervals of time. The methods of the speckle-metrology, being used for this purpose, enable to carry out the control and measurement of the deformations without contacts, in the real time scale, under the complex conditions of the environment. The informational characteristics of the applied laser speckle-signals enable to carry out the analysis of the surfaces directly without the stage of measurement of the separate sections. This report formulates and solves the reverse problem of the configuration measurement of the deformed spatial object. The configuration is presented as the matrix, made up of the coefficients of the equation of the surface of the n-th power [2]. For example, for the surface of the second power it looks as:

$$G = \begin{vmatrix} a_{11} & a_{12} & a_{13} & a_{14} \\ 0 & a_{22} & a_{23} & a_{24} \\ 0 & 0 & a_{33} & a_{34} \\ 0 & 0 & 0 & a_{44} \end{vmatrix} . \tag{1}$$

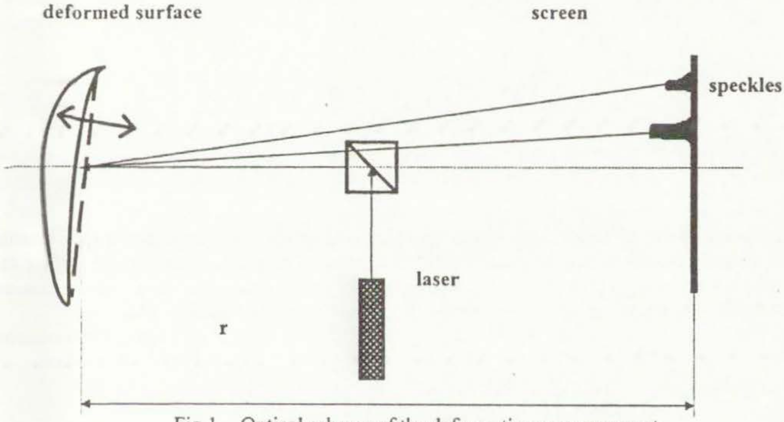

Fig.1. Optical scheme of the deformations measurement.

The similar surface is completely identified by nine coefficients with the accuracy to the constant a_{44}. Defining them we should bear in mind the parameters of the tangent planes with two points on the surface. Thus, we obtain the system of nine equations with nine unknown quantities (2). Where, $F(x,y,z) = 0$ -equation of the surface of the second power in space in the implicit form. The coefficients with the indices 1 and 2 belong respectively to the first and second tangent planes. The solution of the system gives a matrix of the coefficients G.

Fig.1 demonstrates the optical scheme of the deformation measurement. The laser beam scans of the deformed surface. Thus, the obtained diffraction picture is displayed on the screen. For its purpose the matrix of the devices with accumulating connection is used. This speckle picture is a measuring signal. The reverse problem is presented as a simple integral equation. The solution of the similar equation is not stable to the insignificant changes of the input data. The peculiarity of the surfaces of a number of deformed objects is that during mechanical processing they acquire the form of the conjugation of the several phase diffraction lattices. In this case, the analyzed speckle-signal is the result of the interference of the diffraction powers. Their analysis makes the solution of the reverse problem correct.

$$
\begin{cases}
\dfrac{\partial F(x_1,y_1,z_1)}{\partial x} = \cos\alpha_1, \\
\dfrac{\partial F(x_1,y_1,z_1)}{\partial y} = \cos\beta_1, \\
\dfrac{\partial F(x_1,y_1,z_1)}{\partial z} = \cos\gamma_1, \\
\dfrac{\partial F(x_1,y_1,z_1)}{\partial x} x_1 + \dfrac{\partial F(x_1,y_1,z_1)}{\partial y} y_1 + \dfrac{\partial F(x_1,y_1,z_1)}{\partial z} z_1 = p_1, \\
\left(\dfrac{\partial F(x_1,y_1,z_1)}{\partial x}\right)^2 + \left(\dfrac{\partial F(x_1,y_1,z_1)}{\partial y}\right)^2 + \left(\dfrac{\partial F(x_1,y_1,z_1)}{\partial z}\right)^2 = 1, \\
\dfrac{\partial F(x_2,y_2,z_2)}{\partial x} = \cos\alpha_2, \\
\dfrac{\partial F(x_2,y_2,z_2)}{\partial y} = \cos\beta_2, \\
\dfrac{\partial F(x_2,y_2,z_2)}{\partial z} = \cos\gamma_2, \\
\dfrac{\partial F(x_2,y_2,z_2)}{\partial x} x_2 + \dfrac{\partial F(x_2,y_2,z_2)}{\partial y} y_2 + \dfrac{\partial F(x_2,y_2,z_2)}{\partial z} z_2 = p_2 .
\end{cases}
\qquad (2)
$$

Fig.2 demonstrates the geometrical interpretation of the problem of the deformation measurements. Necessary parameters of the tangent planes with the controlled points on the deformed surface can be found by the systems of the equations of the measuring transformations. These systems connect parameters of the speckle- signal with the measured parameters of configuration [4].

The practical use of methods of the speckle-metrology reduces the time of processing the measuring information because of the radical minimizing the quantity of the points that define the surface.

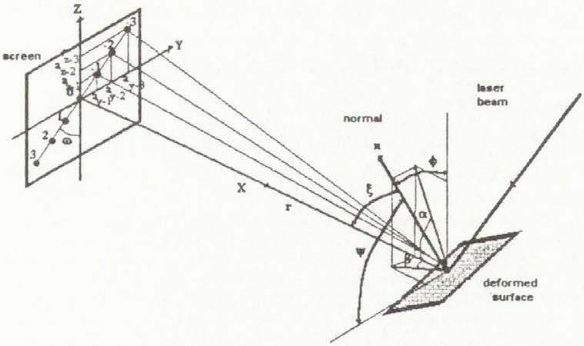

Fig.2. Geometrical problem of the deformations measurement

$$\begin{cases} \operatorname{tg}[\arcsin(\sin\alpha - \dfrac{n\lambda}{d}) - \alpha - \mu] = \left| \dfrac{\sum\limits_{i=-1}^{-n} a_i \cos\omega}{r} - \sin\mu \right| , \\ \operatorname{tg}[\arcsin(\sin\alpha - \dfrac{k\lambda}{d}) - \alpha - \mu] = \left| \dfrac{\sum\limits_{i=-1}^{k} a_i \cos\omega}{r} - \sin\mu \right| , \\ \operatorname{tg}[\arcsin(\sin\beta - \dfrac{m\lambda}{d}) - \beta - \eta] = \left| \dfrac{\sum\limits_{i=-1}^{-m} a_i \sin\omega}{r} - \sin\eta \right| . \end{cases} \tag{3}$$

$$\begin{cases} \operatorname{tg}[\arcsin(\sin\alpha - \dfrac{n\lambda}{d}) + \alpha + \mu] = \left| \dfrac{\sum\limits_{i=-1}^{-n} a_i \cos\omega}{r} + \sin\mu \right| , \\ \operatorname{tg}[\arcsin(\sin\alpha - \dfrac{k\lambda}{d}) + \alpha + \mu] = \left| \dfrac{\sum\limits_{i=-1}^{k} a_i \cos\omega}{r} + \sin\mu \right| , \\ \operatorname{tg}[\arcsin(\sin\beta - \dfrac{m\lambda}{d}) + \beta + \eta] = \left| \dfrac{\sum\limits_{i=-1}^{-m} a_i \sin\omega}{r} + \sin\eta \right| . \end{cases} \tag{4}$$

Their solution gives the distance between the screen and the controlled point on the surface and the angles α and β between the projections of the normal on the planes XOZ and XOY and the axis X in the rectangular system of coordinates. These data allow calculating the distance P between the tangent plane in the lighting point and the beginning of the coordinates

$$p = r\sqrt{\sec^2\alpha + tg^2\beta}\,. \qquad (5)$$

The directional cosines of the normal to the surface in the controlled point are defined by solving the system of three equations in three unknown quantities:

$$\begin{cases} tg\xi = \sqrt{tg^2\alpha + tg^2\beta}; \\ \dfrac{\sin\psi}{\sin\varphi} = \dfrac{\cos\beta}{\cos\alpha}; \\ \cos^2\xi + \cos^2\psi + \cos^2\varphi = 1\,. \end{cases} \qquad (6)$$

Using the first diffraction degrees in the analysis of the speckle signal makes it necessary to solve the incorrect reverse problem of the configuration measurement of the deformed surface. To make this problem correct we should analyze the mutual arrangement by the diffraction maximums of the higher degrees. The basic results of the conducted research are the following:

1. The new kind of the optical-physical measurements for analyzing the deformations based on the methods of the laser speckle-metrology has been developed.
2. The potential opportunities of the speckle-metrology for analyzing the deformations have been estimated.
3. The reverse problem of the deformations measurement and control based on the speckle-signals analysis has been formulated and solved.
4. The results of the laboratory experiments proved the correctness of the theoretical assumptions of the efficiency of the methods of the speckle-metrology.

BIBLIOGRAPHY

1. Jouns R., Wykes K. Holographical and speckle Interferometry. – Moskva: Mir, 1986, 328 p. (in Russian).
2. Mathematics handbook for Ingeneerings and Students of Colleges. Bronstein I.N., Semendyaev K.A. Moskva: Nauka, 1981, 720 p.(in Russian).
3. Tikhonov A.N., Arsenin V.Y. Methods of the solution of incorrect problems. Moskva: Nauka, 1986, 288 p. (in Russian).
4. Prijemko A.A. Algorithmization of reverse problems of speckle-metrology on configuration measurements. In book of sci. Papers of Kharkov aviation institute. V.1. 1998. P.306-309.

A 3D PTV TECHNIQUE FOR GRANULAR MEDIUM IN LIQUIDS

Véronique Latard, Yves Brunet, A. Merlen

Laboratoire de Mécanique de Lille, URA CNRS 1441, cité scientifique 59655 Villeneuve d'Ascq Cedex

Summary. Optical methods or visualizations cannot be performed for granular flows because of the opacity of these materials. Hence, the efficient techniques developed for flows analysis cannot be adapted. This reduces the possibilities to expensive magnetic or radioactive tracking methods or X-rays visualizations. In this paper an optical particle tracking velocimetry is presented for a mixture of oil and glass beads by matching the index refraction of both materials. Lagrangian observations of single colored particle as well as Eulerian statistical fluxes are then possible. The technique is applied on a sedimentation flow in a squared section vertical tunnel.

INTRODUCTION

Previous experiments[1] showed an example of index adaptation between borosilicate beads and oils. Here the flow is created in a transparent vertical hydrodynamic tunnel of square section ($6*6cm^2$) and 1 m length. The beads are initially in a tank at the top of the tunnel. After the aperture of that tank they fall by gravity through the test canal toward the reception tank at the bottom (figure 1). The device is completely filled by oil and by 100000 beads of diameter 3mm. The flow is transparent making possible the introduction of 100 colored beads used as markers. A mirror parallel to the diagonal of the test section allows the observation simultaneously in both directions orthogonal to the tunnel axis and gives the third component of the displacement of the marked beads.

THE FLOW

At a sufficient distance from the tanks the mean flow is steady despite of important individual fluctuations of the beads velocities (figure 2). These fluctuations are due to the strong interaction between the fluid and the particles. As a matter of fact the characteristic Reynolds number of the flow around a bead can be evaluated around 4. This gives rise to a repulsion regime between the beads at least if their distance is less than 8 diameters. This is the case in our mean steady flow where the distance between the beads is ranging from one to two diameters.

THE MEASUREMENT TECHNIQUE

The images are recorded by a video camera and saved on a PC as TIFF files. The position of the marked beads is automatically analyzed by a specific C code. The successive positions of each marked bead are detected by a prediction algorithm similar to the one developed by Kobayashi[2]. It is based on prediction boxes inside which the position of a bead is supposed to be found in the next image. When two or more beads are in the same box, the information is discarded. Hence, it is necessary to work with a low density of markers. In order to increase the number of valid measurements the beads are marked with the help of three colors, which are detected by the software. This method directly gives the trajectories and the instantaneous velocities by dividing the displacement by the time interval. This time has to be chosen smaller than any characteristic time of the fluctuations. Apart of this lagrangian treatment, a statistical eulerian analysis can be performed. The test section is divided in sectors in which the mean density of beads or the fluxes of mass and momentum can be evaluated. Each data is then interpreted as an independent occurrence, which needs to be weighted proportionally to the axial component of the marker velocity. Actually a slow bead is observed more time than a quick one. Each measurement is attributed to the corresponding sector taking into account the symmetries of the geometry (figure 3). All the statistical results begin to converge after at least one thousand occurrences in each sector.

RESULTS

Beads density

The mean density is proportional to the weighted number of beads observed in each sector. The results are given in figure 4, showing a smaller value in vicinity of the walls. Hence, the beads fall more easily in the center of the section underlining repulsive forces naturally stronger between wall and beads than between beads. Correlatively, it can be deduced than the oil moves up more along the walls than in the center of the canal.

Beads velocities repartition

Figure 5 presents the repartition of the axial component U in the central sector. Most of the beads fall down but some of them go up with velocities of the same order. All the sector gives similar results, with an increasing proportion of beads going up near the walls and particularly in the corners. As a result, the mean velocity in the section is about the one of a bead falling alone in the oil, but the effective velocity of the beads going down is higher. According to Jayaweera[3] this indicates that some beads move in clusters. This is corresponding to the overall observation of coherent structures in the flow. Figure 6 shows the gaussian feature of the cross velocities in the center. All the sectors give similar results.

Fluxes

For the beads, the vertical mass flux per unit time and volume is given by: $\overline{\rho}.\overline{U}$, where the upper lines indicate a statistical averaging. The repartition in the section is approximately the same as that for the mean density (figure 7). The cross mass fluxes are zero. The mean cross momentum fluxes due to the velocity fluctuations U', V' and W' are zero so the momentum tensor is diagonal with a maximum component $\overline{\rho}.\overline{U'^2}$.

CONCLUSION

The experiment presented in this paper shows that it is possible to obtain numerous physical values in a complex 3D liquid-granular flow by an optical PTV method. In spite of the imposed choice of material due to the index matching, this technique covers a wide range of applications. It is relatively easy to modify the Reynolds number by changing the size of the

beads. Moreover the density ratio between the borosilicate and the oil is similar to the one existing in many environmental applications. The knowledge of the beads mass fluxes give indirectly the liquid velocity repartition and the granular momentum tensor can then be linked to the liquid strain rate tensor in order to lead to a constitutive law for the mixture.
Finally, such a device allows very clear comparisons with numerical simulations either based on continuous media or on particular approaches.

References

1- **Saleh S.. Larrea J.C., Thovert J.F, Platten J.K., Adler P.M., (1992),** Thermal convection in a model porous medium, Acte of the 6th international symposium on Appl. Of Laser Techniques to fluid Mechanics, Portugal.

2- **Kobayashi T. (1992),** Advances in computer-aided flow visualization, Flow Visualization VI, Ed Y. Taneda & H. Miyashiro, Springer Verlag, pp. 25-38.

3- **Jayweera K. O. L. F., Mason B. J., Slack G.W. (1964),** The behaviour of clusters of spheres falling in a viscous fluid, J. Fluid Mech., vol. 20, pp121-128.

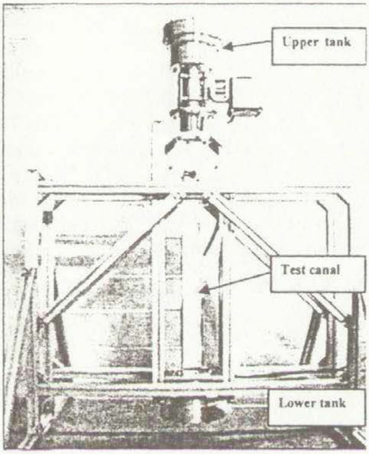

Figure 1 : experimental hydrodynamic tunnel

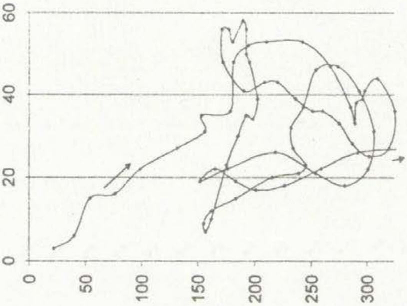

Figure 2 : Example of bead's trajectory

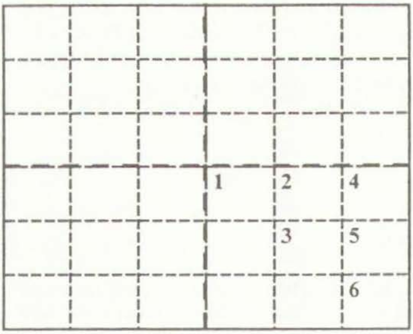

figure 3 : sectors definition

138.0	151.5	106.8
	158.5	111.5
		70.6

Figure 4 : mean density per sectors ($kg.m^{-3}$)

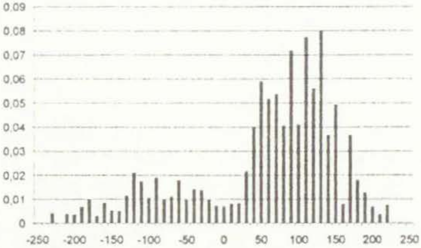

Figure 5 : Longitudinal velocity repartition ($mm.s^{-1}$)

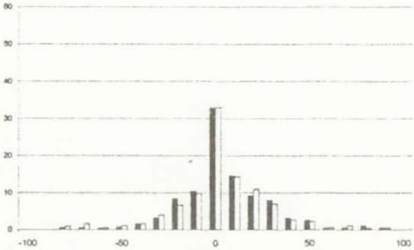

Figure 6 : transverse velocity repartition ($mm.s^{-1}$)

7.4	10.1	6.9
	10.4	6.9
		4.2

Figure 7 : longitudinal mass flow rate ($kg.m^{-2}.s^{-1}$)

MEASUREMENTS OF TRANSLATIONAL AND ROTATIONAL VELOCITIES OF A SPHERE IN STOKES FLOW

N. Lecoq[1], R. Anthore[1], M.L. Ekiel-Jeżewska[2], F. Feuillebois[3]

[1]UMR 6634 CNRS, Place E. Blondel 76821 Mont Saint Aignan Cédex
[2]IPPT, Polish Academy of Sciences, Świętokrzyska 21, 00-049 Warsaw, Poland
[3]LPMMH-ESPCI 10, rue Vauquelin 75231 Paris Cédex 5

Summary. The motion of a sphere sedimenting in a viscous (low-Reynolds-number) fluid is investigated with an interferometric technique and a video system. The laser interferometry is used to measure the translational velocity in the vertical direction (direction of gravity) with a high precision. The laser beam reflected by the sphere in motion as a cone of light is also used as the input to a system controlling the horizontal motion of the sphere. A video system with associated image analysis software is used to measure the rotational velocity of the sphere. Both techniques have been applied to study the relative motion of two rough particles at contact, in a Stokes flow. In this case hydrodynamic interactions and contact forces combine to give rolling and rolling plus slip regimes of the motion.

INTRODUCTION

Hydrodynamic interactions between spheres immersed in a low Reynolds number fluid are extensively investigated theoretically, numerically and experimentally [1]. The main interest is to describe the macrospcopic properties of suspensions, such as sedimentation, diffusion or effective viscosity. There is relatively few experiments made for systems of several spheres only. Theory of hydrodynamic interactions for such a simple system is well-known and the motion of spheres can be easily calculated numerically [1-2]. However, the experiments can provide some information on the hydrodynamic interactions of spheres with walls of various geometry (which is not easy to be calculated theoretically), and they can help to understand physics of the contact between spheres [3-4].

The goal of this paper is to explain the experimental setup used to measure translational [5-7] and rotational velocities of a sphere immersed in a low Reynolds number fluid, sedimenting due to gravity, being close to another obstacle, eg. another fixed sphere. The technique is based on interferometry and video system. The laser interferometric technique is used to measure the translational velocity in the vertical direction (direction of gravity) with a very high precision. The laser beam is reflected back by the moving particle as a cone of light, which in turn is used as the input to a system controlling the horizontal motion of the sphere. A video system with associated image analysis software is used to measure the rotational velocity of the particle.

MEASUREMENT OF TRANSLATIONAL VELOCITIES

Both vertical and horizontal components of the sphere motion have been investigated, but each of them with a different measurement technique. A sketch of the experimental setup is presented in Fig. 1.

Vertical motion

A laser interferometer has been used to measure with a high accuracy the vertical velocity and the vertical displacement of a spherical particle moving in a viscous fluid [5-7].

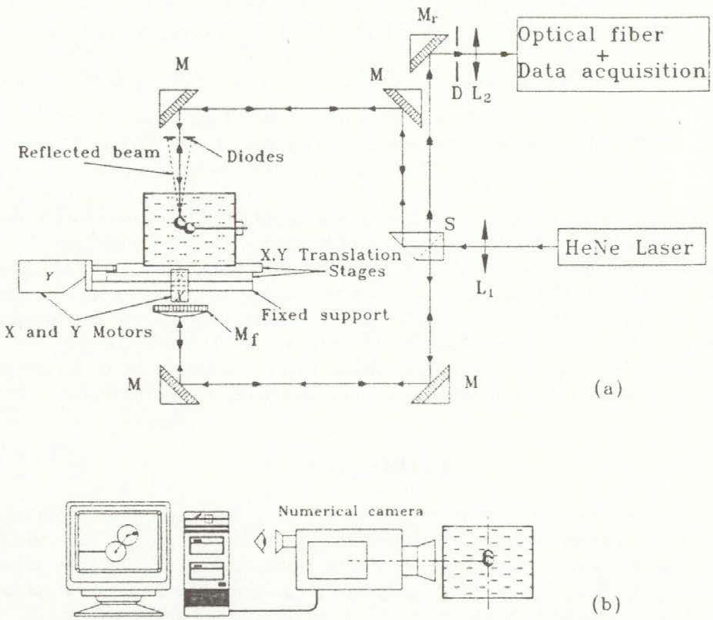

Figure 1: Sketch of the optical interferometry setup (*a*) and of the video system (*b*).

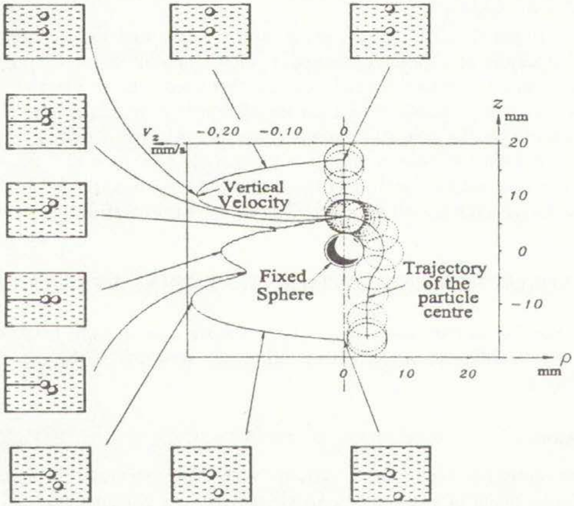

The interference fringes appear as concentric clear and dark rings. Shift from a dark to the next clear fringe (or conversely) determins the particle displacement in terms of the laser wavelength and the refraction index of the fluid. The typical sensitivity of the measured displacement is of the order of 100 *nm*. The times at which the signal reaches successive extremes are measured and used to calculate the particle vertical velocity.

Horizontal motion

The moving particle has to stay in the vertical laser beam if the interfernece fringes are to be observed at each time step. However, when it turns around the fixed sphere, a horizontal component of motion is added to the vertical one. To compensate for this displacement, the whole cell is being driven in such a direction that the moving sphere stays in the laser beam. The measurements of the horizontal relative motion of the spheres are performed with a detector (a system of photodiodes) using the laser beam reflected back by the particle in motion. A horizontal displacement of the sphere is characterized by an unbalance in intensities detected by various photodiodes. When such a difference in intensity is measured, a computer performs data acquisition and calculates corrections in position taking into account that the response of the photodiodes varies with the vertical position of the sphere. Then the corresponding commands are sent to two direct current motors which drive the whole cell to compensate the horizontal motion of the particle.

MEASUREMENT OF ROTATIONAL VELOCITY

For the purpose of visualising the rotational motion of a particle, we mark a dot on the sphere surface and enlighten it. For recording the images, we first performed test measurements using an analog equipment. In our present setup a charged coupled device (CCD) numerical camera (Sony Handycam Vision) is placed close to the cylindrical container, perpendicular to the plane of motion. The camera is connected to a personnal computer equiped with an image processing board (Miro DV300). With the help of a specially developed software, the digitized captured images are analysed to measure the successive positions of the sphere centre and of the dot.

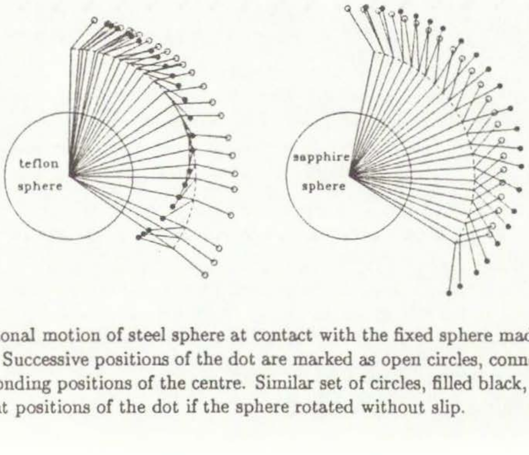

Figure 3: Rotational motion of steel sphere at contact with the fixed sphere made of teflon (left) and sapphire (right). Successive positions of the dot are marked as open circles, connected by stright lines with the corresponding positions of the centre. Similar set of circles, filled black, indicate what would be the subsequent positions of the dot if the sphere rotated without slip.

In general, a system of several spheres in a container does not exhibit symmetries and therefore direction of the angular velocity of a chosen sphere changes during its motion, what makes tracing of a dot (or dots) on its surface complicated. However, when there are only two spheres: one turns around another, which is fixed in the middle of the cyliner, then the trajectory of the sphere centre is flat. Due to the symmetry the angular velocity is perpendicular to the plane of the trajectory and we can fix the camera line of sight to be along the angular velocity. This way the motion of the dot takes place in the plane of the camera frame. Results of the test measuremnts for moving sphere made of steel and the fixed sphere of the same size made of teflon and sapphire are presented in Fig. 3. The graphs indicate that the rotational motion is supplemented by a significant slip. Moreover, the ratio of the angular to translational velocity depends on the type of surface of the fixed sphere - for sapphire it is larger than for teflon.

CONCLUSION

A method to investigate experimentally hydrodynamic interactions between spheres in a Stokes fluid has been developed. It is based on measurements of both translational and angular velocities of a moving sphere, like the technique of Smart *et al.* [8]. Similarly as in Smart *et al.* [8], we use a simple video system to measure the rotational velocity. However, our method to measure the translational velocities is based on an interferometric technique, more accurate than the previous method [8]. We have applied our experimental method to analyze the motion of two spheres at contact.The measurements of the translational velocity have confirmed the existence of two different intervals of motion, pure rolling and rolling with slip, and a sharp transition between them, predicted by the model [3-4]. However, to determine values of the model parameters the analysis of the angular velocity was also needed. This was possible due to a video imaging of the same system.

REFERENCES

1. S. Kim, S.J. Karilla, Microhydrodynamics: Principles and selected Applications, *Butterworth - Heinemann*, Boston, (1991).

2. D. J. Jeffrey and Y. Onishi. Calculation of the resistance and mobility functions for two unequal rigid spheres in low-Reynolds-number flow. *J. Fluid Mech*, **139**:261-290, (1984).

3. M.L. Ekiel-Jeżewska, F. Feuillebois, N. Lecoq, K. Masmoudi R. Anthore, F. Bostel and E. Wajnryb. Contact friction in hydrodynamic interactions between two spheres. In proceedings of the Third Conference on Multiphase Flow, ICMF'98, Lyon, 1998.

4. M.L. Ekiel-Jeżewska, F. Feuillebois, N. Lecoq, K. Masmoudi R. Anthore, F. Bostel and E. Wajnryb. On hydrodynamic interaction between two spheres at contact. *Phys. Rev. E*, **59**, (1999), in print.

5. N. Lecoq, F. Feuillebois, N. Anthore, R. Anthore, F. Bostel and C. Petipas. Precise measurement of particle-wall hydrodynamic interactions at low Reynolds number using laser interferometry. *Phys. Fluids A*, **5**(1), 3 (1993).

6. N. Lecoq, F. Feuillebois, R. Anthore, C. Petipas and F. Bostel. Experimental investigation of the hydrodynamic interactions between sphere and a large spherical obstacle. *J. Physique II*,**5**, (1995).

7. K. Masmoudi, N. Lecoq, R. Anthore, F. Bostel and F. Feuillebois. Accurate measurement of hydrodynamic interactions between a particle and walls. submited to *Experiments in Fluids*, (1999).

8. J.R. Smart, S. Beimfohr, D.T. Leighton, Jr.,*Phys. Fluids A*5, 13 (1993).

PIV ANIMATION OF TURBULENT FLOWS FROM 2-D INCLINED RECTANGULAR PRISMS

Young-Ho LEE*, Jang-Woon CHOI**, Yu-Cheung IM*** and Keun-Taeck SONG***

* School of Mechanical Engineering, Korea Maritime University
1 Dongsam-dong Youngdo-ku Pusan, 606-791, Korea
(lyh@hanara.kmaritime.ac.kr)
** Image Information Technology Co., Ltd.
*** Graduate School, KMU

Summary A PIV experiment to analyse the flow characteristics of two-dimensional Karman vortex from rectangular prisms was performed and its animation procedure routine was developed. Three kinds of aspect ratio(D/H=1, 2 and 3) and three kinds of angle of attack(0° , 30° and 45°)were adopted for the experimentation within a free surface water channel. Reynolds number in the present study was assumed to be 2×10^4. Optimized cross correlation identification to obtain velocity vectors was implemented by direct calculation of correlation coefficients. For natural understanding of complicated bluff body wake flow characteristics, animation technique not relying on any commercial post-processor software was newly developed. Time-sequential AVI image files were produced to display the instantaneous velocity vector distribution, vorticity shedding pattern and macroscopic streaklines distribution.

EXPERIMENT

Figure 1 is the schematic diagram of the present PIV experiment. A circulation water channel was used and its dimension of the test section is 5m× 1.8m× 1.2m(L x W x H). The maximum power of the circulating axial pump(impeller diameter is 0.8m) is 22kW and its inlet time-mean velocity is 0.32m/sec as representative velocity for $Re=2\times10^4$. The transparent acryl bars of three different aspect ratios were traversed by three-axis traverser and angle of attack at every experimental condition was accurately adjusted. Illumination for PIV visualization was made by 5W Argon-Ion laser connected to fiber optic line and cylindrical lens. The water-tight lens assembly was fixed to bottom of the water channel for cleaner illumination effect. CCD camera (B&W, SONY XC77-RR) was adopted to capture the flow field and its image was saved on Hi-8mm Camcoder for the later replay of the original image input to image grabber(DT3155, 640x480 pixels, 8bits). Tapping water was used as working fluid and tracer particles were PVC-made spheres(average diameter is 110 μm). Obtained images are interlaced on each frame at every 1/30 second and it is field-integrated. The single frame image is divided into two fields(odd and even, 1/60 second) and they are used as the first frame(odd) and second frame(even) for the cross correlation identification of direct calculation. Flow images recorded on the Hi-8mm Camcoder tape are replayed and their consecutive images are usually transferred into personal computer RAM memory space by a built-in image grabber slit into PC board space. The analog image signals are digitized and bright particle images are distinguished from the back ground by their corresponding grey-levels(8 bits, $2^8=256$ steps). The image board permits maximum RAM capacity available and it affords simultaneously real-time transferring of the images onto RAM memory.

The identification algorithm to ascertain the same movement of the discrete particles or overlapped particle groups is the key point in PIV performance. The identification method adopted in the present study is an optimized two-frame cross correlation technique[1-2]. This algorithm is quite free from the particle selection limitation, contrary to the particle tracking velocimetry(PTV) where discrete particle centroids must be calculated. The direct calculation of the cross correlation coefficients for the two-dimensional grey level distribution(usually 256 steps) of two consecutive flow images is implemented solely on PC. Interpolated grid number is usually 50 x 50(2500 evenly-spaced vectors) and each correlation area is typically 40 x 40 pixels. The maximum searching distance from the vector origin, grid coordinate of the first frame correlation area, to the presumed maximum distance of vector terminal point, center of the second correlation area is usually selected as 9-10 pixels. Error removal procedure by automatic and manual techniques is also executed by the divergence criterion satisfying the continuity equation. Error probability by automated procedure is averagely less than 1% . The CPU time to calculate all cross correlation coefficients and to sort the maximum value at every frame, on Pentium PC(200MHz), is about 2.5-3.0 seconds.

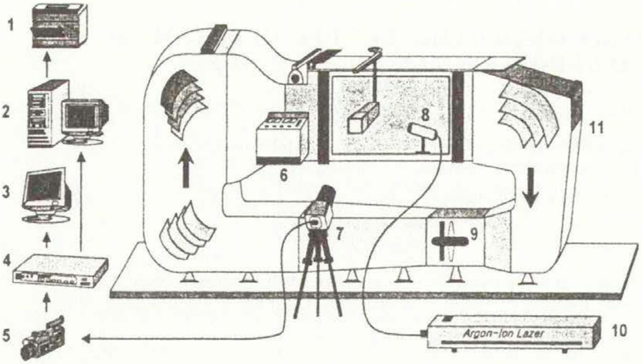

1. **Color Printer**
2. **Host Computer & Software**
3. **Monitor**
4. **Time Base Corrector**
5. **Hi-8mm Camera**
6. **Operation Console**
7. **CCD Camera**
8. **Sheet Light Probe**
9. **Axial Pump**
10. **Argon-Ion Laser**
11. **Circulating Water Channel**

Figure 1. Schematic Arrangement of PIV System

ANIMATION

Figure2 shows, in sequence, the graphic procedure of the animation from the PIV databases. The procedure to obtain the individual 600 frame images for the pre-processing is first required. The analog images from the Hi-8mm Camcorder in the present study are transformed into one AVI file on E-IDE hard disk through a Motion-JPEG board (miro-VIDEO DC 30 plus). The period of replay time is 40 seconds. It corresponds to 600 field images in real-time base(40 seconds x 15 fields/second=600 fields). Spatial resolution is 640 x 480 pixels in 24 bits RGB true colors. Compression ratio is minimized to 2.5, the allowable lower limit for the least-loss image acquisition. The generated AVI file size is 124 MB. The well-known commercial authoring tool, Adobe Premiere4.2 is easily adopted to decompose the single but huge AVI file into 600-field sequences for further frame-by-frame process. The obtained file is BMP format in 24 bits RGB colors. But, in usual PIV process, color information is not so available that the RGB information should be transformed into the Y/C signal(Y:luminance, C:chroma). The Y formula(Y=0.30R + 0.59G+ 0.11B) is adopted here. The simplified 600 files, named X.raws, are all 8 bits and they are used at all stages followed. AVI files for the animation on PC monitor are necessary. Every file is newly obtained by averaging five sequential files at all grids. This process attenuates the sensitive velocity fluctuation and it is quite effective to produce smooth flow development for the visualization convenience. Next, various quantities for flow animation are prepared by calculating the turbulent intensity, turbulent kinetic energy, three Reynolds stress components, vorticity and time-dependent displacement coordinates of all artificial markers for streaklines, trajectories and streamlines. And then, these quantitative informations are changed efficiently into full graphic sources in virtue of the versatile PIV post-processing algorithms. The visual language, Delphi3.0, which is greatly superior to other languages especially in compile speed, is absolutely contributed to the animation work. About 138MB X.bmp files are consequently produced for each animation case. But this file size should be reduced for easy handling. Video Studio2.0(Ulead System) is used for the purpose. The specification of the obtained single AVI file is 382 x 267 pixels in 24 bits resolution and its file size ranges from 9 to 18 MB. Under Windows98 operating system, the built-in Active Movie displays automatically these animation examples on PC monitor by mouse clicks only. The instant animation pictures are represented at last page and their animation movies are displayed at the conference site or Internet homepage, ***http://iit.kmaritime.ac.kr***

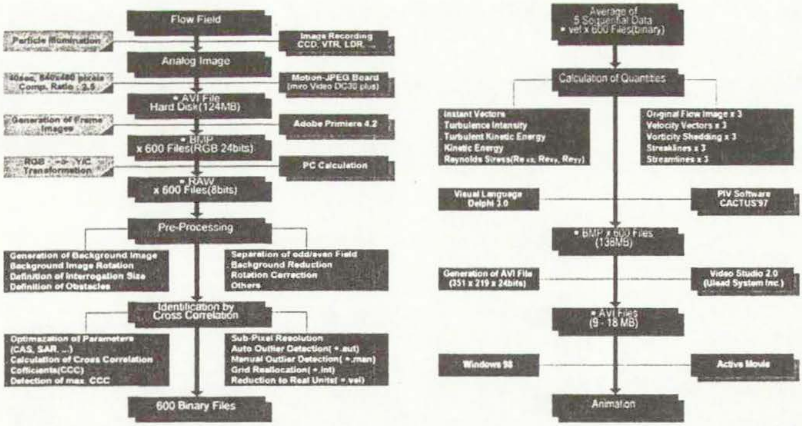

Figure 2. Graphic Procedure of Animation

RESULT & DISCUSSION

Figure3 shows original instant flow images in case of three aspect ratios. Analysed flow area is, for example, 342mm x 239mm in case of D/H=1 and its corresponding pixel area is 382 x 267. Figure4 represents the instantaneous velocity vectors in case of three angles of attack for single aspect ratio, D/H=1. Here, vortex shedding of large scale is found at the rear side of the body and consequent entrainment effect due to this periodic vortex shedding governs the flow behavior. Approaching flow is accelerated at the front edge where a kind of discontinuity point exists and it is detached at two lower and upper side of the body where flow separation is accompanied and aerodynamic pressure is assumed to drop abruptly. At this aspect ratio(D/H=1), separation region beginning at the front edge contributes to the almost of the sheared layer and this layer is coming into rear side of the body with large curvature. Figure5 indicates the shedding pattern of vorticity produced at the front edge of rectangular prism in case of D/H=2. Figure6 shows streakline patterns for three kinds of angle of attacks in case of D/H=3. They show well macroscale entrainment phenomena in the wake region and with increasing angle of attack, larger scale of wake development is noticed .

CONCLUSION

A PIV experiment was carried out to analyse the flow characteristics of the two-dimensional Karman vortex shed from the rectangular prisms. Three kinds of aspect ratios(D/H=1, 2 and 3) and three kinds of angles of attack(0° , 30° and 45°) were selected for the experiment. Reynolds number was $2x10^4$. Optimized cross correlation PIV identification was implemented to obtain velocity vectors by direct calculation of the coefficients. Animation technique not relying on any commercial post-processor software was developed. Time-sequential AVI image files were produced to display the instantaneous velocity vector distribution, vorticity shedding pattern and macroscopic streaklines distribution for the intuitive understanding of bluff body wake dynamics.

REFERENCES

1.Lee Y.H., Cho D.H., Seo M.S., A PIV Analysis of Confined Jet Mixing Flow within Circular Pipe, *Proceedings of JSME Centennial Grand Congress, Int. Conf. of Fluid Eng. Vol.2*, pp.663-668, 1997.
2.Lee Y.H., Choi J.W., Seo M.S., Saga T., Analysis of Uncertainties from PIV Input Devices, *Proceeding of VSJ-SPIE'98 Yokohama*, pp.232-233, 1998.

(a) θ =0° (D/H=1) (b) θ =30° (D/H=2) (c) θ =45° (D/H=3)

Figure 3. Original Flow Image

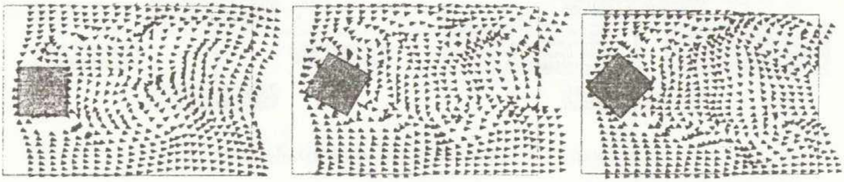

(a) θ =0° (b) θ =30° (c) θ =45°

Figure 4. Velocity Vector(D/H=1)

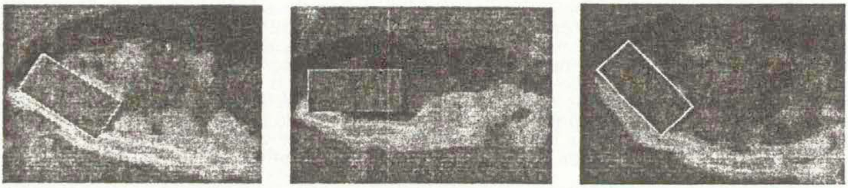

(a) θ =0° (b) θ =30° (c) θ =45°

Figure 5. Vorticity Shedding(D/H=2)

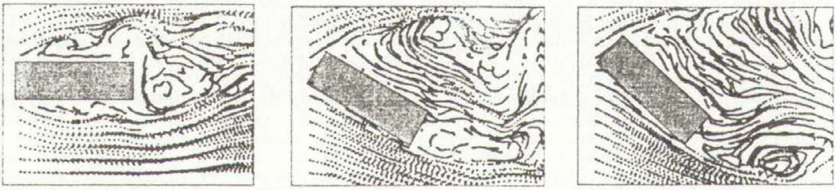

(a) θ =0° (b) θ =30° (c) θ =45°

Figure 6. Streaklines (D/H=3)

TOMOGRAPHIC MEASUREMENT TECHNIQUES – VISUALIZATION OF MULTIPHASE FLOWS

By Marc Lörcher*, Dirk Schmitz and Dieter Mewes

Abstract

A new tomographic measurement technique visualises the field of local void fraction in the two phase flow of air and water in the mixing chamber of a two-phase-nozzle. With this measurement technique a high spatial and temporal resolution can be achieved. The measured physical property is the different electric conductivity of the two fluids water and air. In the measurement plane the conductivity is measured between many wires strained in the investigated cross section. The measurement values are proportional to the relative liquid fraction. With an algebraic reconstruction technique (ART) the field of the liquid fraction in the investigated cross-section is calculated from the measurement values. The quality of the reconstruction is increased by a-priori-knowledge.

Tomographic measurement techniques

With tomographic measurement techniques, the fields of density, concentration, temperature, velocity or local void fraction can be measured in two steps. First linear independent integrals of a physical property in the cross section are measured. In figure 1 this is shown for a physical property f(x,y,t) in two different directions for the integration. For each direction the projection of the distribution of the physical property follows to:

$$\Phi_M = \int_s f(x,y,t)\,ds \tag{1}$$

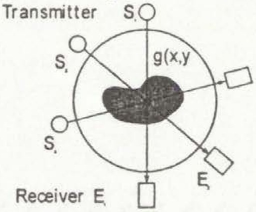

figure1. schema of the tomographic measurement technique

In eq.(1) s is the path along which the physical property f is integrated. The local distribution of the physical property is included in the projections. The local distribution of the physical property can be calculated from these projections with a reconstruction algorithm. The projections can be measured with different measurement techniques. In the following chapter a new electrical tomographic technique with a high spatial and temporal resolution is presented.

Electrical tomographic measurement technique

In figure 2 the new tomographic sensor is represented. The sensor consists of three parallel planes. In each of the planes nine parallel wires with the diameter of 0,1mm and the distance

---

* Prof. Dr.-Ing. D. Mewes, Dipl.-Ing. M. Lörcher, Dipl.-Ing. D. Schmitz, Universität Hannover, Institut für Verfahrenstechnik, Callinstr. 36, 30167 Hannover

of 1mm are strained. The distance between two planes is 1,5mm. The diameter of the measurement cross section is 10mm. Because of the small diameter of the wires the disturbance of the multi phase flow is negligibly.

Between two wires of one plane the conductance is measured. The conductance is a function of the electrical characteristics and the distribution of the two phases. Depending on the flow pattern the wires are connected with different areas of liquid. This corresponds to a parallel arrangement of Ohmsche resistance's. With a negligible conductance of the air the measured conductance is

$$G_m = \sum_{i=1}^{n} \frac{1}{R_i}, \tag{2}$$

where R_i is the resistance of one area between two wires filled with liquid. For the Resistance of one area filled with liquid and the length l_i the resistance can be calculated with

$$R_i = \frac{1}{G_{max}} \frac{l}{l_i}, \tag{3}$$

where l is the maximal possible length of areas filled with liquid between two wires. G_{max} is the maximal conductance that follows when the wires are completely wetted. From eq.(2) and (3) follows for the maximal conductance is

$$G_m = G_{max} \sum_{i=1}^{n} \frac{l_i}{l}, \tag{4}$$

which can be transformed into

$$G^* = \frac{G_m}{G_{max}} = \frac{\sum_{i=1}^{n} l_i}{l}, \tag{5}$$

where G^* is the relative conductance. G^* is equal to the liquid fraction $1-\alpha$

$$G^* = 1-\alpha. \tag{6}$$

The measured integral value of the conductivity is the relative conductance G^* which is denoted in eq.(1) Φ_M. The conductance between every two neighbouring wires in one plane is measured. With the three planes of wires in the sensor there are three linear independent projections of the phase distribution measured. The conductance between two neighbouring wires is measured with a commercial impedance measurement instrument. The measuring instrument includes an alternating voltage bridge with a frequency of 1MHz and an amplitude of the voltage of 0,2V (+/-0,1V). Taking into account the phase distribution between current and voltage the conductance is measured independent from the capacitive part of the impedance. Because of the alternating voltage it is possible to measure only the conductance of one pair of neighbouring wires at each time.

The electric connection between each pair of wires of the sensor and the measurement instrument is made by a multiplexer circuit. With a PC the multiplexer circuit is controlled and the measured conductances are stored. The measurement chain for the wire-mesh sensor is shown in figure 2.

Reconstruction

The goal of the reconstruction is to calculate the local distribution of the conductivity from the integral measured values. For this purpose eq.(1) has to be inverted for all directions of the measured projections. Because of the limited number of projections a direct inversion is not possible. Another problem is that the equation system for the big number of reconstruction elements is underdetermined. A iterative algebraic reconstruction-algorithm (ART) is used to solve the problem iterative [1,2].

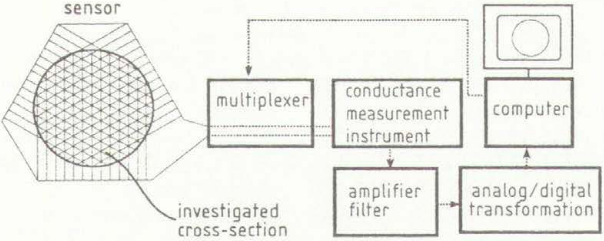

figure 2. measurement chain of the wire-mesh sensor

Reactions of the wires on the flow pattern

The described measuring technique is used for slug-/plug-flow in horizontal tubes, for the two-phase-flow in tubes with big diameters and for the bubble flow in vessels. Optical investigations of the flow patterns before and behind the sensor are taken and integral measurement values with and without the sensor are compared. From prior the investigations it can be concluded that there is no significant influence of the sensor on the flow pattern. In order to do further investigations a device is build up a device which allows to film the flow before and behind the sensor at the same time. The device contents of four mirrors. Two mirrors shift the upper part of the camera-picture so that it is possible to observe the flow before the sensor. The other two mirrors shift the lower part of the camera-picture to observe the flow behind the sensor.

The results are shown in figure 3 for the annular flow and in figure 4 for the bubbly flow. On the left side the flow is shown without and on the right side within the sensor. In addition to this the influence of the sensor will be shown in a film. No distortion of the flow pattern can be observed included the wires. Thus the wires can be considered not to have an influence on the flow pattern.

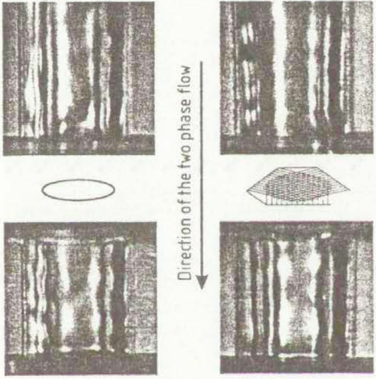

figure 3. annular flow

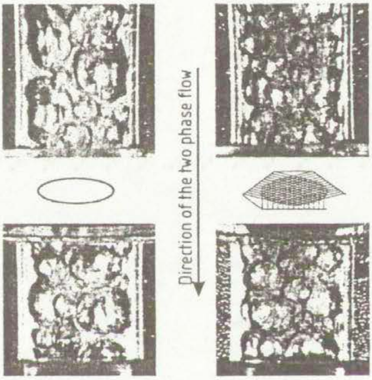

figure 4. bubbly flow

Pilot plant

In this project the investigations are made on two-phase-nozzles with internal mixing. In the nozzles the gas (air) is dispersed in the liquid that has to be atomized. The two-phase mixture is accelerated and in the nozzle exit critical mass flow occurs. Within the nozzle the liquid is the continuos phase. At the exit of the nozzle the liquid becomes the dispersed phase. The gas expands and tears up the liquid in small ligaments. The ligaments disintegrate into drops. The two-phase-atomization has the advantage that even at pressures of 0,5-1MPa before the nozzle exit fine droplets can be achieved. With the one-component atomization fine droplets can be produced only at high pressures and small diameters of the nozzle exit cross section. Such narrow cross sections can easily clog and in addition it is only possible to atomize relative small rates of liquid.

With the two-phase atomization it is possible to produce small droplet diameters even with greater diameters of the nozzle exit cross section or with grater rates of liquid. The main disadvantage is the bad efficiency of the atomization. The efficiency is defined as the relation between the applied power and the power which is used to generate new surfaces. This relation is about one order of magnitude smaller than at the one-component atomization. To produce technical sprays relative high gas rates are used. To increase the efficiency it is necessary to achieve a maximum dispersion of the gas in the liquid. Then the expansion will devoid the liquid optimal into ligaments.

To detect the distribution of the gas in the liquid it is necessary to measure the flow pattern after the gas is dispersed. The flow sheet of the pilot plant is shown in figure 5. Liquid and gas are stored in a vessel under variable pressure. The mass-flow of each phase can be controlled. The mass-flow-rate, the pressure and the temperature of each phase are measured. After the gas is dispersed the flow pattern is measured with the sensor explained in this article. The flow pattern is visualised with a high speed camera. After the nozzle exit cross section the droplet velocity and later the droplet diameter are measured with a PDPA-system.

The presented pilot plant is capable to measure all relevant parameters before, in and behind the nozzle, which are necessary to describe the two-phase flow.

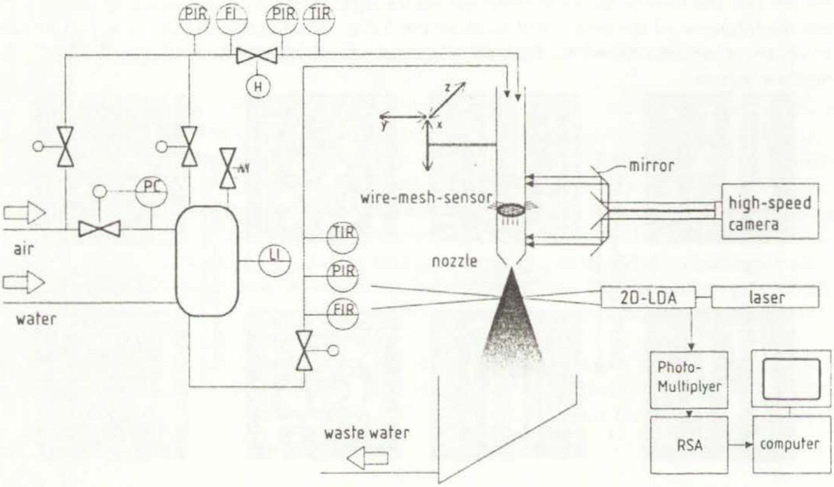

figure 5. flow sheet of the pilot plant

References:

1) N.Reinecke, M. Boddem, G. Petritsch, D. Mewes: Tomographisches Messen der relativen Phasenanteile in zweiphasigen Strömungen fluider Phasen, Chemie Ingenieur Technik 68 (1996) Nr. 11 S. 1404-1412

2) N. Reinecke, G. Petritsch, D. Schmitz, D. Mewes: Tomographic Measurement Techniques- Visualization of Multiphase Flows, Chem. Emg. Technol. 21 (1998) 1 p.7-18

APPLICATION OF ANISOTROPIC METHODS OF IMAGE PROCESSING AT RESEARCH OF AIRCRAFT MODEL WITH THE HELP OF PRESSURE SENSITIVE PAINT.

A. N. Morozov

Central Aero-Hydrodynamic Institute, Zhukovsky, 140160, Russia

Summary. In the given work the digital data processing methods are considered with the purpose of pressure field on an aircraft model surface with the help of the PSP method accuracy of definition increase.

The methods of the image characteristic allocation are considered, including specially put luminescent markers and local - adaptive filtration of the image by means of anisotropic filter keeping sharp intensity differences, that allows using the additional information to increase accuracy of the measuring and reference images alignment.

PSP Method.

PSP method is a new surface pressure measurement method [1]. PSP method is based on deactivation of photo-excited molecules by oxygen contained in the air. A thin polymer layer, penetrable for oxygen covers the model surface. The polymer layer contains luminophore molecules. Luminophore molecules exited by an appropriate light source may be transferred to the ground state with light emission (luminescence) or may lose energy by transferring it to oxygen molecules without light emission (luminescence quenching). This part of lost energy is directly proportional to oxygen concentration in the polymer layer and oxygen mobility. According to Henry's law, concentration of oxygen in a polymer layer is directly proportional to oxygen partial pressure on its external boundary. Therefore, luminescence output is inversely proportional to oxygen partial pressure above a polymer surface.

Processing of the images

The initial image registered in experiment is submitted in figure 1. For presentation all images are given as negatives, in such representation the features of the given methods of processing are better appreciable in case of a black-and-white seal. It is necessary to note, that on the given image markers are absolutely imperceptible (black points) on noisy background.

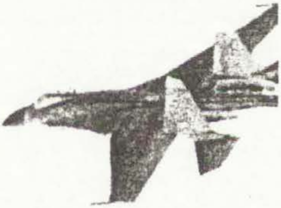

Fig. 1. The initial image

Fig. 2. The image processed by decorrelation filter.

The processing of the initial image by the adaptive decorrelation filter which is taking into account local statistical properties of a signal was for the beginning carried out [4]. The algorithm of a filtration consists in minimization of a root-mean-square mistake (RMS). If **f** - ideal image, **n** - white noise, and covariation matrix $\mathbf{C}_n=\sigma_n^2\mathbf{I}$, the resulting image will be

$$\mathbf{g} = \mathbf{f} + \mathbf{n}$$

Estimation RMS is possible to write down as

$$\hat{\mathbf{f}} = E(\mathbf{f}) + \mathbf{C}_f(\mathbf{C}_f + \mathbf{C}_n)^{-1}[\mathbf{g} - E(\mathbf{g})],$$

In a case, when covariation matrix $\mathbf{C}_f$ is diagonal, after decorrelation with the help Carunen-Loueve transformation [5], $\mathbf{C}_f = diag(\sigma_{f1}^2, \sigma_{f2}^2, \ldots, \sigma_{fN}^2)$, the estimation RMS can be written down for everyone pixel as

$$\hat{f}_i = E(g_i) + \frac{\sigma_{fi}^2}{\sigma_{fi}^2 + \sigma_n^2}[g_i - E(g_i)]. \qquad (1)$$

Carunen-Loueve transformation was carried out as well as in [5] above 2D blocks 8*8 pixel, and the averaging was carried out under the formula (1) above cells 3*3 blocks. The result of the adaptive decorrelation filtration is submitted in a fig. 2. This image was used for the further analysis on allocation of image features, such as markers, borders, intensity differences.

The processing of the received image with the help of gradient filter was carried out, that is nonrecursive filter with a nucleus representing some penalty function from a local gradient of the image [4]. Naturally, such filter smooths the image non-uniformly. A degree of smoothing is higher, than less meaning of a local gradient. In work the penalty functions similar to functions describing processes of molecules energy dissipation in optical spectroscopy were applied - Gauss and Lorentz [11].

$$C_n(x,y) = r \cdot \exp\left(\frac{-\left|\nabla f(x,y)\right|^2}{2k^2}\right) \quad ; \; C_n(x,y) = r \cdot \frac{1}{1 + \left(\frac{\left|\nabla f(x,y)\right|^2}{k^2}\right)} \quad .$$

From figure 3 it is visible, that the image has got rather precise outlines, but small details are not revealed.

Fig. 3. The image processed by the gradient filter.

Fig. 4. The allocated valid markers.

The further processing included anisotropic filtration of the image for preservation and allocation of the image features[4]. The algorithm of a filtration consists in allocation of the block by the size n*n pixel and sorting of each block according to the increase of intensity. Assignment to central pixel the value of an element of the block having average number is known as median filtration, allowing to some extent to clear the image of positive and negative peaks having the small spatial sizes in comparison with a nucleus of the filter. For allocation of such features as luminescent markers the operator *MG* is used so-called "morphological" gradient, representing the sum of gradients of "dilation" *DG* and "erosion" *EG* [7]

The result of similar processing is submitted in figure 4. The received allocated areas contain the images of luminescent markers named valid, as against markers received by the analysis of borders of the image and, therefore, named virtual. Use of the given algorithm together with the course operators [12] allows to allocate image borders (sharp differences of intensity), as is shown in figure 5. The course operators, used in work, represent a set 2D Gabor filters [8], which spatial frequency is determined proceeding from the spatial resolution of system "the objective lens-CCD camera", that is on a level ½ of modulation transfer function value determined with a method of boundary function [15]

$$G(x,y)_{pq} = \exp\left[-\frac{\pi}{a_p^2}(x^2+y^2)\right] \times \exp\left[i2\pi f_p(x\cdot\cos\theta_q + y\cdot\sin\theta_q)\right] ,$$

Where the first multiplier determines spatial function of "window" with width determined in parameter a_p , and second - complex sinusoid. The parameters f_p and θ_q , determines accordingly spatial frequency and orientation of the Gabor filter.

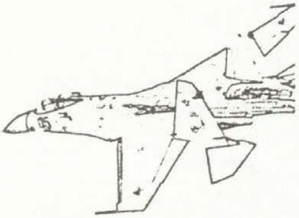

Fig. 5. The allocated information on borders (morphological gradient)

Fig. 6. Markers placed on borders of the image (virtual).

The allocated borders were used for construction of a set of "virtual" markers, that is markers unequivocally placed on borders of the "red" and "dark blue" images. The âøssection method was applied for unequivocal construction of markers [13], and as basic points the "valid" luminescent markers were choosen. The constructed "virtual" markers are submitted in figure 6, and association of sets of "virtual" and "valid" markers - in figure 7.

The pixel set, containing the information on borders of the image, is broken into two subsets belonging to external and internal borders accordingly. The splitting is carried out by check of a condition of excess of a gradient value of "erosion" above gradient value of "dilation". The result of processing is submitted in figure 8. From figure it is visible, that the image contains much more fine details, than previous, submitted on figure 3.

It is necessary to note, that the areas containing "valid" markers were subjected to operation of interpolation, were based on meanings of intensity, given areas, laying on border. To receive as exacter approximation of the valid intensity values is possible, the bilinear interpolation procedure with weight factors described by valley type function was used

$$f(\bar{\delta}x,\bar{\delta}y) = \left[\frac{2}{\pi}arctg(\pi(\bar{\delta}x^2 - \bar{\delta}y^2))\right]^{1/2} ,$$

Where $\bar{\delta}x, \bar{\delta}y$ - local coordinates concerning the geometrical centre of area containing a marker. Thus, in figures 3,5 and 8 markers are absent, hence, initial image is divided into the image of markers and image which is not containing markers.

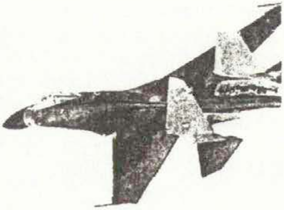

Fig. 7. The image processed by anisotropic filter

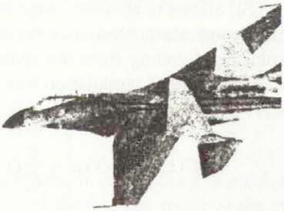

Fig. 8. The restored image

Last step of processing included the weighed sum of the initial image processed by adaptive decorrelation filter (fig. 2), and image processed by anisotropic filter (fig. 7), according to the formula (1). The final result of processing is submitted in figure 8. On the image the fine details are well traced, and, practically, there is no noise.

For presentation in figure 9 the restored image together with a set of virtual and valid markers is given. The received geometrical markers positions are used for overlapping and subsequent rationing of the measuring "blue" and reference "red" images [21].

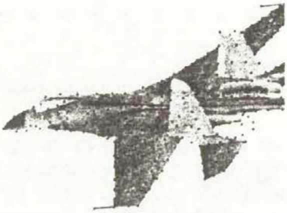

Fig. 9. The restored image with valid and virtual markers

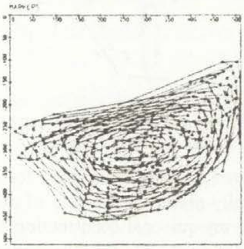

Fig. 10. Two marker images of aircraft model, registered under a different corner of sight

By essential difference from standard to a technique of overlapping of the measuring and basic images on geometrical positions of markers with the help nonlinear affinnae transformation of a degree is not higher than three is the application of rigid binding of markers on the images with subsequent bilinear interpolation inside of unequivocally determined figures, as there is an information on borders of the images, and, hence, there is no necessity to apply methods of extrapolation, which very strongly reduce accuracy of binding. In figure 10 are submitted the measuring and reference marker images received under a different corner of sight. On the marker images the areas of interpolation are traced.

In figure 11 the result of the marker images linked together is submitted [14]. The received additional grid of markers allows not to use extrapolation in zones which are taking place outside the valid markers, where the error nonlinking can achieve 3 pixel and more, and to use interpolation, that allows to reduce an nonlinking error to smaller values, than even the error of a mismatch of markers on the measuring and reference images, that usually makes no more than 0.1-0.5 pixel if to use nonlinear affinnae transformation 1-st - 3-rd orders, or 0 pixel, in case of marker configurations linking.

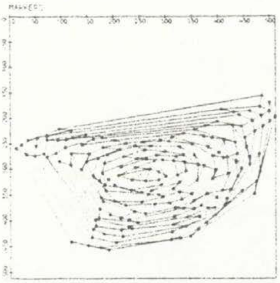

Fig. 11. Linked and interpolated marker image of aircraft model registered up to linking under a different corner of sight

There is a question of gravity marker centres definition accuracy. The decision of the given question was delivered in work [14], where was shown, that the application of nonrecursive adaptive filters allows to receive subpixel accuracy till 0.02 pixel.

References

1. Mosharov V., Orlov A., Radchenko V., Kuzmin M., Sadovskii N., "Luminescent Pressure Sensors for Aerospace Research: Diffusion-Controlled Characteristics", 2nd European conference on optical chemical sensors and biosensors, Firenze, Italy, 19-21 April 1994.
2. Bykov A., Fonov S., Kishalov A., Mosharov V., Orlov A., Ostroukhov S., Radchenko V., "Application of Luminescent Pressure Sensor technology to propellers", Preprint TsAGI No.99, Moscow 1995.
3. Burns S.P., Sullivan J.P., "The Use of Pressure Sensitive Paints on Rotating Machinery", 16th ICIASF Congress, July 18-21, 1995, Dayton, Ohio. 6.
4. J.Crespo, R.W.Schafer, Edge-based Adaptive Smoothing, Opt.Eng., No.36(11), 3081-3092, November 1997.
5. S.S.O.Choy, Yuk-Hee Chan, Wan-Chi Siu, Adaptive Image Noise Filtering Using Transform Domain Local Statistics, Opt.Eng., No.37(8), 2290-2296, August 1998.
6. A.K.Jain, Fundamentals of Digital Image Processing, Prentice-Hall, Englewood Cliffs, NJ(1989)
7. S.Tsekeridou, I.Pitas, Adaptive Order Statistic Filters for the Removal of Noise from Corrupted Images, Opt.Eng., No.37(10), 2798-2816, October 1998.
8. J.Escofet, R.Navarro, M.S.Millan, J.Pladellorens, Detection of Local Defects in Textile Webs Using Gabor Filters, Opt.Eng., No.37(8), 2297-2307, August 1998.
9. Васильев В.Н., Гуров И.П., Компьютерная обработка сигналов в приложении к интерферометрическим системам - СПб.: БХВ - Санкт-Петербург, 1998. - 240 с.
10. Hong Wei, E.Johnston, T.D. Binnie, Experimental approach for Measuring Resolution of Complementary Metal Oxide Semiconductor Imaging Systems. Optical Engineering, 1998, September, pp.2565-2573.
11. C.M.Autorian, C.O.Egiazarian, D.Z.Gevorkian, J.T.Astola, Combining the Discrete Wavelet Transforms and Rank-Order Based Filters for Image Restoration, Opt.Eng., No.37(1), 189-201, January 1998.
12. Морозов А.Н., Применение методов адаптивной обработки изрображений в аэрофизическом эксперименте, Труды Конференции Молодых Ученых ЦАГИ (Жуковский, апрель 1997г.)
13. Морозов А.Н., Спектрально-оптические методы исследования высокоэнтальпийных потоков газа. Вопросы динамики неустойчивостей. (межвед. сборник) Москва 1995.
14. Морозов А.Н., Програмное обеспечение для определения и привязки особенностей изображения применительно к аэрофизическому эксперименту, Труды Конференции Молодых Ученых ЦАГИ (Жуковский, апрель 1997г.)
15. Кулеш В.П., Морозов А.Н., Методика измерения разрешающей способности системы регистрации люминесценции бароиндикаторных покрытий , Труды Конференции Молодых Ученых ЦАГИ (Жуковский, апрель 1998г.)

INCREASE OF ACCURACY OF PRESSURE SENSITIVE PAINT METHOD BY MEANS OF RADIATION SELF-ILLUMINATION ACCOUNT

A. N. Morozov, P. A. Smirnov

Central Aero-Hydrodynamic Institute, Zhukovsky, 140160, Russia

Summary. In the given work the methods of digital data processing are considered with the purpose of aircraft model surface pressure distribution field obtained with the PSP method accuracy increase. The problem consists in correction of luminescent distribution field in places of aircraft elements interface.

The methods of elimination of illumination from various aircraft surfaces are considered in view of real geometry. For the first time given problem was delivered in [14].

For modelling of self-illumination the mixed model of diffuse-mirror reflection with trace of beams was chosen. Was shown that by selection of the reflecting sublayer characteristics it is possible to reduce mirror component practically to negligibly small values. The check was carried out by means of account both mixed model, and complete diffuse model.

PSP Method.

The technique of measurement of pressure on a surface of aircraft model with the help of pressure sensitive paint (PSP) consists in the following [1-5]. On a surface of model the thin layer puts a PSP, which represents a composition containing binding, for example, polymeric, and luminophor, which luminescence is extinguished by oxygen of air. The model is located in an aerodynamic wind tunnel. At the chosen mode of a flow in an aerodynamic wind tunnel the model surface layer is excited by light, which raises luminescence. Distribution of luminescence intensity on a surface of model is registered, for example, by CCD camera. Then, knowing calibration curves of the characteristic put on a surface of model of a PSP, using the received distribution of luminescence intensity determine required distribution of pressure.

Elimination of self-illumination from various aircraft model Surfaces.

At registration of luminescence intensity sensitive to pressure layer used in a method of a PSP, the increase of intensity is appreciable in the field of aircraft model, where there is an interface of various surfaces under a corner less than approximately135 degrees. It arises that the various surfaces shine each other, and value of light intensity grows with approach to places of interface of elements of a model surface. For the account of the given effect the research on self-illumination modeling was carried out in view of real aircraft geometry with factors received by means of research of properties of a covering on modelling samples of special geometry.

The reflection of the directed beam always is accompanied by scattering, thus the amount of scattered light can make as a share of percent from all reflected flow, and to have the large intensity rather than intensity of the mirror reflected beam. The spatial distribution of reflected and scattered light represents its main feature, which leads to necessity of use of special receptions of self-illumination modeling [6-13].

Intensity and spatial distribution of reflected light strongly depend on conditions of illumination. Distinguish three types of illumination [6] - directed, comletely diffuse and diffuse. The directed illumination gives a source covered with a small corporal corner. The size of a corporal corner should be so small, that the further reduction can result in no change of spatial distribution of the reflected flow, to change of its relation to a falling flow. If indicatrix of radiation of a light source is those, that the brightness of a light source is identical in any directions (inside a corporal corner 2π, such illumination refers to as completely diffuse, or submitted to the Lambert law. The intermediate type of illumination refers to as simply diffuse.

As well as in case of illumination, reflection (scattering) can have three type - diffuse (submitted to the Lambert law), mirror (the corner of fall is equal to a corner of reflection), diffuse-mirror (complex type of reflection from a surface of model, which is possible to model by a superposition of diffuse and mirror reflection (scattering) with weight factors dependent from corners of fall and supervision).

Really PSP consists of a luminescent film and reflecting sublayer allowing to increase luminescent output. Therefore in practice it is necessary to take into account as completely diffuse reflection from a sublayer, and diffuse-mirror from a surface of luminophor film.

In work the scattering indicatrix modeling by polynom of some degree of directive cosines of corners of fall was used and supervision [12] with accumulation of the contributions from each elementary act of reflection. Advantage of the mirror act of reflection is that the mirror reflection is in most cases used on the first iteration, how then mirror component does not get any more on a researched surface. For the first time similar consideration was made in work [14].

The mathematical model describing distribution of an effective luminance on model surface has the following kind:

$$E_{af} = E_{prv} + E_{drop}$$

$$E_{af}\left(P_1^i\right) = E_{prv} + \rho \iint\limits_{\Omega 2} E_{af}\left(P_2^j\right)\varphi_{1-2}\,dS_2^j$$

$$E_{af}\left(P_2^j\right) = E_{prv}\left(P_2^j\right) + \rho \iint\limits_{\Omega 1} E_{af}\left(P_1^i\right)\varphi_{2-1}\,dS_1^i$$

$$E_{af}\left(P_1^i\right) = E_{prv}\left(P_1^i\right) + \rho \iint\limits_{\Omega 2}\left[E_{af}\left(P_2^j\right) - \rho \iint\limits_{\Omega 1} E_{af}\left(P_1^i\right)\varphi_{1-2}\,dS_1^i\right]\varphi_{1-2}\,dS_2^j$$

Where E_{af} - an effective luminance in a point of a surface (luminance, which we register by the CCD camera), E_{prv} - an own luminance of a surface, E_{drop} - a luminance, which arises because of falling radiation dissipating on a surface of model, $\Omega 1, \Omega 2$ - two parts of a surface of test - model, φ_{1-2}, φ_{2-1} - factors tests - models, dependent on geometry.

The analysis of results of researches.

In figures the mathematical models of the image of test - object reflected on three-dimensional model are submitted and the model was designed so that the step of a grid on different planes essentially differed (twice). It has allowed at once to check up in practice a correctness of dimension free modelling, as the three-dimensional grids of real models of flying devices have a various step on different elements of model (fig. 1).

For modeling a self-illumination the mixed model of diffuse-mirror reflection with trace of beams was chosen. Was shown, that by selection of the characteristics of a reflecting sublayer it is possible to reduce to a mirror component practically to negligibly small values (fig. 2). The check was carried out by means of account both mixed model, and model of complete diffuse reflection.

On the basis of the given model the task of elimination of illumination on various surfaces of the aircraft (fig. 3-4) is solved. For this purpose the integrated Fredholm equation of the second kind by a method of iterations with adaptive damping is solved. Damping factor (reduction of a step) varies depending on the received result of approach on each iteration.

The expressions for model of a self-illumination on a aircraft model surface are received in view of its real geometry (fig. 5-7) and the algorithm of use of the given model for elimination of influence of a self-illumination is formulated. The estimations of convergence are received at use of this algorithm.

References

1. Morris M.J., Donovan J.F., Kegelman J.T., Schwab S.D., Levy R.L., Crites R.C. "Aerodynamic Applications of Pressure-Sensitive Paint." AIAA 90-0264, Jan. 1992.,
2. Troyanovsky I., Sadovskii N., Kuzmin M., Mosharov V., Orlov A., Radchenko V., Phonov S. "Set of Luminescence Pressure Sensors-LIPS for Aerospace Research.", 1st European conference on optical chemical sensors and biosensors, Graz, Austria 12-15 April 1992.
3. Bykov A.P., Orlov A.A., Mosharov V.E., Pesetsky V.A., Sorokin A.V., Phonov S.D., Alaty L., Colucci V. "Application of Luminescence Quenching for Pressure Field Measurements on the Model Surface in a Wind Tunnel", conference "Wind Tunnels and Wind Tunnel Testing Techniques", Sauth Hempton, September 1992.
4. Crites R.C., Benne M.E., Morris M.J., Donovan J.F. "Optical Surface Pressure Measurements: Initial Experience in the MCAIR PSTWT",conference "Wind Tunnels and Wind Tunnel Testing Techniques", Sauth Hempton, September 1992.
5. Phonov, V. Mosharov, et al. Optical surface pressure measurement: Accuracy and Application field Evaluation. Proc. 73th AGARD Fluid dynamics Symposium on Wall Interference, Support Interference and Flow Field Measurements. Brussels, October 1993.
6. Топорец А.С. Оптика шероховатой поверхности. – Л.: Машиностроение. 1988.
7. A.Appel. The notion of Quantitative Invisibility and the Machine Rendering of Solids. Proc. of ACM 2nd National Conference, 1967.
8. Bouknight W.J., Kelley K.C. An Algorithm for Producing Halftone Computer Graphice Presentation. SJCC 1970, Montvale, N.Y., AFIPS Press. - P.1
9. H.Gourand Computer Display of Curved Surfaces. Ph.D.Thesis, University of Utah, 6-71.
10. M.E.Nevell, R.G.Newell, T.L.Sancha. A New Approach to the Shaded Picture Problem. Proc. of ACM National Conference, vol.1, Boston, 8-1972.
11. W.Newman, R.F.Sproull. Principles of Interactive Computer Graphics. 2nd edition, McGraw-Hill, N.Y., 1979.
12. Warnock. A Hidden Surface Algorithm for Computer Generated Half-Tone Pictures. TR #4-15, Unievrsity of Utah, 6-1970.
13. B.T.Phong. Illumination for Computer Generated Pictures. CACM, vol.18, #6, 6-1975.
14. W.M.Ruyten, Correcting Luminescent Paint Measurements for Self-Illumination,

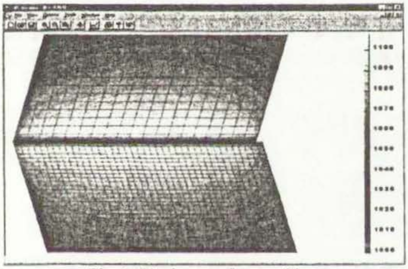

Fig. 1. The image of test - object

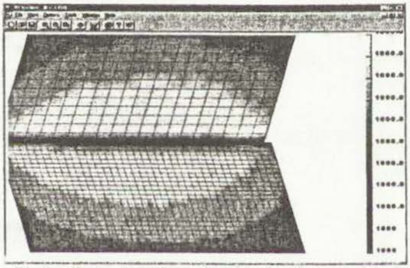

Fig.2. Elimination of an only diffuse self-illumination

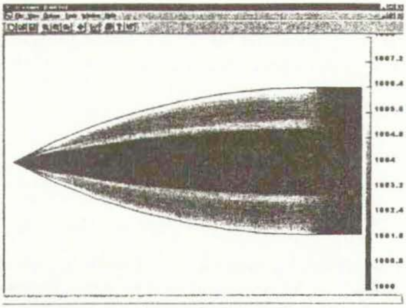

Fig. 3. The image of AIRCRAFT model.
The blue channel

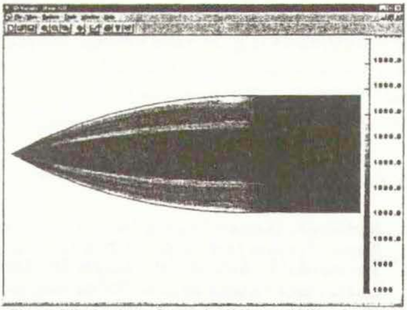

Fig. 4. Elimination of an only diffuse self-illumination.
The blue channel

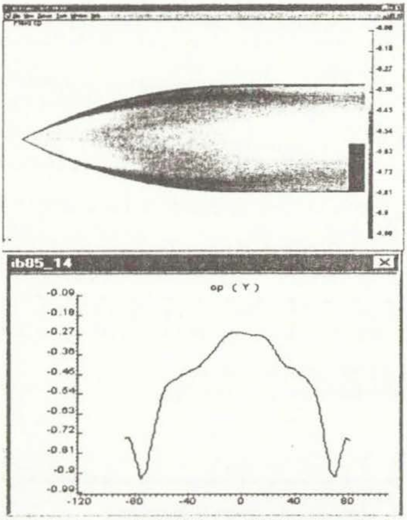

Fig. 5. The image of a field Cp on AIRCRAFT model. The initial image

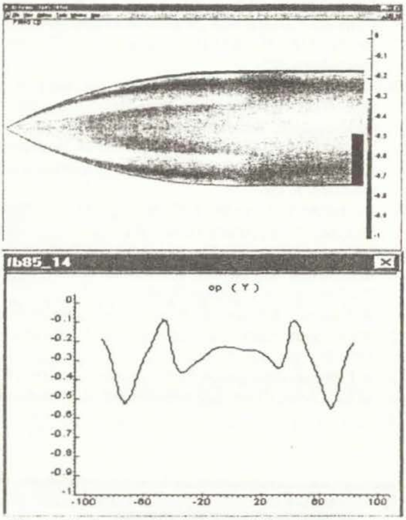

Fig. 6. Elimination of a diffuse self-illumination. A Cp field. Result

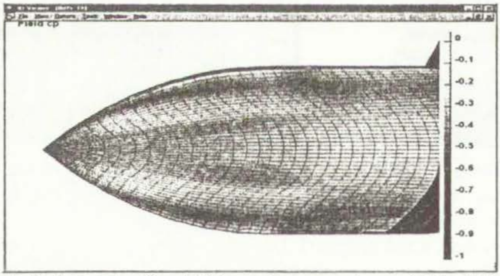

Fig. 7. Real geometry of model (view under a corner to an axis X in 60 deg).

COMPUTER-AIDED SIMULATION FOR INTERACTION BETWEEN PROSTHESIS AND FEMUR

Vladimir Narkevich[*]

[*] Belarusian Academy of Sciences, Institute of Engineering Cybernetics, Surganov 6, 220012 Minsk, Belarus

Summary The attempt to develop a method of the three-dimensional solid geometric bone model reconstruction on the bases of the received CT images is made. The end-to-end design technique hip joint prosthesis and the exploration of the interaction of bone-prosthesis system are proposed.

Presently the development and the improvement of medical prosthesis are impossible without careful study of phenomena that takes place while changing a part of biological objects to mechanical constructions, and consequent evaluation of their ability to work. Therefore, the analysis of the behaviour of prosthesis biological constructions is highly important while designing, producing, and implantation prosthesis to a man.

The workability of the bone-prosthesis system is defined by the level and distribution of the stress in the system, particularly in the contact points of prosthesis elements and bone fabrics. These stresses, caused by external normal and tangent efforts while walking, are the cause of an elastic deformation of a bone and a prosthetic device. As soon as the value of stress' intensity will exceed the allowed, the inconvertible deformation in bone fabrics is to appear, and the destruction of bone-prosthesis system will take place.

According to the above-mentioned information, an urgent problem of optimum prosthesis design arises, in particular, the problems of reconstruction of 3D geometric bone models and the consequent analysis of the durability of bone-prosthesis system.

The aim of a given work is to make an attempt of the development of the system of the end-to-end prosthesis design.

BONE-PROSTHESIS SYSTEM SIMULATION

At traumas of lokomotor system, the patient usually undergoes X-ray examination or CT of the damaged bones. In accordance with this, the ways of the geometric bone models creation are differentiated. The technique of 3D bone models creation according to two roentgenograms is described[1]. In this article a geometric bone models creation based on a preliminary CT.

The CT images represent a set of the parallel cross-sections of bone in the form of raster images. Having such images makes it possible to reconstruct a geometric model of the bone. Presently much sufficiently algorithms for reconstruction the three-dimensional objects exists[2]. All of these by some means or other reconstruct a form of some 3D object, first of all, surface. However, a 3D solid model for following design of the implant should be created.

The modern 3D solid modeling systems have powerful facilities for creation of geometric models by stacking-up parallel cross-sections and defining guidelines (lofting). However, usually it is necessary to present a section in a vector type in order to create these models. Therefore, each CT is to be prepared appropriately for separation of a bone's contour.

For the reason of bone contour separations and its following vectorizations, the editing of a CT image is possible to realize as follows:

It is possible to select distinctive points of bone sections manually on raster images, received from CT, (i.e. this can be done in AutoCAD). Afterwards it is possible to send them to 3D geometric modeling systems (i.e. to SolidWorks) as DXF-files and use them as spline nodes on corresponding sketch of SolidWorks. Then, having built corresponding guidelines, it is possible to reconstruct a geometric bone model. In the offered approach there is no direct vectorization of raster images of the bone sections by means of special programme packages. Vectorization of bone section contour is perfomed by building a spline with nodes in distinctive section points, i.e. right in the CAD-a system (in this case, SolidWorks).

When using this approach, the following difficulties should be noted:

a) sufficiently greater amount of time, requiring for editing;

b) difficulty of separation of distinctive points of section. Hence arising inaccuracy at the spline creation;

c) when building the guidelines, points, not lying on one level, can be chosen on different sections. It might bring a garbling of form geometric models;

The entire scheme of reconstructions bone models on the received CT images is shown below (Fig. 1):

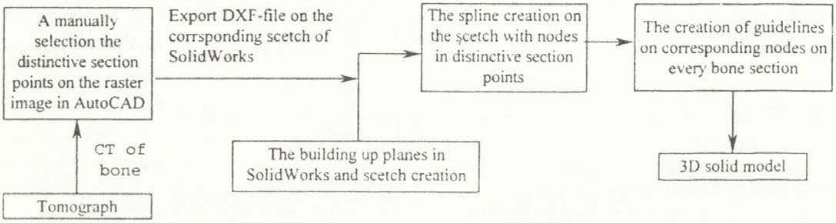

Fig. 1. The scheme of reconstruction 3D solid bone model

FINITE ELEMENT ANALYSIS OF BONE-PROSTHESIS SYSTEM

When a human moves, hip joint feels the most pressure. It is explained by joint's completion of the most important functions, like walking or performing a certain work by a human being. Hip joint loads have a complex structure of forces and moments. Here the body mass, as well as, a type of work, perfomed by a man, are taken into account. Therefore the reconstruction of an exact power scheme and moments, acting in the joint, is practically impossible[3].

To simplify the evaluation of stress distribution in bones simplified models are used, where is expected, the bone is deformed in accordance with the Hooke's law.

The bone construction at the bone-prosthesis system analysis is of important sense. Femur is the most extracted element of human skeleton. Characteristics of bone material are greatly differentiated and depend on bone positions and directions. The bone is heterogenous and anisotropic.

The received geometric model of bone-prosthesis system can be a subject of finite-element analysis, in order to get a dangerous stress and moves to internal and outer face of existing prosthesis distribution. Moreover, this model can define the places of the most concentration of stress and areas, where a performing of constructive changes without particular losses of toughness is possible. This can be done in a CosmosWorks system, which is integrated to SolidWorks.

The received results can be used for improving the construction prosthesis and for provision of more even distribution of the stress in the prosthesis, which will enlarge prosthesis lifetime.

REFERENCES

1. Caponetti L., Fanelli A M.: Computer-aided simulation for bone surgery. *IEEE Copmut. Graph. and Appl.* vol.3, No.6, 1993
2. Higgins W.E., Chung N., Ritman E.L.: LV chamber extraction from 3-D CT images – accuracy and precision. *Comput. Med. Imaging and Graphics.* vol.16, No.1, pp.17-26, 1992.
3. Będziński R.: Biomechanika inżynerska. Oficyna Wydawnicza Politechniki Wrocławskiej, Wrocław 1997.

MORPHOLOGICAL DETECTION AND FEATURE-BASED CLASSIFICATION OF CRACKED REGIONS IN FERRITES

Mariusz Nieniewski[*,****], Leszek Chmielewski[**,****], Adam Jóźwik[***] and Marek Skłodowski[**,****]

[*]Department of Fundamental Research in Electrical Engineering, PAS `www.iel.waw.pl/nbp`
[**]Institute of Fundamental Technological Research, PAS `www.ippt.gov.pl`
[***]Institute of Biocybernetics and Biomedical Engineering, PAS `www.ibib.waw.pl`
[****]Association for Image Processing `www.tpo.org.pl`

Summary Automatic quality inspection of ferrite products is difficult as their surfaces are dark and in many cases covered with traces of grinding. A two-stage vision system for detection and measurement of crack regions was devised. In the first stage the regions with strong evidence for cracks are found using a morphological detector of irregular brightness changes and a morphological reconstruction. In the second stage the feature-based K-nearest neighbor classifier analyzes the pixels indicated in the first stage. The classifier is optimized by using procedures of reclassification and replacement made on the reference pattern set of pixels to achieve low error rate and a maximum speed of computation. The whole system is at a final stage of development and gives acceptable results within a reasonable time.

INTRODUCTION

Automatic quality inspection of ferrite products is a challenging task. The main difficulties in defect detection stem from the fact that the surface of ferrite cores is relatively dark, and in many cases it is covered by a pattern of traces of the grinding, called *grooves*. A two-stage vision system for detection and measurement of crack regions was devised. In the first, detection stage the regions with strong evidence for cracks are detected. The main tool used are morphological operations detecting irregular changes of brightness in the image. Subsequently, a morphological reconstruction of cracks is carried out. By changing the threshold for the binarization of the gray level map of defects one obtains both the marker and the mask necessary for the reconstruction. The resulting reconstucted binary map usually contains most of the cracks together with the undesired information on the grooves. The second stage of the vision system includes a feature-based parallel K-nearest neighbor classifier which analyzes only the pixels detected in the first stage. The detector is fast, but it assigns too many pixels to cracks. The classifier, which is slower, corrects the result. The detector is indispensable for reduction of data for the classifier. Experimental results obtained at the present stage of system development are presented in the end of the paper.

DETECTION OF CRACKS

An example of grooves resulting from the grinding is shown in Fig. 1a. They form a pattern of more or less parallel dark and bright lines, which complicates the detection of cracks. To carry out the morphological operations for crack detection the structuring element should be rotated relative to the image. However, rotation of small structuring elements by an arbitrary angle can only be made in a very rough manner, and it is more practical to rotate the image so that the grooves are parallel to the vertical or horizontal line, with the allowable deviation of 10 to 20°. Fig. 1a shows the rotated image.

Morphological detection of various kinds of defects, such as pull-outs, chips etc. has already been described[1,2], in particular, the detection of cracks on the surface void of grooves[2]. In Table 1 the sequences of operations for detecting the cracks are shown. The first five lines of these sequences, used for detection of defects brighter than the surroundings, are described by the equation[1,2]

$$T = I - \min[(I \bullet S) \circ S, I], \qquad (1)$$

where I is the input image, T the output image and S is the structuring element. The symbols $\bullet$ and $\circ$ denote the operations of closing and opening, respectively. The structuring element in the form of a line segment of length of five pixels was selected experimentally. For detecting (parts of) horizontal cracks the vertical element 1x5s is used, and for vertical cracks the horizontal element 5x1s is used.

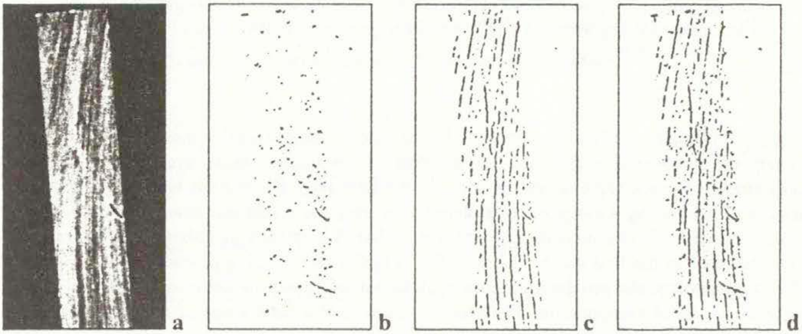

Figure 1. Detection of cracks. a) original; b) result for vertical structuring element; c) result for horizontal structuring element; d) summation of maps of b and c.

The described crack detection results in gray level maps of cracks denoted by d.tif. By thresholding the complemented maps (d.tif) one can obtain the gray level maps indicating the position of cracks. However, using Eq. (1) results in detection of irregular changes of brightness rather than brighter spots in the image, so the exact shape of cracks remains unknown. As shown in Fig. 1, it is quite hard to distinguish between cracks and brighter grooves resulting form grinding. Thresholding the gray level maps of cracks gives gives binary maps containing the masks of both the cracks and the bright grooves resulting from the grinding In order to improve the maps the following approach is used. The gray level maps are thresholded twice: with a low threshold equal equal to 5, and with a higher one equal to 15. The idea is the following. In the binary map dt15.tif the information about the cracks is prevalent since cracks are usually to some degree brighter than the grooves obtained from grinding. However, quite often the difference is not pronounced. By using a relatively high threshold one obtains information on the cracks, but the masks of cracks are relatively incomplete. In order to restore the exact shape of the cracks and only the cracks, the binary reconstruction[2,3] is carried out as shown in the second line from bottom in Table 1. The map dt5.tif is used as a mask, and the map dt15.tif is used as a marker. The result is the map rec5.tif, shown in complemented form rec5i.tif in Figs. 1b, c.

The map in Fig. 1b is in principle satisfactory. The map in Fig. 1c contains the masks of cracks together with the masks of bright grooves resulting from grinding. The classification procedure for removing the masks of the bright grooves is discussed in the next section.

Sequence of operations for detecting horizontal cracks

```
CLOSING input.tif a.tif 1x5s
OPENING a.tif b.tif 1x5s
MINIMUM input.tif b.tif c.tif
SUBTRACTION input.tif c.tif d.tif
COMPLEMENT d.tif di.tif
THRESHOLD d.tif dt5.tif 5
THRESHOLD d.tif dt15.tif 15
RECGRAY dt5.tif dt15.tif rec5.tif
COMPLEMENT rec5.tif rec5i.tif
```

Sequence of operations for detecting vertical cracks

```
CLOSING input.tif a.tif 5x1s
OPENING a.tif b.tif 5x1s
MINIMUM input.tif b.tif c.tif
SUBTRACTION input.tif c.tif d.tif
COMPLEMENT d.tif di.tif
THRESHOLD d.tif dt5.tif 5
THRESHOLD d.tif dt15.tif 15
RECGRAY dt5.tif dt15.tif rec5.tif
COMPLEMENT rec5.tif rec5i.tif
```

Table 1. Sequences of operations for detecting the cracks.

CLASSIFICATION

The second stage of the system system is a *nearest neighbors* classifier[4,5,6]. Feature selection and reduction of the reference set is used. Such reduction is made primarily to increase the speed, however it can also increase the classification accuracy. Here, the parallel net of binary decision k-NN classifiers is used, one for each pair of classes. The final result is obtained by voting carried out between the component classifiers. Each of these classifiers is approximated by a fast 1-NN classifier with the reduced reference set. Classification speed is about 180 pix/s (Pentium 200).

For feature selection and selection of optimum *k*, the *leave-one-out* method is used. The condition of *minimum class overlap rate* is used rather than the most frequently used condition of *minimum classification error*. Then, an approximation of a k-NN classifier by a 1-NN one is obtained by *reclassfication* of the obtained reference set with the (k+1)-NN rule. Finally, the reference set is reduced with the modified[7,8] Hart algorithm[9]. The details will be available in another paper[6].

Each pixel is treated as a pattern. For calculating its features, square and linear neighborhoods in the image domain are used, each rotated around its central pixel to make the edges normal to the locally dominating direction of texture[10]. 64 features were experimentally selected from a large set of statistical and textural measures[8,11] (see[7,8,12]). All the details can be found in technical reports[8,11].

The training set had 1821 pixels (patterns) obtained by manually pointing the pixels in training images. Names of some of the used 15 classes are self-explaining, like *good surface* and *background*. Others correspond to such typical defects of ferrites as *chip*, *pull-out*, and the vital class in the described application: *crack*. The *groove* is another class. Our extensive practice indicated that the classes should be very specific, therefore, some were divided, as *e.g. bright crack* and *dark crack*, so the total number of classes is large, although actually we need only two general classes: *crack* and *no-crack*, into which the specific classes are merged after classification. The necessity of such specificity of classes results directly from that a parallel net of classifiers for pairs of classes as a rule performs better than a single classifier for all the classes. Suppose we have three classes, *A*, *B* and *C*. The choice of optimum parameters can be performed for a classifier for classes *A* and *B*. There is no reason why the patterns from class *C* should influence this choice.

EXAMPLE OF RESULTS AND CONCLUSION

An example of results received for a fragment of image of Fig. 1 has been shown in Fig. 2. It can be noticed that while a large number of false positive errors made by the morphological detector has been successfully removed by the classifier, some of them still remained. Note that some of the classified pixels shown in Fig. 2b and c belonged to the training set (Fig. 2d). Only the class *crack* was represented. However, most of the classified pixels were not used for training.

In conclusion, it can be said that encouraging results have been received at the present stage of research. A larger set of about 4000 training patterns is currently at the preparatory stage. It is expected that with this new set the accuracy of the results will reach the level required by the industry.

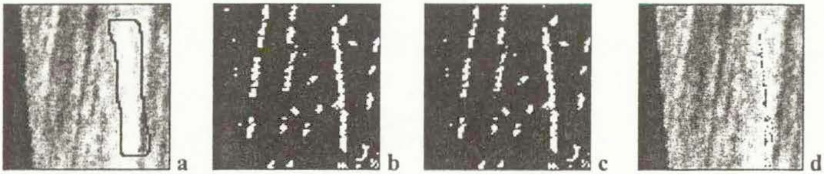

Figure 2. Example of results. a) input image with the crack outlined; b) output from the morphological method; c) fragments of image b rejected by the classifier are indicated by dark gray; d) training pixels present in this fragment, all of class *crack*.

REFERENCES

1. Nieniewski M., Morphological method of detection of defects on the surface of ferrite cores, *Proc. 10th Scandinavian Conf. Image Analysis*, Lappeenranta, Finland, Jun 9-11, 1997, pp 323-330.
2. Nieniewski M., Mathematical Morphology in Image Processing (book in Polish). Akademicka Oficyna Wydawnicza PLJ, Warsaw 1998.
3. Vincent L., Morphological Gray Scale Reconstruction in Image Analysis: Applications and Efficient Algorithms. *IEEE Trans. Image Processing*, 2, 2, pp 583-598, Jun 1991.
4. Jóźwik A.: Object Recognition Method Based on k Nearest Neighbor Rule. *J. of Communications*, **XLV**, Jul-Aug 1994, pp 27-29.
5. Jóźwik A., Chmielewski L., Cudny W., Skłodowski M.: A 1-NN Preclassifier for Fuzzy k-NN Rule. *Proc. 13th Int. Conf. Pattern Recogn.*, Wien, Austria, Aug 25-29, 1996, vol. 4, pp D-234 - D-238.
6. Jóźwik A., Chmielewski L., Skłodowski M., Cudny W.: Class Overlap Rate as a Design Criterion for a Parallel Nearest Neighbour Classifier. Submitted to *Proc. Computer Recognition Systems KOSYR'99*, May 24-27, Trzebieszowice, Poland.
7. Jóźwik A., Chmielewski L., Skłodowski M., Cudny W.: A Parallel Net of (1-NN, k-NN) Classifiers for Optical Inspection of Surface Defects in Ferrites. *Machine Graphics & Vision*, 7, 1-2, 1998, pp 99-112.
8. Mari M., Fontana F., Vernazza G., Chetverikov D., Verestoy J., Lugg M, Postupolski T., Wiśniewska A., Okoniewska E., Jóźwik A., Chmielewski L., Skłodowski M., Nieniewski M., Cudny W., Thang N.C.: Standard compliant QUAlity control System for High-level ceramic material manufacturing – Final Technical Report of the project SQUASH. SQUASH Consortium, Jan 1999.
9. Hart P.E.: The condensed Nearest Neighbor rule. *IEEE Trans. Information Theory*, **IT-14**, 3, May 1968, pp 515-516.
10. Yang G. Z., Burger P., Firmin D. N., Underwood S. R.: Structure Adaptive Anisotropic Filtering for Magnetic Resonance Image Enhancement. *Proc. 6th Int. Conf. CAIP*, Prague, Czech Republic, Sept. 6-8, 1995, pp 384-391. Lecture Notes on Computer Science. Springer Verlag, 1995.
11. Fontana F., Mari M., Chetverikov D., Lugg M., Postupolski T., Jóźwik A., Sklodowski M., Nieniewski M., Cudny W., Chmielewski L., CRAck and SHape defect detection in ferrite cores – Final Technical Report of the project CRASH, CRASH Consortium, Jan 1997.
12. Chmielewski L., Skłodowski M., Cudny W., Nieniewski M., Jóźwik A.: Optical System for Detection and Classification of Surface Defects in Ferrites. *Proc. 3rd Symp. Image Processing Techniques (3TPO)*, Serock, Poland, Oct 29-31, 1997, pp 1-13.

CREATING COLOUR TABLES FOR THE EXPLORATORY DATA ANALYSIS

Sławomir Nikiel
IRIO, Technical University of Zielona Góra, Podgórna 50, 65-246 Zielona Góra

Introduction

The main objective of visualisation is to get more insight into complex data sets. To help make sense of the output data we have consider our visual perception. We need to know the nature of the data and we need tools to make it visible and ready for analysis.

The key is the colour table, which may be defined as a conversion from two-dimensional array of numbers to colour images. This way we can easily generate an image representing millions of data values. This is constantly increasing with the development of data acquisition systems. However, human physiology and psychology of vision reduces perception to only a few dozen grayscale and a few hundred of colour coded data levels (presented simultaneously). The problem is how to choose the colours in order to maximize our insight into the visualised data?

Perception of colours

Colour is a perceptual as well as physical phenomenon[1,2,3,5]. There are a few colour models representing the whole range of spectrum. Red - Green - Blue is derived form the eye physiology and naturally used in hardware displays. Cyan – Magenta – Yellow - blacK is used to prepare images for printing. Hue – Saturation - Brightness is the most natural for human classification of colours. Hue represents visible spectrum, saturation is the admixture of white and brightness describes intensity of colour. Changes in HSB parameters result in different colours. Additionally the parameters' relationship to what is perceived is not linear. The same intensity for yellow looks brighter than for red. There is another problem when we have to define boundary between colours. Unless the colours are „far" from each other the eye averages all the mid-tones.

Creating colour tables

Generally visualisation deals with three procedures: interpretation, segmentation and highlighting. Interpretation depends on matching equal steps in the data to equal steps in perception (e.g. lighter shades represent higher values). Segmentation process is necessary to extract areas of particular interest form the whole bulk of data. Highlighting is used to focus our attention on specific features displayed in the full context of the underlying data. We have to choose proper colour models to meet these tasks and to improve efficiency in creating visualisations.

The most common colour table is a rainbow one, offered perhaps to provide the greatest possible range of colours: the full extent of the visible light spectrum. To avoid wrong interpretation and masking some features of displayed data we have to consider other colour models:

- Monochrome, often grayscale, tables is another standard where brightness levels are analytically proportional to the data values;
- Red-white-blue, purple-white-yellow tables are useful in data sets representing values oscillating around zero, positive-zero-negative;
- Sharp transitions, non-linear colour maps, are used to extract contours or objects of the interesting range of data values;

- Fractal colour tables are an interesting proposition offering features specific to smooth colour models plus visible contours[4]. They are especially useful when we deal with images representing continuous transitions in experimental data values

Figures presented below illustrate how the visualised data (bathymetry) varies with different colour tables.

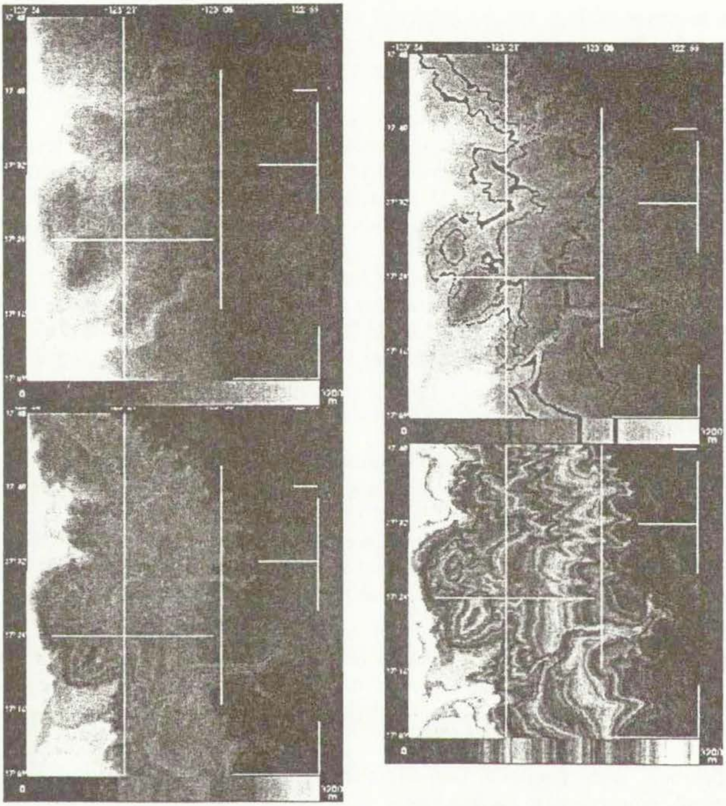

Fig.1 Bathymery images with different colour tables

Literature

[1] B.E. Rogowitz: *„Data visualization: the end of the rainbow"*, IEEE Spectrum, 1998 Vol. 34, No. 12, pg.52-59

[2] *„Is Visualization Struggling under the Myth of Objectivity?"*, Proc. Visualization '95, Atlanta, GA, IEEE Comp. Soc. Press, pp. 412-415 (1995).

[3] B.Fortner, T.E. Meyer: *"Number by Colors: A Guide to Using Colour to Understand Technical Data*", Springer-Verlag (1997).

[4] G. Landini: *"Fractal Anamorphosis:Look Up Table Transforms using Self-Affine Series"*, Computer &Graphics, Vol. 21, No.1, pp. 105-111 (1997).

[5] *„The Psychology of Visualization"*, Proc. Visualization '93, San Jose, CA, IEEE Comp. Soc. Press, pp. 351-354 (1993).

PIV, LIF AND 3D-PIV MEASUREMENTS APPLIED ON THE WAKE BEHIND A SPHERE

J. Nunez v.Voigt, A.Ziemann, H.E.Fiedler
Hermann Föttinger Institut, Technische Universität Berlin, Germany

To analyse the dynamics of coherent structures and the vortex structures themselves, three-dimensional (3-D) measurements are needed.
Compared to the wake of a cylinder, the wake of a sphere is more difficult to investigate due to the complex flow-structures and a strong three-dimensional character of that flow.
PIV (Particle Image Velocimetry) provides a non intrucive method to measure an instantaneous two dimensional velocity field. To investigate the behavior of this flow, this is not sufficient. Hence the idea of a 3-D measurement system is realized with LIF (Laser Induced Fluorescence) and a quasi 3-D-PIV system is tested in the wake of a sphere at Reynolds-numbers ($Re=U*D/\nu$) in the range of 100 to 700 in a vertical water-channel as shown in figure 1.

PIV

For the PIV system a 5 Watt Argon-Ion Laser is used. The laser-beam is focused with two plane-convex lenses and then expanded to a light-sheet with two cylindrical lenses. With the help of the four lenses the light sheet thickness and width can be adjusted. The illuminated test section of our particle seeded vertical water-channel is recorded with an analog 3-CCD (charge-coupled device) Sony video-camera. The sensor resolution is 768x576 pixel. The particles have a diameter of 20μm and a density of 1.02. After the recording the videotapes are digitized with a frame-grabber that supports video time-code. The video-camera records 25 full-frames or 50 half-frames per second. In order to calculate the velocity field a pair of consecutive video-frames is used and the cross-correlation is calculated on 32x32 or 64x64 pixel subimages with the help of the Fast Fourier Transformation (FFT). The time-interval is 2-5 milliseconds at a frame rate of 50 Hz.

Quasi 3-D-PIV

To obtain quasi instantaneous velocity informations of a flow volume it is possible to scan the laser sheet through the test-section and to record the illuminated light-planes at different positions. The volume data consist of 2-D velocity vectors from ten parallel adjacent planes.
A first scan provides the ten first half-images at the ten adjacent positions and a second scan provides the second ten half-images. The cross-correlation between the first and second half-images are calculated. In addition to the optics of the PIV-system described above a mirror is mounted on a stepper-motor which is placed between the convex and cylindrical lenses. The stepper-motor is syncronized to a high resolution video camera (Adimec MX12) and changes the angle of deflection. Since the distance between the mirror and the illuminated region in the water channel is large compared to the small step angle the light plane is almost shifted parallel to the flow axis. The schematic arrangement of the optics is shown in figure 2.

The camera has a resolution of 1024x1024 pixels at full-frame and 1024x512 pixel at single frame operation. The consecutive frames are transferred to PC RAM using a fast frame grabber. The recorded sequence is limited by the RAM of the PC, at 64 MByte of RAM 2 seconds or 100 frames can be recorded. The measured volume is scanned twice for each set of picture pairs. The first scan provides 10 equal-distant frames with a time separation of 20ms. The second scan provides 10 frames at the same location. The time-step between each picture-pair at the same location is 250ms. A test of four consecutive double snapshots of velocity vectors at the same position for Re=100 is shown in figure 3. It is obvious that a stable flow in time is indeed measured. This relatively simple optical and electronic setup provides good results for the relatively low Reynolds-number flow tested in the wake of a sphere.

LIF

With Laser Induced Fluorescenc (LIF) it is possible to obtain informations about the structures in the wake. It is a method to get qualitative visualization for flow diagnostics. A dye solution is introduced into the flow from a thin pipe 50mm above the sphere. The wake is visualized by the luminophor, dinatriumfluoresceen ($Na_2C_{20}H_{10}O_5$) at a concentration of 2*10exp-5 mol/liter (ph = 6.1) which is illuminated in a light sheet by a five Watt Argon-Ion Laser. The light-sheet parallel to the flow is used for normal visualization and a perpendicular light-sheet at different positions behind the sphere is recorded with the Sony video-camera and digitized for flow reconstruction.

LIF - RECONSTRUCTION

From the 2-D LIF image data it is possible to reconstruct a 3-D dataset with the help of a computer. The consecutive planes with illuminated dye are digitized, decomposed in gray-values and reconstructed by joining the points of corresponding gray-levels. Iso-surfaces are then provided by surfaces of equal gray-levels. The quality of the results is very good, yet because of the high Schmidt-number of the flow ($Sc=\nu/D=1000$) it is not exactly possible to deduce the vorticity distribution directly from the gray-level. The program for the reconstruction was written by Blümel (1993).

Two different methods of reconstruction were used. The first is a temporal one, where the light sheet is fixed and the flow passes through the illuminated plane. The second is a spacial reconstruction, where the light sheet is quickly scanned (250 – 500 mm/s) through the flow (3 to 25 mm/s). In this case more information on the vortex structures are possible.

WAKE OF THE SPHERE

The measurement methods described were applied on the wake of the sphere at stationary and starting flows in a water-channel at Reynolds-number from 100 to 700. The vortex structure in the wake are comparable to those found earlier by R.Magarvey, W.Möller and H.Sakamoto. The dynamics and arrangement of these structures depending on the Reynolds-number are found to be somewhat different.

The wake of the sphere is very sensible to the blockage ratio in the channel. Thus, at a blockage of 7% the known phenomena are shifted to higher Reynolds-numbers. A blockage ratio of 1.6% is used in this investigation to describe the arrangement of structures depending on Reynolds-number.

STARTING FLOW

To charactrize the starting flow a dimensionless time $t = t_r*U/D$ is introduced, where U is the channel speed, D the diameter of the sphere and t_r the real time . The reciprocal of the dimensionless time interval Δt between two events is equal to the Strouhal-number $St=f*D/U$.

In the first instance the flow envelops the sphere completely. After some time during, which the boundary layer develops, a ringvortex behind the sphere is formed. In the range of $290<Re<650$ the boundary layer needs t=1.6 to develop the axial-symmetric ringvortex. At t=2.3 the ringvortex is no longer axi-symmetric and the boundary of the ringvortex coils up at t=3.0. Vorticity is transported from the ringvortex into the downstream region and a vortex-loop appears. The vortex-loop has the head downstream, its feet connected to the upper ringvortex. The vortex-loop is detached from the ringvortex at t=5.0, when the boundary layer of the ringvortex coils up again for the next loop. The time interval between two consecutive loops is from Δt=6.25 for Re=420 and Δt= 5.55 for Re=510 corresponding to St= 0.16 and St=0.18. These different Strouhal-numbers are due to the loop length and loop detachment sequence.

STATIONARY FLOW

The loops can detach uniformly to one side or alternatively to both sides. Loops detaching three dimensionally were also observed, however seldom.

For Re<25 the flow is almost symmetric about the sphere. In the range from Re=25 to 250 an axial- symmetric ringvortex is formed. Between Re =290 and 380 the wake is characterised by an oscillating tail of two vortices, intertwined into each other, often appearing as longer vortex loops.

From Re=380 to 510 the loops detach uniformly to one side. From Re= 530 to 650 the loops detach alternatingly to opposite sides. A plane-symmetry can be observed in these two cases. In the range Re= 370 to 410 and Re=510 to 530 the loops detach to different sides where the angles between the plane-symmetry of successive vortex-loops are three dimensional.

The length of the loops is reduced with higher Reynolds-number between Re=340 and 640 with an increasing step between 510 and 530 due to the different form of loop detachment as shown in figure 4.

Another interesting result is the variation of the loop geometry at different Reynolds-number.

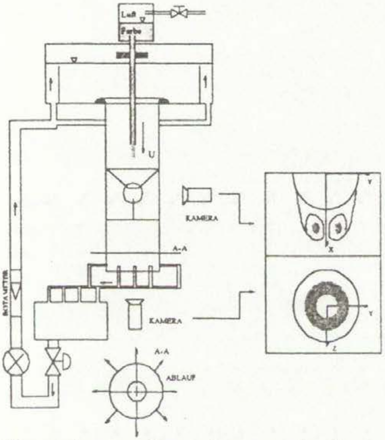

Figure 1: *experimental set up for the investigation on the wake of a sphere with PIV and LIF.*

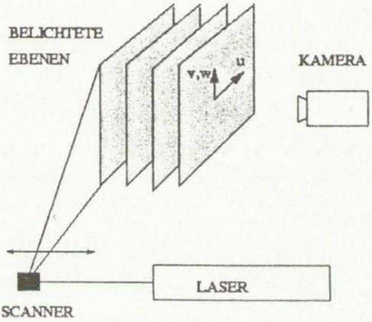

Figure 2: *experimental set up for the 3-D-PIV with a scanning light sheet.*

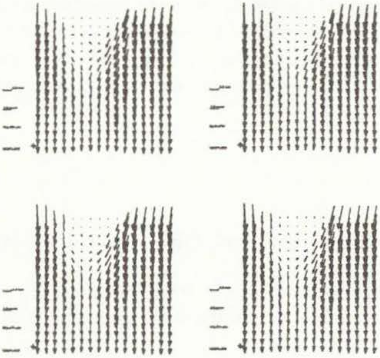

Figure 3: *Four consecutive 2-D-PIV velocity vectors at the same position for Re=100. For the 3-D-PIV a flow with stable vortices in time is measured.*

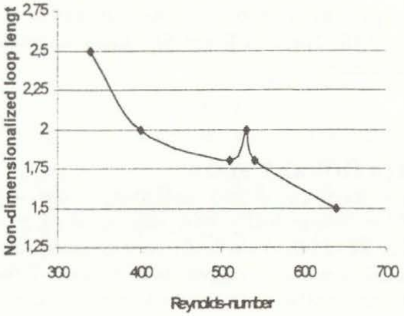

Figure 4: *Non-dimensionalized Loop length versus Reynolds-number.*

NEW ALGORITHMS IN PARTICLE TRACKING VELOCIMETRY

Kazuo Ohmi*, Li Hang Yu* and Shashidhar Ram Joshi*

*Osaka Sangyo University, Department of Information Systems Engineering,
Osaka 574-8530, Japan

Summary New algorithms for the use in particle tracking velocimetry (PTV) have been implemented and tested using several types of particle image in fluid flows. The new algorithms have been introduced in order to improve not only the performance of the particle tracking itself but also that of the individual particles extraction. As regards the particle tracking, the relaxation algorithm is used with some improvement and refinement from the original form. For the extraction of individual particles, there are four algorithms tested in the present work, among which are included two new algorithms: the modified Moravec operator method and the dynamic threshold binarization method.

INTRODUCTION

The PIV or the Particle Image Velocimetry is nowadays a powerful tool for flow measurement and there have been plenty of experimental results using this technique, which are full of whole field velocity and vorticity data. But most of these experiments are concerned with two dimensional measurement and the algorithm adopted in their systems is a FFT or pattern tracking cross correlation method. But since the goal of every PIV fluid experiment is three dimensional flow measurement and the conventional cross correlation PIV is not necessarily suitable for this 3-D measurement, the most promising method would be the PTV or the Particle Tracking Velocimetry, in which the flow velocity is analyzed from the motion of individual particles. What is needed then is a powerful and reliable algorithm for particle tracking as well as that for recognizing individual particles.

PARTICLE TRACKING ALGORITHM

As regards the first point, the present authors have found it the best solution to use the relaxation method[1-2] (especially the improved algorithm by the authors[3]), because it is able to deal better with typical tracking problems in PTV without losing the number of velocity data recorded in the original particle images. When referring to the earlier algorithms of particle tracking, the binary image cross correlation method[4] (BCC) tries to find out the best frame-to-frame link of particles from the cross correlation functions calculated between the interrogation window (in the first image frame) and the object windows (in the second image frame), centered around the reference particle and the candidate particles respectively. But a parallel motion and the rotating and/or shearing motions are not taken into account. The four-frame in-line tracking method[5] (FIT) is capable of tracking the particles even in the rotating and/or shearing flows, because it tries to trace the particle paths over the four sequential image frames while taking into account the geometric consistency of every possible path. But this method is not advantageous from the viewpoint of computing time and acceptable particle distribution density.

The cluster-based particle tracking algorithms, such as the spring model method[6] and the velocity gradient tensor method[7], are also capable of particle tracking in the rotating and/or shearing flows but the problem is the way of defining the clusters. Finally, there are some cost function methods, mostly two frame methods, in which the best particle links are determined as solutions of an optimal value problem. A typical example of this is the genetic algorithm PTV[8], in which the best particle-to-particle links are picked up by the use of a fitness function minimizing the total sum of the squares of particle displacements. The computation process is rather time-consuming but the results are generally satisfactory, if only there are no loss of particle pairs between the two frames.

In comparison to all these earlier algorithms, the relaxation method incorporates the qualities of the first, second and probably the forth types of particle tracking without suffering from disadvantage of any of these three algorithms. The original form of the relaxation algorithm (ORX) was proposed by Barnard & Thompson[1] and was applied to PIV measurement by Lee & Baek[2]. But in this original algorithm, the no match particle probability is defined implicitly, in the form of the remainder of all the positive particle-link probabilities. Obviously, this type of definition does not seem suitable for PIV images, where several percents of particle images are usually lost between frames. Therefore, the authors have proposed an improved algorithm (NRX) with a new explicit definition of the no match probability. The performance of particle tracking by the relaxation method is satisfactory even in the original form[1], but the results of the improved algorithm are furthermore successful. In the present work, the authors try to check the four algorithms for recognizing individual particles. The first one is the single-threshold binarization (STB) method and the second one is the particle mask correlation (PMC) method proposed by Etoh *et al.*,[9]. In the second method, a particle image mask with a 2-D Gaussian intensity distribution is scanned pixel by pixel over the entire target image. In addition to these, the authors are proposing two new algorithms, the first one of which is the Moravec operator (MOR) method and the second one is the dynamic threshold binarization (DTB) method. The first new method uses a modified Moravec operator[10] and is able to detect the particle image centers directly from multi-bit gray scale images. The second one is classified as a variation of variable-threshold binarization methods, but the threshold level is not determined by portion by portion of the original image, but particle by particle according to the mean brightness level of each particle image.

PARTICLE TRACKING AND EXTRACTION RESULTS

The PIV Standard Image #301 (http://www.vsj.or.jp/piv/) is considered for the verification of the four PTV algorithms and it is clearly observed the superiority of NRX, which are shown in Fig. 1.

(a) PIV Standard Image #01 (b) BCC (c) FIT

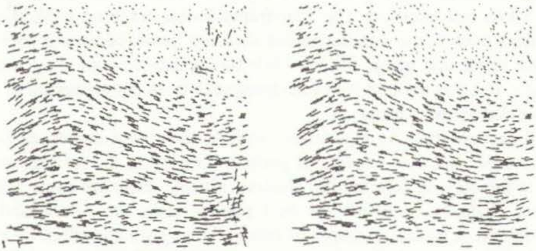

(d) ORX (e) NRX

Fig. 1 PIV Standard Image #01 and results of 4 particle tracking algorithms.

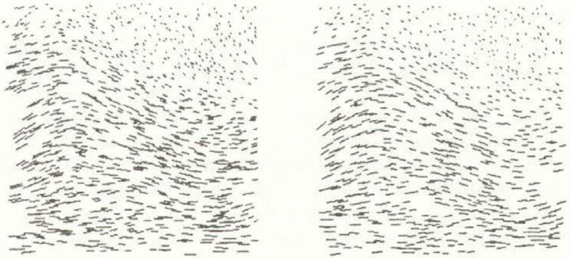

(a) Single-threshold binarization (b) Particle mask correlation + binarization

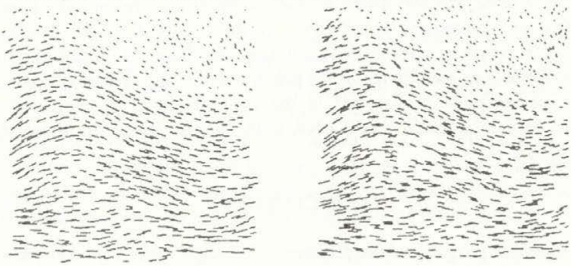

(c) Moravec operator binarization (d) Dynamic threshold binarization

Fig.2 Comparison of the four particle center detection methods with the improved relaxation algorithm for particle tracking (PIV Standard Image #01).

(a) Single-threshold binarization (b) Particle mask correlation + binarization

(c) Moravec operator binarization (d) Dynamic threshold binarization

Fig.3 Comparison of the four particle center detection methods with the improved relaxation algorithm for particle tracking (between spg1500 and spg1502).

The four algorithms for particle centers detection are tested by the use of two types of particle images showing quasi 3-D jet flows. The first test image is the same PIV standard image (#01) as before and the PTV results obtained by the four different algorithms are given in Fig. 2. It is clearly observed here that even the simplest BIN algorithm provides acceptable condition, but other three algorithms PMC, MOR, and DTB can be considered as better algorithms for particle center detection. Among them the DTB shows better reproduction of vectors than the BIN but, as a whole, these two methods show a similar tendency to each other in the balance of vector distribution. The PTV results of the PMC and MOR algorithms are slightly better in balance and very comparative to each other. The second test image originates from the PIV Standard Experiment, one of the latest activities of the PIV Standard Project inaugurated by the Visualization Society of Japan. The comparison is performed for two selected frames from the experimental images in Fig. 3. As earlier, the BIN algorithm falls under the acceptable to good category and the outline of the fluid motion is clearly captured. Due to its excessive sensitivity to random noise, the PMC has demonstrated here very poor performance, which is unacceptable. On the other hand, the MOR algorithm can extract the particle from acceptable to good range, if the preset value of the operator's mask size is properly selected. The best performance is obtained in the case of the DTB compared to all its three counterparts, if the particle extraction is started from slightly lower threshold than the optimal threshold level for BIN.

CONCLUSION

As a result of comparative analysis of the different PTV algorithms, it is convinced again that the relaxation method is nearly the best particle tracking algorithm for current PTV systems. A question arises then as to which type of particle detection algorithm should be selected. If it is necessary to select only one algorithm from the four tests in the present work, the dynamic threshold binarization algorithm would be the most almighty one in spite the long computation time required for its recursive calculation. More precisely, this DTB algorithm is more suitably applicable to relatively low-density particle images. The PMC algorithm is at the best if applied to high-density particle images. The Moravec operator gives rise to good to acceptable PIV results for any of the present test images, but if this mask size is not properly determined, the resultant detection of particle centers may include many errors. This operator is usually best applicable to such a case where the distribution of the particles is quite even and so is the geometry of the captured particle image. Needless to say, the single-threshold binarization scheme is the least satisfactory method of particle image detection.

REFERENCES

1. Barnard,S.T., Thompson,W.B.: Disparity analysis of images, *IEEE Trans on Pattern Analysis and Machine Intelligence*, Vol.2, No.4, p.333, 1980.
2. Lee,S.J., Baek,S.J.: Two-frame PIV and its application to a turbulent channel flow, *Proc. PIV-Fukui '95*, p.217, 1995.
3. Ohmi,K., Dao Hai Lam: New particle tracking PIV using an improved relaxation method, *Proc. 8th Int. Symp. on Flow Visualization*, #209, 1998.
4. Uemura,T., Yamamoto,F., Ohmi,K.: High speed algorithm of image analysis for real time measurement of two dimensional velocity distribution, *ASME Winter Annual Meeting FED*, Vol.8, p.121. 1989.
5. Kobayashi,T., Saga,T., Segawa,S.: Multipoint velocity measurement for unsteady flow field by digital image processing, *Flow Visualization V*, p.197, 1989.
6. Okamoto,K., Schmidl,W.D., Hassan,Y.A.: Least force technique for the particle tracking algorithm, *Flow Visualization VII*, p.647, 1995.
7. Ishikawa,M., Yamamoto,F., Murai,Y., Iguchi,M., Wada,A.: A novel PIV algorithm using velocity gradient tensor, *Proc. PIV-Fukui '97*, p.51, 1997.
8. Ohyama,R., Takagi,T., Tsukiji,T., Nakanishi,A., Kaneko,K.: Particle tracking technique and velocity measurement of visualized flow fields by means of genetic algorithm, *J. Visualization Soc. Japan (in Japanese)*, Vol.13-S1, p.35, 1993.
9 . Etoh,T., Takehara,K.: The particle mask correlation method, *Proc. 8th Int. Symp. on Flow Visualization*, #283, 1998.
10. Moravec,H.P.: Towards automatic visual obstacle avoidance, *Proc. 5th Int. Conf. Artificial Int.*, p.584, 1977.

APPLICATION OF MOIRÉ INTERFEROMETRY FOR MODEL DEFORMATION MEASUREMENTS IN LARGE SCALE WIND TUNNELS

D. Pallek*, P.H. Baumann**, K.A. Bütefisch*, J. Kompenhans*

*DLR, Institute of Fluid Mechanics, Bunsenstr. 10, D-37073 Göttingen
**Basler AG, An der Strusbek 60-62, D-22926 Ahrensburg

Summary

A non-intrusive Moiré interferometry system has been designed to acquire the instantaneous deformation of models during wind tunnel testing. The resulting interferograms are evaluated without manual intervention using a technique based on the Fourier Transform. The system has been installed in the cryogenic European Transonic Wind Tunnel (ETW). The deformation of a model wing (generic model of a transport aircraft with a full span of 1.60 m) has been measured. In a second experiment, the bending angle of a flap of a hypersonic vehicle was measured in order to determine the hinge moment due to aerodynamic loads. The experiment was carried out in the Transonic Wind Tunnel Göttingen (TWG).

Introduction

As it has been formerly described [1], the movements, deformations and vibrations of a model in a wind tunnel due to aerodynamic load can be precisely determined by Moiré interferometry without disturbing the flow.

The present paper describes two Moiré systems for large scale wind tunnels, and one application of each system is presented.

Measurement technique

Moiré interferometry uses the interference of periodic patterns to measure the topology of a given surface [2][3]. Its principle is described in Fig. 1:

A ruling is projected onto a plane surface S_1, and the image of the stripes is focused onto a reference ruling. The stripes of the imaged and the reference rulings are parallel to each other, and superimpose to a interferogram. If the surface is then translated to location S_2, the stripes on the surface move in the x-direction, and a projection ray indicated in Fig 1 shifts on the surface from P to P′. P′ in turn is now focused onto R′, thus producing an interference pattern with a different intensity.

A translation of the surface in the x- or y-direction does not lead to a shift of the ruling focused onto the surface, and so does not influence the interferogram. The technique is therefore only sensitive to translations in z-direction.

If the observed surface is curved, the resulting fringes in the interferogram represent lines of equal elevation. This implies that large surface gradients lead to large fringe frequencies in the interferogram. So by using Fourier Transform the topology of the surface can be evaluated.

Furthermore, if the surface is deformed or shifted in z-direction, the change of the z-coordinates of the surface can be calculated by comparing the actual interferograms.

Deformation measurement of a model wing

The DLR Moiré interferometry system described here has been installed in the cryogenic European Transonic Wind Tunnel (ETW) in Köln. It determines the instantaneous deformations and movements of models during wind tunnel testing.

The ETW has a test section of 2.4 x 2 m and runs from Ma = 0.15 to 1.3. Temperature varies from 90 to 313 K, and pressure from 1.25 to 4.5 bars. As a test, the deformation of the right wing (DLR F4 profile) of the ETW generic model of a transport aircraft with a full span of 1.6 m was measured. Due to the swept back configuration of the wings, they do not only bend, but also twist under aerodynamic load.

The observation area of the Moiré interferometer (Fig. 2) is about 0.60 x 0.45 m at an observation distance from 0.9 to 1.1 m. The resolution is 0.2 mm for bending (z-direction) and 0.1^o for twist.

The interferometer presented here differs from a conventional Moiré system, as the image of the projection pattern is directly projected on the pixel matrix of the observation camera, without using a reference ruling. The interference pattern is then produced digitally by evaluating every second line of the video picture.

Fig. 3 shows the averaged results for wing bending and twist along the span for different angles of incidence. As the model vibrates during testing, ten individual measurements were averaged. Also the mean values α of measured twist and bending inwards from the kink (at y = 280 mm) of the wing were subtracted for comparison.

Measurement of hinge moment

The hinge moment of a flap on the wing of a hypersonic vehicle (HYTEX, see Fig. 4) was measured in the Transonic Wind Tunnel Göttingen (TWG). The flap was attached to the model via flexible hinges, so the flap angle would change due to aerodynamic load. To check for accuracy, comparison data was obtained simultaneously using strain gauges.

The interferometer was inclined by 7^o, just as the model was, to align the apparatus to be perpendicular to the model axis. The observation distance was 650 mm, and the resolution in z-direction (viewing direction) was 0.05 mm.

For both the no-wind and the on-wind conditions, the momentary angle of incidence of the flap was computed using two-dimensional linear regression from the 6500 data points of the flap surface. By subtracting the angle of attack α of the model from the change in flap angle β, the flap bending angle $\Delta\beta$ was derived. The results for different Mach numbers are shown in Fig. 5, compared to the measurements obtained by the strain gauges.

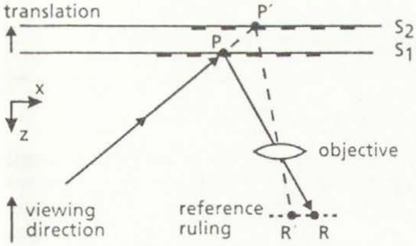

Figure 1: Moiré measurement model for the acquisition of deformations in viewing direction

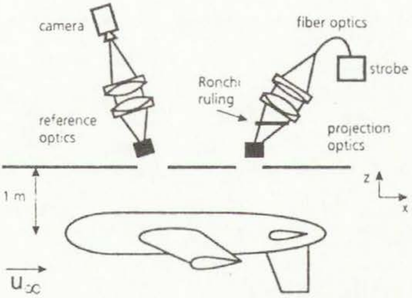

Figure 2: Setup of the Moiré optics in the European Transonic Wind Tunnel (ETW)

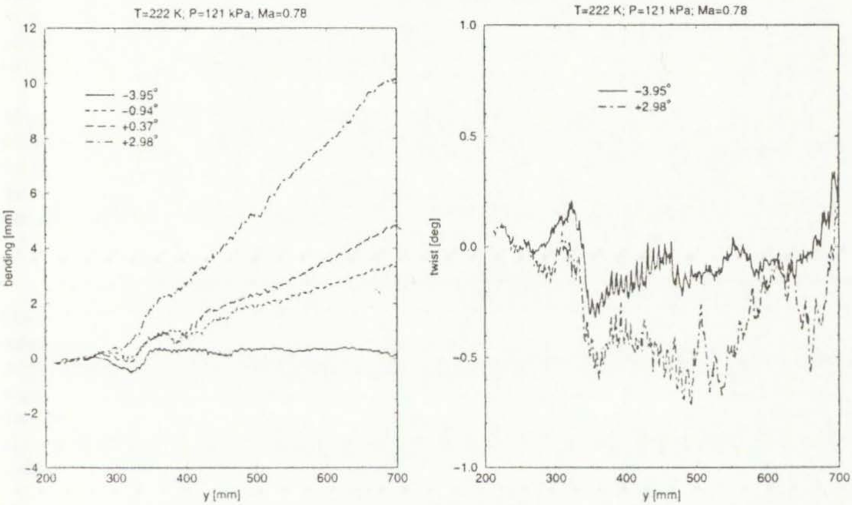

Figure 3: Measured average wing bending and twist for different angles α of attack

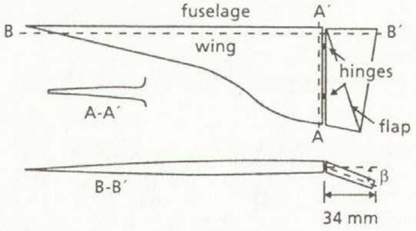

Figure 4: Sketch of wing and flap of the HYTEX model

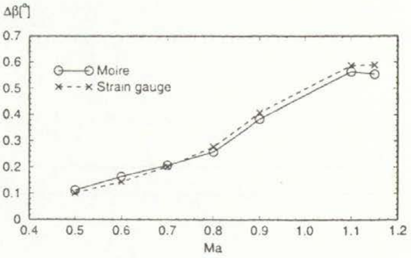

Figure 5: Change in flap angle due to aerodynamic load

References

[1] P.H. Baumann and K.A. Bütefisch: Measurement of hinge moments and model deformations in wind tunnels by means of Moiré interferometry, *SPIE* **2546**, pp 16-32, 1997

[2] H. Grauer-Carstensen: Eine Meßeinrichtung zur Erfassung der Verformung eines Modells im Windkanal, *DFVLR-AVA* Bericht Nr. 251 78 G 02, 1978

[3] O. Kafri and I. Glatt: The Physics of Moiré Metrology, John Wiley & Sons, New York, 1978

USING LIQUID CRYSTALS FOR ANALYZING THERMOFLUIDDYNAMICAL PROCESSES IN LIQUIDS DURING PRESSURIZATION

Michael Pehl, Franz Werner, and Antonio Delgado
Technical University of Munich, Institute of Fluid Mechanics and Process Automation
Weihenstephaner Steig 23, D-85350 Freising, Germany

Summary In this study thermochromic liquid crystals (TLC) have been used to visualize temperature and velocity fields in pressurized water up to 700 MPa. The change of the reflected wavelength of the used TLCs due to pressure is inverse to the effect of temperature. Hence, the detectable temperature range shifts to a higher temperature level as pressure increases. The colour play keeps reversible and a good temperature resolution is achievable. In order to predict applicative TLCs for high pressure investigations a simple empirical relation between the start temperature at normal pressure and the slope of the isochromes in the pressure-temperature plane was found. Furthermore, experiments have been performed for analyzing the pressure induced convection in the high pressure cell.

INTRODUCTION

Processes under high pressure occur in many fields of nature and technology such as geology, oceanic biology, mechanical and chemical engineering, and high pressure treatment of foods (up to 1000 MPa). The last named research field is a promising technology, but basic understanding of physico-chemical and thermofluiddynamical processes under high pressure are needed for future advancement. Inhomogeneities of temperature and convection in the biotechnical substances have to be taken into consideration, because they may effect processes of heat and mass transfer decisively.

At normal pressure the liquid crystal measuring technique is well known and described in literature whereas only few investigations have been performed with TLCs at higher pressures[1,2]. As a result of the found pressure sensitivity of TLCs they were suggested to be used as pressure sensors. The aim of the present study is to investigate the feasibility and efficiency of the TLC measuring technique for the simultaneous detection of temperature and velocity fields in liquids at high pressure.

MATERIALS AND METHODS

Seven different types of TLCs obtained from the manufacturer Hallcrest (UK) have been tested. In order to achieve the required temperature response this manufacturer mixes 8 or more components of chiral nematic liquid crystals in the correct proportions. The start temperatures t_{SR} (temperature at the beginning of red colour) of the used TLCs are in the range of –30 to +60 and the bandwidths b_{RB} (temperture difference corresponding to start of red and blue colour) range between 0.7 and 10 K. The TLC-particles (∅ ≈ 10 to 15 μm) are encapsulated in a mixture of gum arabic and gelatin. These encapsulated particles were dispersed in distilled water and pressurized afterwards.

The investigations have been performed by means of a high pressure optical cell (2 ml) which is equipped with four sapphire windows (∅ = 6 mm). The cell is all-round surrounded by a tempering bath and the maximum operating pressure amounts 700 MPa. The temperature of the compressed liquid is measured by a thermocouple in the optical cell. Right angled to the incident lightsheet the field is recorded by a fixed 3-chip RGB-camera, as illustrated in Figure 1. Temperature and velocity fields were videotaped and estimated by eye. It has been shown[3] that an image analyzing system is an adequate means for the simultaneous evaluation of temperature and velocity fields and will be adapted therefore at present.

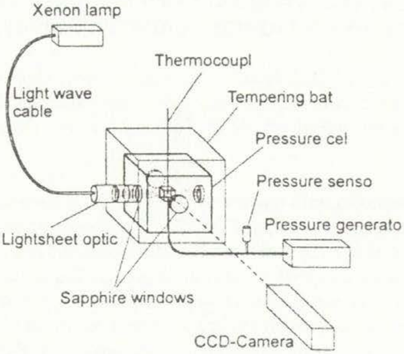

Figure 1. Arrangement of the experimental setup

RESULTS AND DISCUSSION

In accordance with previous findings[1, 2] for most TLCs, results have shown that the change of reflected wavelength of tested TLCs due to pressure is inverse to the effect of temperature. This can be seen from Figure 2 which shows the calibration curve of a TLC with t_{SR} = 10 °C and b_{RB} = 1 K. The data have been taken after reaching a thermal equilibrium at constant pressure. For all narrow bandwidth TLCs a linear pressure-temperature relation with slope m for the isochromes has been found in good approximation. In case of wider bandwidths (b_{RB} = 5 to 10 K) the estimation of colours becomes more difficult due to subjective valuation by eye.

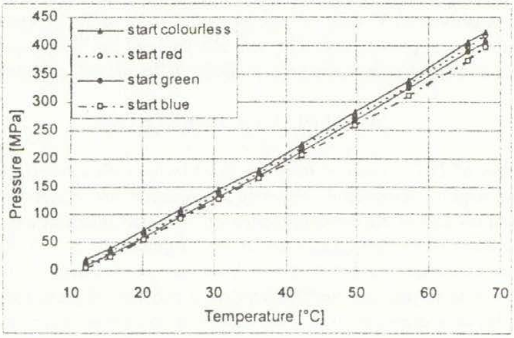

Figure 2. Isochromes in the diagram of temperature vs. pressure

The temperature resolution diminishes with pressure as recognizable by a slight enlargement of the bandwidth, see Figure 2. At 700 MPa an enlargement-factor of about 2.5 has been estimated. Using TLCs with a normal pressure bandwidth of 0.7 K a temperature resolution of about 0.6 K can be achieved at 700 MPa.

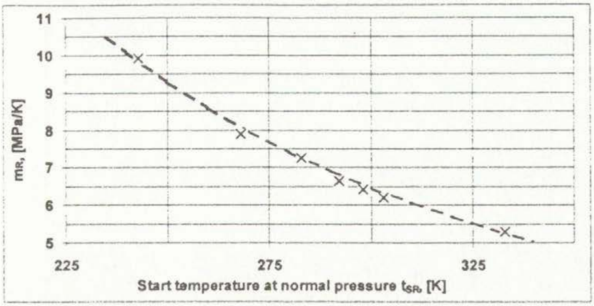

Figure 3. Slope m_R of the red isochromes in the p-t plane vs. start temperature t_{SR} at normal pressure

By comparing the calibration curves of TLCs with different start temperatures the following relation has been found: the slope of the isochromes diminishes as the start temperature increases. This is shown in Figure 3 for the red isochromes. The dotted line marks the slope m_R of the red isochrome after the empirical equation

$$m_R = 581000 \cdot t_{SR}^{-2}.$$

This relation is of importance for the selection of suitable TLCs for the detection of a certain temperature range at given pressure.

During the experiments a pressure induced convection has been observed. The flow is composed of forced convection due to mass flux into the cell and of thermal convection which was indicated by the reflected colours from the TLCs. The starting point of measuring the decay time of velocity was set after pressurization. The experiments have resulted in an exponential law of velocity decrease in time. For reasons of comparability the reaching of the limiting velocity of 0.01 mm/s has been chosen as definition of the decay time t_d. Additionally, data of decay time have been calculated after the equation

$$t_d = c \cdot \frac{l^2}{\nu} .$$

The inner diameter of the optical cell (14 mm) is the characteristic length l and ν the kinematic viscosity of water at the regarded pressure and temperature in the optical cell. The physically reasonable (in the order of one) constant $c = 1.15$ has been determined from experimental data.

In Figure 4 the decay times of the total convection at different temperatures are shown, whereby calculated data (o, •) are compared with measured data (x, ▲). Taking into account that the measured data have been estimated by eye, only small differences between measured and calculated data have been found. An effect of the pressurizing rate is not noticeable. This can be explained by the increasing damping for larger pressurizing rates. In contrast to this, the decay time is obviously larger, if the temperature at the beginning of pressurization is higher. This was expected, because the kinematic viscosity decreases with increasing temperature also at high pressure.

Though the above equation is based on fluid dynamical dimension analysis reasonable decay times can be calculated. The above mentioned constant c comprises forced and thermal convection. The estimation of both the rates of forced and thermal convection are subject of future investigations.

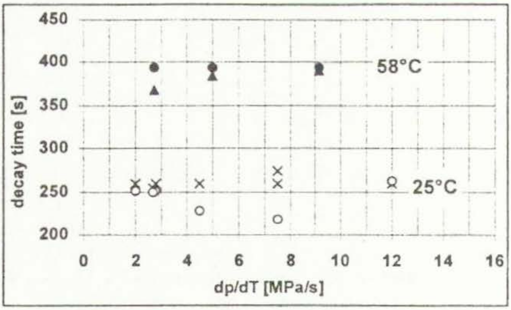

Figure 4. Decay time of the convection after pressurizing at 25 and 58°C

CONCLUSION

It has been shown that the liquid crystal measuring technique is an adequate means to visualize temperature and velocity fields in pressurized liquids. Also at high pressure a good temperature resolution has been found. A model for choosing applicative TLCs is suggested based on experimental data. Furthermore, by means of this technique pressure induced convection in liquids has been detected and analyzed. The decay time of the composed thermal and forced convection has been quantified.

REFERENCES

1. Pollmann P., Wiege B.: Helix Inversion of Cholesteric Liquid Crystals at High Pressure. Selective Light Reflection Measurements on Binary Mixtures up to 3000 Bar and 130°C. *Mol. Cryst. Liq. Cryst.* **150b**, pp 375-386, 1987.
2. Dabrowski R., Wolinski T.R., Brodzik M., Dziaduszek J., Jarmolik A., Bock W.J., Klosowicz S.: Polar Systems with Induced A_d Phase and Selective Reflection for High Pressure Sensing. *Mol. Cryst. Liq. Cryst.* **263**, pp 607-621, 1995.
3. Koch S.: Berührungslose Messung von Temperatur und Geschwindigkeit in freier Konvektion. *PhD Thesis*, Institut für Angewandte Mechanik und Strömungsphysik, Universität Göttingen, 1992.
4. Pehl M., Delgado A.: An In-Situ Technique to Visualize Temperature and Velocity Fields in Liquid Biotechnical Substances at High Pressure. *Proceedings of High Pressure Bioscience&Biotechnology*, Heidelberg, August 1998.

PROSPECTS OF X-RAY MICROTOMOGRAPHY FOR STUDIES OF COMPOSITE MATERIALS

Ryszard Pyrz
Institute of Mechanical Engineering, Aalborg University
Pontoppidanstraede 101, 9220 Aalborg East, Denmark

Summary The ability to make precise X-ray attenuation measurements on a very small volume elements is a developing technology. This technology is known as X-ray microtomography to delineate the method as a form of X-ray microscopy that uses tomographic reconstruction techniques to build three-dimensional images of microstructure. Since the morphological data of a microstructure are usually collected from plane cross sections taken through an opaque material then this necessary step results in a great loss of information regarding spatial features of the dispersion. In order to overcome this difficulty X-ray microtomography is applied to extract the 3-D information that may be used for micromechanical modelling purposes.

INTRODUCTION

The physical properties of a material are strongly influenced by the microstructure which is designed during processing. Amount of constituent elements forming the material is in many cases known beforehand as for example the volume fraction of reinforcing phase in composite materials. However, the final archtecture of a microstructure is controlled only to a limited extend, and on the microscale the geometrical arrangement of second-phase inclusions is a result of complex and interacting processing micromechanisms rather than a design variable. This seems to create an obstacle in modelling the relation between microstructure and overall material properties.

In order to overcome this difficulty it is usually assumed that the geometrical features of a microstructure are randomly distributed without any precise explanation of what randomness means and how it can be quatified. On the other extreme lies the assumption that the dispersion of fillers is regular. It significantly simplifies calculations, especially with the finite element method, and provides satisfactory results as far as highly nonlinear phenomena are not concerned. For strongly localized effects such as initiation of microcracks and plastic zones which subsequently propagate at different scale lengths, the regularity assumption may lead to seriously erroneous results. Therefore, it is important to describe dispersion characteristics of the microstructure in an unambiguous way by quantitative factors which eventually could be related to physical properties of the material.

When we examine the microstructure of a material we are looking at a very small sample of the structure. From this limited view we have tried to understand how the properties of the material relate to microstructure. The approach must necessarily be statistical in particular with respect to the measurements of the microstructure. A selection of representative volume elements where we seek to find microstructure-property relations must be based upon sound sampling techniques. Furthermore, the investigation of three-dimensional microstructures is possible in most cases only on the internal surfaces generated by taking planar sections for microscopy. This necessary step from spatial microstructures to their planar sections involves a great loss of information.

X-RAY MICROTOMOGRAPHY

Developments of X-ray microscopy and computer tomography provide a new tool for the assessment of materials morphology. A common problem in morphological analysis is that three-dimensional information on microstructure is required, but its images are two-dimensional. In X-ray microtomography, the object is rotated so as to obtain radiographic projections from different viewing angles. An enlarged radiograph of the object is recorded by an X-ray sensitive camera after the object has been traversed by the conical X-ray beam. All these projections are used in a reconstruction algorithm which calculates a set of serial non-destructive sections where the interpretation of the image, i.e. cross section, can be done in terms of attenuation of the X-rays in the object. Then, a three-dimensional image of the specimen can be reconstructed from serial sections and can be processed to show and measure three-dimensional features.

X-ray microscopy is a relatively new technique that has not been applied to any significant extent in materials science. Most X-ray microscope development has so far been made using large synchrotron sources.This has limited X-ray microscopy to a research tool available only at the major synchrotron facilities. The use of X-ray tubes with a very small focus and an energy in the order of 20-100keV together with a very sensitive recording devices enable the design of a bench-top X-ray microscope with a spatial resolution less than 8 micrometers.

ANALYSIS

In the present context we are concerned with a well defined shape of the inclusions such as spherical particles and continuous fibres. The following question arises if we attempt to characterize the distribution of centre points of fibres in unidirectional composites recorded on the transverse sections or the centre points of spherical particles' traces in particulate composites: "What is the shape of a set of points and how it can be quantified.

The distribution is neither regular nor random in a strict sense of the word. On the other hand it is generally recognized that dispersion pattern of fillers strongly influences the mechanical properties of composites and, in particular, causes extreme fluctuations of local stresses that may exceed a microfailure threshold. Hence, relevant data concerning classification of the inclusions distribution, i.e. as to whether it is random, non-random, clustered or any other is necessary. The characterization of complex aspects of disorder is performed using the idea of fractal dimension: a dimension that corresponds in a unique fashion to the geometrical entity under study and often is not an integer.

It is shown that the fractal dimension of unidirectional fibres loaded in a transverse direction is related to the interfacial radial stresses and that this relation is changing depending upon fibres waviness. For the particulate composite a correlation map has been established between particles' diameters and corresponding diameters of traces. In both situations the non-destructive,three-dimensional reconstruction of the composite microstructure has been an indispensable element of the analysis.

PERFORMANCE EVALUATION OF AN OPTICAL FLOW TECHNIQUE FOR PARTICLE IMAGE VELOCIMETRY

Georges M. QUÉNOT

CLIPS-IMAG, 385, rue de la Bibliothèque, B.P. 53, 38041 Grenoble Cedex 9, France

Summary This paper presents a quantitative performance evaluation of an Optical Flow technique on the test data of the PIV-STD group of the Visualization Society of Japan. Near the optimal conditions for the method, the accuracy (average velocity error divided by the average velocity module) is below 2 % and it is below 4 % in all other cases except for very high and very low in-plane velocities.

INTRODUCTION

The experimental fluid mechanics technique of Particle Image Velocimetry (PIV) has proven to be a valuable method for quantitative, two-dimensional flow structure evaluation[1]. It enables the measurement of the instantaneous in-plane velocity vector field within a planar section of the flow field. Nowadays, almost all PIV is done by computer image processing on digital images[2] and most methods are based on image intercorrelation. Optical Flow techniques[3-4], conventionally developed for detecting motion of large objects in a real world scene, were also recently successfully applied to the PIV problem[5]. The objective of the present study is to better characterize the performance of the optical flow technique for PIV and how it is influenced by experimental parameters (particle density and size, in-plane and out-of-plane velocities). For convenience and easy comparison of results, a standard PIV test set was used[6].

OPTICAL FLOW FOR PIV

Many techniques have been developed for the computation of optical flow. Not all of these are well suited for the DPIV problem. Many require long image sequences that are not easily obtainable experimentally and/or do not perform very well on the particle image texture (especially multi-resolution methods). The technique that was chosen for the PIV application was introduced as the Orthogonal Dynamic Programming (ODP) algorithm for optical flow detection from a pair of images[3]. It has been extended to be able to operate on longer sequences of images and to search for subpixel displacements[4]. The ODP based PIV will be referred to as ODP-PIV. The technique cannot be detailed here but it is fully explained in [5]; it can be related to classical intercorrelation techniques but with the following differences:

- Basic matching is searched on elastic image strips (either horizontal or vertical) instead of being searched on rigid blocks, and strip matching is performed using Dynamic Programming which enforces continuity and regularity constraints.
- A global, dense, continuous and coherent image matching is iteratively updated and refined using alternatively horizontal and vertical strip matchings and by reducing the strips' width and spacing along with the iterations.

THE VSJ PIV-STD PROJECT

A research group (PIV-STD) organized by the Visualization Society of Japan (VSJ) has developped standard image test sets for quantitative performance evaluation and comparison of PIV systems[6]. They are distributed via internet (`http://www.vsj.or.jp/piv/`) and publicly available. The site offers "standard" image sequences for 2D and 3D flows and a program able to generate custom image sequences with several independently tunable parameters (particle size, particle density, average in-plane velocity and average out-of-plane velocity). Results are presented here using standard and custom sequences.

RESULTS ON STANDARD IMAGES

The first standard image sequence (s01) is a "typical" case defined by the following parameters : $N = 4000$ (number of particles), $T = 33$ ms (time interval, defining the scale of the in-plane velocity), $v = 7.39$ pixel/interval (in-plane velocity), $L = 20.0$ mm (light sheet thickness, defining the scale of the out-of-plane velocity), $w = 0.017$ -/interval (out-of-plane velocity, fraction of the particles leaving and entering the light sheet per interval), $P_a = 5.0$ pixel (average particle diameter) and $P_d = 1.4$ pixel (standard deviation of particle diameter). The seven following standard image sequence (s02 to s08) differ from the typical case by only one parameter. The images are 256 × 256 pixels representing an actual 100 mm × 100 mm area. The ratio between the in-plane and out-of-plane average velocities is of about 0.12 (defining a 2D flow). Figure 1 shows one image of the first sequence and the used velocity field.

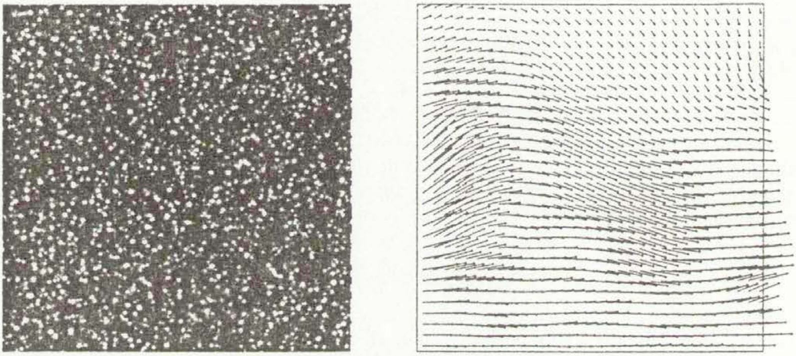

Figure 1: One particle image and the correct velocity field

Table 1 displays the parameter set used for the eight standard sequences as well as the accuracy results for the ODP-PIV method using repsectively two, three and four images. ODP-PIV control parameters are tuned differently for low and high out of plane velocity (s08 sequence). Accuracy results are displayed in percentage as mean error ± standard deviation of error, the error being the relative error (absolute error in pixel/interval divided by the average in-plane velocity also in pixel/interval).

As it will be seen in the next section, the typical case parameters are not optimal for the ODP-PIV method (they are probably tuned for Particle Tracking methods) for the particle density (at least 2.5 times too small) and size (twice too big). However, the default in-plane velocity

No.	N	T	v	L	w	P_a	P_d	2 images	3 images	4 images
s01	4000	33	7.39	20.0	0.017	5.0	1.4	3.52±2.91	3.29±2.74	3.21±2.66
s02	4000	**100**	22.4	20.0	0.053	5.0	1.4	10.8±11.7	10.2±10.2	10.2±10.5
s03	4000	**10**	2.24	20.0	0.005	5.0	1.4	9.82±5.14	9.74±5.00	9.75±4.96
s04	**10000**	33	7.39	20.0	0.017	5.0	1.4	1.97±2.67	1.45±1.82	1.33±1.53
s05	**1000**	33	7.39	20.0	0.017	5.0	1.4	3.53±3.42	2.68±3.14	2.33±2.98
s06	4000	33	7.39	20.0	0.017	5.0	**0.0**	2.30±4.13	1.50±1.57	1.33±1.41
s07	4000	33	7.39	20.0	0.017	**10.**	4.0	2.93±4.51	2.23±2.95	2.08±2.89
s08	4000	33	7.39	**2.0**	0.176	5.0	1.4	7.79±13.0	5.05±4.57	3.90±3.82

Table 1: Results on standard images

scale is near the optimum and the out-of-plane velocity has negligeable effect (except for the s08 sequence).

The accuracy for the typical case (s01) is below 4 % for the three variants. Severe accuracy degradation occurs when the average in-plane velocity is far (3 times smaller or larger, s02 and s03) from the optimum one. Increasing the particle density (s04) highly improves the accuracy while decreasing again the particle density (s05) does not further degrade the accuracy. Reducing the particle diameter standard deviation improves the accuracy (s06) as well as incresing the particle diameter (s07, however this is linked to the insufficient particle density). Finally, high out-of-plane velocity (s08, 17 % of particle appearance and disappearance per interval) significantly degrades the accuracy. However, even in this case, using the four images, we still get an accuracy of about 4 %. Near the optimal particle density (s04), the accuracy is as good as 2 % using only two images and below 1.5 % using the four images.

RESULTS ON CUSTOM-MADE IMAGES

Custom image sequences were generated using the version 2 of the custom made standard image program in order to evaluate the effect of the various tunable parametrs. These image sequences are also publicly available from the VSJ server from: `http://www.vsj.or.jp/piv/java/tmp2/-<No.>/index.html`. The `<No.>` field is to be replaced by the corresponding test set number indicated below.

Tables 2, 3 and 4 respectively the effect of the variation of the particle density, the particle size and the average in-plane velocity on the accuracy. In all image sequences the light sheet thickness has been set so that the same rate of particle appearance and disappearance (5 %, about three times the one of the standard images) is used for all image sequences. The image parameters and the accuracy results are displayed exactly in the same way as for standard images.

No.	N	T	v	L	w	P_a	P_d	2 images	3 images	4 images
100	6000	30	6.66	6.42	0.050	2.0	1.0	2.85±2.44	2.25±2.17	1.97±1.76
101	8000	30	6.66	6.42	0.050	3.0	1.0	2.51±2.68	1.93±2.54	1.67±1.79
102	10000	30	6.66	6.42	0.050	3.0	1.0	2.36±2.27	1.80±1.78	1.63±1.75

Table 2: Results on custom images, variation with particle density

The optimal number of particles is 10000 (one particle by 6.4 square pixels density), which is the maximum allowed by the sequence generation program. However, it is estimated from the data that the optimal density without that limitation would be about the same. The optimal

No.	N	T	v	L	w	P_a	P_d	2 images	3 images	4 images
106	10000	30	6.66	6.42	0.050	1.0	0.6	3.32±3.40	2.43±1.89	2.15±1.51
105	10000	30	6.66	6.42	0.050	2.0	1.0	2.46±2.57	1.96±2.01	1.77±1.71
107	10000	30	6.66	6.42	0.050	2.5	1.0	2.34±2.00	1.74±1.42	1.54±1.29
102	10000	30	6.66	6.42	0.050	3.0	1.0	2.36±2.27	1.80±1.78	1.63±1.75
103	10000	30	6.66	6.42	0.050	4.0	1.5	2.48±2.34	1.88±1.59	1.68±1.47
104	10000	30	6.66	6.42	0.050	5.0	2.0	2.88±3.93	2.14±2.18	1.87±1.80

Table 3: Results on custom images, variation with particle size

No.	N	T	v	L	w	P_a	P_d	2 images	3 images	4 images
111	10000	25	5.55	5.35	0.050	2.5	1.0	2.51±1.97	2.07±1.75	1.89±1.64
107	10000	30	6.66	6.42	0.050	2.5	1.0	2.34±2.00	1.74±1.42	1.54±1.29
112	10000	35	7.77	7.49	0.050	2.5	1.0	2.29±2.36	1.71±1.61	1.57±1.62
108	10000	40	8.88	8.56	0.050	2.5	1.0	2.16±3.50	1.76±2.79	1.53±2.49
113	10000	45	9.99	9.63	0.050	2.5	1.0	2.20±4.29	1.79±3.97	1.61±3.05
114	10000	50	11.1	10.7	0.050	2.5	1.0	2.63±7.45	1.89±4.90	1.68±4.58

Table 4: Results on custom images, variation with average in-plane velocity

particle diameter is around 2.5-3.0 pixel. The optimal average in-plane velocity is of about 8-9 pixel/interval. This last value may change for higher relative out-of-plane velocities (w, a value of 0.05 is used here).

In the neighborhood of the optimal parameters, the accuracy is always better than 3 % using only 2 images and better than 2 % using four images. These results might degrade if noise is added (no noise model is implemented in the standard image generator) but it has been shown using another test set that the method is rather robust to noise[5].

CONCLUSION

This study has confirmed that Optical Flow based on the use of Dynamic Programming is a very efficient technique for PIV. Under controlled and optimal conditions (particle density, size and in-plane velocity) the average relative accuracy of the velocity for the whole image can be as good as 2 % and still below 4 % for a wide range of conditions around the optimal ones.

Further investigations will be conducted in order to also quantify the effects of noise, higher out-of-plane components and three-dimensional flow structures.

REFERENCES

1. Hesselink L.: Digital Image Processing in Flow Visualization, *Ann. Rev. Fluid Mech.*, Vol. 20, pp. 421-485, 1988.

2. Willert C. E., Gharib M.: Digital particle image velocimetry, *Experiments in fluids*, Vol 10, pp. 181-193, 1991.

3. Quénot G.M.: The "orthogonal algorithm" for optical flow detection using dynamic programming, *Intl. Conf. on Acoustics, Speech and Signal Proc.*, pp. 249-52, San Francisco CA, 23-26 mar. 1992

4. Quénot G.M.: Computation of Optical Flow Using Dynamic Programming, *IAPR Workshop on Machine Vision Applications*, pp. 249-52, Tokyo, Japan, 12-14 nov. 1996.

5. Quénot G.M., Pakleza J., Kowalewski T.A.: Particle Image Velocimetry with Optical Flow, *Experiments in fluids*, Vol. 25, No. 3, pp. 177-189, 1998.

6. Okamoto K., Nishio S., Kobayashi T., Saga T.: Standard Images for Particle Image Velocimetry, *Proc. of the Second Inter. Workshop on PIV*, Fukui, Japan, pp. 229-236, 1997.

PARTICLE RESUSPENSION CHARACTERISATION BY OPTICAL METHODS

Alecsandra Rambert*, Laurent Huber** and Pierre Gougat*
*LIMSI-CNRS, B.P. 133 ,91403 Orsay FRANCE
** Laboratoire de Bioclimatologie , INRA, 78850 Plaisir-Grignon, FRANCE

Abstract The removal of small particles from the surfaces is important in a wide range of disciplines in which there is concern regarding the loss of particles from a surface, or contamination of fluids. Source mechanisms for particles are complex because the removal of particles from a surface involves an interaction of forces including fluid drag and lift and adhesion of particles to the surface.

Particle resuspension from a surface by a fluid flow has been examined experimentally by observing the intermittent particle resuspension process using optical methods. The particle concentration was computed using image processing and the particle velocity during resuspension was measured by PIV.

INTODUCTION

The resuspension rate, defined as the ratio between the number of resuspended particles by unit surface and unit time, is the main parameter that characterises the resuspension process. Ziskind and al[1] made an exhaustive review of resuspension models and experimental techniques which were developed for small particles (diameter greater than 5 μm and smaller than 50 μm). The experimental techniques developed to characterise resuspension are difficult to employ (particle counting under microscope) and they are not able to describe the characteristic time scale of the resuspension phenomena (<1s). In this study we propose a new technique based on image processing to quantify the particle resuspension process.

PARTICLE CONCENTRATION MEASUREMENT

To compute particle resuspension rate, we have developed an optical technique for the measurement of particle surface concentration, based on image processing [Kheyar[2]]. Images of particles deposited on the surface are recorded by a CCD camera (484×786 pixels). The analysis of the light intensity histogram of the CCD matrix, permitted to obtain binary images (''0'' for the fluid and ''1'' for the particles) and sampled them in N×N blocks. The optical method is based on a counting process. The particle surface concentration, Cs, is calculated for each block as the ratio of the images containing particles: Cs=Nt/(N×N), where Nt is the number of illuminated pixels. A linear relationship between the surface concentration and the volume concentration can be deduced considering the particle size and the laser sheet dimension. The program developed to compute particle concentration was tested with artificial images generated at different concentrations.

EXPERIMENTAL DEVICE

The removal particle experiments were conducted in a wind tunnel for a wind velocity profile corresponding to a laminar (U∞=1.27 m/s) and a turbulent boundary layer (U∞=5 m/s). Particles chosen for resuspension were Lycopodium spores which have monodisperse size (diameter is about 30 μm) and adhesion forces which permitted resuspension within the range of velocities possible in the wind tunnel. The particles were deposited as singlets on a glass cover using a settling tower and then placed flush with the floor of the wind tunnel working section.

The fraction remaining on the surface was determined by monitoring the number of particles on a surface over time (30 minutes).

EXPERIMENTAL RESULTS

The velocity profile in the bondary layer mesured by hot wire just before the particle deposit are presented in the Figures 1a for a laminar bondary layer and in Figure 1b for a turbulent one.

Observations based on the image processing showed that the total number of Lycopodium particles did not decrease during the flow under laminar conditions. However, the position of some particles changed during the runs.

In Figure 2 we presented a time series of particles images during resuspension under turbulent boundary layer conditions. In general, more particles are resuspended in the first minutes. Real-time observations using image processing show that several particles may be resuspended nearly simoultaneously in brief episodes, interspersed with periods of no apparent resuspension. In Figure 3 , the average fraction of particles remaining on the surface is plotted versus the exposure time.

In the first moments of the removal process, we have recorded images of particles on the surface and then processed them by PIV technique in order to obtain some information about the particle velocity during resuspension. The velocity field which was obtained in these conditions is presented in Figure 4. The particle velocity during resuspension is an important parameter in a particle transport model.

CONCLUSION

Wind tunnel experiments were conducted to study particle resuspension. Resuspension was characterised by the variation over time of the fraction of particles remaining on the surface. In order to measure this parameter, an optical technique based on image processing was developed.

The fraction of particles removed as a function of time was found to be governed by two regimes, the first occurring in the first minutes of the experimental trial and the second in the remainder of the trial. Theses results have to be compared with numerical results which were obtained using a model of resuspension based on a force balance model and a vortex interaction with a boundary layer (Rambert[3]).

REFERENCES

1. Ziskind, G, Fichman, M. and Gutfinger C.: Resuspension of particulates from surfaces to turbulent flows-review and analysis, J. Aerosol Sci., vol 26, no4, pp613-644, 1995.
2 Kheyar N.: "Etude d'écoulements par méthode PIV", Thèse de l'Université Paris XI, 1997.
3. Rambert, A. "Etude de l'interaction particules-écoulement" Thèse ParisXI 1998.

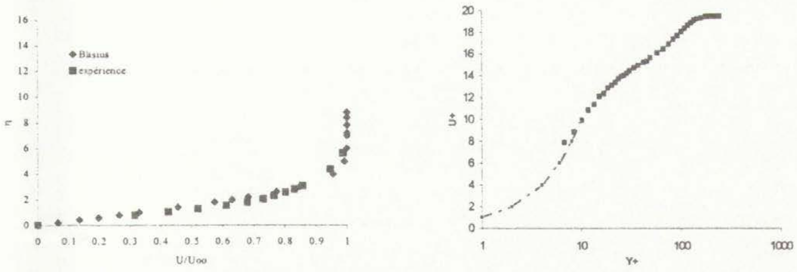

Figure 1a

Figure 1b

Figure 1: Boundary layer velocity profile: (1a) laminar boundary layer U_∞=1.27 m/s and (1b) turbulent boundary layer U_∞=5 m/s

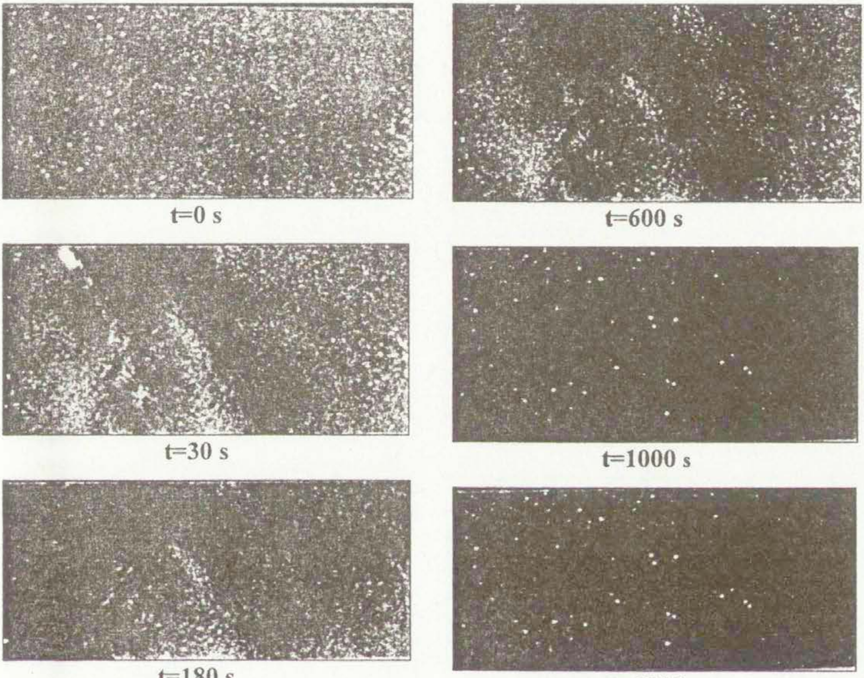

t=0 s

t=600 s

t=30 s

t=1000 s

t=180 s

t=1800

Figure 2: Evolution over time of particle resuspension process for a wind speed of 5 m/s

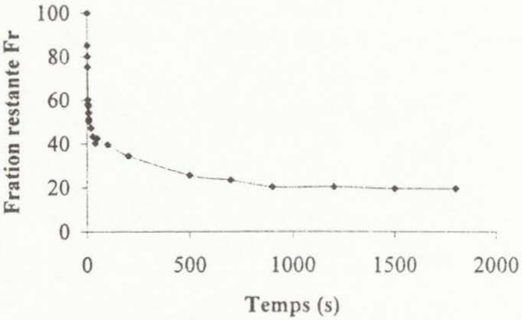

Figure 3 The average fraction of particles remaining on the surface at a wind speed of 5 m/s

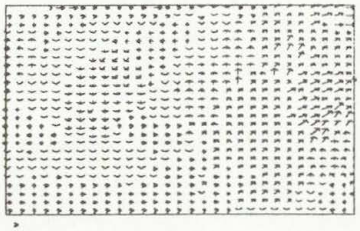

Figure 4: Instantaneous velocity field of particles during resuspension

USING CONTINUUM MECHANICS OPERATORS FOR DETECTION AND QUANTIFICATION OF EVOLVING PROCESSES IN 3D MEDICAL IMAGES

David Rey, Hervé Delingette, Gérard Subsol, and Nicholas Ayache
EPIDAURE Project, INRIA
2004, route des Lucioles. B.P. 93
06902 SOPHIA ANTIPOLIS Cedex. FRANCE

Summary Physicians often perform diagnoses based on the evolution of lesions, tumours or anatomical structures over time. The objective of this paper is to describe several vector field operators to detect regions with local variations between two 3D images. These operators are applied to displacement fields obtained after a non-rigid registration between successive 3D temporal images. We used continuum mechanics theory to develop operators which aim at emphasizing the deformations between several temporal states.

PRESENTATION OF THE PROBLEM

Medical motivations

The measure of the evolutions in temporal series of the 3D medical images of a patient is very helpful for a medical diagnosis. The evolution of processes over time concerns many different medical fields: cancerology, neurology (Alzheimer's disease, epilepsy, Multiple Sclerosis, etc.), pharmacology, surgery, etc. For example in this paper, we show the detection of Multiple Sclerosis lesions using MRI data.

Currently, physicians use visual methods to detect and quantify the evolutions between several time acquisitions. But these methods are not reproducible, not very accurate, and very tedious. In this paper we present several tools based on the continuum mechanics theory that make it possible to detect and quantify evolving processes between two 3D images.

Computation of a displacement field

Between two examinations, a patient does not have the same position in the acquisition device. Therefore images at different times are not directly comparable. We have to apply a transformation to each image to compensate for the difference in position (translation) and orientation (rotation). Then we can compare the two images, and apply automatic computerized tools to detect and quantify evolving processes.

The subtraction between two successive images to find areas where the lesions have changed is not sufficient because it is extremely dependent on the registration process and because it does not give information with respect to the amplitude of each evolution[1]. Therefore, our idea is to replace a voxel by voxel comparison with a study of the apparent motion between two images. We compute this displacement field with a non-rigid registration algorithm which diffuses an image towards another one (an example of the resulting field is given in Figure 1).

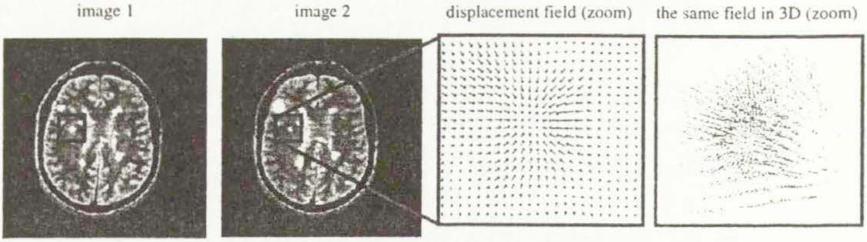

Figure 1. *Slices of two rigidly registered images and of the projection of the 3D apparent displacement field on a region of interest. On the right, a 3D view of a small area of the field.*

Then each point $P = (x,y,z)^T$ of the reference image has a vector $\mathbf{u}(u_1(P),\ u_2(P),\ u_3(P))$ which gives its apparent **displacement** towards the second image. We can define the **deformation** which is the function $\Phi(\Phi_1(P),\ \Phi_2(P),\ \Phi_3(P))$ that transforms $P = (x,y,z)^T$ onto $P' = (x',y',z')^T$. Therefore we have:

$$x' = x + u_1(x,\ y,\ z) = \Phi_1(x,\ y,\ z)$$

$$y' = y + u_2(x,\ y,\ z) = \Phi_2(x,\ y,\ z)$$

$$z' = z + u_3(x,\ y,\ z) = \Phi_3(x,\ y,\ z)$$

Since we want to analyze the deformations between images, we use the framework of continuum mechanics to develop appropriate vector field operators. In particular, the operators aim at emphasizing large or particular deformations.

A symmetric approach

In fact, several problems occur due to the discretization of the vector field. If there is a large expansion, the direct displacement field cannot express that one voxel should deform towards several voxels. Due to limited resolution of the image, we would need to define a one-to-many mapping. By combining the direct and reverse displacement fields we obtain a better description of the motion between the two images (Figure 2).

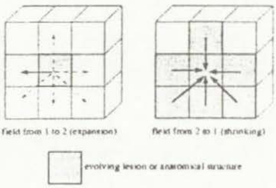

Figure 2. *The displacement field information is more relevant when we consider ``shrinking" voxels of direct and reverse fields. If there is a large expansion, the direct displacement field cannot express that one voxel should deform towards several voxels. Due to limited resolution of the image, we would need to define a one-to-many mapping. By combining the direct and reverse field we obtain a better description of the motion.*

3D VECTOR FIELD OPERATORS

Notations

In the following $C = I + \nabla u + (\nabla u)^T + (\nabla u)^T(\nabla u) = (\nabla\Phi)^T(\nabla\Phi)$ is the Right Cauchy-Green strain tensor, and $E = ½(C - I) = ½[\nabla u + (\nabla u)^T + (\nabla u)^T(\nabla u)]$ is the Green-St. Venant strain tensor. These matrices are real and symmetric and therefore their eigenvalues are real numbers. We note $c_1<c_2<c_3$ the eigenvalues of C and $e_1<e_2<e_3$ the eigenvalues of E.

Vectorial filter

We have implemented a vectorial filter which gives at each voxel the eigenvector (of C or E) corresponding to the largest eigenvalue at this point. Thus we obtain a filtered vector field which does not take into account the smallest components of the deformation. First results with this filter are encouraging because they visually emphasize the center of some lesions (Figure 3).

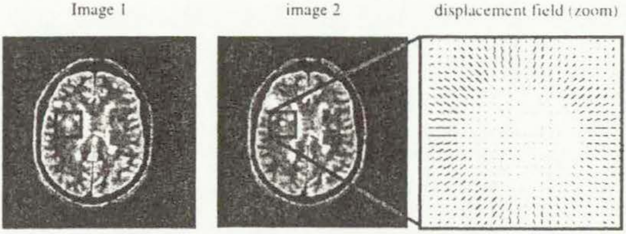

Figure 3. *Slices of two rigidly registered images in 3D and the projection of the 3D associated filtered vector field on a region of interest, to be compared with Figure 1.*

Scalar operator

As the vector field is very complex to analyze directly, we apply differential operators to transform a 3D vector field in a simpler representation which is a 3D scalar image. This scalar image should be contrasted with respect to the time evolutions. Moreover we need to introduce operators which have a physical meaning for a better interpretation. First of all we can compute a shear value at each point P with the extremal eigenvalues of C or E. Therefore, we have $shear_C = c_1/c_3$ or $shear_E = e_1/e_3$. Moreover the product of the eigenvalues of C expresses a local variation of volume: we can compute the Jacobian of the deformation[2] $Jac(\Phi) = det(\nabla\Phi) = [det(\nabla\Phi)^T(\nabla\Phi)]^{1/2} = [det(C)]^{1/2}$ with $det(C) = c_1c_2c_3$. This result is verified by comparing this method with a direct discrete computation of the local volume variation[3]. Finally, we can compute a deformation energy, assuming that we have an elastic, homogeneous, and isotropic matter; we use the St. Venant-Kirchhoff model: $W = (\lambda/2)(tr\ E)^2 + \mu.tr(E^2)$ where λ and μ are the Lamé constants of the considered tissue[4]. We have not found physical values of these constants for the brain matter, and we have chosen two values which give good results but do not have a clear physical meaning: $\lambda=0.5$ and $\mu=0$. Figure 4 shows the application of these three operators on the same displacement field. For Multiple Sclerosis applications we have principally worked with the Jacobian operator which gives a contrasted image and has a simple meaning.

Figure 4. *Comparison between different existing operators.*

Results

We can notice that our operators are theoretically robust with respect to rigid misregistration because E and C are representative of the pure deformation without translation and rotation. An example of segmentation based on thresholding the scalar value of the Jacobian ($Jac<0.3$) is given on Figure 5. More details can be found in a previously published paper[1]. We plan to find a more realistic model of the physical behaviour of the brain with appropriate values of the brain tissue constants to study the deformations between images.

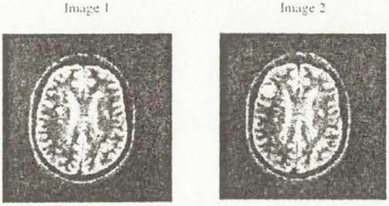

Figure 5. *By thresholding operator outputs, we can segment evolving lesions in 3D.*

ACKNOWLEDGEMENT

We would like to thank Charles Guttman and Ron Kikinis, Brigham and Women's Hospital, and Harvard Medical School, Boston USA, who provided us with Multiple Sclerosis images time series.

REFERENCES

1. D. Rey, G. Subsol, H. Delingette, and N. Ayache. Automatic detection and segmentation of evolving processes in 3D medical images: application to Multiple Sclerosis. Research Report 3559, INRIA, November 1998. Electronic version: http://www.inria.fr/RRRT/RR-3559.html.

2. C. Davatzikos, M. Vaillant, S.M. Resnick, J.L. Prince, S. Letovsky, and R.N. Bryan. A Computerized Approach for Morphological Analysis of the Corpus Callosum. *Journal of Computer Assisted Tomography*, 20:88-97, January 96. Electronic version: http://ditzel.rad.jhu.edu/~hristos/html/christos_bio.html

3. S. Prima, J.P. Thirion, G. Subsol, and N. Roberts. Automatic Analysis of Normal Brain Dissymmetry of Males and Females in MR Images. In W.M. Wells, A. Colchester, and S. Delp, editors, *First International Conference on Medical Image Computing and Computer-Assisted Intervention, MICCAI'98*, volume 1496 of *Lecture Notes in Computer Science*, Springer, pages 770-779, Boston, USA, October 1998.

4. Bro-Nielsen. *Medical Image Registration and Surgery Simulation*. PhD thesis, IMM, July 1997. Electronic version: http://www.imm.dtu.dk/documents/users/bro/phd.html

COMBINATORIAL 3-D SEQUENCING THEORY AND METHODS IN APPLIED MECHANICS

V. V. Riznyk[*]

Academy of Technology and Agriculture, Al. S.Kaliskiego 7, 85-796 Bydgoszcz, Poland

Summary. Combinatorial 3-D Sequencing Theory, namely the concept of three-dimensional Ideal Ring Bundles (3D-IRB)s, can be used for finding optimal solutions for wide classes of problems in applied mechanics. 3D-IRBs are cyclic sequences of integer 3D-vectors, which form perfect 3D-partitions of a finite 3D-space of vectors. The vector sums of connected sub-sequences of 3-D IRB enumerate the set of integer 3D-vectors exactly k-times. This property makes 3-D IRBs useful in applications, which need to partition sets with the smallest possible number of intersections.

Combinatorial theory as well as innovative combinatorial techniques is known to be of great important for finding optimal solutions for wide classes of problems in applied mechanics. For example, finite-field theory [1] and appropriate technique, based on wide-aperture interferometric synthesis in which a telescope aperture is equipped with non-redundant masks or sets of opening, is well applicable [2]. Some regular methods for constructing non-redundant two-dimensional (2-D) n-elements masks over $n \times n$ grids, based on special combinatorial structures known as difference sets [3] are suggested in the publication [2]. Applications of modern algebraic theory and combinatorial analysis obtain a lot of problems of signal design for radar, sonar, and data communications [4]. However, the classical theory of combinatorial configurations, namely the difference sets, finite projective geometry, or general block designs theory [1] can hardly be expected effective for solving 3-dimensional problems using methods, based on the theory. Therefore, both an advanced theory and regular method for finding optimal solutions these problems are needed.

In this paper general principles and ideas of three-dimensional (3-D) Ideal Ring Bundles, constructed on cyclic groups in extensions of Galois fields are presented. Research into the underlying combinatorial principles relate to the optimal placement of structural elements in spatially/temporally distributed 3-D systems or processes using IRB algebra and techniques, based on "perfect distribution phenomenon" and the idea of "perfect" 3-D combinatorial constructions. This design techniques will make it possible to configure 3-D systems with non-uniform structure (e.g. 3-D antenna arrays or non-redundant aperture mask systems) with fewer elements than at

---

[*] *On leave from* Lviv Polytechnic State University, 12 S. Bandera Street, 290646 Lviv, Ukraine

present, while maintaining or improving on resolving ability and the other significant operating characteristics of the system. It is shown that the construction of the optimal 3-D system can be reduced to a similar one-dimensional problem [5,6].

Let us consider an n-stage chain sequence of elements $C= \{K_1, K_2, \ldots K_i \ldots, K_n\}$ as being cyclic, so that K_n is following by K_1, and we require all terms in each sum to be consecutive elements of the sequence. A sum of consecutive terms in the ring sequence can be have any of the n terms as its starting points, and can be of any length (number of terms) from 1 to $n - 1$. In addition, there is the sum of all n terms, which is the same independent of the starting point. Hence, the maximum number of distinct sums S of consecutive terms of the ring sequence is given by

$$S = n\,(n - 1) + 1 \qquad (1)$$

An n-stage ring sequence $C= \{K_1, K_2, \ldots K_i, \ldots, K_n\}$ of terms $K_i = \{k_1, k_2, k_3\}_i$ for which the set of all circular 3-D sums of the consecutive terms (sums is calculated, its own modulo m_j, j=1,2,3) enumerate a set of 3- stage integers, which form 3-D grid, each node of the grid meets exactly k-times, is named "Three-dimensional Ideal Ring Bundle" (3D-IRB). So, any 3D-IRB can be described by parameters n, k and sizes $M_1 \times M_2 \times M_3$ of the 3-D grids.

General formulas for representation of 3-D IRB with underlying parameters can be written, as follows:

$$(n^2 - n + 1)/\,k = M_1 \times M_2 \times M_3 \qquad (2)$$

$$(M_1, M_2, M_3) = 1.$$

Further research leads to associate combinatorial 3-D sequencing theory with a cyclic difference set theory and algebraic theory of cyclic groups in extensions of Galois field [1]. Development of new algebraic results and techniques, based on the idea of "perfect" combinatorial constructions, can be applied for generalization of these methods and results to the improvement and optimization of a larger class of technological systems and processes.

CONCLUSION

Three- dimensional Ideal Ring Bundle is a perfect combinatorial model of 3-D system with the optimal structure from the point of the convenience to reproduce the maximum number of combinatorial varieties in the system with the limited number of elements and bonds. Moreover, the structural perfection has been embedded in the underlying models. Combinatorial 3-D sequencing theory and methods based on the idea of the combinatorial models provide many opportunities to apply them to numerous problems in applied mechanics, including synthesis of non-redundant aperture mask systems for holographic image, 3-D image coding and compression, pattern recognition and three-dimensional image analysis.

REFERENCES

1. Hall M.Jr.: Combinatorial Theory. Waltham (Mass.), Blaisdell Publ.Co, 1967.
2. Kopilovich L.E.: Construction of Nonredundant Masks Over Square Grids Using Difference Sets. *Optics Communications* **68**, pp 7-10, 1988.
3. Baumert L.D. Cyclic Difference Sets. Springer, Berlin 1971.
4. Golomb S.W. Applications of Combinatorial Mathematics to Communication Signal Design. *Proceedings of the IAM Conference on Applications of Combinatorial Mathematics*, London, U.K., 1995.
5. Golomb S.W., Osmera P., Riznyk V. Combinatorial Sequencing Theory for Optimization of Signal Data Vectors Converting and Signal Processing. *Proceedings of Workshop on Design Methodologies for Signal Processing,* Zakopane, Poland, 29-30 August 1996, pp 43-44, Inst.of Electronics, Silesian Techn.Univ., Glivice 1996.
6. Riznyk V.V. Multidimensional Systems Based on Perfect Combinatorial Models. *Colloquium on Multidimensional Systems: Problems and Solutions*, Savoy Place, London, 14 January 1998, Ref.No: **1998/225**, pp 5/1-5/4, IEE, London 1998.

CONVERSION OF DISPLACEMENT/STRAIN FULL-FIELD EXPERIMENTAL DATA INTO FEM

Leszek Sałbut, Małgorzata Kujawińska, Robert Sitnik

Warsaw University of Technology, Institute of Micromechanics and Photonics IMiF,
Chodkiewicza 8, 02-525 Warszawa, Poland

Summary The paper describes the methodology of experimental data pre-processing and converting of the cloud of experimental values into the FEM mesh. Additionally the problem of domains matching between experimental field of view and FEM is discussed. The methodology is presented on the example of hybrid analysis of ceramic-to-metal joints. The specific problems connected with high noise and high strain gradients are presented.

INTRODUCTION

Hybrid techniques enable to combine the advantages of numerical analysis with those of experimental investigations. Various types of hybrid techniques exist which represent different levels of "collaboration" between experimental and numerical data [1]. The full hybrid technique requires a close linkage between numerical solution and experimental results through all stages of the analysis and due to its complication, at the moment, it is not widely used in solid mechanics. In contrast a basic or a localised hybrid method is extensively used in analysis of the most difficult problems in mechanics, including fracture mechanics, analysis of joints, mechanics of composite materials etc. Below we focus on preparation of experimental data obtained by the grating interferometry into data and files accepted by FEM procedures. The methodology proposed is illustrated by the process of ceramic-to-metal joint hybrid analysis [2].

LOCALISED HYBRID TECHNIQUES FOR CERAMIC-TO-METAL JOINT TESTING

The experimental data should support (alternatively or parallelly) the numerical model by determination of:

- material constants distribution in the case of inhomogeneous materials (Fig.1)
- boundary conditions, e.g. in the form of the real surface maps of in-plane displacements or strains for extended domain 2D strain/stress analysis and 3D modelling (Fig.2)

Such procedures are possible under certain conditions:

1. the experimental data should have high signal-to-noise (S/N) ratio, i.e. the noise should be minimised,
2. the surface zones with determined material constants should be given on the base of experimental data,
3. displacements or/and strains values in the nodes of FEM mesh should be determined.

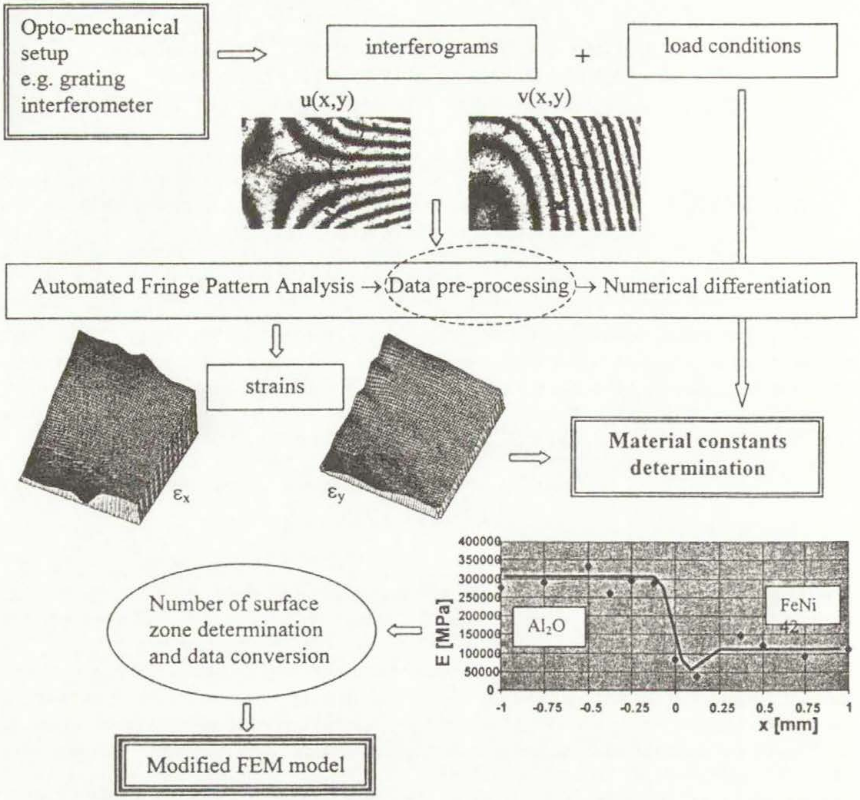

Fig. 1. Scheme of FEM model modification by introducing the experimental material constant distribution (on example of ceramic-to-metal joint studies).

Figure 1 presents the methodology of FEM model modification by inserting the experimental data about local material constants distribution. It requires pre-processing of interferograms and displacement/strain maps to improve S/N ratio. For "zero-field" interferograms (low frequency fringes) an averaging filter (3 x 3 window) is applied, while the interferograms with carrier frequency are treated by one-directional median filtering. The displacement and especially strain maps require heavy median filtering with the window size adaptively changing according to the local gradient of the map analysed [3]. The enhanced strain maps may be than used for the local material constant determination. This distribution is applied for modifying of FEM model by inserting the proper number of surface zones with the local values of material constants. At the example of ceramic-to-metal joint the local Young's modulus was calculated as the average value in each zone.

Figure 2 presents the methodology for experimental data conversion into files required as the boundary conditions e.g. for 3D strain/stress FEM modelling. In the first stage again data pre-processing procedures are applied to improve the S/N ratio in displacement/strain maps.

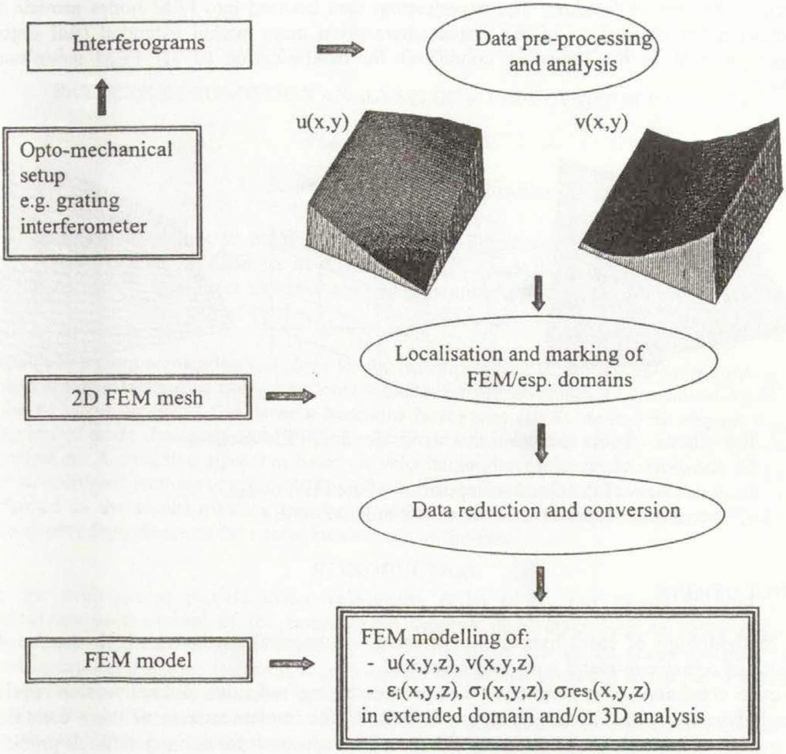

Fig. 2. Scheme of experimental data conversion into the file accepted as the boundary condition in 3D FEM modelling.

These maps are the files of discrete values at the regular mesh with usual dimension of 512 x 512 or 256 x 256 points. The coordinates of experimental domain have to be provided in order to assure the proper localisation of these data within FEM mesh. The FEM mesh has lower resolution and nodes often are not uniformly spaced. In order to use experimental data, they have to be reduced and the values in the FEM nodes location have to be determined. These is realised by calculating the weighted average from the experimental values taken within the local window with the sizes s_x and s_y equal:

$$s_x = \frac{N1X}{2} + \frac{N2Y}{2} \qquad s_y = \frac{N1Y}{2} + \frac{N2Y}{2}$$

where N1X (N2X) are the distances between actual node AN and the neighbourhood nodes N in X and Y directions.

Additionally the points with mask (no data available) have to be marked as the nodes with unlocking degrees of freedom. The experimental data inserted into FEM nodes provide the information for calculation of the displacement/strain maps within extended (full object) domain as well as the boundary conditions for determination of 3D FEM strain/stress analysis.

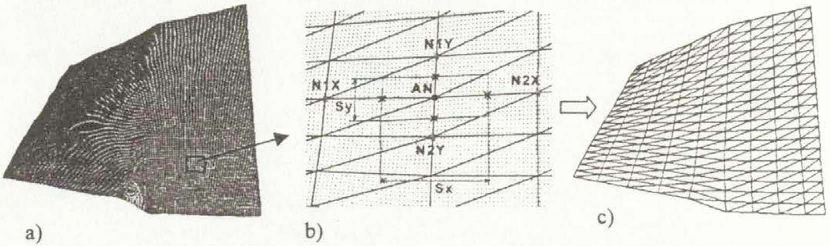

Fig. 3. The scheme of data reduction and conversion into FEM mesh
- a) the cloud of experimental points
- b) local view of the cloud with position of the FEM nodes
- c) a triangular representation of values in FEM mesh

CONCLUSIONS

The methodology of local hybrid experimental – numerical methods, which support the analysis of ceramic-to-metal joint, was presented.

The main conditions of experimental data pre-processing, reduction and conversion required for collaboration with FEM systems are discussed. The implementation of these conditions into numerical procedure shows the usefulness of the approach for solving difficult problems in solid mechanics.

REFERENCES

1. Laerman K.H.: Ueber das Prinzip der hybriden Technik in der experimentellen Spannungsanalyse. *Messen+Pruefen/Automatic*, pp 184-190, 1983
2. Sałbut L., Kujawińska M., Bułhak J., Golański D., Krajewski A.: Ceramic-to-metal joints testing by automated grating interferometry. *Proc. 11th Interfnational Conf. on Experimental Mechanics*, Oxford 1998, pp 633-638
3. Kujawińska M., Sałbut L., Sitnik R.: Local measurements of high-gradient in-plane displacement/strain by automated grating interferometry, *Proc. SPIE 3478*, 1998

PATTERN RECOGNITION ANALYSIS OF A TURBULENT SEPARATED FLOW WITH D-PIV

F. Scarano[1-2], M. L. Riethmuller[1]

[1] von Kármán Institute for Fluid Dynamics, Environmental and Applied Fluid Mechanics
Department, 72 Chaussée de Waterloo, B-1640 Rhode Saint Genèse, Belgium
[2] Department of Energetics and Thermo Fluid Dynamics Applied to Environmental Control
University of Naples, P.le V. Tecchio 80, I-80125 Naples, Italy

Summary A pattern recognition technique for the investigation of large-scale coherent structures, is applied to the instantaneous two-dimensional velocity distribution obtained by means of digital PIV in the turbulent separated flow over a backward facing step (BFS). Span-wise aligned vortices footprints of scale d ranging from $0.25h$ to $0.65h$ (h being the step height) are the subjects of investigation. A detection algorithm based on velocity pattern spatial cross-correlation is applied with an additional isotropy condition to improve the vortex detection. Conditional data averaging is performed to the results yielding structural properties such as coherent velocity and vorticity patterns with dependence on the spatial location and on the size.

INTRODUCTION

The fast evolution of particle image velocimetry (PIV) in the last decade [3,4,9] allows the simultaneous measurement of the instantaneous velocity distribution over an entire plane of measurement with enough spatial resolution to describe large part of the scales spectrum. This aspect constitutes a unique feature if considering the application of such a technique to educe of spatially coherent unsteady structures in the flow.

The transitional flow over a turbulent BFS exhibits a high degree of organisation due to the formation and growth of primary spanwise vortices linked to the Kelvin Helmoltz instability of the plane shear layer. Early visualisations described the flow in terms of Kármán vortices shedding even though the process is not periodic at high Reynolds numbers. Extensive and accurate works with experimental [6, 9] and numerical [5] approaches provided data sets describing the turbulent flow past a BFS even though most of the results were related to a statistical description of the flow.

The use of pattern recognition based on cross-correlation of velocity or vorticity patterns was demonstrated to be a suitable strategy for the detection of coherent structures [1,2].

A challenging task still is the choice of an appropriate definition of the pattern to be extracted from the flow, as the matching procedure needs at least a first guess prototype.

The pattern recognition technique developed in the present study performs the cross correlation of the instantaneous velocity distribution with a pre-defined vortex pattern. In order to improve the mentioned ambiguity between vortex cores and shear, an isotropy condition is applied to the velocity correlation maps.

The basic principle of this implementation relied on a vortex definition as given by Robinson [7]: *"a vortex exists when instantaneous streamlines mapped onto a plane normal to the vortex core exhibit a roughly circular or spiral pattern, when viewed from a reference frame moving with the centre of the vortex core"*.

A method to distinguish a vorticity peak belonging to a vortex core is suggested. The contribution to the vorticity or any integral derived quantity, as velocity circulation, must be weakly dependent of the considered direction where the velocity gradient is evaluated.

EXPERIMENT

The experiments have been performed in a wind tunnel of square cross section with 20cm-side and 20cm-depth test section. The step height was h=2cm with an expansion ratio of 1.2. The step height based Reynolds number was Re_h=5000, with U_o=3.8m/s and $\nu=1.52\cdot 10^{-5}$ m^2/s.

The PIV image processing is based on cross correlation applied an iterative window refinement with discrete window offset[9].

PATTERN RECOGNITION ALGORITHM

The method implemented aims to the detection of the footprints of span-wise aligned vortices. The spatial cross-correlation operator is built starting from a vortex pattern prototype defined in terms of velocity spatial distribution ***Vp****(x, y)* described in polar system of co-ordinates:

$$Vp_\theta = \frac{1}{2\pi r}\cdot\left(1 - e^{\left(-r^2/\sigma^2\right)}\right) \tag{1}$$

$$Vp_r = 0 \tag{2}$$

The procedure implemented for this flow must take in consideration that the vorticity level associated to the shear layer has the same magnitude as the characteristic level associated to the vortices. For this reason, an additional constraint has been imposed to the detection scheme, in terms of signal isotropy. The correlation of the instantaneous velocity field with the prototype pattern is performed considering the projection along different directions θ covering a range from 0 to π. The result yields a series of correlation maps in function of the direction

$$R_\theta(x, y) = \left(\vec{V}p \cdot \hat{i}_\theta\right) \otimes \left(\vec{V} \cdot \hat{i}_\theta\right) \tag{3}$$

Where both *Vp* and *V* have been properly shifted and normalised in order to make the result independent of any signal linear transformation.

The mean and rms of R_θ are considered in order to quantify the correlation intensity and the correlation isotropy respectively.

$$\overline{R}(x, y) = < R_\theta(x, y) > \tag{4}$$

$$R'(x, y) = \sqrt{< \left(R_\theta - \overline{R}\right)^2 >} \tag{5}$$

Finally, a proper enhanced correlation is built such to compensate for the high shear region peaks.

$$R*(x, y) = \frac{\overline{R}}{\left(1 + c \cdot R'\right)} \tag{6}$$

The weighting function does not alter the signal if a perfect isotropy is found, differently, the ratio decreases when the correlation exhibits intense fluctuation with varying θ. The parameter c (typically set to a value of three) defines the isotropy constraint strength. With the chosen value, the weighting function reduces the mean correlation of a factor two for non-zero gradient only along one direction (condition of maximum anisotropy).

Each instantaneous velocity field is analysed seeking for vortices of different size. A single threshold correlation level is selected to extract the signal maxima over all the mentioned size dependent correlation maps. The minimum number of grid points necessary for representing appropriately the vortex pattern determines the lower end of the scale parameter range. Given the measurement spatial resolution $\Delta r=0.05h$, vortices corresponding to $d/h=0.25$ are represented with a 5x5 stencil. The upper end of the size range was not limited by experimental constraints and reached $d/h=0.65$.

RESULTS

In the analysis of the instantaneous velocity distributions, the local extrema were searched in the correlation maps. Each detected extremum was selected as corresponding to a vortex. In addition to this the instantaneous separation streamline, defined as the locus where the reverse flow integral equals the forward flow, was displayed.

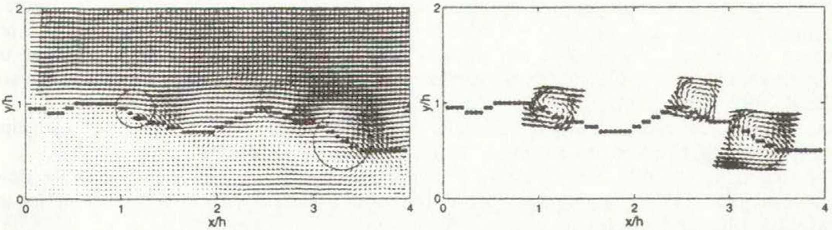

Figure 1 Detected vortices and shear layer axis pattern: instantaneous velocity field vortices with local mean velocity subtraction.

In Figure 1 it is shown the analysis of an instantaneous velocity field. The shear layer pattern is distorted by the intense span-wise vortices shed from the step edge. A Galilean transformation is applied within each region subtracting the local average velocity in order to visualise the vortex pattern and to check the precision of the detection scheme in determining the vortex centre.

The application of the mentioned algorithm on a series of 208 instantaneous flow field measurements allowed to draw some statistical characteristics related to the vortex occurrence.

Figure 2 shows the vortices spatial occurrence distribution at a value of d/h=0.65 of the normalised diameter. A quasi-linear spreading of clockwise rollers (labelled as dots) is shown starting from *x/h*=1 and reaching the wall at about *x/h*=3.5. The nature of these coherent structures due to Kelvin Helmoltz instability of the plane shear layer has been widely investigated and linear stability analyses predicted their existence and partially described their behaviour[16, 17].

These vortices are expected to play a dominant role in extracting energy from the mean shear and transferring it through this first mode to subsequent smaller eddies. Downstream this abscissa, the vortex population essentially propagates along the streamwise direction. This indicates that the structures can be considered in passive advection after a few step units and even upstream the reattachment location. Counter-clockwise rotating vortices of this size are found in large numbers only inside the bottom corner. These structures have a characteristic vorticity closer to the mean flow level than to the rollers shedding from the step. Thus the existence of these organised structures seems to be linked to the secondary re-circulation shown in the mean flow field.

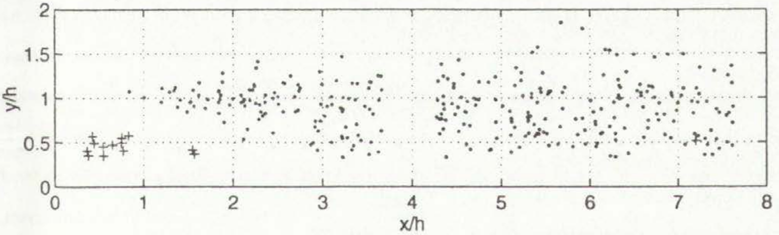

Figure 2 Vortices occurrence. Red dots clockwise vortices blue crosses counter-clockwise vortices (*d/h=0.65*).

The structures detected within the same domain subregion and classified with the same size are selected for the conditional averaging.

A procedure for centre alignment is applied in order to compute the averaged quantities corresponding to the vortex characteristics. Without this arrangement, the sharp instantaneous patterns would be significantly smeared out by the typical jitter in the structure appearance location. The sub-domain extention for the conditional averaging D_{xy} is set depending on the streamwise location as the flow characteristics vary significantly over the whole observed domain. Figure 3 shows the velocity and vorticity patterns of conditionally averaged data at x/h=1.25, y/h=1 and related to d/h=0.65. The local average velocity is uniformly removed in order to visualize the circulatory motion. The size correspondence found with the initial template confirms both the size classification and the centering procedure precision.

The stream pattern is distorted from the circular shape resulting elongated in direction of a principal axis oriented 30° clockwise rotated with respect to the streamwise direction.

The vorticity distribution (normalized with respect to the maximum mean strain rate in the flow) shows that a strong interaction occurs between the vortex and the shear layer accounting for the observed distortion from the circular pattern.

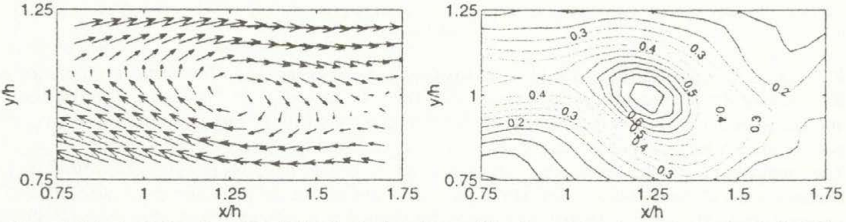

Figure 3 Velocity (left) and vorticity (right) distribution after conditional averaging of span-wise vortices ($x/h=1.25$; $y/h=1.0$) for $d/h=0.25$.

CONCLUSION

The authors reported results from the application of a velocity correlation algorithm to PIV measurements of the turbulent flow past a BFS. The isotropy condition used in the pattern recognition showed a significant improvement of the detection performances. The occurrence of vortices over the separated region and downstream the reattachment brought evidence of a significant vortex-shear layer interaction. The conditional averaging procedure brought results consistent with the target pattern initial choice.

REFERENCES

1. Ferré J. A. and Giralt F.: Pattern Recognition analysis of the velocity field in plane turbulent wakes, J. Fluid Mech. **198**, pp 27-64 1989.
2. Hussain A. K. M. F. and Hayakawa M.: Eduction of large-scale organized structures in a turbulent plane wake. J. Fluid Mech. **180**, pp 193-229 1987.
3. Keane R. D.,Adrian R. J. and Zhang Y.: Super-resolution particle imaging velocimetry, Meas. Sci. Technol. **6**, pp 754-768 1995.
4. Westerweel J., Dabiri D. and Gharib M.: The effect of a discrete window offset on the accuracy of cross-correlation analysis of digital PIV recordings, Exp. Fluids **10**, pp 20-28, 1997.
5. Le H., Moin P. and Kim J.: Direct numerical simulation of turbulent flow over a backward facing step, J. Fluid Mech. **330**, pp 349 374, 1997.
6. Jovic S. and Driver D. M.: Backward facing step measurements at low Reynolds number, Reh=5000: NASA technical memorandum **108807**, 1994.
7. Robinson S. K.: A review of vortex structures and associated coherent motions in turbulent boundary layers, Proc. IUTAM Symp. Struct. Turbul. and Drag Reduct., 2nd, Zurich (1989).
8. Jeong J. and Hussain F.: On the definition of a vortex, J. Fluid Mech. **185**, pp 69-94, 1995.
9. Scarano F. and Riethmuller M. L.: Iterative multigrid approach in PIV image processing, Exp. Fluids **26**, 1999.

OPTIMISING RAY TRACING FOR VISUALISATION OF VOLUMETRIC MEDICAL IMAGE DATA

Ernst Schuster, Thomas Lorang, Manfred Gengler and Michael Prinz
Department of Medical Computer Sciences
University of Vienna
Währinger Gürtel 18-20 1090 Vienna, Austria

Summary: The presented algorithms provide an approach to fast rendering of medical volume data. It is based on the ray casting algorithm, which is substantially speeded up in terms of voxel addressing and interpolation.

INTRODUCTION

3-D visualisation of medical image data is essential to diagnosis and treatment planning The presented rendering algorithm is to be used within a medical image visualisation framework, which is currently under development at the Department of Medical Computer Sciences and already in use at the Department of Radiotherapy. The speed of rendering is important because of the framework's ability to cope with multi-modal volume data sets (mostly Computer Tomography data and Magnetic Resonance data) which have to be rendered simultaneously within an interactive registration process. The proposed algorithm is fast enough to provide for interactive 3-D navigation in real time.

We present an integer-based approach for voxel extraction in rendering of volumetric data, allowing for both high accuracy and high speed. The volumetric data generally is composed of regular slices at irregular slice intervals. The voxel density is constant at the x- and y-axes, but it varies at the z-axis. Voxels are discrete intensities existing only at discrete intervals. A volume composed of voxels then fills a continuous world, where intensities have to exist everywhere, not only at the voxel grid points. This leads to two problems:

(i) Identifying voxel coordinates (addresses) upon world coordinates
(ii) Reconstructing sub-voxel values upon neighbouring voxels

VOXEL ADDRESSING

Retrieving the voxel address for a given world coordinate is the bottleneck of ray casting and therefore should be optimally enhanced. For regular and sequential volume sets, voxel addressing may easily be achieved by

$$\mathit{Voxel\ Address}(x,y,z) = \mathit{Base\ Address} + z * \mathit{SliceSize} + y * \mathit{SliceWidth} + x$$

Multiplications are time consuming operations. As both x and y range are bounded by the slice width and slice height resp., a first optimisation is achieved by precomputing possible multiplications for both y and z in lookup tables and adding the base address to entries in the z-lookup table

$$\mathit{Voxel\ Address}(x,y,z) = \mathit{SliceAddresses}[z] + \mathit{SliceWidths}[y] + x$$

Extending the voxel addressing to handle varying slice distances is essential due to the fact that many radiological studies are acquired in such a way that the slice distance is smaller at regions of interest and larger at outer regions. In our scenario, the z-position of each slice is known, so that we may define the range of possible z-coordinates. This range is subdivided into regular intervals in a way that each interval start position fits exactly one slice positions, remaining entries in the lookup table are set so that they point to the latest slice. For each z-coordinate, the above z-lookup table than again contains the starting address of the corresponding slice. Voxel addressing – regardless of whether slice distances vary or not - comprises the calculation of the slice start address upon z and the inner slice offset upon x and y, requiring a total of two additions and two lookups.

INTERPOLATION

When displaying volumetric data at a large zoom factor, the sparse density of voxels usually requires an interpolation process. Interpolation slows down the whole rendering process and therefore should be intensively optimised. In trilinear interpolation, a point in world co-ordinates is not represented by a single voxel, but by a cell composed of 8 voxels. The first of these 8 voxels may be retrieved by the above mentioned voxel addressing function, the remaining 7 voxels are retrieved incrementally, the next three voxels belonging to the same slice and the remaining four belonging to the neighbouring slice

$$\begin{aligned}
a_0 &= \mathit{SliceAddresses}[z] + \mathit{SliceWidths}[y] + x \\
a_1 &= a_0 + 1 \\
a_2 &= a_0 + \mathit{SliceWidth} \\
a_3 &= a_2 + 1
\end{aligned}$$

$$\begin{aligned}
a_4 &= \mathit{SliceAddresses}[z_{next}] + \mathit{SliceWidths}[y] + x \\
a_5 &= a_4 + 1 \\
a_6 &= a_5 + \mathit{SliceWidth} \\
a_7 &= a_6 + 1
\end{aligned}$$

$\mathit{SliceWidths}[y] + x$ is stored as o to avoid it's duplicate evaluation. z_{next} requires to be a z-coordinate so that the next slice is addressed. Considering variable slice distances, evaluating z_{next} upon z may get computational expensive. We solved this problem by modifying the z-lookup table to contain not the effective slice address but a slice index. This slice index is then used to retrieve the slice address from a slice lookup table. When calculating a_0, the index of the first slice is calculated, the index of the neighbouring slice simply is the next index and so calculating a_4 is fairly easy. The remaining voxel addresses are calculated like mentioned earlier.

$$\begin{aligned}
i &= \mathit{SliceIndexes}[z] \\
o &= \mathit{SliceWidths}[y] + x \\
a_0 &= \mathit{Slices}[i] + o \\
a_4 &= \mathit{Slices}[i+1] + o
\end{aligned}$$

Thus, calculating all 8 voxel addresses related to one cell requires 4 lookups and 9 additions. The sequence of looking up the i^{th} slice immediately followed by looking up the $i+1^{th}$ slice is very advantageous to many microprocessors due to the fact that the base address of the lookup table may be kept in register and automatically be incremented for the next lookup.

Interpolation is a mechanism to calculate sub-voxel values, i.e. values at positions between two voxels. This of course requires sub-voxel addresses, i.e. positions between two voxels. The interpolation process will be explained in detail for the one dimensional case. Let us assume two points $v_0 = 200$ *and* $v_1 = 360$ at the positions $t_0 = 0$ and $t_1 = 1$ resp. If we want to interpolate at the position $t = 0.25$ *and* $t = [0..1]$, then $v_t = (v_1 - v_o) * t + v_o = 240$. An easy approach to this are floating point world coordinates, but these are computational expensive. We have scaled 32 bit world coordinates by a scaling factor of $N=32768$ and defined the upper 16 bit to represent the integer part and the lower 16 bit the residue. Within this coordinate system, a voxel address at a world coordinate w is calculated by first calculating $w' = w/N$ and then using $w' = (x',y',z')$ as coordinates for the above described address computation. We have chosen N to be 2^n to replace the division by arithmetical shifts right of $n=16$. By this means, calculating the index and offset for voxel addresses results in

$$i = SliceIndexes[z>>n]$$
$$o = SliceWidths[y>>n] + (x>>n)$$

The remaining voxel address calculations are not affected. To achieve a sub-voxel accuracy of 2^{16}, only three supplementary shifts are required. Now $t=[0..1]$ is mapped to $t' = [0..N]$, so interpolating at $t=0.25$ results in interpolating at $t'=16384$ or $v_{t'} = (((v_1 - v_o) * t') >> n) + v_o$. The one dimensional interpolation requires 2 additions, one multiplication and one arithmetical shift to the right. Three dimensional interpolation requires 7 times these operations.

t is the residue of the world coordinate and may be calculated for x and y by masking out the lower part of the coordinate. The z-residue may be calculated the same way for regular slice intervals, but for irregular slice intervals the residues at z-coordinates are precomputed in a ancillary z-lookup table. The calculation of the residues needs only to be done once and requires 2 logical masks and one lookup.

$$t_x' = x \,\&\, (N-1)$$
$$t_y' = y \,\&\, (N-1)$$
$$t_z' = Residues[z]$$

The amount of operations required for the whole process of trilinear interpolation – with irregular slice intervals – is figured out in Table 1.

	Additions	Multiplications	Lookups	Shifts	Masks
Address calculation	9		4	3	
Residue calculation			1		2
Voxel Fetching			8		
Interpolation	14	7		7	
Total	**23**	**7**	**13**	**10**	**2**

Table 1: Interpolation Operations

Because of using discrete intervals for the parameter t', the error will be maximal where $|t-t'|$ is maximal, i.e. at $t=1/(2*N)$, where $t'=0$. The maximal error therefore is $1/(2*N)$. In bilinear and trilinear interpolation, this error can cumulate, but does not produce any visible artefacts however. Reducing the sub-voxel accuracy N will of course lead to larger errors, but as long as the sub-voxel accuracy is larger than the rendering bitmap, no visible artefacts can be observed. Machband effects - produced by abrupt gradient changes due to piecewise linear interpolation – are the main drawback of linear interpolation.

RESULTS

Results were achieved using a 333 MHz (Pentium II) PC with standard hardware. All volumes had a voxel depth of 16 bit and did not require any preprocessing. For oblique slice reconstructions (CT-Abdomen), volumes were composed of 512*512 voxel slices, volumes for surface rendering and maximum intensity projections (MIP) were composed of 256*256 voxel slices. Table 1 figures the total rendering times in msec for slice reconstruction, surface reconstruction and MIP for a bitmap of 256*256 pixels. Using 8 bit volume data sets decreased rendering times for about 5% only.

Volume	Slices	Oblique Slice		Surface		MIP	
		Min	Max	Min	Max	Min	Max
CT-Abdomen	45 (512*512)	46	78	187	2.250	1.625	26.891
MR-Head	32 (256*256)	32	48	203	402	1.035	3.645
CT-Skull	28 (256*256)	32	48	250	1.033	782	3.645
CT-Chest	31 (256*256)	32	48	173	1.157	1.002	7.330

Table 1: Rendering Times in msec

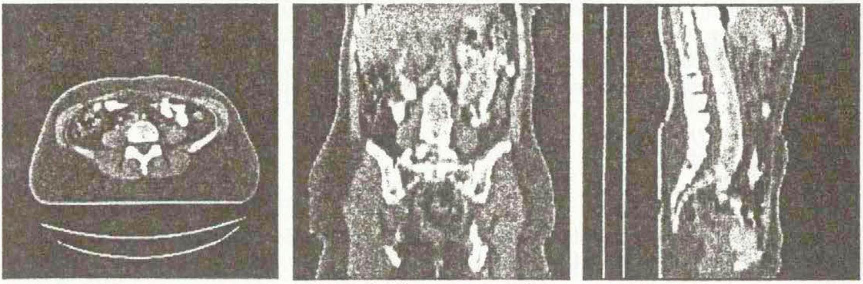

Figure 2: Slice reconstructions

Figure 1: Surface reconstructions

CONCLUSIONS

We have been able to achieve high speed rendering only by optimising interpolation and voxel addressing. The function for retrieving the voxel address upon world co-ordinates is the most frequently used function during the rendering process, it should therefore by optimally enhanced. Performing ray casting with integer co-ordinates has proven to be fast, resulting mainly from eliminating all divisions and reducing the amount of multiplications. The algorithm has proven to be sufficiently accurate for medical purposes, even in the domain of virtual endoscopy.

FUTURE WORK

Our ray caster is currently using a fast, but brute force algorithm for determining the sampling positions during volume traversal. Currently we are developing traversal algorithms specially suited for rendering at large zoom factors; an application of such algorithms is virtual endoscopy. We expect these caching strategies to reduce surface rendering times to less than 40% of the current rendering time and thus make real-time virtual endoscopy applicable in for clinical routine tasks.

REFERENCES

[1] R. Vandenhouten, R. Kottenhoff, and R. Grebe. 3D colour visualization of label images using volume rendering techniques Med.Inf.Lond., vol. 20, pp. 149-159, Apr. 1995.

[2] S.K. Semwal and B.K. Barnhart, Ray casting and the enclosing-net algorithm for extracting shapes from volume data Comput.Biol.Med., vol. 25, pp. 261-276, Mar, 1995.

[3] G.W. Sherouse, K. Novins, and E.L. Chaney, Computation of digitally reconstructed radiographs for use in radiotherapy treatment design Int.J.Radiat.Oncol.Biol.Phys., vol. 18, pp. 651-658, Mar, 1990.

VIDEO RECORDING OF FAST AND ULTRAFAST EVENTS

B. Stasicki, G.E.A. Meier

DLR (German Aerospace Center), Bunsenstr. 10, D-37073 Göttingen, Germany
e-mail: boleslaw.stasicki@dlr.de

Summary Commonly used video cameras provide 25 (CCIR) or 30 (EIA) frames per second (fps). By increasing the camera readout speed and/or reducing its spatial resolution frame rates of some thousand per second can be reached. Higher performances can be obtained only with more sophisticated systems. An **Ultra High-Speed Video Camera System** for single and a **High-Speed Video Stroboscope** for fast periodic and repeatable non-periodic events, both developed and constructed by the authors, are presented. The operation principle and some examples of application are given.

ULTRA HIGH-SPEED VIDEO CAMERA SYSTEM

The camera system presented has been designed for investigation of single ultra fast events. It can capture a sequence of up to eight high-resolution pictures with an extremely short interval. The camera head (Fig. 1) consists of eight CCD sensors placed around a eight-faced mirrored pyramid mounted just behind the single, interchangeable objective lens. The investigated object can be illuminated with a common flood light e.g., a halogen lamp or, as in the case shown in Fig. 2 with a single xenon light pulse. The image of the object is projected simultaneously onto all eight sensors. The frames are resolved temporally due to the sequential triggering of the asynchronous electronic shutters which are implemented into the control circuitry of each sensor. After the sensors have been exposed the images are read out in parallel with a standard speed of 20 ms, digitised and stored onto the eight frame grabbers placed in the slots of an industrial computer. The integration (shutter) time of each sensor can be set in the range of 20 ms down to 1 μs so that a framing rate of up to 1 million fps can be achieved without time overlap. For even higher framing speed (up to 100 millions fpm) fast gated image intensifiers can be placed in front of each CCD sensor. The precise synchronisation of the whole system is performed by means of a sequencer. This software programmable unit generates the control pulses for the camera shutters and optionally for the other components of the experimental set-up. The time resolution of the sequencer is 50 ns. Both the shutter and the inter frame time can be set individually for each sensor. All system settings and parameters are controlled by the integrated software. The captured images can be viewed immediately on the monitor and stored on the hard disk as a standard BMP or TIFF files. Additionally, a standard CCIR video signal is output for monitoring and recording.

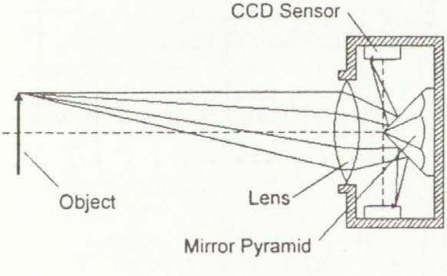

Fig. 1 Principle of the camera

Both the standard and the intesified version of the camera system has been licensed to the Cordin Company of Salt Lake City / USA.

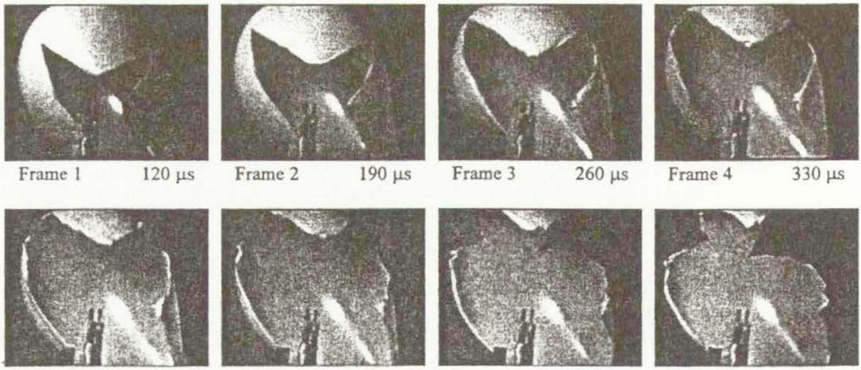
Frame 1 120 μs
Frame 2 190 μs
Frame 3 260 μs
Frame 4 330 μs
Frame 5 400 μs
Frame 6 470 μs
Frame 7 540 μs
Frame 8 610 μs

Fig. 2 Example of the camera application: Punctured balloon.

In Fig. 2 can be seen that the balloon diameter remains constant during the whole explosion process as its rupture proceeds faster than the speed of the sound in air. The object was illuminated with a single light pulse of a xenon lamp. The pulse duration of about 500 μs was long enough to record the whole sequence of 8 images. The shutter time was 20 μs. The frames are labelled with the time delays after the balloon puncture.

HIGH-SPEED VIDEO STROBOSCOPE

An alternative way[2, 3] to realise the concept of a stroboscope is to substitute the commonly used pulsed light source by an external asynchronously shuttered video camera connected to a triggerable frame grabber. By triggering the camera shutter with a pulse train which is synchronous with the examined object one will obtain a train of object images, each taken at the same phase shift. By using a frequency independent phase shifter and changing slowly its phase shift, a real time slow motion effect will occur. The apparatus described is a complete PC-controlled image acquisition system for investigation of the visualised periodic and repeatable non-periodic events. Fast moving objects are displayed in slow motion on the PC monitor in real-time. No flash light is necessary i.e. the object can be illuminated by a standard CW light source such as a halogen lamp or by daylight. Hence, self-luminous objects can also be examined.

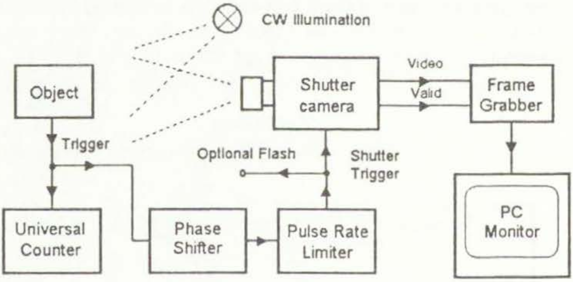

Fig. 3. Principle of the Video Stroboscope

The principle of the Video Stroboscope is shown in Fig. 3. It consists of a progressive scan CCD camera with an asynchronous high-speed shutter, a frequency-independent digital phase shifter[4], a PCI-bus frame grabber, a universal counter and a frequency synthesiser. Apart from the camera, all electronic components of the system are located in the slots of a Pentium computer. They have been specially designed and manufactured to meet the system requirements.

According to the nature of the object the system can be run in two ways. From self-running objects such as engines, turbines and machines, the trigger pulses can be picked up via an appropriate sensor e.g., photo cell, magnetic coil, microphone, pressure transducer. The pulse frequency or period can be measured by the universal counter and displayed on the screen. In the case of objects which must be driven by an electrical signal such as electro-acoustic transducers, actuators and injection nozzles, the system's frequency synthesiser (not shown in Fig. 3) can be used to control the object and to trigger the stroboscope. This direct digital synthesis (DDS) unit is a precise generator providing both a low distortion sine wave and TTL signal in the range from 0.05 Hz up to 1 MHz. The digital phase shifter provides exact operation in the same range.

The camera integration (shutter) time can be selected between 1,25 µs and 16 ms. This allows the stroboscopic observation and recording of very fast oscillating (above 10 kHz) and rotating (above 100,000 rpm) objects. Sequences of 300 full frame images of 659 x 494 pixel at 256 grey levels can be stored simultaneously for documentation, evaluation and playback. The size of displayed and stored images can be reduced to the region of interest (ROI). Thus, for a given amount of installed RAM, longer image sequences can be saved. The images are stored as single automatically numbered bmp or tiff compressed files or as an .avi video clip. The bmp and tiff sequences can be played back within the software frame by frame or as a video clip at user selected speed. For .avi format commercial multimedia players can be used.

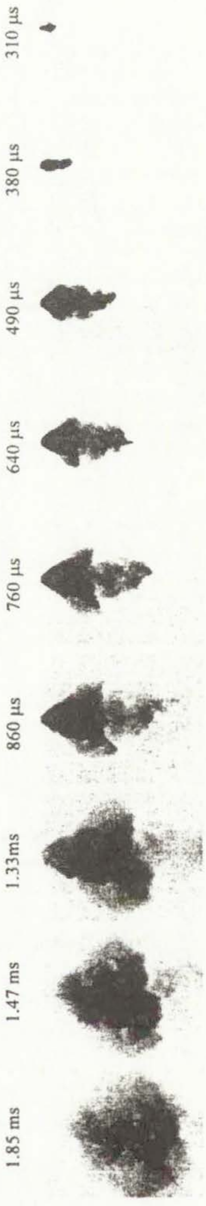

Fig. 4 Application example: The gasoline injection process. Gasoline has been supplied with an initial pressure of 100 bar to an electrically controlled automotive injection nozzle. The injection process was performed at an ambient pressure of 2.4 bar and ambient temperature of 20° C. The 9 images shown have been selected from a sequence of 300 full frames acquired. They are labelled with the delays after the leading edge of the nozzle opening control pulse. The field of camera view was 60 x 40 mm^2; the shutter time 1/800,000 s. Time between two successive images of the recorded sequence corresponds to 10 ∝s, i.e. to an effective framing rate of 100,000 fps.

Sequence courtesy
of A. Homburg and R. Schulz, Volkswagen AG

Integrated software controls all components of the system i.e. the camera, frame grabber, digital phase shifter, frequency synthesiser and the universal counter. For easy documentation and archiving of the images and image sequences, a image labelling system is provided. Each of the captured and stored frames is labelled with the most important parameters of the investigated object, the settings of the camera, present value of the phase shift / time delay, measured frequency or period, generated frequency by means of the frequency synthesiser as well as the number of the acquired frame with the date and time of its acquisition. These parameters are displayed on the screen during the observation of the object and during the play back of the stored pictures and sequences.

Unsteady objects, i.e. those having a temporal/phase jitter and/or spatial fluctuations, lead to an unstable object display. To improve and stabilise the display of such objects the real-time frame averaging routines newly added to the software can be used. When this "Mean Pix" mode has been chosen, the system acquires a selected number of images at each phase or delay value and calculates in real time a mean picture. This mean picture can be displayed on the screen instead of the original picture. Then, the next phase shift or delay value will be carried out automatically or manually. In some applications however, one may be interested in the study of the event instability. In this case a difference picture between the mean picture and the single picture can be calculated. This picture shows the offset of the momentary object position or shape from the average one. Besides the sequence of the single images, the sequences of mean and difference images can be automatically stored on the HD.

With respect to object illumination, good results have been obtained using standard halogen lamps of 20 to 150 W. However, in the case of high speed events requiring very short shutter times or when the examined object is of large dimensions, high power lamps must be used for satisfactory exposure. In that case a pulsed light source such as a xenon lamp triggered simultaneously with the camera shutter (see Fig. 3) might be a better choice.

The described High-Speed Video Stroboscope system is protected by patents[3,4] and patent applications. It is manufactured under license agreement by VISIT GmbH & Co KG, Würzburg, Germany.

REFERENCES

1. Stasicki, B. and Meier, G.E.A.: "A computer controlled ultra high-speed video camera system," *Proc. of the 21th Int. Congr. on High Speed Photography and Photonics, Taejon, Korea, 29 Aug. - 2 Sept. 94*, SPIE Vol. 2513, pp. 196-208, 1995.
2. Stasicki, B., Meier, G.E.A. and Renschke,J.: "Flash-Free High-Speed Video Stroboscope," *Proc. of the 22th Int. Congr. on High Speed Photography and Photonics, Santa-Fe, USA, 27 Oct. - 1 Nov. 1996*, SPIE Vol. 2869, pp. 409-417, 1997.
3. "Verwendung einer Videokamera und Vorrichtung zur stroboskopischen Aufzeichnung von Vorgängen," *Patent No. 43 09 353, (Germany)*, 1993.
4. "Digitaler Phasenschieber," *Patents No. 105 44 642, (Germany)*, 1997 and *No. 5,808,497 (USA)*, 1998

HEAT TRANSFER MEASUREMENTS IN HEAT EXCHANGERS BY LIQUID CRYSTAL THERMOGRAPHY

Jan STASIEK*, Giovanni TANDA** and Michele CIOFALO***
*Technical University of Gdansk, G.Narutowicza 11/12, 80-952 Gdansk, Poland
**University of Genoa, Italy
***University of Palermo, Italy

EXTENDED ABSTRACT

Liquid crystals have been employed in heat transfer experiments for years. However, their use has mainly been qualitative until the recent development and wide-spread availability of inexpensive image digitiser has made routine digital image analysis feasible. As known, thermochromic liquid crystals modify incident white light and display colours whose wavelength is a function of temperature. They can be painted or sprayed on a surface or suspended in a fluid and used to visualise temperature fields. Liquid crystal change in appearance is concentrated over a narrow range, typically few Kelvin degrees: this field is called "colour-play interval" and represents the temperature range within they can be used as temperature indicators. The interpretation of colour images displayed by liquid crystals is performed by the true-image processing. The image-processing system includes a video-camera to record the image, a frame grabber to digitise it and an appropriate software to convert the colour pattern into the temperature field. This last step can be performed under two distinct procedure: (i) the use of the separate colour component red, blue and green (R,G,B) and either a multiple regression method or a neural network to obtain the correlation equation between colour and temperature; (ii) the conversion of the image, pixel by pixel, from the RGB domain into the HSI (Hue, Saturation, Intensity) domain. In this way, only the Hue parameter can be retained since it is related to temperature through a relationship that can be obtained by a calibration experiment. The hue-temperature relationship depends not only on the liquid crystal compound but also on the experimental conditions, i.e. lighting, angle of view, presence of glasses between the video-camera and the LC layer. Information about saturation and intensity are not useful for the temperature reconstruction and can be abandoned, thus reducing the size of the digitised image and saving memory into the computer.

In this work examples of liquid crystals applications to the study of convective heat transfer are illustrated[1-5]. Attention is focused to the use of liquid crystal thermography to the study of compact heat exchangers performance. The complex geometry that often characterises these devices do not generally allow heat transfer investigation by traditional invasive sensors; conversely, optical methods, and in particular the liquid crystal thermography, are useful tools to gain whole-field and real-time information about flow and thermal fields.

Three different configurations have been considered: (i) a corrugated-undulated passage, (ii) a rectangular channel roughened by square ribs, and (iii) a rectangular channel finned with staggered or in-line diamond-shaped elements. All these geometry are frequently encountered in compact heat exchangers. In particular, the corrugated geometry consists in closely packed plates, bearing sine-wave corrugations, as those found in rotary air pre-heaters. The rectangular channel with one surface (end wall) roughened by square ribs or finned with diamond-shaped elements simulates heat transfer conditions occurring in the cooling of gas turbine blade.

Experiments were performed by using pre-packaged liquid crystal films consisting of a liquid crystal layer deposited onto a plastic sheet having a background colour with black paint. The film is glued onto the surface that is thermally active. Once the hue-temperature relationship has been determined, the coloured image of the heat transfer surface is converted into the pattern of isothermal lines. From these, the heat transfer boundary condition being known (for instance controlled heat flux), the lines at equal heat transfer coefficient can be extracted.

Figure 1 shows three images obtained by the liquid crystal thermography for the end wall heat transfer in presence of turbulence promoters (in-line square ribs). Each image corresponds to a different heat flux at the wall, the air mass flow rate (from the right to the left) being the same. In principle, one lone image contains all information required for the heat transfer analysis. Unfortunately, the temperature range in which the liquid crystals are active is limited; thus only a portion of the heat transfer surface displays colours, while the other parts remain black. In order to recover heat transfer information over the whole test section, one colour (usually the green band, centred in the colour-play interval and corresponding to a given surface temperature with a 0.2 K uncertainty) can be used for the heat transfer coefficient reconstruction. This procedure, suitable for stationary phenomena in which heat transfer coefficient is scarcely affected by surface-to-fluid temperature difference (as occurs in most forced convection problems), enables a careful heat-transfer coefficient reconstruction to be performed. For the same experiment (at a given mass flow rate), the heat flux at the wall is varied stepwise; after the steady state is reached, the colour pattern is recorded and analysed, in order to extract the position of the green "reference" band. The contours of the green band are then overlapped in order to obtain the pattern of lines at equal heat transfer coefficient in form of Nusselt number, as shown in Figure 2.

REFERENCES

1. G.Tanda, J.Stasiek and M.W.Collins "Application of holographic interferometry and liquid crystal thermography to forced convection heat transfer from a rib-roughened channel", Proc. of Int. Conf. on Energy and Environment ICEE '95, pp. 434-441, Shanghai, China, 8-10 May 1995.
2. G.Tanda M.Ciofalo, J.Stasiek, M.W.Collins "Experimental and numerical study of forced convection heat transfer in a rib-roughened channel", Proc. of XIII Italian Heat Transfer Conf., pp. 243-254, Bologna, 22-23 June 1995.
3. G.Tanda, J.Stasiek and M.W.Collins "An experimental study by liquid crystals of forced convection heat transfer from a flat plate with vortex generators", Proc. of IV UK National Conference on Heat Transfer, pp. 141-145, Manchester, UK, 26-27 September 1995.
4. Stasiek J., Collins M.W., Ciofalo M., and Chew P. " Investigation of Flow and Heat Transfer in Corrugated Passages. Part I: Experimental Results", Int. J. Heat Mass Transfer, Vol. 39, 1996, pp. 149-164.
5. Stasiek J., "Experimental Study of hat Transfer and fluid Flow Across Corrugated-Undulated Heat Exchanger Surfaces", Int. J. Heat Mass Transfer, Vol. 41, 1998, pp. 899-914.

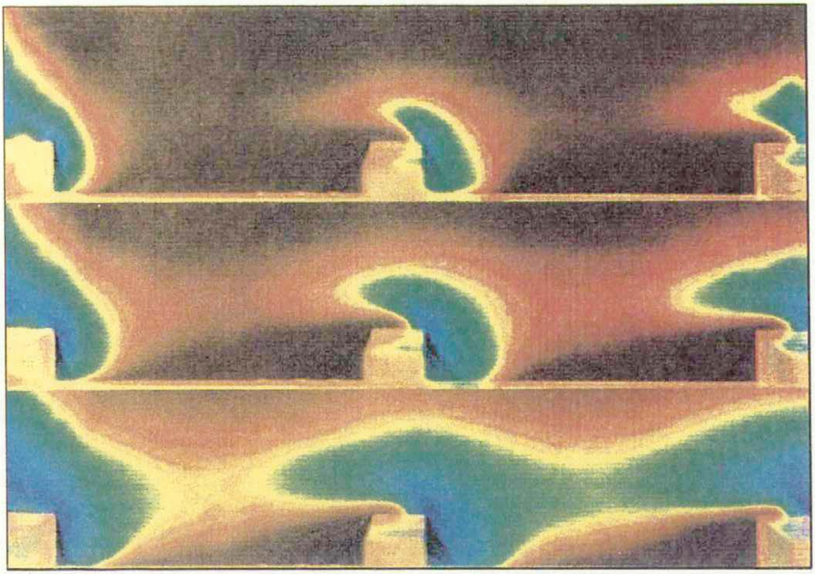

Figure 1. Three true-colour images obtained by liquid crystal thermography for an endwall surface with in-line square ribs.

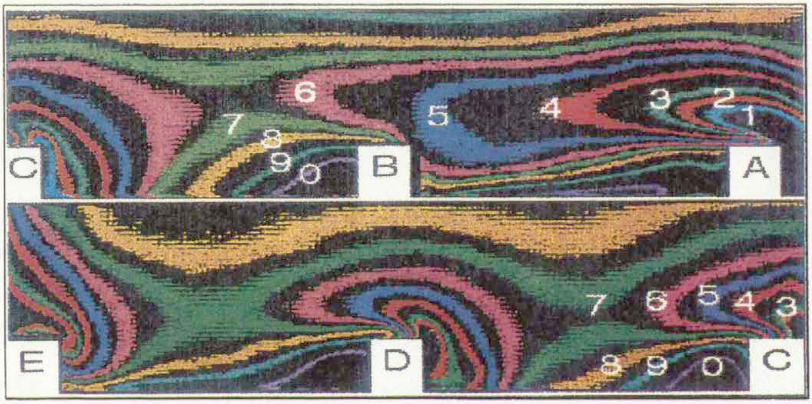

Figure 2. Pattern of ten Nusselt number Nu reconstructed by false colour images of the heat transfer surface (the value increases from No. 0 to No. 9; 0-79; 9-99; 8-113; 7-123; 6-136; 5-147; 4-160; 3-175; 2-185; 1-209).

High-Speed Digital and Video Recording of Fast Events for Motion Analysis

Don Thomas and Wojciech Majewski
Redlake Imaging Corporation
USA

History of Imaging for Motion Analysis

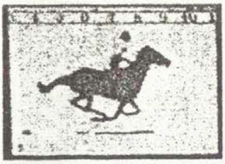

Film-based motion analysis was born in 1879 when California millionaire and former governor Leland Stanford hired photographer Edweard Muybridge to conduct the now famous running horse experiment. Stanford and others questioned if a running horse ever assumed the posture frequently depicted in paintings: front legs thrust forward and rear legs to the back, all four hooves off the ground. Stanford offered Muybridge his well-known steed Occidental as a test model for the experiment.

Working in Palo Alto, Muybridge set up a battery of 24 cameras in a long shed with controlled lighting. As Occidental ran the length of the shed, he triggered the cameras by breaking a string attached to each shutter. The result was a rapidly recorded image sequence that allowed viewers to observe, measure and understand motion that was too fast for the eye to perceive. The photographs revealed that at one instant, all of Occidental's four hooves were indeed off the ground, but they were suspended underneath him, rather than being thrust out behind and in front of him. Through this rudimentary motion analysis, Stanford scientifically proved his point.

In the 1970s, motion analysis came into a new era when the high-speed video industry was launched with the introduction of enhanced-speed reel-to-reel tape systems that were capable of recording up to 240 frames per second. Professional video cameras record 25 to 30 images (frames) per second. High-speed digital video, however, has the capacity to record thousands of images per second, allowing for precise motion analysis. The industry grew, as the advantages of high-speed video motion analysis became apparent, despite the equipment's high price. By 1982, tape-based video systems reached record speeds of up to 12,000 pictures per second. Such products typically cost over $120,000 and weighed near two hundred pounds.

In the mid 1980s, the first 1,000 frame per second digital memory high-speed video systems were introduced. These systems recorded high-speed images into solid state memory chips (video output) and eliminated many of the problems associated with the tape-based systems; however the systems, although smaller in size, still weighed 50 pounds and often exceeded $75,000 in cost. The problem that was not easily overcome was getting the images into a computer for analysis.

Although these early digital-based recorders used RAM as the original image capture medium they often output NTSC or PAL compatible video. For users that did not require the images to be in a PC for in-depth motion analysis this was a very useful technology, and still remains so today. It was often a long, difficult task for those that required getting images into the PC. The results were often unsatisfactory as frame grabbers (convert analog video into digital image) induced image artifacts from the conversion that lowered image resolution.

Technology Today

Several technology breakthroughs in the late 1990's revolutionized the method for recording high-speed digital images for motion analysis. Recognizing the need for small, low-cost digital high-speed cameras, Redlake Imaging introduced the *Motion*Scope® family of stand-alone and computer based products. This series of products redefined the high-speed video motion analysis industry in terms of technology and performance. The most innovative product in the series is the computer-based PCI system.

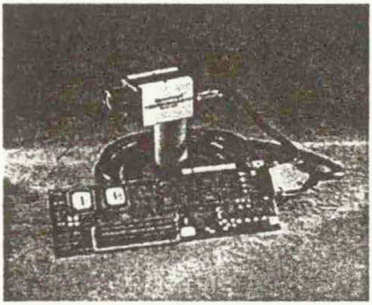

The *Motion*Scope® PCI system is comprised of a full-length Camera Control/Memory PCI board (Windows NT4 operating system), application software, high-speed camera head, camera cable, and documentation. The PCI system can record up to 8,000 digital images per second with shutter speeds up to 10 microseconds per image. Image resolution is up to 480 x 420 x 8 bit pixels per frame, adjusting down as frame rate increase.

High-speed images are initially captured in RAM memory on the *Motion*Scope® PCI Camera Control/Memory board. Once captured, images are held in memory to be played over the PCI bus and displayed on the PC monitor. Images can be archived to the PC hard drive or removable media such as Zip or Jazz drive. Playback is simple through a point-and-click interface familiar to PC operations. Playback rates range from single frame or automated frame playback from 1 through 8,000 frames per second.

System Architecture

The *Motion*Scope® PCI system architecture alleviates the problems that users have when installing and operating a high-speed imaging system within a PC. No longer does the user need to acquire components from several different sources and try to piece together a system (usually very time consuming and with limited results). The PCI system is a complete "plug & play" integrated architecture. The camera, PCI board, and application software are specifically designed as a hardware/software kit.

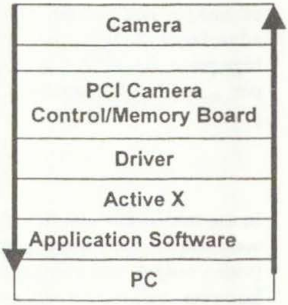

Digital Recording Architecture

Conventional thinking on tape or film based high-speed recording methods is to initiate the start recording sequence and stop when the media has been consumed. This method dictates that the event must occur (be timed or triggered to occur) before the media runs out. This method has limitations, particularly if the event to be recorded is intermittent or unpredictable. The use of RAM (solid state memory) as the recording medium simplifies the recording process.

By using RAM as the image capture media the high-speed system recording method overcomes the media timing issues of tape and film based systems. Once in the record mode, the memory will fill and continue to record by writing over the oldest image frame with the newest image. The image memory acts as a circular buffer. Recording is stopped when a manual stop command or trigger signal (contact closure, TTL, or voltage up to 30VDC) is received.

Since RAM allows the user to record until a stop command or trigger signal is received, and the nature of the circular buffer approach, the user may select where to locate the trigger input (time zero) in the memory bank. For example, if the high-speed system memory can store 65,536 frames, the user may pre-select to have the trigger pulse position located at the 50% point. In this example half of the frames would pre-trigger with the remaining frames post-trigger. This function is selectable in increments of 10% (range is 0% through 100%).

The flexibility of the trigger functionality creates an adjustable "event window" to capture the event as it occurs, or just after it has occurred, allowing easier image acquisitions. Since most high-speed events occur in a few seconds or less, most events can be successfully captured using this architecture.

User Interface

The "point and click" application software supports operation of up to four *Motion*Scope® PCI systems in a single PC. Each PCI system operates independently of the others or can be phase-locked together to assure that frame zero is the same on all four cameras

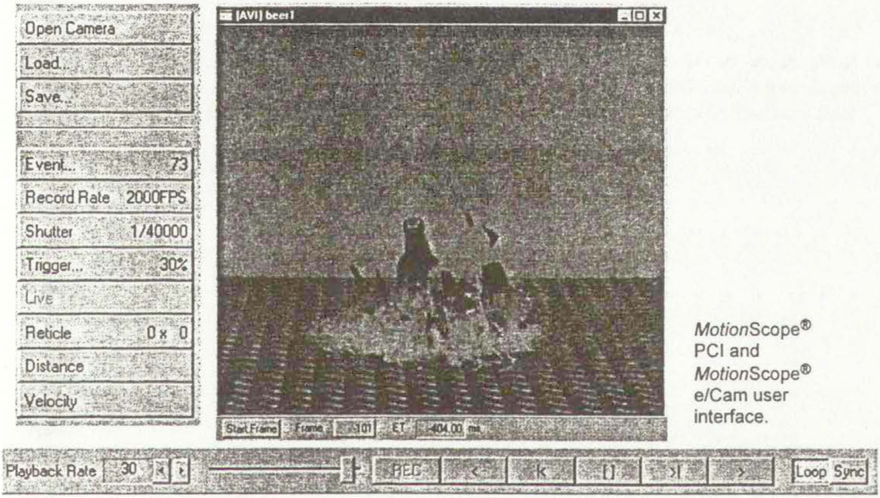

Event... 73
Record Rate 2000FPS
Shutter 1/40000
Trigger... 30%
Reticle 0 x 0
Frame 101
ET 404.00 ms
Playback Rate 30

*Motion*Scope® PCI and *Motion*Scope® e/Cam user interface.

The X-Y reticle system allows for easy calibration and manual tracking of a single point over all of the images in memory. Distance and velocity is displayed for each frame as well as recorded as a report for export to programs such as Excel.

High-Speed Imaging via the Ethernet

Technology limitations can create both problems and opportunities when working with high-speed imaging systems. One such limitation is the cable distance from camera to PCI board. Although few users need more than 10 meters of camera-to-processor cable, some applications may require cable lengths of 50 meters or more (currently outside of the capability of high-speed camera technology). The solution to this is in the form of the *Motion*Scope® e/Cam (Ethernet high-speed imaging system). This system is built on the PCI architecture and is controlled by the same application software. Up to four PCI systems (internal to the PC) and up to 255 Ethernet camera systems can be controlled by a single PC with 10/100 NIC interface.

The *Motion*Scope® e/Cam system has all of the core functionality of the *Motion*Scope® PCI system. The two systems do however differ greatly in hardware configuration. Unlike the PCI system, the Ethernet camera system is an external (to the PC) device that connect to the PC using standard 10/100 Ethernet hardware (running at 100 MBPS). The 10/100 Ethernet hardware includes category 5 cables, 10/100 switchers, hubs and related Ethernet devices.

Although every high-speed application is unique, high-speed motion analysis applications generally fall into four broad functional areas: design, testing, research and production. These categories cut across many industry and product lines, and include dozens of specific applications where high-speed imaging is required to capture, observe and measure high-speed motions that are too fast for the eye to see.

In order to meet the technical requirements of varied applications, high-speed imaging products in the form of high-speed video stand-alone systems, high-speed digital PCI systems, and high-speed digital Ethernet peripheral systems exist.

The Future of High-Speed Imaging

The applications for Motion Analysis high-speed imaging will continue to drive the development of high-speed digital imaging products in both stand-alone and laptop/PC configurations. Over the next 5 years most of the remaining high-speed analog video imaging systems will adopt digital technology.

REDLAKE IMAGING
RL
http://www.redlake.com

ULTRASOUND TRANSDUCER VIBRATION MEASUREMENTS WITH AN IMAGE PATTERN RECOGNITION APPPLICATION

Mircea Vaida[1], Arghir Suciu[2], Titus Moldovan[1]
[1]Technical University of Cluj-Napoca, Romania
[2]Eng. Software ITC Cluj-Napoca, Romania

Abstract: The paper will present an image pattern recognition application based on statistical parameters and Fourier's coefficients and the facility of this application to measure the vibration of ultrasound transducers concerning the acquisition of a sequence of images. The application is developed using Microsoft Visual C++ 5 software and the MFC libraries.

INTRODUCTION

The application from this paper represents an image analysis program which implements a pattern recognition and form detection method based on Fourier and statistical descriptors. For this implementation we used the latest concepts of visual and objectual programming from Microsoft Visual C++ Development Environment under Windows'9x and NT.

The objective of this work is to create an efficient and powerful instrument for image analysis and pattern recognition for use in varied domains: medical applications (diagnosis, microscopic analysis), industrial applications (defectoscopy, granulometry, inspection), and others. The application is hardware independent considering an image frame-grabber, but has the possibility to consider the standard MCI (Media Control Interface) offered by (semi) professional frame-grabbers and multimedia boards. In this case we considered the FAST multimedia board, Movie Machine II, *(Buza and.col., 1995)*. Considering the possibility to use extra software to store significant images from a sequence of images (Adobe Premier, etc.) we have the possibility to determine the dynamic evolution of some medical organs (heart, lung, etc.) or the transducers vibration in case of an image acquisition of their evolution.

QUANTITATIVE MEASUREMENTS

Image processing stages are:
- low-level processing (input and output data are images represented by pixel matrices)
    - acquisition, visualization;
    - image improvement;
    - emphasize of essential characteristics;
- intermediary processing (input data are images and output data are represented by symbolic structures)
    - feature extraction:
        - locals;
        - global;
- high-level processing (operating on symbolic representations)
        - image recognition based on patterns
- results interpretation.

The objective of image analysis is to determine the objects, which appear in the image, and to describe the surfaces of these objects. The input is a digital image and the output is a symbolic representation of the initial image. The first step in image analysis is to determine object boundaries. This can be made by edge detection techniques, followed by an algorithm of edges following and closing.

Another problem, which appears in image analysis, is region segmentation, by which it tries to identify the homogenous regions of the image. The final purpose is object recognition, which can be made by using a model database or other adequate techniques, and by the correct interpretation of the results.

The quantitative parameters of objects resulted after analyses are:

- -perimeter, area
- -form factor
- -eccentricity
- -regularity
- -undulation factor
- -mass center coordinates
- -minimum, medium and maximum axis

These parameters can be used for a first identification of image objects and a classification of these objects based on their size and the statistical analysis. The estimation of quantitative parameters is made as based on object area (A), perimeter (P) and edge points coordinates that are found first.

FOURIER DESCRIPTORS

After we have estimated objects edges from one image as points arrays, we can consider that one edge point (x(i) , y(i)) can be represented as a complex number, as follows:

$$u(i) = x(i) + j^*y(i);$$

So the edge of one object can be considered as the function

$$u(n) = x(n) + j^*y(n) \quad \text{for } n = 0,1,\ldots N-1$$

which, for a closed edge, is a periodic function with period N.

Its DCT representation is:

$$u(n) = \frac{1}{N}\sum_{k=0}^{N-1} a(k)\exp\left(\frac{j2\pi k_n}{N}\right) \quad 0 \leq n \leq N-1 \text{ where}$$

$$a(k) = \sum_{n=0}^{N-1} u(n)\exp\left(\frac{-j2\pi k_n}{N}\right) \quad 0 \leq n \leq N-1$$

Complex coefficients from DCT transform applied to edge function u(n) are the ***Fourier Descriptors***. These descriptors can be used for the recognition of similar objects even if they have different orientations or dimensions.

Considering a(k) and b(k) the Fourier Descriptors of the searched object u(n) and respectively, of the known model v(n). The shape of the object is similar to that of the model if the distance:

$$d(u_0,\alpha,\phi_0,n_0) = \min\left\{\sum_{n=0}^{N-1}\left|u(n) - \alpha v(n+n_0)e^{j\phi_0} - u_0\right|^2\right\} \text{ is minimal.}$$

The parameters are chosen so that the translation, scaling and rotation effect be minimal. If u(n) and v(n) are normalized:

$$\sum u(n) = \sum v(n) = 0\,,$$

then, for a known translation u_0, distance d is minimal, when:

$$u_0 = 0$$

$$\alpha = \frac{\sum_k c(k)\cos(\Psi_k + k\phi + \phi_0)}{\sum_k |b(k)|^2}$$

$$tg\phi_k = \frac{\sum_k c(k)\sin(\Psi_k + k\phi)}{\sum_k c(k)\cos(\Psi_k + k\phi)} \quad \text{,where}$$

$$a(k)b^*(k) = c(k)e^{j\psi k}, \phi = \frac{-2\pi n_0}{N} \quad \text{and } c(k) \text{ is a real number.}$$

PATTERN RECOGNITION METHODS AND DEDICATED MEASUREMENTS

With the *quantitative parameters* of the objects (features) we can separate different pattern classes. Experimentally we separated circles, rectangles, squares, stars, and irregular objects. In medical applications, we used this method to separate nuclei, micronuclei, mitoses, using a dynamic adaptability model method, *(Vaida and col., 1993)*.

This dynamic adaptability model method can be used in a lot of domains of interest.

In the recognition stage, we determine an attributed distance between the model features and the real features with:

$$d_{atrb} = \sqrt{\sum_{i=1}^{n} \left[\left(atrb_i \cdot \mathrm{mod} - atrb_i \right) / atrb_i \cdot \mathrm{mod} \right]^2}$$

We can impose weights to any feature, and in this case we will determine a weighed attributed distance.

The method is relatively simple and can be used in medical or industrial applications if the acquired image has a good quality, *(Vaida and col., 1998)*.

Considering the Fourier Descriptors of the searched object we can determine α and ϕ_0, and the minimum distance for the matching process will be:

$$d = \min[d(\phi)] = \min\left\{ \sum_{k}^{N-1} \left| a(k) - \alpha b(k) \cdot \exp[j(k\phi + \phi_0)] \right|^2 \right\}$$

This method offers good results considering normal images *(Suciu and Vaida, 1998)*.

Considering invariant moments, *(Gonzalez and Woods, 1993)* we try to develop a pattern recognition method too. This method use invariant moment based on different degree inertial moments, but the results was irrelevant in the recognition process.

In the DNA measurement process we are trying now to use pattern recognition methods based on color representation. If we consider the optical density of some regions, the intensity level can be irrelevant in some cases, the constancy of the color being a very important element.

In this case, different algorithms were developed to maintain this element considering RGB representation and YUV representation. The results show that RGB representation is more adequate in pattern recognition techniques, Willemse, *(Willemse & col., 1993)*, C.D.Fermin, *(Fermin & col., 1992)*.

Considering the ultrasound transducer vibration measurements we developed an algorithm to consider only two significant images from a sequence of images. These images will be the minimum and the maximum vibration images that are selected using Adobe Premier 4.0 application by an interactive procedure. From these two images we consider the medium axe of the minimum vibration image and the medium axe of the maximum vibration image. These values are used to determine the transducer deviation in the vibration process.

The method can be used in the dynamic evolution process of the heart and some other medical organs. In these cases we consider some other features such as: area, min/max diameter, Ferret diameter, etc.

The main components of the dedicated application are described in the annex 1.1.

CONCLUSIONS

Image analysis and pattern recognition methods can be used in different dedicated applications from microscopic medical and industrial images to macroscopic image too, *(Olinici and Vaida, 1997)*. The adequate ratio, price/performance of multimedia boards allow to develop low cost application in different fields.

References

Ayache N., Faugeras O. D., HYPER: A New Approach for the Recognition and Positioning of Two-dimensional Objects, IEEE Transaction on Pattern Analysis and Machine Intelligence, PAMI, Vol. 8, no. 1, January 1986, pp. 44-54

Buza O, Terec A., Vaida M., Echipamente multimedia utilizate in aplicatii biomedicale, Simpozion REP'95, ICEE Bucuresti, octombrie 1995, pp. 10-13 (Romanian language)

Gonzalez R. C., Woods R. E., Digital Image Processing, Addison-Wesley Publishing, 1993

Fermin C. D., Gerber M. A., Torre-Bueno J. R., Colour Thresholding and Objective Quantification in Bioimaging, Journal of Microscopy, Vol.167, Pt.1, July 1992, pp.85-95

C.D. Olinici, F. M. Vaida, Methods of Quantitative and Morphological Analysis in Biology and Medicine, Edit. Tehnica Bucuresti, 1997 (Romanian language with an English abstract)

A. Suciu, M. Vaida, Image Analysis and Form Detection with Fourier and Statistical Descriptors, At the Summer School in Image Processing, SSIP'98, Debrecen, Hungary, 5-18 July, 1998

Vaida M., Olinici C. D., Arsinte R., Application System for the Determination of Tumor Micronucleation and Morphometry by Computer Vision, Medinf93, 3-6 Nov. 1993, Timisoara, pp. 42-43

Vaida M., Pattern Recognition, At the Summer School in Image Processing, SSIP'97, Szeged, Hungary, 14-19 July, 1997

M. Vaida, S. Arghir, O. Buza, Video Inspection in Industrial and Medical Applications, AQ'98, IPA-UTC-N., Cluj-Napoca, 28-29 May 1998, pp.111-115

Willemse F., Nap M., de Kok L. B., Eggink H. F., Image Analysis in Immunohistochemesty, Analytical and Quantitative Cytology and Histology, vol.15, no.2, April 1993, pp. 136-143

Annex 1.1

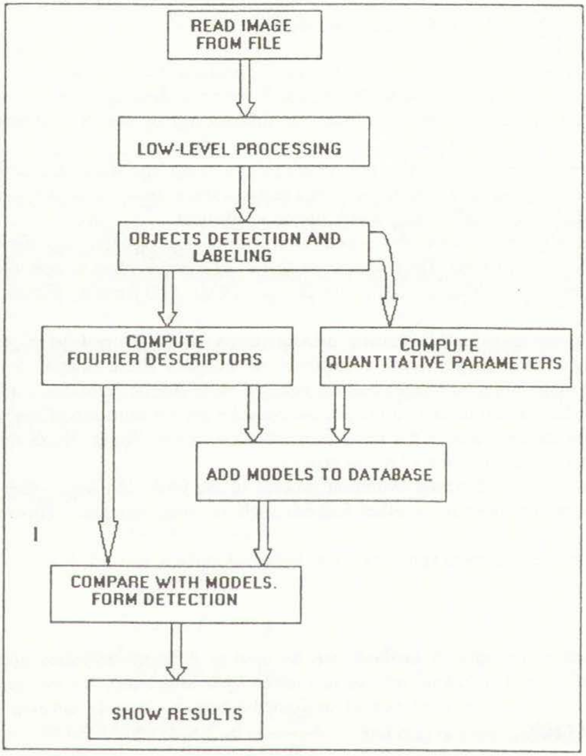

APPLYING FEATURE BASED TRACKING TO PARTICLE IMAGE VELOCIMETRY

Judit Verestóy[*]
[*]Computer and Automation Research Institute, Budapest, Kende u.13-17, H-1111 Hungary,
Email: verestoy@sztaki.hu

Summary Motion tracking is an important step of the analysis of flow image sequences. However, PIV techniques rarely use tracking methods developed in computer vision, they usually work with FFT and correlation based methods. Two major types of motion estimation algorithms exist: the optical flow and the feature based ones. Promising results have been obtained by applying optical flow techniques to PIV. The applicability of feature based tracking algorithms to PIV images is examined in this article. Two tracking algorithms are considered and preliminary flow visualisation results for standard PIV sequences are presented.

The aim of this work is to investigate the applicability and efficiency of the feature based tracking algorithms in flow velocity measurement.

PIV, DPIV. Flow visualisation and measurement of flow dynamics are important tasks appearing in the analysis and understanding of combustion processes, aeronautical phenomena, flame propagation, heat exchange problems, construction of artificial heart pumps, etc.[1].

In particle image velocimetry applications, the fluid is seeded with particles that follow the flow and efficiently scatter light. The fluid is illuminated by a two-dimensional light sheet (laser beam). Conventionally, multiple exposure cameras are used to capture images of the flow at different time instants, and the images are recorded on photographic film. By optical correlation methods applied point-by-point to the entire negative, the in-plane velocity of the particles between two consecutive images is determined. The obtained velocity field is then used to estimate the instantaneous dynamics of the local fluid.

With the development of high-performance CCD cameras and frame-grabbers a new PIV approach emerged: the digital PIV, or DPIV. Here, image sequences are stored and processed directly by the computer. The conventional cross-correlation methods could easily be implemented, and the ambiguity of the sign of the displacement has also been removed. A major drawback of correlation-based motion estimation methods is their inaccuracy in regions where the velocity gradient is high. To compensate for this imperfection, alternative methods have been developed which improved correlation techniques by combining them with gradient methods used in physics and computer vision[2].

Tracking in computer vision. On the other side, estimation and tracking of motion in image sequences is an important branch of computer vision. Usually, real world scenes with large, rigid or deformable moving objects are considered, where rigidity constraints can also be imposed to improve tracking results. Two main classes of motion estimation algorithms exist: the optical flow based, and the local feature based algorithms.

The optical flow techniques extract a dense velocity field from an image sequence assuming that image intensity is conserved during the displacement. An overview of their performance can be found in[3]. Feature based techniques extract regions of interest (features) from the images and identify the corresponding features in each image of the sequence[7,9]. A number of algorithms are available in each class. Applying them to particle image sequences can lead to considerable improvements in visualisation and measurement results.

Recently, Quenot et al.[4] presented an optical flow algorithm based on dynamic programming and tested it with PIV sequences. The dynamic programming technique was originally used for searching optimal matching between two one-dimensional patterns. The authors extended it to two dimensions and used it for finding a dense velocity field between two consecutive images of a sequence. The results obtained for both synthetic and real sequences[5] compare favorably to those obtained using the classical 2D DFT based DPIV method. An increase in both accuracy and spatial resolution of the velocity field has been achieved.

Both correlation methods and optical flow techniques imply matching performed for the whole image, which can be very time consuming. In image sequences where the individual particles can be detected, and when there is no need to obtain a velocity vector in each pixel of the image, feature based techniques are also applicable and provide a faster solution.

Feature based tracking. The feature based algorithms have initially been developed for tracking a small number of salient features in long image sequences. One can divide the tracking process into two major subtasks: feature extraction and feature tracking. The two phases can be carried out sequentially or simultaneously. The first possibility is to extract features from each image and later find the corresponding features along the sequence. The other possibility is to extract features only from the first image and search for the same features in the following images. An example for both approaches will be presented below together with their results given for a standard PIV sequence.

In[7], a comparative performance evaluation of five feature point tracking algorithms is given. Besides, there is a possibility to test the five candidate algorithms via an on-line Internet demo[8] with both generated synthetic motion and user-defined input data. Image sequences consisting of at least three frames are considered. Each algorithm assumes that feature points have been extracted prior to tracking in each image of the sequence. Among them, the algorithm called IPAN Tracker[6] can be selected as the one which best fits the particle image velocimetry applications. The criteria for the selection were, beside the accuracy of the result and the low computational cost, the algorithm's capability to cope with large point densities and disturbing events such as appearance and disappearance of feature points.

IPAN Tracker is a non-iterative, competitive feature point linking algorithm. It is based on a repetitive hypothesis testing procedure which switches between 3 consecutive image frames and maximises the smoothness of the evolving trajectories. When proceeding to a new frame, the already established partial trajectories are extended. A feature point having no successor or no predecessor closes or, respectively, opens a trajectory. In this way, feature points that appear or disappear due to the non-planar nature of motion or due to shortcomings of image formation can also be tracked.

Figure 1 (bottom left) shows preliminary results obtained for a standard PIV sequence downloadable from[11]. The sequence consists of four frames of size 256 x 256 pixels, containing 4000 particles. The mean particle displacement is 7.5 pixels/frame, the mean particle diameter is 5.0 pixels.

The results can further be improved by a local directional coherency filtering which eliminates the noisy velocity vectors. One can observe that the velocity field is not uniformly distributed over the image. This is the drawback of the feature extraction procedure. In the present version, the strongest features are selected, based on the brightness and the size of the feature, with no spatial distribution taken into account. This will be improved in the future.

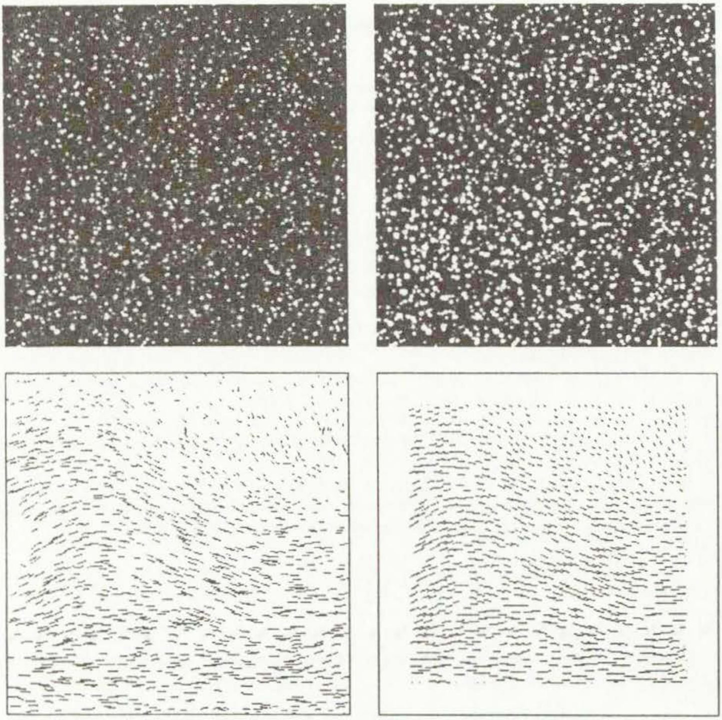

Figure 1. Flow visualisation results.
Top row: The first frame of a standard PIV sequence (256 x 256 image, 4000 particles).
Original image (left) and adaptive histogram equalised image (right).
Bottom row: Results of tracking over four frames.
IPAN Tracker result for 1200 feature points (left). KLT result for 1000 feature points (right).

In[9], Shi and Tomasi present an algorithm called KLT for selecting features which are optimal for tracking: in their conception, a good feature is one that can be tracked well. They define a measure of feature quality which quantifies the change of appearance of the feature between the first and the current image frame, allowing for affine image changes. A pure translation model is then used to track the selected best features through the image sequence. The source code of the KLT algorithm can be downloaded from the Internet[10] and tried out on arbitrary image sequences.

The results obtained for the same standard PIV sequence are shown in figure 1 (bottom right). One obtains an uniformly distributed velocity field. The empty strip near image borders appears because the feature extraction is performed in a relatively large window (usually 25 x 25 pixels).

In the future, the two algorithms will be thoroughly tested on standard images originating from both sources[5,11]. The velocity fields will be evaluated and compared with the available ground truth.

Conclusion. A new approach to flow visualisation and measurement has been presented. Feature based tracking algorithms represent a fast and apparently precise tool in solving PIV problems.

REFERENCES

[1] Grant: Particle image velocity: a review. *Proc. Instn Mechanical Engineers*, 1997, vol.211, Part C, pp.55-76

[2] Tokumaru, P.E. Dimotakis: Image correlation velocimetry. *Experiments in Fluids*, Springer-Verlag, 1995, vol.19, pp.1-15

[3] Barron, D.J. Fleet, S.S. Beauchemin: Performance of optical flow techniques. *Int'l Journal of Computer Vision*, 1994, vol.12, pp.43-77

[4] Quénot, J. Pakleza, T. Kowalewski: Particle image velocimetry using optical flow for image analysis. *Proc. 8th International Symposium on Flow Visualisation*, 1998, pp.47-1-47-10

[5] *ftp://ftp.limsi.fr/pub/quenot/opflow/testdata/piv*

[6] Chetverikov, J. Verestóy: Tracking Feature Points: a New Algorithm. *Proc. 14th International Conference on Pattern Recognition*, 1998, Brisbane, Australia, pp.1436-1438.

[7] Verestóy, D. Chetverikov: Experimental Comparative Evaluation of Feature Point Tracking Algorithms. To appear in the *Proc. of the Dagstuhl Workshop on Evaluation and Validation of Computer Vision Algorithms*, Kluwer Academic Publishers, series Computational Imaging and Vision.

[8] *http://visual.ipan.sztaki.hu*

[9] Shi, C. Tomasi: Good features to track. *Proc. IEEE Conf. on Computer Vision and Pattern Recognition (CVPR94)*, Seattle, June 1994

[10] *http://vision.stanford.edu/~birch/klt/*

[11] *http://sap.gen.u-tokyo.ac.jp/*

VISION-BASED DEVICE FOR IN-VIVO MEASUREMENT OF ELASTO-MECHANICAL PROPERTIES OF SOFT TISSUES

Vladimir Vuskovic, Riccardo Blaser, Andrea Spiga
Institute of Robotics, ETH-Zurich, CLA, ETH-Center, CH-8092 Zurich, Switzerland

Summary A device, which performs in-vivo measurement of elasto-mechanical properties of human soft-tissue is described. The device permits the controlled application of vacuum to small spots of organic tissue and registers the small deformations caused during the whole measurement process. Deformations are measured with a vision based technique and the grabbed images are processed in real-time to avoid storage problems. Subsequently, several elasto-mechanical properties of the tissue can be determined via the inverse finite element method.

INTRODUCTION

The ETH-Zurich is developing a virtual reality based endoscopic surgical simulator that should exceed in realism the already existing endoscopic surgical trainers. There is a need for realistic endoscopic surgical trainers, due to the fact that traditional minimal-invasive surgical techniques require the surgeon to have very special skills, which can only be acquired with extensive training.

The force feedback device, which simulates the contact of operating instruments with living organic tissue, should ideally provide realistic haptic sensations resulting from an FEM simulation of tissue deformation[1-3]. The selection of the constitutive equation for modeling a specific organic material should, therefore, be followed by the determination of the actual numerical values of material parameters. Since there are significant differences between the mechanical properties of dead and living tissue, the measurements should be performed in-vivo. In particular, accurate data cannot be obtained from the usual testing setups, which need tissue preparation for experimental testing. In the past, a number of experiments were performed on a variety of tissues under different loading conditions[4], but very little data from in-vivo-measurements exist[5].

MEASUREMENT METHOD

Measuring mechanical properties of an organic tissue in-vivo is a complex task. The measurement must not cause any tissue damage and the measuring device must be sterilizable and easily manageable. A further problem is presented by the difficulty of keeping track of the boundary conditions during the measurements, because any interaction with the organ, whose parameters are to be determined, produces the motion of the whole organ. One technique able to provide accurate data, while overcoming the latter problem is tissue aspiration in conjunction with the inverse finite element method. The inverse finite element method allows the greatest freedom concerning the boundary conditions and the geometry of the problem and, due to the complexity encountered in in-vivo experiments, it seems to be a suitable way to determine material parameters[6-7]. The method consists in leaning a tube on the target tissue and applying a weak vacuum. The organ remains fixed to the tube specifying well defined boundary conditions, and a small deformation of tissue is caused inside the tube. The measurement process consists in increasing the applied vacuum over time and determining the function $\underline{d}(P(t), t)$, where $\underline{d}$ is a measure of the surface deformation under the tube; t, the time from the start of the measurement; and $P(t)$, the negative relative pressure at time t. Thus, we track over time the applied vacuum and the resulting deformation. Measuring the whole deformation cycle permits estimation of time-dependent factors such as viscoelasticity. Assuming axisymmetry and homogenous tissue in the portion contained under the aspiration tube, a complete description of the deformation is given by a profile of the deformed tissue (or more exactly by one half of a profile). The aspiration setup and the profile to be determined are illustrated in Figure 1. Therefore, the measuring process reduces to the determination of the function $y(x, P(t), t)$, which is shown in Figure 2.

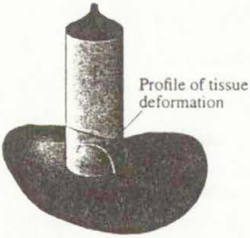

Figure 1. Aspiration experiment

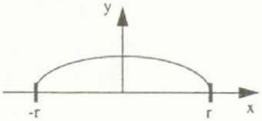

with:
r: radius of the tube
y: axis of symmetry of the tube

Figure 2. Profile function of a deformation at a time t

The measured function profile has to be passed off-line to the parameter estimator, which determines the parameters of the finite-element model of the investigated tissue via the inverse finite element method. The parameter identification algorithm performs a minimization of squared differences between measured and simulated load-displacement relations. Another advantage of this technique, is that not only one-dimensional load-displacement curves are obtained. This is important because one dimensional load-displacement curves give only limited information and can be simulated with practically any material constitutive equation.

MEASUREMENT DEVICE

We developed a vision technique to measure the profile illustrated in Figure 1. Slight modification of the tube's geometry makes it possible to place a small mirror beside the aspiration hole and to track the silhouette of the deformed tissue with a camera placed at the other end of the tube. This geometry allows a side look at the desired profile. This is illustrated in Figure 3. This method allows to measure the desired profile very accurately, rapidly and without contact with the tissue. An optical fiber, placed just below the camera, illuminates the aspirated tissue. The camera with telecentric close-up lenses, the tube, the light-fiber and the control switches are mounted onto an aluminium body, which also gives maneuverability to the instrument. A photograph of the device is shown in Figure 4.

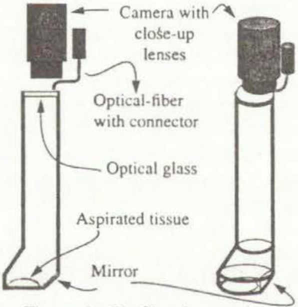

Figure 3. Profile observation

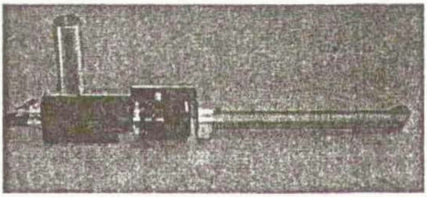

Figure 4. Instrument

The pneumatic system is connected to the aspiration tube via a flexible silicon tube and is designed to allow easy and secure control of the pressure in the tube and to measure the pressure very accurately. All the components of the pneumatic system are inert and can be sterilized.

Image processing

If the deformation is to be tracked over time, a very large number of images must be taken. To reduce the quantity of information, a real-time silhouette extraction of measured profiles is of great advantage. In our setup we achieve a processing frequency of 25 Hz, i.e. we grab and process 25 images per second. A typical image grabbed during the measurement process (experiment on ex-vivo bovine uterus) and a short description of the image processing algorithm are shown in Figure 5.

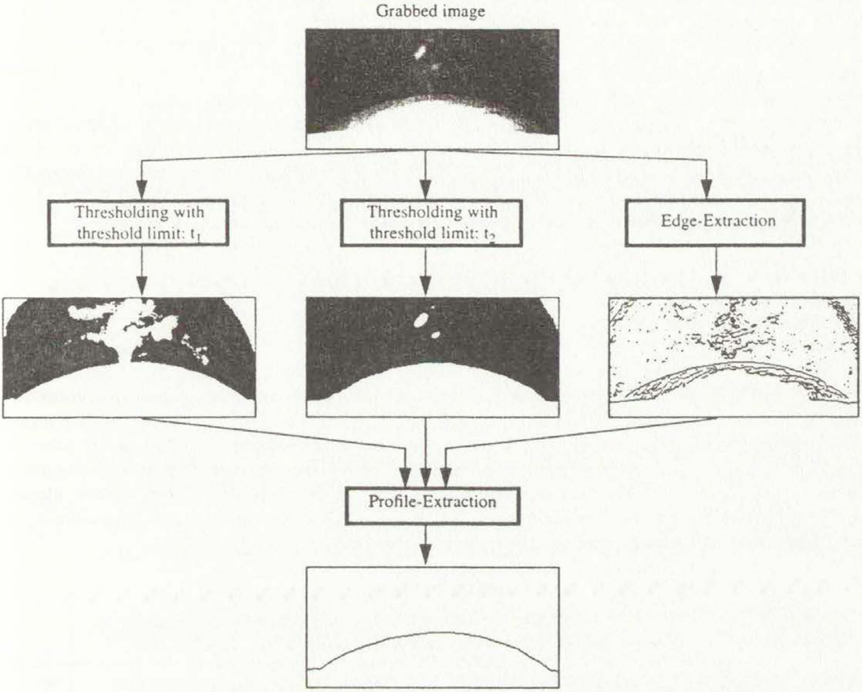

Figure 5. Algorithm for profile extraction

The approach chosen here combines the precision of edge extraction with the ease of interpretation of thresholded images. The two thresholded images give an approximation of the searched silhouette, while the edge image gives a set of points in which the silhouette is to be searched. The reason for thresholding the image with two different threshold levels is that the first thresholded image often gives a good approximation, but fails to describe the curve in zones with specular reflections (for example, due to rests of organic liquids on tube walls), while the second thresholded image describes the curve conservatively and is less sensible to perturbations. In order to describe the profile-extraction block, let us first introduce the pixels coordinates of the images as (x, y). The profile-extraction block extracts a function $y = f(x)$, thus, it extracts for every $x \in [1,n]$ exactly one $y \in [1,m]$, where n and m are the dimensions of images in pixels. The selection of the y coordinate for a given x is done by minimizing a cost function, which is evaluated over the whole set of previously determined "candidate-y-values", which are mainly obtained from the edge-image. The cost function takes into account the distance from the silhouettes given by the two thresholded images, from the previous extracted contour points etc. The superposition of the original image and the extracted curve is given in Figure 6.

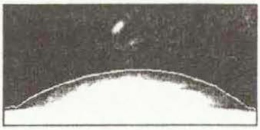

Figure 6. Contour superposed to image

Supporting hardware and software

Magnetic valves of the pneumatic system, the vision system, the pressure sensor and all other instrument controls are connected to a fast PowerPC based computer system, on top of which runs a hard real time operating system XOberon[8]. The acquired curves, pressures and times collected during the whole measurement are transferred (by pushing a button on the instrument) from the RAM of the computer-system, via an ethernet connection, to a remote data storage system.

RESULTS

We implemented a device able to apply controlled vacuum to the surface of organic tissue and to accurately measure the resulting deformations. The method allows to generate well defined boundary conditions during in-vivo measurements. The deformations are tracked during the whole measurement cycle. This permits the determination of time-dependent properties also, such as viscoelasticity. The deformation is measured via profile with a vision based method. The images are taken at a rate of 25 per second and processed in real time. The amount of data to be stored for subsequent parameter identification is in this way drastically reduced. The subsequent parameter identification via inverse finite element method has proven to be capable of precisely determining several elastomechanical properties of the measured tissue. We performed first experiments on ex-vivo animal tissue. The device will soon be applied in-vivo on human patients.

REFERENCES

1. Ogden, R. W., 1984, "Nonlinear Elastic Deformations," Ellis Horwood Limited.
2. Rivlin, R. S., and Saunders, D. W., 1951, "Large Elastic Deformations of Isotropic Materials. VII Experiments on the Deformation of Rubber," Philosophical Transactions of the Royal Society, Series A, Vol. 243, pp. 251-288.
3. Sussman, T., Bathe, K. J., 1987, "A Finite Element Formulation for Nonlinear Incompressible Elastic and Inelastic Analysis," Computers and Structures, Vol. 26, No. 1/2, pp. 357-409.
4. Fung, Y. C., 1993, "Biomechanics: Mechanical Properties of Living Tissues," Springer-Verlag, New York.
5. Moulton, M. J. et al., 1995,"An Inverse Approach to Determining Myocardial Material Properties," J. Biomechanics, Vol. 28, pp. 935-948.
6. Aoki, T. et al., 1997, "The Pipette Aspiration Applied to the Local Stiffness Measurement of Soft Tissues," Annals of Biomedical Engineering, Vol. 25, pp. 581-587.
7. Kyriacou, S. K., Shah, A. D., Humphrey, J. D., 1997, "Inverse Finite Element Characterization of Nonlinear Hyperelastic Membranes," Journal of Applied Mechanics, Vol. 64, pp. 257-262.
8. Brega. R, 1998, "A Real-Time Operating System Designed for Predictability and Run-Time Safety", Proceedings, Movic-98, Vol.1 pp. 379-384

FLOW-REGIME DISCRIMINATION IN BUBBLE COLUMNS USING ELECTRICAL CAPACITANCE TOMOGRAPHY

Robert M West[*], Mark A Bennett[**], Xiaodong Jia[*], Steven P Luke[**], Krzysztof L Ostrowski[*], and Richard A Williams[*]

[*]Centre for Particle and Colloid Engineering, School of Process, Environmental, and Materials Engineering, University of Leeds, UK

[**]Camborne School of Mines, University of Exeter, Redruth, Cornwall, UK

Summary Electrical capacitance tomography has been used to image a bubble column. Sets of linear back projection tomograms are then analysed to yield gas hold-up values and to determine flow regime in a traditional manner. Further analysis is performed producing a statistic (Heterogeneity Index for Tomograms) that is independent of the average hold-up. This is used to provide an alternative and superior means to determine flow regime.

Introduction

The use of Electrical Capacitance Tomography (ECT) to visualize two- and three-phase flows is reviewed by Reinecke *et al*[1]. Some tomographic data have been used to characterize flows, for example in trickle-bed reactors[2] and pneumatic conveying[3,4].

Here ECT is used to distinguishing homogeneous bubble flow and churn flow in a bubble column. Various operational conditions were created to test viability using different spargers, frother concentrations, and height between sparger and sensor.

Traditional flow-regime identification is undertaken using the hold-up calculated from the tomograms. A new method is used to assess the heterogeneity of the flow and so identify the flow regime more accurately.

Bubble column

Flow-regime transitions are traditionally identified from a graph (Figure 1) of the gas flow rate against the gas hold-up[5] (ε_m).

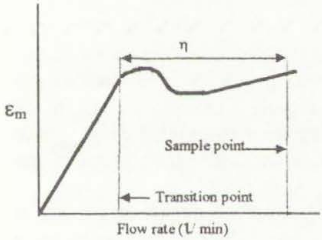

Figure 1: An idealized gas flow rate against gas fraction graph.

A series of sensor measurements taken at different gas flow rates under the same column conditions is called a *set*. In taking the measurements for a set, the flow rate is incremented between successive measurements. From calibration a mean value of the gas voidage in the sensing region is deduced[4] and used to construct a flow curve as in Figure 1. Sensor measurements consist of data taken for 30 seconds at 100 frames per second (3000 frames each based on dielectric pair measurements). Each frame was reconstructed using a linear back projection method.

The liquid in the bubble column was double-distilled water, the width of the column internal diameter 56 mm, and the length 1.025 m. An increase in gas flow rate was capable of producing an ideal succession of flow regimes, from homogeneous bubble flow through transition to churn flow.

Traditional flow-regime identification

Combinations of spargers, frother concentrations, gas flow rate and height were used to give a range of conditions for analysis work.

In practice, the definitions of flow regime are often unclear, with latest research pointing to up to five regimes, and additional gradual transitions between them[6].

Transition points were chosen as points at which the gas flow rate ε_T deviates from the initial straight line through the origin. An example is given in Figure 2.

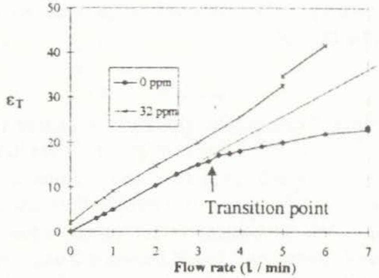

Figure 2: The ε_T values obtained for different flow rates and frother concentrations for a sparger of plain filter cloth.

Note that:

- Transition occurs with 0 ppm frother but not with 32 ppm frother.
- Deviation from the initial straight line is gradual. This makes exact determination of the transition point difficult and may be inaccurate in some cases.

Heterogeneity analysis

In Section 2, the ECT tomogram was used to calculate gas hold-up for various gas flow rates and thereby successfully identify flow-regime transition points in the traditional manner. Only the average gas hold-up over the tomographic cross section was used. There is further information available from the tomogram areas of gas hold-up are associated with spatial locations.

Sets of tomograms and video-recorded sequences were thoroughly inspected. It was observed that when bubbles aggregate or churns form, they tend to do so more often at, or near to, the centre of the column cross section than at the column wall. Thus there is stochastic information available from consideration of the hold-up in central zones relative to those zones near to the wall.

It should also be noted that known artefacts of linear back projection accentuate the above behaviour, producing slightly lower hold-up at the wall when there is large hold-up at the centre. There is also a slight shift of anomalous regions towards the centre of the image. These artefacts however appear to assist distinguishability here.

The mesh shown in Figure 3 was chosen to match the geometry of the 12-electrode sensor whilst dividing the tomogram into zones of interest for bubble-column flow. The entire tomogram comprises 812 pixels and ten equally sized zones.

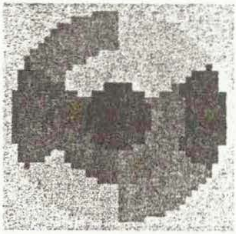

Figure 3: The mesh implemented with the HIT statistic.

Stochastically, the 812 pixel values will be strongly correlated since they arise from only 66 measured capacitances. Their probability distribution will also be complex and dependent upon the dielectric configuration within the sensing volume. Consequently the pixel values in the tomogram were first ranked and only the 812 ranks used to proceed in a distribution-free manner.

Another important consequence of using ranks only (and not pixel values) is that the ranks become independent of the relative scale of the tomogram. Note that the average pixel value was used to identify flow-regime transitions. The ranks are independent of that level and it is only their configuration within the tomogram (heterogeneity or pattern) that is now to be utilized.

For homogeneous flow, bubbles are well dispersed throughout the tomographic cross section whereas for churn flow, bubbles aggregate and coalesce to form churns. Thus for homogeneous flow, pixel ranks will be uniformly distributed apart from clustering induced by correlation from the linear back projection reconstruction procedure, whilst for churn flow, low ranks will dominate in some zones (with high gas hold-up) and high ranks will dominate in others. The change due to heterogeneity is seen to have a much larger effect than that due to correlation.

If the ranks were uncorrelated, which they are not, then the variation between zones could be tested with the well-known Kruskal–Wallis test [7]. Here the test is not valid due to the correlation, but the test statistic H suggested by the test can still be used as a powerful summary of variation between zones. This is then transformed, for reasons relating to work beyond the scope of this paper, to a statistic Z that will be less dependent upon the number of zones produced by the mesh:

$$H = (6/55)*\text{Sum over zones (rank sum squared/number in zone)} - 33$$
$$Z = (H-9)/\text{sqrt}(18).$$

The HIT statistic Z can be regarded as a quantification of heterogeneity or pattern. Large positive values indicate heterogeneity is present.

Plots of the HIT statistic against flow rate, as evidenced in Figure 4, show marked changes between flow regimes. The HIT values plotted have been averaged over all frames (3000 tomograms) taken under identical flow conditions. Thus sharper and more accurate distinguishability is given by considering heterogeneity rather than average gas hold-up. The HIT statistic has proven a reliable indicator of flow regime over the full range of operating conditions imposed in the above sequences of experiments.

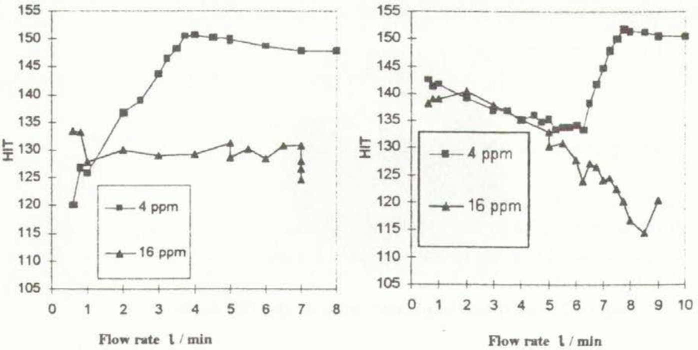

Figure 4: The HIT statistic for the filter cloth sparger (left) and rubber sparger (right).

Figure 4 shows the results from two spargers and two frother concentrations (4 and 16 ppm). For both spargers, with 4 ppm frother, a transition occurs, whilst with 16 ppm the flow remains homogeneous throughout the range of gas flow rates applied. For homogeneous flow the HIT statistic either remains constant or decreases with increased gas flow rate. Transition is clearly identified by a step increase in the HIT statistic. These characteristics were evident throughout the sequences of experiments.

CONCLUSIONS

ECT has been shown an effective tool for the identification of flow regime within a bubble column. The gas hold-up was calculated from the tomogram and used to identify flow regime. A second independent approach, where the HIT statistic Z was used to quantify heterogeneity, produced a sharper more accurate discriminant.

Further work could be undertaken to combine these approaches, using both gas hold-up and spatial heterogeneity. This should improve the discriminant. Alternatively, the two values could be reported to a control system. There is potential to accurately control the gas flow rate at as high a level as practical whilst maintaining homogeneous flow and avoiding disruptive churns. In this way the gas–liquid interface area can be maximized, a benefit in column reactors. For froth-flotation processes, homogeneous flow is maintained whilst maximizing the size of particulates that can be floated. This last can reduce grinding costs in mineral processing.

REFERENCES

[1] N. Reinecke, G. Petritsch, D. Schmitz and D. Mewes, *Tomographic measurement techniques - visualization of multiphase flows*, Chemical Engineering and Technology, **21** (1998) 7–18.

[2] N. Reinecke and D. Mewes, *Tomographic imaging of trickle bed reactors*, Chemical Engineering Science, **51** (1996) 2131–2138.

[3] K. L. Ostrowski, S. P. Luke, M. A. Bennett and R. A. Williams, *Real time visualisation and analysis of dense phase powder conveying*, Powder Technology, in press.

[4] M.A. Bennett, Ph.D. thesis (1999), University of Exeter, UK.

[5] J.A. Finch and G.S. Dobby, (1990) *Column Flotation*, Pergamon Press PLC, Oxford.

[6] P.L. Spedding, G.S. Woods, R.S. Raghunathan and J.K. Watterson, *Vertical two-phase flow - Part I: Flow regimes*, Chemical Engineering Research and Design, **76** (1998) 612–619.

[7] E. L. Lehmann and H. J. M. D'Abrera (1975) *Nonparametrics*. Holden-Day, San Francisco.

Measurements on the mixing of a passive scalar in a turbulent pipe flow using PIV and LIF.

J. Westerweel and L. Aanen
Delft University of Technology
Laboratory for Aero and Hydrodynamics
Rotterdamseweg 145, 2628 AL Delft, The Netherlands

The process of turbulent mixing is encountered in many engineering applications. Of interest are for example: maximum concentration levels, micromixing in relation to chemical reactions, and the influence of coherent structures on mixing. A detailed study of turbulent mixing enables the development of models that can be used in numerical solutions.

To understand the mechanisms of mixing, the simplified case of a stationairy and axisymmetric turbulent flow is considered. The Reynolds averaged equation for the mean concentration is then given by:

$$U_x \frac{\partial \bar{c}}{\partial x} = D\left\{\frac{\partial^2 \bar{c}}{\partial x^2} + \frac{1}{r}\frac{\partial}{\partial r}\left(r\frac{\partial \bar{c}}{\partial r}\right)\right\} - \frac{\partial \overline{u'_x c'}}{\partial x} - \frac{\partial \overline{u'_r c'}}{\partial r}, \tag{1}$$

where x and r are the axial and radial coordinates respectively, U_x is the mean axial component of the velocity, u'_x and u'_r are the axial and radial velocity fluctuations respectively, $\bar{c}$ is the mean concentration, c' the concentration fluctuation, and D the diffusion coefficient.

The term on the left hand side and the first term on the right hand side can be evaluated by separate measurements of the mean velocity and the mean concentration. The remaining terms in the equation are two correlation terms between the fluctuations of the velocity and the fluctuations of the concentration, namely: $\overline{u'_x c'}$ and $\overline{u'_r c'}$. The *only* way to study these terms experimentally it is by means of simultaneous measurement of the instantaneous velocity and concentration fields.

For this purpose two measurement techniques are combined, namely *particle image velocimetry* (PIV) for measuring the velocity, and *light induced fluorescence* (LIF) for measuring the concentration. The optical configuration is shown in Figure 1.

The measurements are carried out in a turbulent flow through a smooth pipe with an inner diameter of 50 mm. The mean flow rate is 106 mm/s, so that the flow Reynolds number is 5,300. This Reynolds number matches that of a direct numerical simulation, which will be used for comparison. The measurements are carried out at distance of 5 m from the pipe inlet. This is 100 pipe diameters, so that the turbulence is fully developed at the measurement location. To reduce image deformation due to light refracted by the curved pipe wall, the pipe at the measurement location is fitted in a rectangular water-filled box (not shown in Fig. 1). In

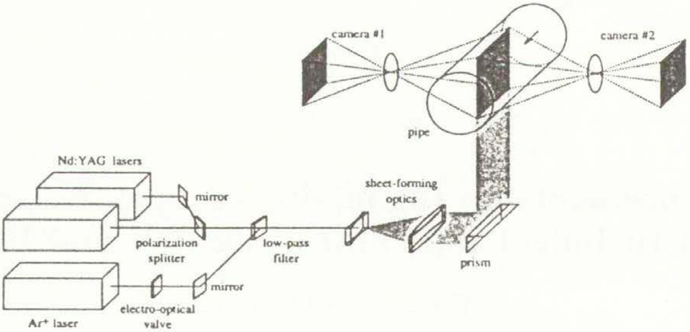

Figure 1: Optical configuration of the experiment.

addition, the pipe wall inside this box has been replaced by a thin glass cylinder with a wall thickness of 1.8 mm. Hence, the image deformation is reduced to within 0.1% of the field of view.

For the PIV measurements the flow is seeded with 5 micron tracer particles that are almost neutrally buoyant in water. A planar cross section of the flow is illuminated with a thin light sheet, and the flow velocity is determined from the displacement of the tracer particles between two exposures. The exposures are generated by a twin Nd:YAG laser system (Spectra Physics PIV-200). Each light pulse has an energy of 200 mJ at a wavelength of 532 nm (viz., green). The light scattered by the tracer particles is recorded by a CCD camera for which the optical axis is perpendicular to the light sheet plane. The camera has a resolution of 992×1008 pixels (Kodak ES-1.0), and its field of view is approximately 45×45 mm^2, i.e. slightly less than one pipe diameter in both the axial and radial directions.

For the LIF measurements the injected fluid is labelled with a fluorescent dye (i.e., fluorescein). The intensity of the emitted fluorescent light is directly proportional to the dye concentration. The fluorescence is induced by the light from a 5 W argon-ion laser (Spectra Physics) at a wavelength of 488 nm (viz., blue). This particular light wavelength is selected by passing the output laser beam through an ethalon. The dye emits fluorescent light at a lower wavelength. The maximum intensity of the fluorescent light is at a wavelength of about 530 nm (viz., green). The fluorescent light is observed by a second camera that is identical to the first camera but that is located on the opposite side of the light sheet. The camera is also equipped with a special filter that only transmits the fluorescent light, so that light that is reflected from the tracer particles and the pipe wall, which maintain the same wavelength as the laser source, is rejected.

The PIV and LIF measurements cannot be carried out at exactly the same time, as the wavelength of the Nd:YAG laser is near the wavelength of the fluorescent light. Instead, the two measurements are carried out separately, but within a total time that is small with respect to the Kolomogorov time scale of the flow, which is about 50 ms. The exposure time delay for

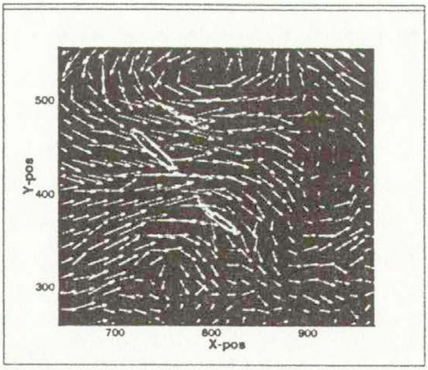

Figure 2: Detail from the result of a combined PIV-LIF measurement.

the PIV measurement is 3 ms, whereas the exposure time for the LIF measurement is 1 ms, so that the total both measurements are carried out within 4 ms, which is well within the Kolmogorov time scale for this flow. Hence, during the measurement period the flow field is essentially frozen, and the PIV and LIF measurements can be considered as simultaneous.

The measurements are performed at a rate of 30 Hz, which is equal to the repetition rate of the twin Nd:YAG system and the frame rate of the cameras. The images are digitized and stored in the memory of a double pipeline processor system (DataCube MaxVideo-200). This system has a total throughput rate of 60 Mbyte/sec, and has a total storage capacity of 256 Mbytes. A complete sequence is recorded in less than 4.5 s, which covers approximately 10 integral time scales.

The PIV images are interrogated in 32×32-pixel interrogation regions, with a 50% overlap between adjacent interrogations. This yields a total of 3,721 velocity vectors per image field. A detail from the result of a combined concentration-velocity measurement is shown in Figure 2.
It should be noted that the LIF image shows only a small amount of dye. This is because the rate at which fluid is injected must be small, in order not to disturb the turbulent flow. Hence, a large number of image sequences is required in order to obtain results in which the sample uncertainty is within acceptable limits. Presently, extended measurements are carried out in which the concentration-velocity correlation tensor is measured from 0.5 to 4.5 pipe diameters from the injection needle, with a total of 12 image sequences per measurement position. The total volume of image data will be 12 Gbyte. The results from these measurements will be presented at the workshop.

SET OF OPTIC-PHYSICAL EQUIPMENT FOR PHASE-STRUCTURE VISUALIZING UNHOMOGENEOUS GAS FLOW IN WIND TUNNEL.

V.A.Yakovlev

Central Aerohydrodynamic Institute (TsAGI), Zhukovsky, 140160, Moscow region, Russia

Resume. Brief description both mobile and stationary set of optical research equipment created for investigations in wind tunnel are presented. Examples of interferograms and holograms, created during experiments in wind tunnel are produced.

Purpose of equipment

The purpose of optical setup is equipping of modern wind tunnels to solve fundamental and applied problems of aerohydrodynamics and aeroacoustics.

Base element of complex

1. System for visualizing two-dimensional and axially symmetric gas flows:
   a) on the basis of mirror interferometers with lateral shift of the wave front – IT-144, IT-228 scheme and general view – Fig. 1, examples of interferograms – Fig. 2).
   b) on the basis of laser holography interferometer IT-243 with four-mirror concept of holographic technique (scheme and general view – Fig. 3, examples of interferograms – Fig. 4).
2. Setup LGU (stationary equipment) and LGU-M (portable version of LGU). Their scheme at Fig. 5 and example of holographic interferogram at Fig. 6 are presented.

Main advantages

Main advantages of new optic-physical equipment in comparison with classical equipment are following:

1. Enlarging the visualization field at 2–3 times (up to 1000mm and more).
2. Solving the problem of three-dimensional structures visualizing within flows.
3. Increasing the information from single experiment-
   a) using shift interferometers – to 2–3 times,
   b) using IT-243 – to 4 times,
   c) using LGU, LGU-M – more, then 4 times.
4. Providing opportunity mobile utilizing new systems at different experimental installations (IT-144, IT-228, IT-243 – in case of 500 mm visualization field).
5. Providing a high technical and economic efficiency of the equipment.

Conclusions

1. Present multifunction set for data acquisition systems with optical research equipment meets major requirements laid by modern gas-dynamics experiments.
2. IT-144, IT-228 and IT-243 systems are successfully using for investigations inhomogeneous non-stationary rapidly elapse processes at different experimental set-ups.
3. LGU system is successively passed experimental exploitation. At complicated conditions of aerodynamics experiment are performed:

a) procedure information recording about three-dimensional flow structures on single flat hologram in light, scattering on surface of model or screen near it,
b) procedure of real and imaginary images of domains stream reconstruction from this hologram for qualitative investigation of flow,
c) procedure of series multiforeshortening holographic interferograms reconstruction for local quantitative information about stream's structure.

First probe processing series of hologram with utilizing tomographic method are performed. The results obtained promising works in this direction are confirmed. Yet, it is necessary to give some financial support for completion all works planed.

4. Our equipment has the following features:
   a) the underlying technical solutions are unique;
   b) a wide selection of scientific and technological issues may be resolved successfully;
   c) the information about obtained during a particular experiment can be increased as compared with traditional analogues;
   d) the devices have high cost effectiveness;
   e) the devices could be perfected further;
   f) the devices could be utilized by other scientific and technological branches for studying unhomogeneous transparent liquid or solid media.

References

1. В.А.Яковлев. Многоцелевой комплекс для оптико-физических исследований в аэродинамических трубах, *Измерительная техника*, стр. 49-53, № 9, 1994 г., Москва.

2. Ф.Н.Горюнов, Н.Н.Морковин, А.Д.Фролова, Г.К.Шаповалов, В.А.Яковлев, Применение голографической интерферометрии для исследования обтекания двумерных моделей, *Уч. зап. ЦАГИ*, том XVII, № 6, 1986 г.

3. В.Г.Беспалов, Ф.Н.Горюнов, В.Н.Крылов, В.Н.Михайлов, Н.Н.Морковин, В.Н.Сизов, Д.И.Стаселько, А.Д.Фролова, Г.К.Шаповалов, В.А.Яковлев. Визуализация фазовой структуры неоднородных трёхмерных течений газа в аэродинамических трубах методом голографической интерферометрии, *Уч. зап. ЦАГИ*, стр. 34-39, том XXIII, №3, 1992 г.

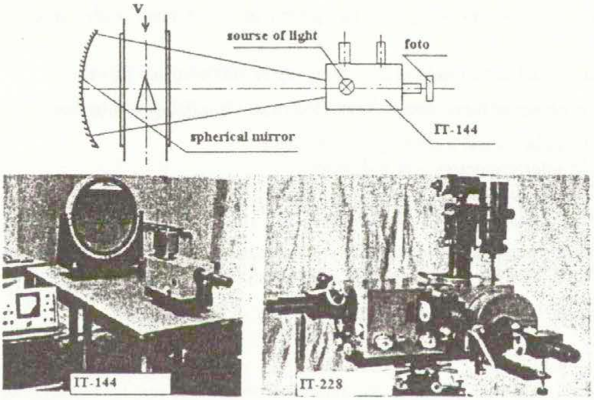

Fig. 1

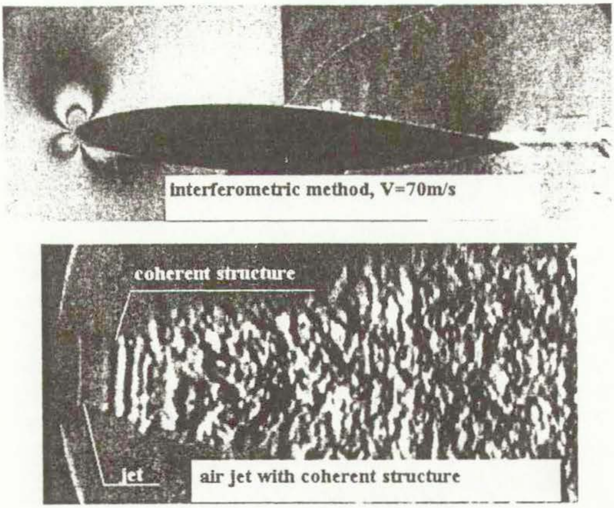
interferometric method, V=70m/s
coherent structure
jet
air jet with coherent structure

Fig. 2

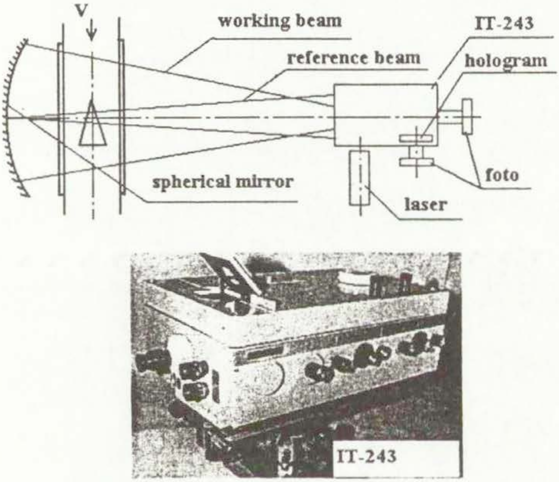
V
working beam
IT-243
reference beam
hologram
spherical mirror
foto
laser
IT-243

Fig. 3

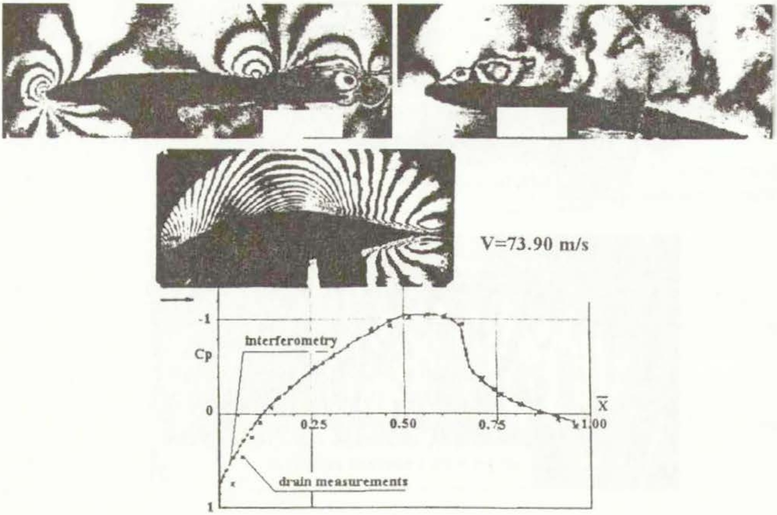

Fig. 4

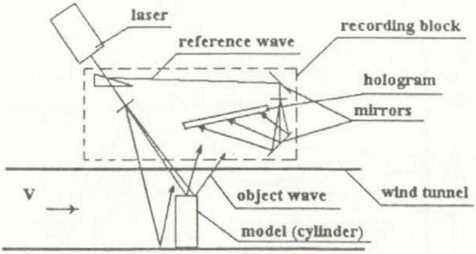

Fig.5

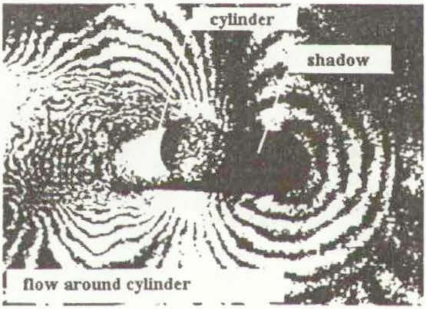

Fig. 6

DIGITAL MICROGRAM PROCESSING IN TRIBODIAGNOSTICS

František Zuzák* and Pavel Mautner*
*University of West Bohemia, Univerzitní 22, 306 14 Pilsen, Czech Republic

Summary: This article presents the image processing techniques suitable for the automation of tribodiagnostics. Processing of digital microgram displaying the wear particles in the lubricating oil gives a set of separated objects representing the wear particles. The feature vectors of objects input the consequent particle classification and machine condition estimation. Therefore, the precise retrieval of all wear particles (i.e. the application of the optimal processing techniques on the microgram) is the crucial problem of computer aided tribodiagnostics.

INTRODUCTION TO COMPUTER AIDED TRIBODIAGNOSTICS

Tribodiagnostics is a non-intrusive machine condition monitoring method. It is based on the microscopic analysis of the oil samples taken from the examined machine. Simply, the lubricating oil in the machine (e.g. gearbox or engine) is contaminated with the debris produced as the result of the wear process of the movable machine parts. The microscopic debris, known as the *wear particles*, is the subject of tribodiagnostics expert's interest. Considering the morphology, dimensions, forms, concentration, distribution and other physical and geometrical features of the wear particles he/she can determine the machine condition, because these particles carry the essential information about the operating conditions under which they were generated. These properties of the wear particles are sufficient to specify the wear mode and predict the machine failure.

Tribodiagnostics consists of the two fundamental subtasks – the *wear particle identification* (including image processing and particle classification) and the *machine condition estimation*. Both of them can be solved in the human-like fashion or with the computer support. Traditional approach requires a large knowledge and experience of a human expert. Moreover, the microscopic analysis of the wear particles is complicated and time-consuming. Furthermore, working with the microscope is uncomfortable and eye-straining. In this point of view, computer aided tribodiagnostics seems to be very helpful and effective method for the workaday wear condition monitoring.

The aim of our work is to automate the expert's visual examination of the *microgram* – the oil sample containing the wear particles. At the first step of our project we tested a variety of suitable image processing techniques. We would like to present achieved results in the following text.

DIGITAL MICROGRAM PROCESSING

The input for our experiments is the matrix of snaps mapping the microgram. These snaps are the output of the color CCD camera integrated to the light microscope and connected to the computer. We obtain the set of 24-bit/pixel color images (standard truecolor BMP pictures, 768x576 pixels) in required magnification (for higher magnification we get better results, but it increases the number of images to process).

When taking the image, the green filter is used on the background and the red one is used to enlighten the wear particles from the top. Hence, the oil appears greenish, dirt is dark grayish and the wear particles are reddish. The intensity of the red color depends on the metallic surface of the particle. Simply, metals are bright red, metal oxides are dark red and non-metal particles are dark red-grayish. Therefore we can easily use the RGB color planes to extract desired objects (red plane for the wear particles, green plane for the oil and dirt and blue one is omitted). We process the red and green color planes separately and we treat them as the gray-level 8-bit/pixel images. However, for the feature extraction, we have to keep it in the mind that the type of the wear particle depends both on its color and intensity.

Now, let us describe the implemented and tested microgram processing techniques.

Preprocessing

The inadequate and/or non-uniform illumination of the microgram is not considered (in this view, the light microscope with the CCD camera produces perfect images). Therefore, no technique solving this problem, such as the local equalization, is used.

For the *noise filtering* we used the neighborhood averaging implemented as the 2D discrete convolution. The Gaussian masks were chosen for the microgram filtration (but the convolution procedure is designed for the usage of the arbitrary mask). The blurring effect of the averaging can be neglected in respect of the microgram character.

Morphological operations of dilation and erosion are also necessary. We use the opening (erosion followed by dilation) for processing of the wear particles in the red plane.

Our goal is to optimize the microgram preprocessing as much as possible (to perform the minimal number of preprocessing steps) to speed up the whole diagnostics process.

Segmentation

Segmentation is the process of finding and separating the objects in the image. In our particular case, the goal of the microgram segmentation is to obtain a set of the separated wear particles (that do not touch the microgram border). It consists of the image binarization, dirt removal and object finding.

Our image *binarization* technique is based on the *optimal thresholding*. We implemented the non-parametric and unsupervised Otsu's method of the automatic threshold selection from the gray-level histogram The Otsu's method is derived from the viewpoint of discriminant analysis. It directly deals with the problem of evaluating the goodness of the thresholds. The optimal thresholds are selected by the discriminant criterion, namely, so as to minimize the separability of the resultant classes in gray-levels. Instead of the gray-level histogram we use the histograms for the red and green planes. The optimal thresholds given by the Otsu's statistical method seems to be adequate for the microgram thresholding.

The objects smaller than the given critical size are considered as the dirt and removed (objects touching the border are displaced as well). Then we can find all objects representing the original wear particles and describe them by the feature vectors (color, texture, size, excentricity, etc.). These vectors are the inputs for the consequent classification. Selection of the appropriate object features for the classification is another task to be solved in the near future.

RESULTS AND CONCLUSION

Digital image processing techniques presented in the previous text fit the demands on the automatic microgram processing in tribodiagnostics. Their sequential application on the microgram produces separated objects corresponding to the original wear particles in the carrier oil.

Since the particles in general do not have the sharply defined edges, we do not use the segmentation by the edge detection (and the edge preserving filtering techniques, such as the median filtering). The texture thresholding is also inappropriate because the oil background does not form any regular texture. The watershed segmentation using the Euclidean Distance Map is not suitable for the separation of the overlapping particles due to the very different sizes of the particles.

The wear particles have the big differences in size, shape, color, intensity etc. This property is quite favorable for the particle classification but it brings a lot of problems to their automatic separation, especially if the particles are overlapping. The disadvantage of overlapping particles and very different types of particles in one image solves the usage of the ferrogram instead of the microgram, but it prolongs the whole diagnostic process due to the preparation of the ferrogram (processing techniques remain the same).

Our experiments were at first performed using the Khoros system. Then the selected methods were implemented in C++ on the platform of Windows 95+.

Finally, let us state that our project is in the beginning and we hope that computer aided tribodiagnostics can save a lot of laborious work and bring a significant cost saving, foreseeing the machine failures in time.

REFERENCES

1. Parker, J.R.: Algorithms for Image Processing and Computer Vision, John Willey & Sons, 1997
2. Russ, J. C.: The Image Processing Handbook, CRC Press, 1995
3. Young, T. Y., Fu, K.: Handbook of Pattern Recognition and Image Processing, Academic Press, 1986
4. Otsu, N.: A Threshold Selection Method from Gray-Level Histograms,
   IEEE Transactions on Systems, Man and Cybernetics, SMC–9/I, 1979, pp 62–66
5. Babinec, F., Dorazil. P., Kolář. D., Mazůrek, I.: Tribodiagnostics, Image Processing and Fuzzy Expert Systems,
   In.: Proceedings of the 4th European Congress on Intelligent Techniques and Soft Computing, pp 1468–1473,
   Aachen, Germany, 1996
6. Fitch, J. C.: The 10 Most Common Reasons Why Oil Analysis Programs Fail And The Strategies That Effectivelly
   Overcome Them, Diagnetics, 1997